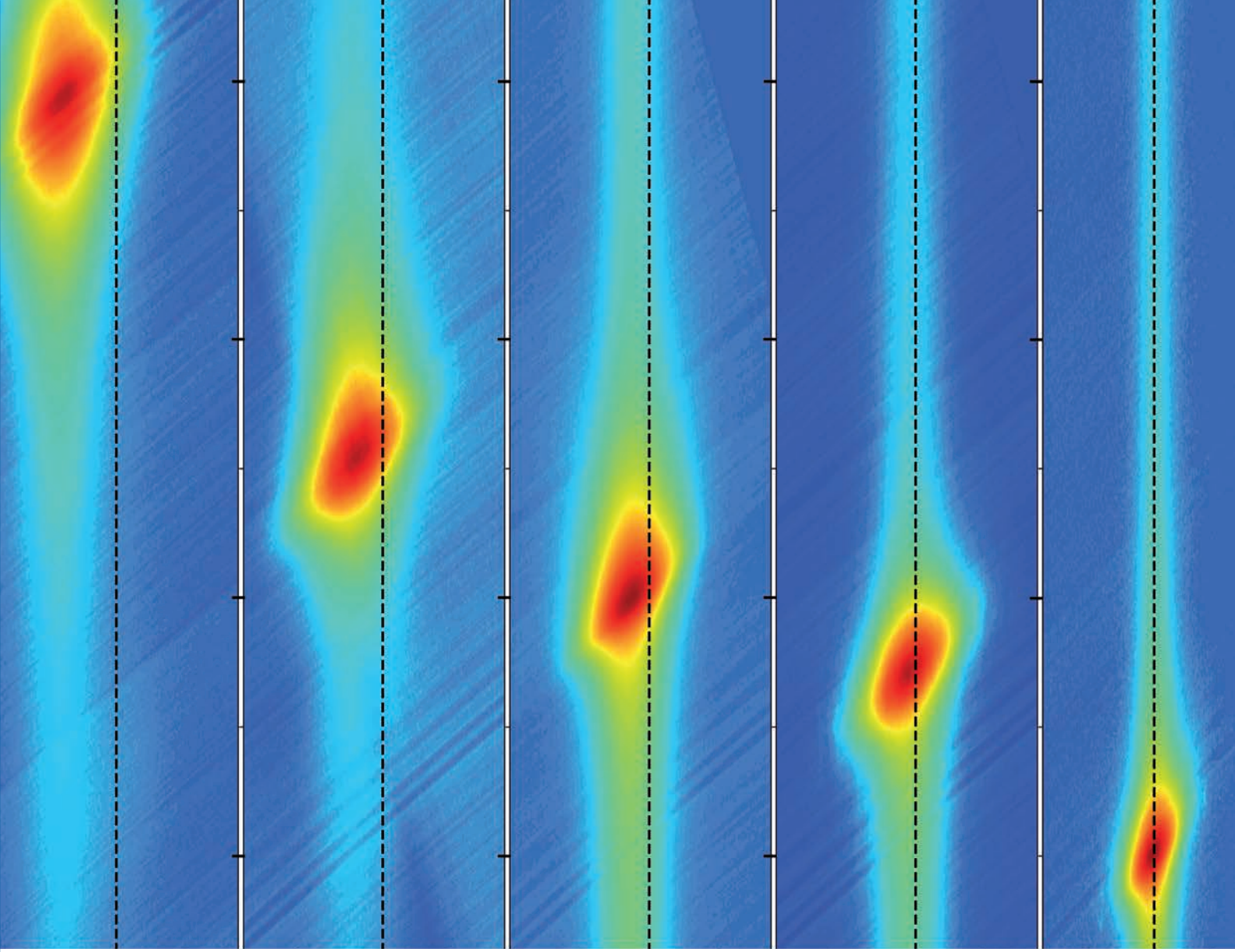

PHOTON SCIENCE 2020.

Highlights and Annual Report

Deutsches Elektronen-Synchrotron DESY
A Research Centre of the Helmholtz Association

Cover

Traditionally, both silicon (Si) and silicon-germanium (SiGe) have a cubic crystal structure. Silicon is extremely successful in the electronics industry and has provided the basis for electronic devices like personal computers and smartphones. However, cubic silicon is not able to emit light, meaning it cannot be used for fabricating light emitting diodes or lasers for optical communication. Si and SiGe with a hexagonal crystal structure, known as hex-SiGe was fabricated. Its hexagonal crystal structure is the key to transforming SiGe into a very efficient light-emitting semiconductor for germanium compositions above 65%. Taking advantage of synchrotron radiation, an international team from the Netherlands, Germany, Austria and Canada measured the crystalline properties of the hex-SiGe polytypes for the first time.

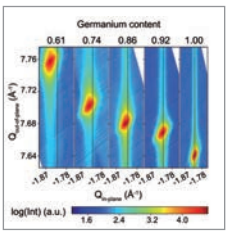

The cover picture shows high resolution X-ray diffraction measurements performed at PETRA III beamline P08. The position of the ($\bar{1}$018) Bragg reflection (in red) shifts as a function of different Ge concentrations from 61% to 100% from left to right (details see page 52/53).

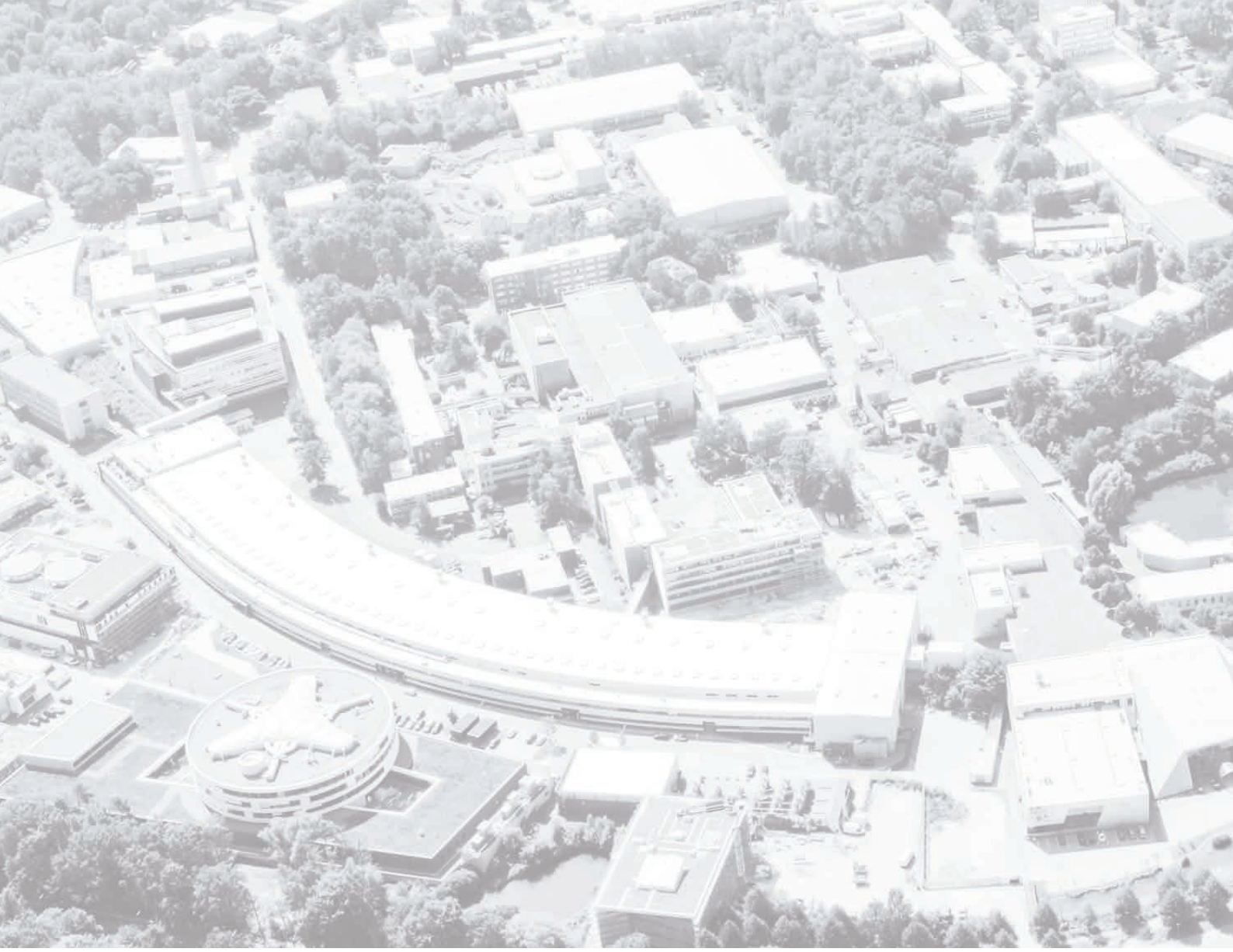

PHOTON SCIENCE 2020.

Highlights and Annual Report

Contents

Publications

The list of publications based on work done at DESY Photon Science is accessible online:
http://photon-science.desy.de/research/publications/list_of_publications/index_eng.html

DESY tries to keep this list as complete and as updated as possible, and relies on the support by all users, who are kindly requested to register their publications via DOOR (door.desy.de).

The year 2020 at DESY

Chairman's foreword

Dear Colleagues and Friends of DESY,

2020 was a truly unusual year for the global society. In March, the coronavirus brought our accustomed everyday life to a standstill and mercilessly exposed the vulnerability of our modern society to such crisis. We will have to put many of our habits, that have finally proven to be unsustainable, to test and find new ways forward. We have already learned a great deal in recent months, most importantly that our society can rely on science and on decision makers who listen to scientists.

We at DESY reacted quickly and very cautiously to the pandemic and moved the research centre into a safe mode that kept the laboratories and our research largely in operation while protecting all staff from infection chains as efficiently as possible.

These measures were critical with respect to the user operation of our large-scale research facilities PETRA III and FLASH. Especially the unique analysis capabilities at PETRA III have proven to be most important for the fight against the SARS-CoV-2 coronavirus. We have to ensure that these technologies will be even more targeted to molecular drug research and even more crisis-proven in the future. To this end, we have drawn up a major proposal for the establishment of a 'National Analysis Center for Molecular Infection Research' in which new digital and technical concepts like artificial intelligence, remote control and robotics are to be incorporated. 'Digital DESY' has become a new building block in our DESY strategy, in response to the challenges of the current pandemic and of future crisis situations. We will

Part of the DESY staff in Hamburg holds the DESY-60 logo.

Senate reception for the 60th DESY anniversary in Hamburg: with forward-looking cutting-edge research into the new decade.

also pay even greater attention to sustainable concepts in all our activities and future projects.

DESY is well on its way into this future. The priority project is PETRA IV which has now entered the technical design phase. We are very pleased that with Riccardo Bartolini, who joined DESY in April 2020, we have been able to attract an internationally renowned accelerator physicist for this future project. In the next few years, the task will be to prepare all the logistical and personnel prerequisites for the upgrade of the synchrotron radiation source PETRA III and to raise the necessary financial resources for this complex project. Nearly all areas of DESY will be involved here in the upcoming decade.

In 2020 we have made good progress in various projects, as in the development of the CMWS, the 'Centre for Molecular Water Science', the commissioning of the Detector Assembly Facility and the construction of the 'Bahrenfeld Start-Up Labs' as well as in the CXNS, the 'Centre for X-ray and Nano Science' which will open next year. An active innovation culture, which interlinks basic research and fast transfer of innovative concepts to the market will remain an integral part of DESY's future strategy.

In the coming years, further projects are on the agenda: Major new construction measures include the DESYUM visitor centre, the building for the accelerator division, the TECHNICUM for technical groups, the DESY Innovation Factory and the 'Wolfgang Pauli Centre' WPC for theoretical physics.

Important research and upgrade projects such as of the free-electron laser FLASH to FLASH2020+, the KALDERA-ATHENA project for future accelerator technologies, the 'Any Light Particle Search' ALPS II, and the telescope in search of dark-matter particles BabyIAXO, as well as the 'Cherenkov Telescope Array' CTA and Data Centre will be implemented. Promoting our top scientists and our young talents is an essential component of the DESY strategy. The new Helmholtz graduate school DASHH has been well-established in 2020. The aim here is to educate the future generation of data scientists who can efficiently analyse measured data by using, e.g. AI or machine learning. This year, we have implemented the COAST programme which will assist our postdocs to shape their individual career pathways. Our HR department has done a remarkable job here. Over the coming months, we must and will develop concepts to offer our top academic performers new career paths within the research centre.

DESY has celebrated its 60th anniversary in the Hamburg City Hall at the beginning of the year. Many congratulations also came from the global science community and have honoured DESY as a world-leading centre in the exploration of matter. We are well-prepared for the coming decades to continue the legacy of DESY.

Even in these challenging times, the extraordinary commitment of the staff and all users and partners, national and international, made research possible at DESY – I would like to thank all who contributed to the joint efforts!

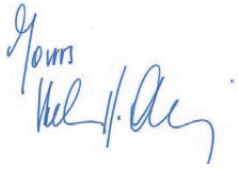

Helmut Dosch
Chairman of the DESY Board of Directors

Photon Science at DESY

Introduction

The DESY site in Hamburg with the curved PETRA III experimental hall 'Max von Laue' in the middle and the 'Ada Yonath' as well as the 'Paul Peter Ewald' halls to the left and right, respectively. The FLASH experimental halls 'Albert Einstein' and 'Kai Siegbahn' are located between the two PETRA III halls on the right side (August 2020).

Dear Colleagues and Friends of DESY Photon Science,

The year 2020 started very promising with an extremely well-attended DESY and European XFEL Users' Meeting end of January. More than 1300 participants from 28 countries registered for this event. At that time, the spread of the SARS-CoV-2 virus was considered to be a rather local epidemic in China. However, this changed quickly. Soon afterwards the 'World Health Organization' WHO classified Covid-19 as a pandemic, that is still severely affecting our lives and also the way we carry out research at large-scale facilities. Not knowing how heavily the coronavirus might hit Germany and other countries, and considering the uncertainties on upcoming lockdown measures and related travel restrictions of user groups, DESY decided to shut down the operation of its user facilties PETRA III and FLASH by mid of March.

However, within a week, first requests for beamtime came from DESY scientists, collaborators and users to contribute to the fight against the pandemic. PETRA III was restarted mainly for SARS-CoV-2-related research already at the end of March. These experiments ranged from screening by X-ray crystallography for possible inhibitors to slow down or even to stop the reproduction of the virus after an infection (DESY, Univ. Hamburg, BNITM, Fraunhofer, EMBL, and many more) over high-resolution X-ray phase contrast tomography of lung and heart tissue from patients deceased due to SARS-CoV-2

(Univ. Göttingen, Medical Hospital Hannover) to SAXS measurements on the bio-physical properties of lipid nanoparticles containing mRNA of the virus as candidates for possible vaccines (Univ. Mainz, BioNTech GmbH, EMBL). A summary of this research is compiled in the 'Corona Special' section and in the EMBL article in this report. Regular operation of PETRA III for users commenced beginning of May under very strict safety measures.

At FLASH, the shutdown period due to the pandemic was used to carry out an important, time consuming safety check of the superconducting linear accelerator, and operation for users restarted at the beginning of August. Of course, user operation under the conditions of a pandemic is different from what we were used to before. Besides strict safety rules as wearing masks, providing negative Corona tests or even quarantine, only few users were allowed to work at the experimental stations at the same time in order to keep the number of personal contacts low. Where possible, mail-in experiments were carried out or users were participating in or controlling the experiments remotely since travel restrictions did not allow them to get on-site. This resulted in a heavy workload for the beamline staff and was also stressful for many users since a number of scheduled experiments had to be shifted to next year. Despite all challenges, the lessons that we learned during this year will help us in defining the requirements for an increased fraction of mail-in and remote experiments in the future for a more sustainable operation scheme.

European XFEL also went into a safety shutdown during spring and resumed operation in summer. Significant progress has been made in the implementation of the instrumentation of the three major user consortia (SFX, HiBEF, hRIXS) with DESY participation.

Despite the pandemic situation, the progress for planning the upgrades of our large-scale photon science facilities was hardly slowed down, even if many people were in home office and nearly all meetings were organised as video conferences. For both future upgrade projects, PETRA IV and FLASH2020+, conceptual design reports were published by the end of 2019 and work on the detailed technical designs has started. Even though a series of scientific instruments workshops for PETRA IV was organised as video conferences there was a huge enthusiasm among the user community reflected in almost 1400 registered participants in total.

In order to prepare a joint future strategy for a complementary ensemble of photon sources in Germany, Helmholtz-Zentrum Berlin (HZB), Helmholtz-Zentrum Dresden-Rossendorf (HZDR) and DESY have finalised a 'National Photon Science Roadmap' document.

Unfortunately, the pandemic situation also affected construction work on-site. Therefore, the building for the Center for X-ray and Nano Science (CXNS) including the DESY NanoLab will get ready in spring 2021 with slight delay. In addition to the already existing partners Helmholtz-Zentrum Geesthacht (HZG) and the Kiel University (CAU), the Hamburg University of Technology (TUHH) and the Institut für Kristallzüchtung in Berlin (IKZ) joint in as new partners into this scientific activity. Furthermore, the proposed Center for Molecular Water Science (CMWS) has been pushed forward with the well-attended 'DESY Water Week' forum before the lockdown. A white paper on the CMWS science activities is close to completion.

The year 2020 was exceptional due to the pandemic situation both for research and in particular for the user operation at our facilities. I would like to thank everyone who has helped to ensure that we could continue to do science even under these difficult conditions. Finally, I wish us all that the newly approved vaccines will ease the situation and allow us to return towards normal life during 2021.

Edgar Weckert
Director DESY Photon Science

News and Events

News and Events

A busy year 2020

January

29 – 31 January:
The Annual joint Users' Meeting of DESY Photon Science and European XFEL

During the joint DESY Photon Science and European XFEL Users' Meeting, 1300 scientists from 28 countries discussed research at the local X-ray light sources. The Users' Meeting was accompanied by 20 satellite meetings and workshops mainly dedicated to technical developments at the facilities, as well as more than 400 scientific posters and an industrial fair. Central topics were the plans for DESY's free-electron laser FLASH and the planned expansion of the synchrotron radiation source PETRA III to a fourth-generation light source, PETRA IV. The technical design report (TDR) phase of the PETRA IV project started on 1 January 2020.

February

7 February:
HELIOS: Helmholtz Association and City of Hamburg support German-Swedish Graduate School

The new 'Helmholtz-Lund International Graduate School' (HELIOS) is intended to create educational opportunities for 22 doctoral students in Hamburg and Lund (Sweden) over two three-year periods. Students at both locations have the opportunity to acquire the skills needed to plan, conduct and evaluate results from complex research experiments to study matter on different time and length scales. The international school is funded by the three partner institutions as well as by the Helmholtz Association of German Research Centres (HGF) and the Hamburg Ministry of Science, Research, Equalities and Districts (BWFGB).

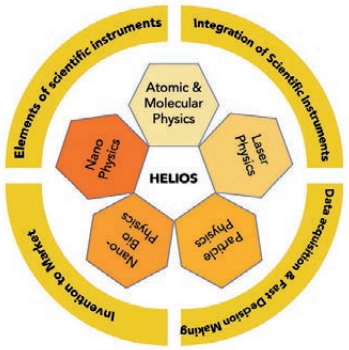

17 February:
Francesca Calegari is vice chair of the new international network 'AttoChem'

Francesca Calegari, lead scientist at DESY and professor at the Universität Hamburg, is vice chair of a new EU-funded international network on attosecond chemistry. The AttoChem network aims at investigating the course of chemical reactions using attosecond laser beams. The research network has been established in the framework of The European Cooperation in Science and Technology (COST), whose mission is to provide networking opportunities for researchers and innovators to strengthen Europe's capacity to address scientific, technological and societal challenges.

March

19 February:
EU and Russia strengthen scientific cooperation

Research institutes from the EU and Russia will cooperate even more closely in the future. For this purpose, 35 partners have joined forces in the EU project ‘CREMLINplus’, coordinated by DESY, ten of them from Russia and 25 from the EU and associated countries. During the kick-off meeting at DESY with about 100 representatives of the participating institutions, the Russian Ministry of Research announced in-kind contributions worth 15 million Euro for the project. The European Union is funding the four-year project with 25 million Euro within the framework of the EU's Horizon 2020 research framework programme.

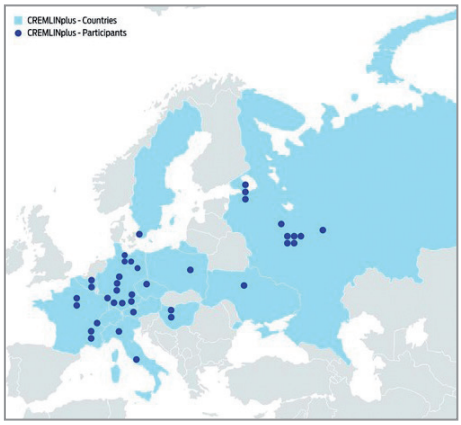

25 – 28 February:
DESY water week

Almost 200 researchers from 15 countries met at the ‘DESY water week’ to work on a White Paper for the planned Centre for Molecular Water Science (CMWS), which will concentrate research efforts in the field of molecular processes in water and at water interfaces in the future.

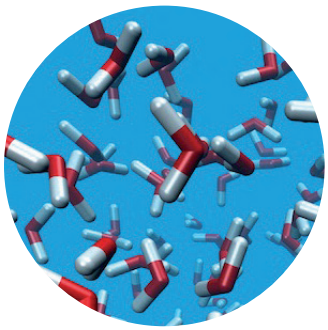

21 March:
DESY operates in reduced mode due to the corona pandemic

DESY has entered a reduced operating mode as a measure against further spread of the coronavirus. Both sites in Hamburg and Zeuthen remained open, however, employees worked in home offices as far as possible to reduce their presence on campus to the required minimum. Particle accelerators and other facilities have been put into a so-called ‘safe mode’. The X-ray source PETRA III remained in standby mode to be able to rapidly restart for SARS-CoV-2-relevant research.

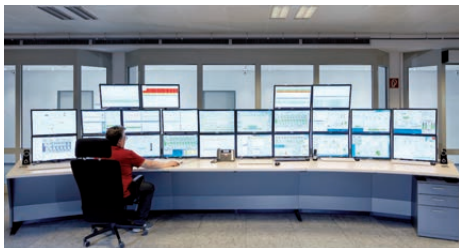

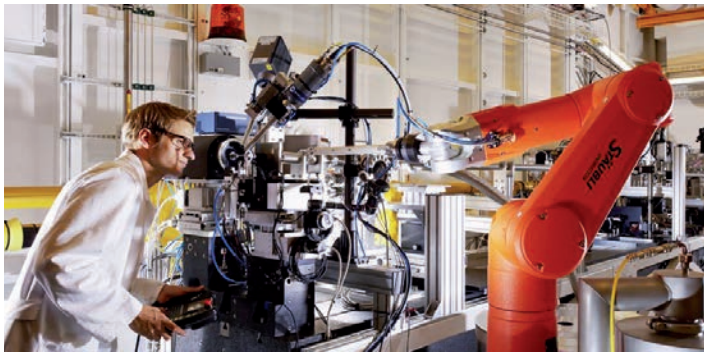

31 March:
PETRA III restarts operation for X-ray screening to identify potential candidates for corona drugs

With the help of DESY’s X-ray light source PETRA III, a research team started to screen candidates for possible active substances that bind to a main protease of the coronavirus SARS-CoV-2. This was the first experiment which was conducted within the frame of the ‘fast track access’ to PETRA III for corona-related research. For further information on this and other projects, refer to the ‘Corona Special’ section in this report.

May

4 May:
Henry Chapman becomes a Fellow of the Royal Society

The Royal Society has elected DESY researcher Henry Chapman as a Fellow. The DESY lead scientist and professor at the Universität Hamburg is a pioneer of lensless imaging using X-ray lasers and has provided previously unattainable insights into the inner structure of matter with the numerous methods he has developed or proposed. Chapman is regarded as the pioneer of serial femtosecond X-ray crystallography which, among other things, makes it possible to explore the spatial structure of sensitive biological molecules with atomic precision even under near-functional conditions. The Royal Society of London for Improving Natural Knowledge is the oldest national scientific society in the world.

4 May:
DESY begins transition to operation during the corona pandemic

DESY started with an adjustment of the reduced operating mode after the decisions of the federal and state governments on cautious relaxation of the corona measures. This included a restart of the research facilities and a resumption of a large part of the research operations at the DESY sites in Hamburg and Zeuthen.

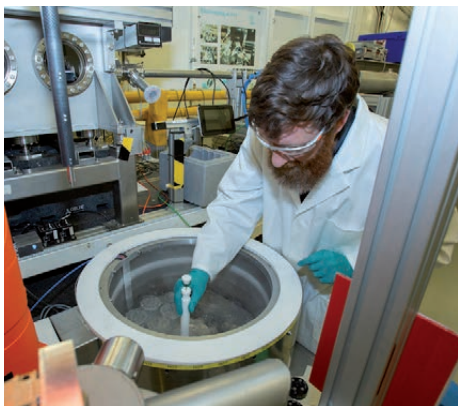

July

3 July:
FLASH2020+ technical design phase started

The technical design phase of the FLASH2020+ project at DESY started with an internal virtual kick-off meeting. Over 270 participants, mainly from DESY and the campus in Hamburg, joined the project team online. Key topics were the upgrade project of the free-electron laser FLASH, scientific goals, the embedding at DESY and into the international scientific landscape, the project structure, and its timeline over the next five years.

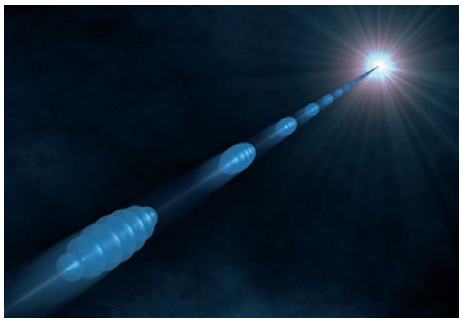

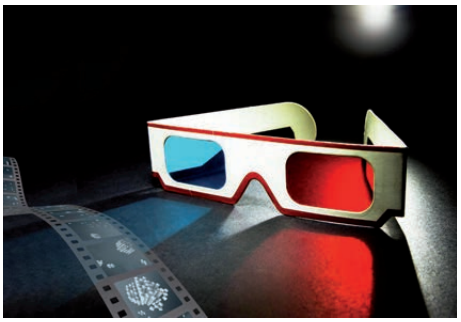

28 July:
3D-view of the nanocosm

A German-Swedish collaboration of three research groups from Universität Hamburg, DESY and KTH Royal Institute of Technology in Stockholm (Sweden) has been awarded a grant in the framework of the ‘Röntgen-Ångström Cluster’. In their joint project ‘XStereoVision’, the scientists will develop a new X-ray imaging technique for 3D *in situ* investigations of nanoparticle formation in liquid environments on the nanoscale.

August

20 August:
Tailor-made crystals for research

The cooperation between DESY and the Leibniz Institute for Crystal Growth (IKZ) in Berlin will become closer in the future. The IKZ will establish a branch office on the campus in Hamburg. The use of tailor-made crystals is of great importance in research with synchrotron radiation sources. They are the object of research themselves, serve as reference objects as well as carrier material and are used in a variety of fields.

25 – 26 August:
MOLEC scientific highlights online workshop

The 23rd 'European Conference on the Dynamics of Molecular Systems' (MOLEC 2020) in Hamburg was cancelled and postponed to August 2022 due to the global Covid-19 pandemic. Instead, an online workshop was held to highlight the most recent advances in molecular physics and to foster scientific discussions on the most important breakthroughs regarding the topics of the MOLEC conference.

September

1 September:
The bacteria whisperer

Holger Sondermann joined DESY's team of lead scientists, the first biologist ever to do so. At the beginning of August 2020, he started working at the Center for Structural Systems Biology (CSSB) and as a professor at Kiel University, leading a team of scientists who will observe the communication between bacteria – and might find new approaches to combat pathogens along the way. With the help of X-ray crystallography and complementary techniques, Holger Sondermann wants to better understand how bacteria form biofilms.

15 September:
Aminoff Prize for Henry Chapman

DESY lead scientist Henry Chapman will receive the Gregori Aminoff Prize for Crystallography 2021 from the Royal Swedish Academy of Sciences in Stockholm (Sweden). Together with Janos Hajdu from the University of Uppsala and John Spence from Arizona State University, Chapman will be honoured for 'fundamental contributions to the development of X-ray free-electron laser-based structural biology', as the academy announced. Most processes in cells and organisms are controlled by proteins, making them the target of nearly all therapeutic drugs. The crystals formed by proteins diffract X-rays, allowing detailed atomic-level information about their molecular structure to be determined using X-ray crystallography. This is vital for understanding how these biomolecules function and can help with the development of novel and improved drugs.

14 – 16 September:
Science@FELs 2020 virtual conference attracted record virtual attendance

The Science@FELs conference is organised biannually by the 'FELs of Europe' collaboration and has evolved into one of the most important international conferences in free-electron laser (FEL) science, highlighting scientific progress made in this field. With a record registration number of more than 700 participants for the first virtual edition of this conference, internet cables were 'running hot' from 14 – 16 September 2020 to host the exchange of most recent results from FELs around the world. This year's 'FELs of Europe' prize in recognition of recent work for scientific excellence in the area of FEL science and applications was awarded to Dr. Rebecca Boll (European XFEL) 'for her outstanding research on multiple ionisation of rare gases and photoinduced dynamics of ring-type molecules'.

October

19 October:
PETRA IV workshops

In a series of four workshops from October to November 2020, the science case and technical requirements for the ultralow-emittance storage ring PETRA IV were discussed with experts and future users from many fields of science. Within the process of developing the PETRA IV 'scientific instrumentation proposals' (SIPs), the dedicated PETRA IV workshops were aiming to strengthen the scientific exchange among different user communities.

November

18 November:
EU innovation funds for five DESY projects

Research projects under DESY coordination or with DESY involvement will receive more than 48 million Euro from the European Commission over the next four years. These European projects range from driving innovation in synchrotrons and free-electron lasers to nanotechnologies showcasing DESY's varied fields of expertise and its drive for innovation and close ties to industry. Four of the five projects succeeded within the European Commission's Horizon 2020 programme under a special 'Innovation Pilots' call that aims to guide the Commission in designing the upcoming 'Horizon Europe' programme. The League of European Accelerator-based Photon Sources pilot project (LEAPS-INNOV), with Elke Plönjes being the scientific coordinator, will foster open innovation for accelerator-based light sources in Europe.
DESY scientists Franz Kärtner, Tobias Herr and Neetesh Singh, together with a European consortium, have been awarded a FET (Future Emerging Technologies) Open project for the development of an integrated femtosecond laser in chip format. The Horizon 2020-funded project 'Nanoscience Foundries and Fine Analysis' (EU-NFFA) will continue its transnational user access programme as strengthened research infrastructure 'NEP' (NFFA-Europe-Pilot).

November 2020:
Helmholtz funding for new teams at DESY Photon Science

Researchers from DESY Photon Science have applied successfully for Helmholtz funding. Sadia Bari (bottom right), who leads a Helmholtz Young Investigator group at DESY, will receive funding for first-time professorial appointments. With her research she focuses on probing the dynamical local structure of isolated to solvated proteins. In addition, three Helmholtz Young Investigator Groups will be founded at DESY. Researcher Andrea Trabattoni (bottom left) will work on time-resolved spectroscopy of photo-induced electron dynamics, Thomas J. Lane (top left) investigates photoactive biological systems and Tobias Herr (top right) works on ultrafast nonlinear microphotonics.

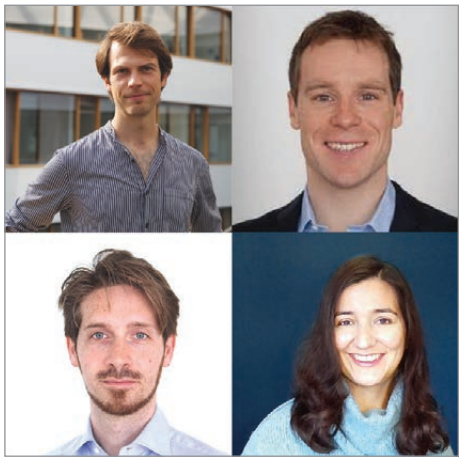

23 November:
Melanie Schnell to receive 2020 B. H. Wiik Prize

DESY lead scientist Melanie Schnell was awarded the 2020 Bjørn H. Wiik Prize. She is also a professor at Kiel University and received this prestigious science prize, awarded by the research center DESY, for her pioneering work in molecular microwave spectroscopy and for her leading role in setting up the CMWS at DESY. Melanie Schnell is one of the international frontrunners in the field of molecular spectroscopy and has moved the field forward decisively by developing a special experimental method, known as microwave three-wave mixing, which is based on the method of rotational spectroscopy. The technique is capable of distinguishing between so-called chiral molecules, which exist in two mirror-symmetrical forms but normally look identical spectroscopically.

December

9 December:
FLASH2020+ kick-off meeting

The FLASH2020+ kick-off meeting was held online. Within FLASH2020+, a major upgrade of the FLASH facility is planned within the next five years. While the whole machine will get an energy upgrade, the undulator line FLASH1 will be enhanced with a variable gap undulator section and high repetition rate external seeding. FLASH2 will aim for shorter pulses and also variable polarisation. New pump-probe laser systems will deliver synchronised pulses across the whole optical spectrum and beyond.

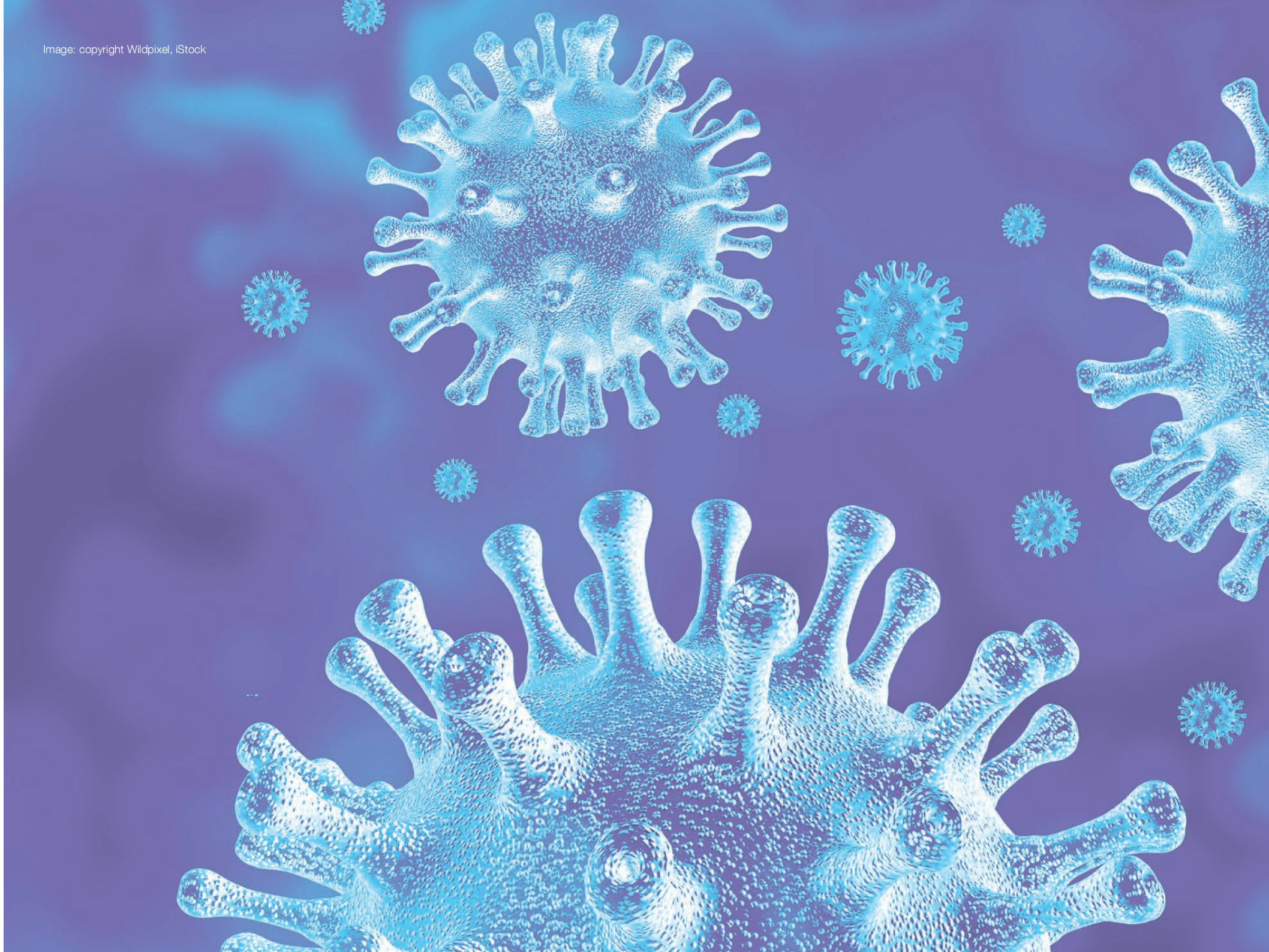

Image: copyright Wildpixel, iStock

Corona Special

Corona-related research at DESY Photon Science

The Covid-19 pandemic is an enormous challenge for our society, and science is essential to resolve urgent questions arising in this situation. Since new findings and concrete solutions for fighting the SARS-CoV-2 pathogen are required within a very short time, worldwide collaborations between scientists are crucial in response to this crisis. Also researchers from DESY, its campus partners and users of its facilities are contributing in various ways. DESY's light sources are ideal tools for studying the virus and possible drugs at the molecular level.

Within a very short time, DESY and other national and international research institutions started to offer ‘fast track access’ for scientific users from academia or industry to perform research related to the fight of the Covid-19 pandemic at their light sources and facilities. Furthermore, DESY supported SARS-CoV-2-related research projects by providing strategic funding in the frame of the ‘DESY Strategy Fund’ (DSF). Examples of ongoing projects are illustrated in this section. Additional information on DESY partners’ activities is described in the ‘Campus and Collaboration’ section of this report.

Corona Special

Corona-related research at DESY Photon Science

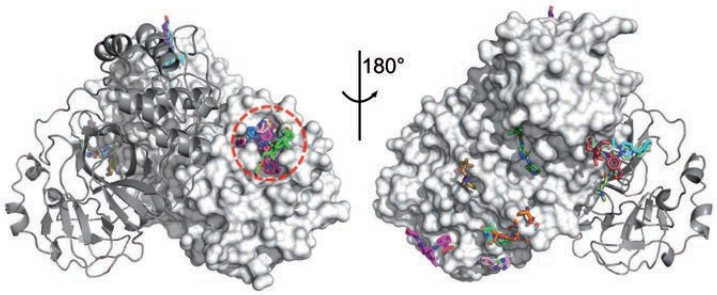

37 compounds from the screening campaign bind at different sites of Mpro.

Massive X-ray screening against the SARS-CoV-2 main protease

A collaboration with more than 100 scientists, mainly coming from the Hamburg area, has performed a large screening campaign to identify new drugs against the main protease (Mpro) of the SARS-CoV-2 virus. For this, 5953 individual compounds from two drug repurposing libraries were co-crystallised with the main protease. Almost 8000 crystals were then subjected to X-ray structure determinations at the PETRA III beamlines P11, P12 and P14 over a period of one month. In total, diffraction data from 3955 different compounds were collected, with 1152 data sets being suitable for automatic data processing. From inspection of the resulting electron densities, the scientists identified 37 different compounds binding to Mpro with the majority binding to the active site. These hit compounds were subsequently tested for their antiviral activity in 'Vero E6' cell cultures at the Bernhard Nocht Institute for Tropical Medicine, Hamburg, and indeed 6 compounds showed a more than 100-fold reduction in viral RNA levels in combination with a favourable cytotoxicity. Two compounds show an antiviral activity with an EC50 (effective concentration at which a half-maximal effect is observed) smaller than 1.5 µmol. Interestingly, the research team also identified novel inhibitors with antiviral activity binding at two allosteric binding sites outside the catalytic cleft of Mpro.

In addition, the methods developed during this effort have laid the basis for future drug screening campaigns against target proteins from other infectious diseases.
(*PETRA III Corona fast track access*)

Contact: Alke Meents (DESY)

Structure-based design of inhibitors of the SARS-CoV-2 main protease

After having published the first crystal structure of the SARS-CoV-2 main protease (Mpro) in early 2020 (DOI:10.1126/science.abb3405, diffraction data sets collected at BESSY, Berlin, Germany), we used PETRA III beamline P11 to collect diffraction data from several complexes of the enzyme with candidate inhibitors. We further elucidated the structures of the Mpro in complex with the repurposing candidates boceprivir and telaprivir. Finally, we determined the crystal structure of a molecular probe in complex with the Mpro which can be used to detect the virus in human samples even seven days or more after infection (DOI:10.1038/s41589-020-00689-z).
(*PETRA III Corona fast track access*)

Contact: Linlin Zhang and Rolf Hilgenfeld (Institute of Molecular Medicine, University of Lübeck)

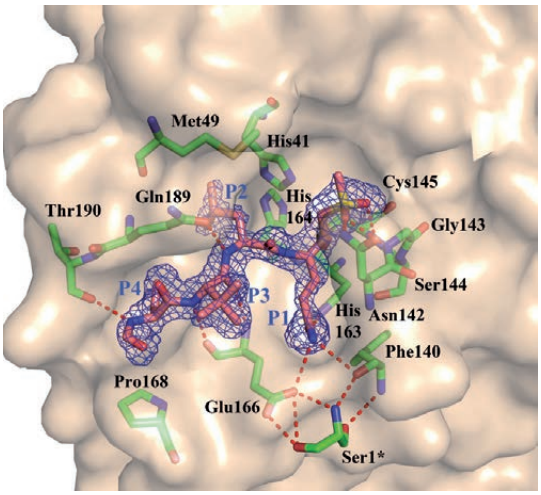

Crystal structure of a molecular probe in complex with the SARS-CoV-2 Mpro. (Image: Linlin Zhang)

Polymorph stabilities of pharmaceuticals used in the treatment of Covid-19

A DESY research team investigates polymorph stabilities of antiviral drugs by X-ray diffraction at the PETRA III beamline P02.2 which is optimised for research at extreme conditions. New polymorphs realised by high pressure of several GPa may have improved therapeutic properties or identify limitations of the marketed form. Single crystals, suitable for structural studies, are exposed to high pressures in order to induce phase transitions. Recent experiments indicate nitazoxanide transforms at ~ 6 GPa.
(*PETRA III Corona fast track access*)

Contact: Nico Giordano and Hanns-Peter Liermann (DESY)

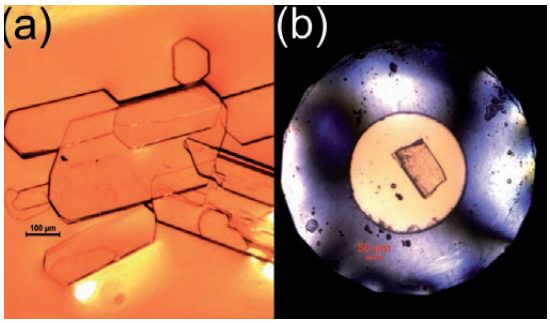

(a) Nitazoxanide single crystals grown in the lab and (b) a single crystal of nitazoxanide loaded in the pressure cell at 0.2 GPa.

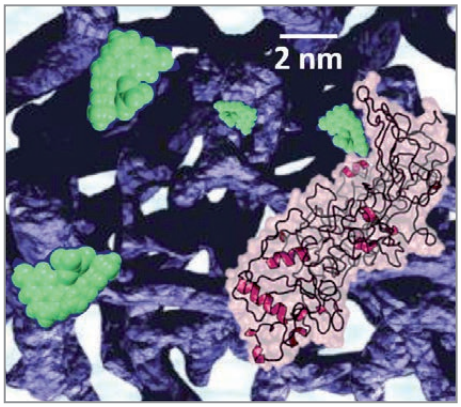

Nanosized low-dose anti-Corona drug (green) embedded in a novel drug template (violet/white). Electron density and the backbone structure of a peptide unit involved in the mesh is depicted in pink.

Mechanisms of antiviral medication

The research team from KTH Stockholm and DESY investigates various low-dose drug delivery options for local, antiviral medication of drugs with severe medical side effects and which therefore require careful dosing. Nanostructures of the investigated novel drug template (hydrogel mesh) can be tuned in their hydrophilic and lipophilic characteristics. The studied drugs include selected examples of the SOLIDARITY project recently launched by the WHO against SARS-CoV-2. The study makes use of *in situ* and time-resolved grazing incidence X-ray scattering at the PETRA III beamline P03 equipped with modern Lambda Medipix-based detectors which are essential for high-speed and high-resolution investigations, at the same time greatly enlarging the *q*-range.
(*PETRA III Corona fast track access*)

Contact: Simone Techert and Stephan Roth (DESY)

High-throughput antibody screening

The scientists working on this project aim to determine the specific ways that antibodies bind to the spike protein of SARS-CoV-2 using a new analysis pipeline that joins cryo-electron microscopy (cryoEM) of the components and their complexes together with time-resolved small-angle X-ray scattering (SAXS) of solutions as they are mixed together. Using novel fast jet-injection technologies, the team intends to find the antibodies with the highest binding affinity to the spike surface protein. They will characterise most specific antibody binding using cryoEM thereby assessing the specific interference in host-cell infection. (*DSF-funded*)

Contact: Henry Chapman (CFEL, DESY),
Carolin Seuring (CSSB, UHH), Cy Jeffries (EMBL)

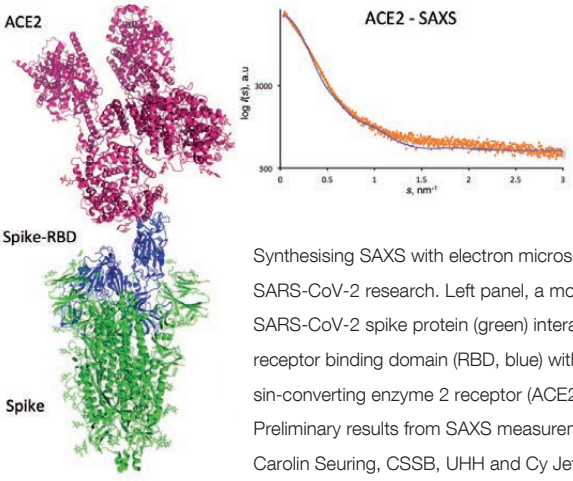

Synthesising SAXS with electron microscopy for SARS-CoV-2 research. Left panel, a model of the SARS-CoV-2 spike protein (green) interacting via its receptor binding domain (RBD, blue) with the angiotensin-converting enzyme 2 receptor (ACE2). Right panel: Preliminary results from SAXS measurement. (Image: Carolin Seuring, CSSB, UHH and Cy Jeffries, EMBL)

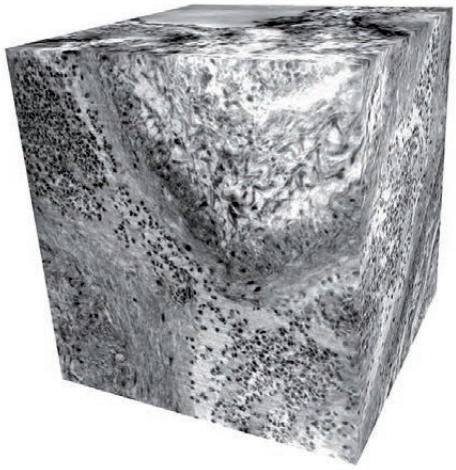

3D virtual histology of lung tissue effected by Covid-19. (Image: M. Eckermann, T. Salditt, Univ. Göttingen)

3D virtual histology of lung and heart tissue affected by severe cases of Covid-19

A research team from University of Göttingen and Medizinische Hochschule Hannover investigated the histo-pathology of human lung and heart autopsies affected by severe cases of the Covid-19 disease. X-ray phase contrast tomography carried out at PETRA III beamline P10 GINIX holo-tomography end station adds a third dimension to conventional pathology and allows tracking small capillaries and alveoli walls in three dimensions. These investigations revealed significant structural alterations of the tissue due to the Covid-19 disease. For more information, see contribution to the 'Scientific Highlight' section of this report.
(*PETRA III Corona fast track access*)

Contact: Tim Salditt (Univ. Göttingen), Mark Kühnel and Danny Jonigk (Hannover Medical School)

Automated X-ray crystallography data collection and analysis

Extensive X-ray screening campaigns depend on the ability of reliably capturing, storing and disseminating data and metadata. With this in mind, scientists designed and deployed a database which recorded about 6000 diffraction data sets collected at PETRA III beamlines P11, P13 and P14 and more than 50000 analysis results produced by different tools. Thanks to DESY Strategy Funds the team is now improving and extending this prototype database, and addressing automation of data collection and analysis. (*DSF-funded*)

Contact: Luca Gelisio (DESY)

Interaction between the SARS-CoV-2 envelope protein and biomembranes

A research team from DESY, University of Leipzig, Nanyang Technology University and University of Vienna studied interactions between the SARS-CoV-2 envelope protein and reconstituted model biomembranes at the PETRA III beamlines P08, P23, P12 (EMBL) and the EMBL SPC facility. This protein enables the viral core to be encapsulated by the ERGIC membrane of infected cells. The findings will aid the understanding of the viral assembly mechanism and help to design drug candidates that target the viral replication process. (*PETRA III Corona fast track access*)

Contact: Gianluca Bello and Richard Harvey (Universität Wien), Chen Shen (DESY), Jaume Torres (Nanyang Technological University) and Christian Wölk (Universität Leipzig)

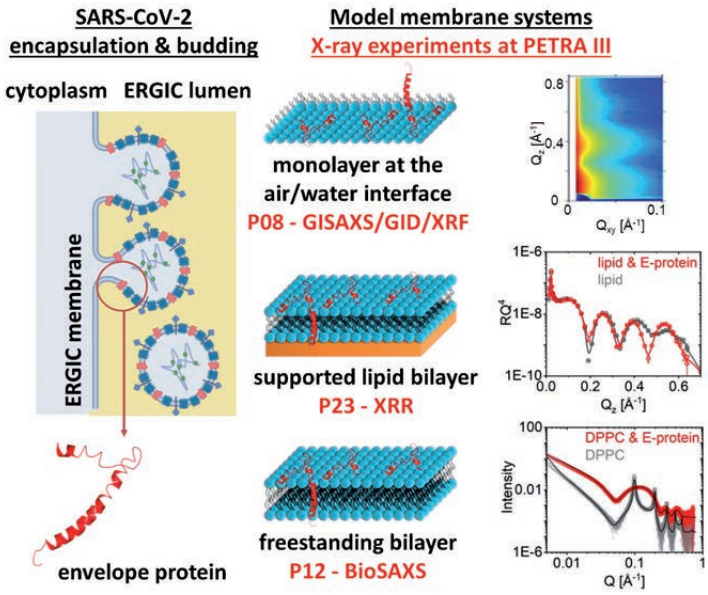

Overview of the work carried out to study the interaction between SARS-CoV-2 envelope protein and biomembranes.

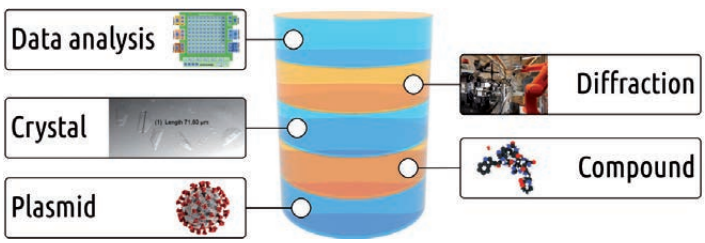

Database addressing automation of data collection and analysis.

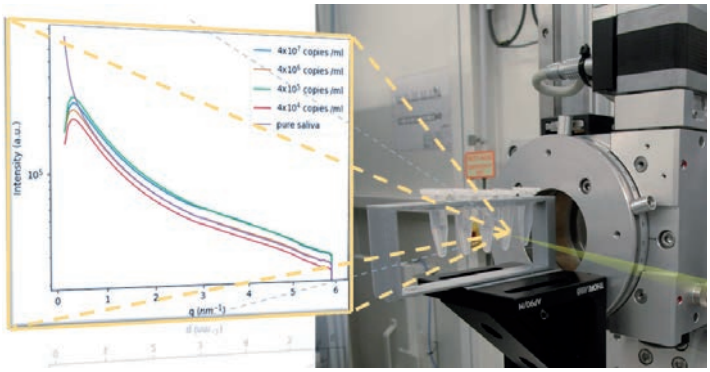

High-throughput setup for detecting SARS-CoV-2 in saliva samples using SAXS.

Concentration of the SARS-CoV-2 virus in saliva specimens

Considering no specific drugs or vaccines are yet available for Covid-19, early diagnosis and management are crucial for containing the outbreak. Therefore, scientists are investigating the potential of SAXS to detect and determine the concentration of the virus in saliva specimens. Very promising results were obtained in the first trial at PETRA III beamline P08 which encouraged the team to check the suitability of SAXS as provided at PETRA III beamline P03 in detecting SARS-CoV-2 and Influenza A viruses and to verify if there is a competition between both for resources.
(*PETRA III Corona fast track access*)

Contact: Andre L. C. Conceição (DESY) and Sylvio Haas (DESY)

Photocatalysts may clean air from coronavirus

Titanium oxide photocatalysts irradiated with UV light can play an active role in the inactivation of SARS-CoV-2. A detailed chemical characterisation of the virus/TiO_2 interface, bond breaking and formation by UV light will be investigated by HAXPES and GISAX at PETRA III beamlines P22 and P03 in combination with complementary techniques, such as focused ion beam and scanning electron microscopy at the DESY NanoLab. First experiments performed at Elettra SuperESCA beamline confirmed a strong adsorption of protein on TiO_2 and the UV light-induced changes. The result of this study may provide a framework for the development of efficient air purification technologies by self-cleaning TiO_2 using sustainable energy. (*DSF-funded*)

Contact: Heshmat Noei (DESY) and Christoph Schlueter (DESY)

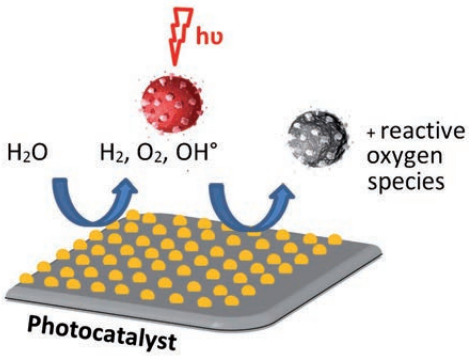

Schematic image of the photocatalyst's function.

Inhibitor screening and structural characterisation of virulence factors from SARS-CoV-2

Research groups from DESY, FZJ, HZI, CSSB, UHH and Fraunhofer IME joined forces to identify novel therapeutics against SARS-CoV-2. Using a high-throughput screening approach, compound libraries of approved drugs will be used for the discovery of potent inhibitors for enzymes involved in the coronavirus replication–transcription complex. Structural determination of the enzyme-inhibitor complexes will reveal the binding mode of the identified inhibitors, the *in vivo* efficacy of which will be evaluated in a future stage of this project. (*DSF-funded*)

Contact: Johanna Hakanpää (DESY), Michael Kolbe (HZI, UHH, CSSB), Björn Windshügel (Fraunhofer IME, ScreeningPort, Hamburg, UHH), Jörg Labahn (FZJ, CSSB), Spyros D. Chatziefthymiou (DESY), Maria Kuzikov (Fraunhofer IME, ScreeningPort, Hamburg)

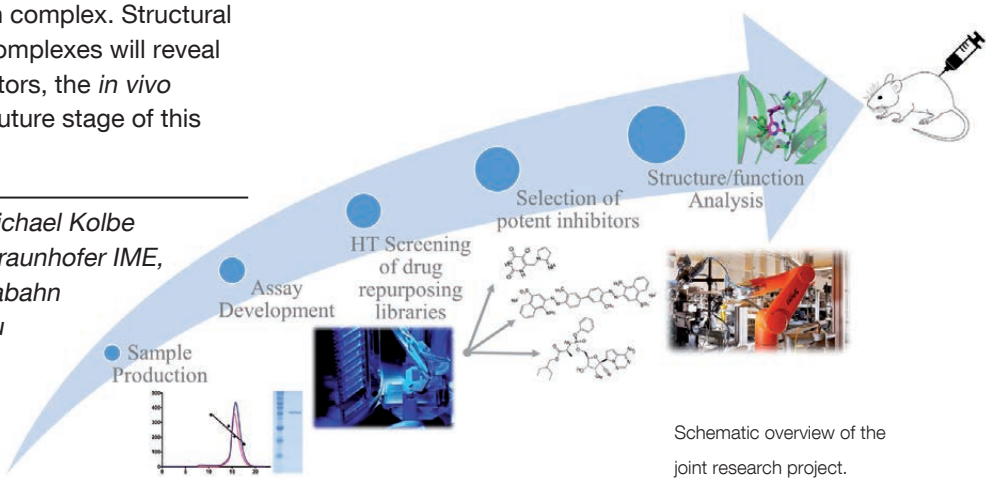

Schematic overview of the joint research project.

Science Highlights

Insights into the crime scene of Covid-19

Propagation-based phase-contrast tomography visualises lung tissue damage caused by Covid-19

Severe progression of Covid-19 is frequently accompanied by lethal respiratory failure. The goal of tracking down what goes wrong in the lung and ultimately finding medication does not only require expert knowledge but also expert tools. In order to better understand the remodelling and damage mechanisms in the lung after SARS-CoV-2 viral infection, the affected tissue has to be imaged at high resolution. Propagation-based phase-contrast tomography at the GINIX instrument of beamline P10 at PETRA III has augmented pathohistology of Covid-19 by three-dimensional views of inflammation sites, alveolar damage and alterations in the vasculature.

In severe progression of Covid-19, the underlying lung injury can be detected by radiographic chest imaging and clinical computed tomography (CT). However, in order to study disease mechanisms at the cellular level, higher resolution histological characterisation is required. For this purpose, the tissue obtained by surgical intervention or from a *post mortem* autopsy is cut into thin sections, stained and observed in an optical microscope. However, conventional histology suffers from some important limitations. Images are obtained only of two-dimensional sections but not of the entire three-dimensional (3D) volume. In order to accurately track the tree of blood vessels, to visualise alveolar morphology and to perform precise measurements of alveolar wall thickness which is important for gas exchange in the lung, the cyto-architecture of the lung has to be visualised in 3D and at high resolution, after locating regions of interest such as inflammation sites. For this purpose, we have adapted phase-contrast X-ray computerised tomography (CT) such that three-dimensional imaging tasks can be performed non-destructively on lung autopsies or biopsies. We have used this new technique to investigate tissue samples from Covid-19 patients, as well healthy control samples.

CT is a well-known 3D imaging technique for medical applications. However, the resolution and contrast of the standard absorption CT, which is based on attenuation differences, are not sufficient to detect the tissue structure with cellular or sub-cellular resolution. In contrast, phase contrast exploits the different propagation velocities of X-rays in tissue, reflecting the local electron density. This results in minute wavefront distortions which evolve into an intensity pattern on the detector. We have developed a special illumination optic based on

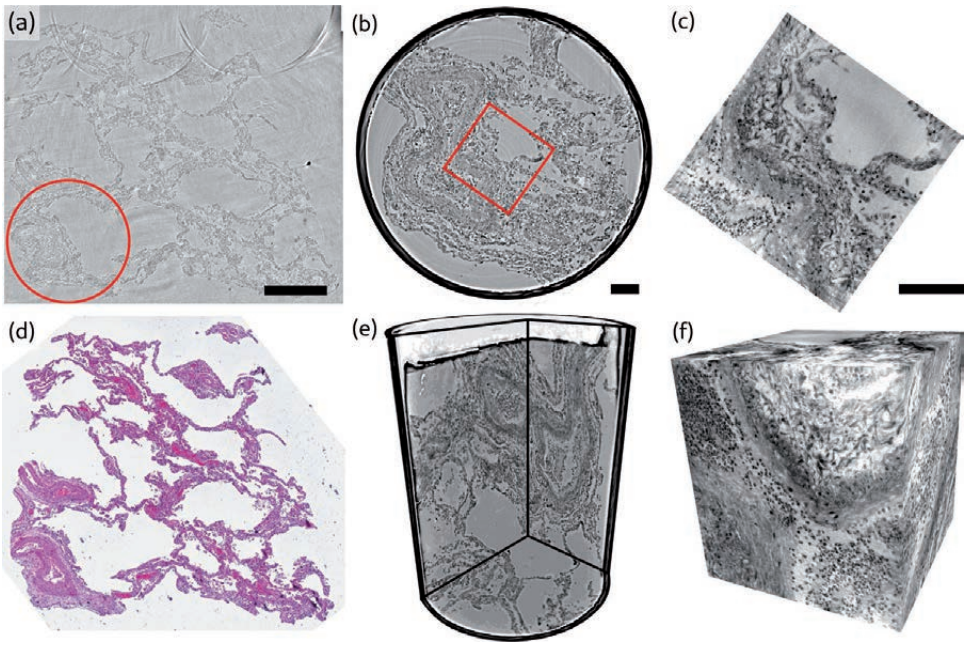

Figure 1

Multi-scale phase-contrast tomography results. (a) Virtual section through a reconstruction volume obtained from a paraffin-embedded tissue block, showing alveoli, blood vessels and immune cells. The circle in red indicates the location where a 1 mm biopsy punch is taken for further analysis. (b) Virtual section through the reconstruction of the 1 mm biopsy punch volume with indicated position for the cone-beam dataset. (c) Virtual section through the cone-beam dataset. (d) Image of an HE-stained histological section, which is in close proximity to the virtual slice in (a). (e) 3D views of the biopsy punch. (f) 3D views of the cone-beam datasets. Scale bars: (a) 500 µm and (b,c) 100 µm. The entire reconstruction volume can be downloaded online [5].

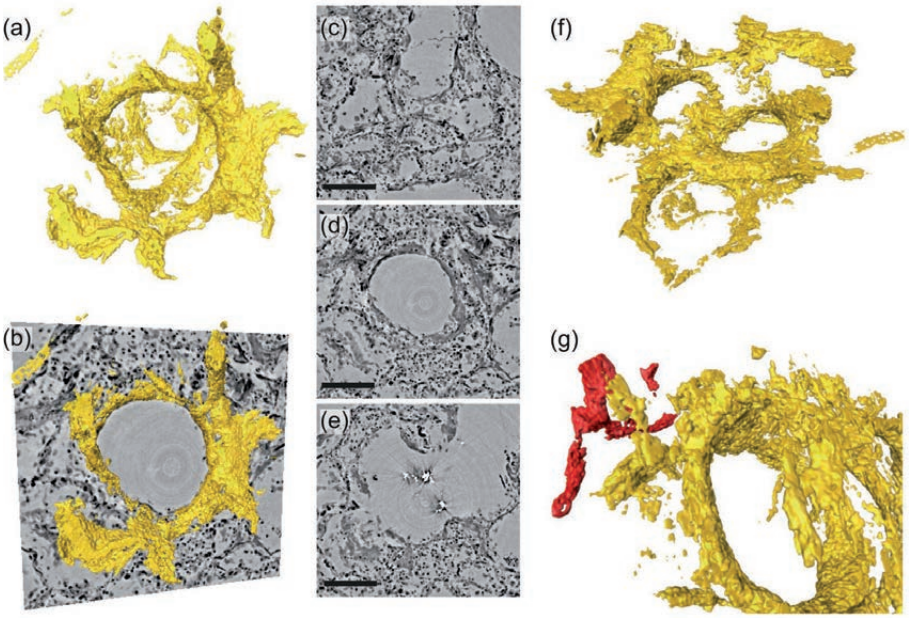

Figure 2

Hyaline membrane. As part of the damage, the alveolar walls (tiny air sacs) can be clogged with protein and cellular debris resulting from the inflammatory response. This so-called hyaline membrane, which is here visualized in 3D, can reduce or impede the gas exchange between the air compartment and the tiny neighbouring capillaries. Here, virtual slices through the reconstructed volume around an alveolus are shown, with superimposed rendering of the hyaline membrane attached to alveolar walls (sub-volume of a parallel-beam reconstruction of a 1 mm punch). (a) Volume rendering of the segmented hyaline membrane in same spatial orientation as (c–e), which show virtual slices through the (c) top, (d) centre and (e) bottom of the alveolus. For a better spatial classification, (b) gives a combination of the volume in (a) and the slice in (d). (f) Volume rendering of the entire subvolume including neighbouring alveoli. (g) zoom-in to a major blood vessel (red) which is directly connected with the hyaline membrane. Scale bars: (c–e) 300 µm.

X-ray waveguides which enables coherence and wavefront filtering. Using this optic, we have recorded near-field holographic intensity patterns at high magnification. We have applied phase-retrieval algorithms to reconstruct sharp projection images [2], followed by tomographic reconstruction.

First, overview scans of the Covid-19 lung samples were recorded with an extended unfocused undulator beam (13.8 keV). Regions of interest were identified and then studied at high resolution based on the cone-beam illumination emanating from the waveguide. The data was acquired at the GINIX end station of beamline P10 at PETRA III [3], at which the multi-scale approach with parallel and cone-beam recordings is implemented in direct proximity [4]. In this way, lung autopsies with a maximum cross section of 4 mm were first imaged at a voxel size of 650 nm and an image quality which allowed for the segmentation of individual cells. Using the zoom capability of the cone-beam geometry, regions of interest were then scanned with a minimum voxel size of 167 nm, and fused into the larger field of view (Fig. 1). The reconstructions revealed a wealth of structural details: deposition of cellular debris forming a thick so-called hyaline membrane on the alveolar walls (Fig. 2), damage around vessels, inflammations, massive recruitment of immune cells to the sites of inflammation and formation of new vessels (*angiogenesis*). This could, under normal circumstances, be a helpful reaction to laboured breathing. However, here the capillaries and vessels formed in response to the inflammatory stress are soon after already filled with thrombi and therefore result in further damage.

The total data recorded during the first beamtime in May 2020 exceed 10 TByte and the reconstructed volumes have been made publicly available for further use [5]. In a follow-up beamtime in September 2020, we have extended the study to cultured lung tissue deliberately infected with SARS-CoV-2 to test whether comparable damage can also occur in lung tissue without the involvement of the patient's immune system. In addition, we have extended the phase-contrast CT studies to heart tissue to investigate changes in the vasculature. The novel methodology and results of our studies will hopefully contribute to a better understanding of the causes of severe Covid-19 progressions and ultimately also aid the development of novel treatments.

Author contact: Tim Salditt, tsaldit@gwdg.de
Danny Jonigk, jonigk.danny@mh-hannover.de

References

1. M. Ackermann, S.E. Verleden, M. Kuehnel, A. Haverich, T. Welte, F. Laenger, A. Vanstapel, C. Werlein, H. Stark, A. Tzankov, W.W. Li, V.W. Li, S.J. Mentzer and D. Jonigk, 'Pulmonary vascular endothelialitis, thrombosis, and angiogenesis in Covid-19', N. Engl. J. Med. 383,120–128 (2020).
2. L. M. Lohse, A.-L. Robisch, M. Töpperwien, S. Maretzke, M. Krenkel, J. Hagemann and T. Salditt, 'A phase-retrieval toolbox for X-ray holography and tomography', J. Synchrotron Rad. 27, 852–859 (2020).
3. T. Salditt, M. Osterhoff, M. Krenkel, R. N. Wilke, M. Priebe, M. Bartels, S. Kalbfleisch and M. Sprung, 'Compound focusing mirror and X-ray waveguide optics for coherent imaging and nano-diffraction', J. Synchrotron Rad. 22, 867–878 (2015).
4. J. Frohn, D. Pinkert-Leetsch, J. Missbach-Güntner, M. Reichardt, M. Osterhoff, F. Alves and T. Salditt, '3D virtual histology of human pancreatic tissue by multiscale phase-contrast X-ray tomography', J. Synchrotron Rad. 27, 1707–1719 (2020).
5. https://zenodo.org/record/3892637#.XypmwOdCQ-U

Original publication

'3D virtual patho-histology of lung tissue from Covid-19 patients based on phase contrast X-ray tomography', eLife 9:e60408 (2020). DOI: 10.7554/eLife.60408

Marina Eckermann[1], Jasper Frohn[1], Marius Reichardt[1], Markus Osterhoff[1], Michael Sprung[2], Fabian Westermeier[2], Alexandar Tzankov[3], Christopher Werlein[4,5], Mark Kühnel[4,5], Danny Jonigk[4,5] and Tim Salditt[1]

1. Institut für Röntgenphysik, Georg-August-Universität Göttingen, Göttingen, Germany
2. Deutsches Elektronen-Synchrotron DESY, Hamburg, Germany
3. Universitätsspital Basel, Basel, Switzerland
4. Medizinische Hochschule Hannover (MHH), Hannover, Germany
5. Deutsches Zentrum für Lungenforschung (DZL), Hannover, Germany

Multimodal X-ray imaging of biological samples

Concurrent ptychography and X-ray fluorescence imaging for biomedical research

Studies of biological specimens often require the combination of several complementary methods. X-ray ptychography is a robust scanning coherent imaging method providing quantitative optical density contrast at dose-limited spatial resolution beyond the fabrication limits of X-ray optics. Its scanning nature allows for concurrent X-ray fluorescence (XRF) mapping, which enables artefact-free correlation of trace elements with highly resolved specimen's morphology. Using a novel X-ray scanner implemented at PETRA III beamline P11, simultaneous X-ray ptychography and XRF mapping were used for biomedical experiments in the fields of drug delivery for tuberculosis treatment with nanocontainers and human bone research.

Iron-oxide nanocarriers represent a novel tool for targeted delivery of anti-tuberculosis antibiotics to infected macrophages [1]. Tuberculosis (TB) is one of the most important bacterial infections worldwide causing high mortality and morbidity. The causative agent, *Mycobacterium tuberculosis*, is a facultative intracellular pathogen which can survive and grow in phagosomes upon phagocytosis by macrophages. These host cells, otherwise well-equipped to kill bacterial invaders, serve as niches for mycobacteria. More importantly, the membrane-enclosed phagosome and the lipid-rich cell wall of the mycobacteria pose a significant challenge for an efficient drug delivery as they hinder antibiotics entering the bacteria. A potential solution to this inherent problem of TB treatment are hollow Fe_2O_3 nano-spheres loaded with antibiotics, which can target anti-TB drugs to intracellular mycobacteria. The nanocontainers are actively internalised into macrophages and release antibiotics in close proximity to the mycobacteria. This happens upon slow metabolic dissolution of the Fe_2O_3 wall, exploiting the mycobacteria's need for iron. Here, the uptake of iron-oxide nanocontainers in macrophages has been studied by correlating iron XRF mapping with respect to the sub-cellular structure obtained by simultaneous ptychographic imaging at a photon energy of 7.35 keV. Figure 1(a) shows a representative macrophage treated with Fe_2O_3 nanocontainers. The image allows the identification of basic cellular structures. The two high-density spots, indicated with black arrows, are two nanocontainer agglomerates internalised within the cytosol. Figure 1(b) shows, for comparison, the cytoplasm of two control cells. In Fig. 1(c), the ptychographic phase of the nanocontainer-treated macrophage is overlaid with the corresponding iron areal mass distribution map. Two distinct iron spots coincide well with the positions of nanocontainer agglomerates obtained by ptychography.

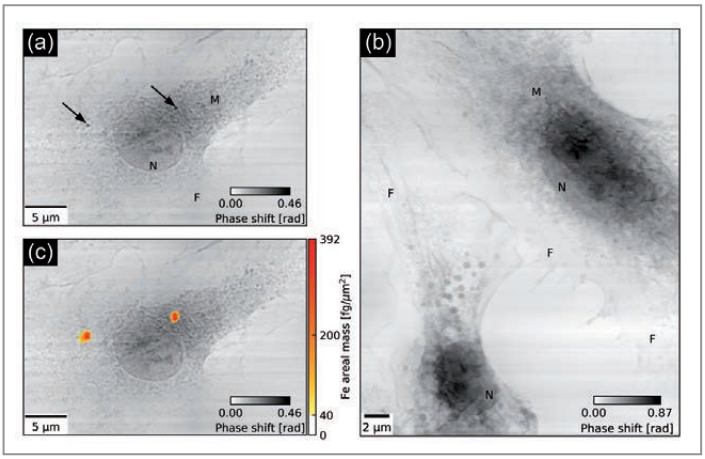

Studying a large number of macrophages further allowed to obtain the distribution of antibiotic load per agglomerate from the quantitative iron areal mass maps. This result can serve as a complementary assessment of the nanocontainer efficacy in tuberculosis infection treatment. Despite still missing depth information, the multimodal X-ray imaging enables looking beyond the sample surface and investigating the whole cellular volume on the nanoscale without the need for thin sectioning.

In the second biomedical application, the multimodal imaging technique was used to investigate the calcium content in human bone tissue. Pathologies of the skeleton, such as osteoporosis, are among the most common morbidities worldwide. Bone quality is a result of the complexity of the bone micro and nanostructure and the tissue remodelling process. It has been

Figure 1

Multimodal imaging of two groups of macrophage cells at a photon energy of 7.35 keV. (a) Reconstructed ptychographic phase of a macrophage treated with Fe_2O_3 nanocontainers targeting *Mycobacterium tuberculosis*. Black arrows indicate the internalisation of two agglomerates of nanocontainers in the cell. (b) Ptychographic phase of two untreated control cells. Both images allow for identification of cellular nuclei (N), membrane ruffles (M) and filopodia (F). (c) Iron areal mass map obtained simultaneously by means of XRF superimposed on the ptychographic phase (a) of the representative nanocontainer-treated macrophage.

Figure 2

Simultaneous ptychography and XRF of a thin and unstained human bone section at 7.15 keV. (a) Calcium distribution as obtained by XRF mapping and (b) the ptychographic phase shift. Both (a,b) allow to identify a Haversian canal (H) and concentric lamellae (L). In (a), the Ca depletion areas (black arrows) indicate perilacunar matrices of two osteocyte lacunae, while the corresponding areas in (b) exhibit no change in phase shift, which is proportional to the projected density. (c) Lower half of the Ca map corrected for the mass-thickness effect by ptychography.

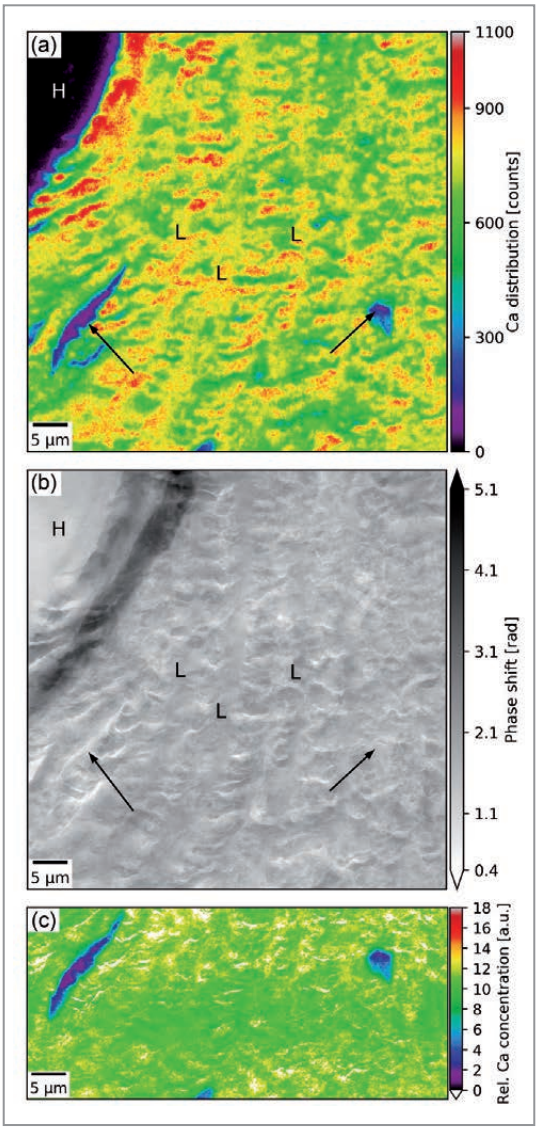

demonstrated that the bone-resorbing osteocytes govern a local volume of matrix surrounding the osteocyte lacunae (perilacunar matrix), which is actively turned over by the osteocytic activity [2]. Osteocytes acidify their lacuno-canalicular volume to demineralise the local bone matrix. This mechanism appears to serve as a response to an increased calcium demand, e.g. during lactation. Yet, mechanistic studies show that osteocytes utilise a far less acidic pH than osteoclasts to dissolve the bone mineral [3]. Therefore, the perilacunar matrix would need to be more susceptible to the demineralisation by means of a differential elemental or structural composition. Perilacunar matrix governed by osteocytes is hypothesised to be significantly different from the remaining bone matrix. It is thought to allow demineralisation by the osteocytic bone resorption and easier lacuna-shape adaptation in differential loading scenarios.

Here, simultaneous ptychography and XRF were utilised to map the Ca concentration in human cortical bone tissue at a photon energy of 7.15 keV. The human bone consists to a large extent of a form of hydroxyapatite making Ca the major structural element of the bone. Figure 2 shows the Ca map (a) and the ptychographic phase (b) of the selected bone region in the vicinity of a Haversian canal. Although both imaging modalities allow for general structure identification, XRF analysis benefits here from the simultaneously-obtained ptychographic phase which removes the mass-thickness effect. The concurrent acquisition frees both measurements from any relative image distortions. The resulting relative Ca concentration map in Fig. 2(c) presents a much more uniform Ca distribution than the raw Ca map. Within single micrometres around the osteocyte lacunae, the Ca content notably decreases. The comparison with concentrations in the remaining bone matrix further indicates a locally lower degree of mineralisation in the perilacunar matrix [4]. Nonetheless, this must further be verified by investigating a statistically significant population of lacunae. As an additional improvement, a local increase of the spatial resolution of Ca maps could, for example, be realised by utilising multilayer Laue lenses as a probe-forming focussing optic, able to focus efficiently the X-ray beam into a sub-10-nm focus [5].

Concurrent ptychography and XRF should find their main application at diffraction-limited synchrotron light sources. Their extremely high coherent flux will favour hybrid measurement schemes facilitating high-throughput characterisation of statistically relevant populations of specimens, which is especially required in biomedical research.

Author contact:
Karolina Stachnik, karolina.stachnik@physnet.uni-hamburg.de

References

1. P. Leidinger et al., 'Isoniazid@Fe_2O_3 nanocontainers and their antibacterial effect on Tuberculosis Mycobacteria', Angew. Chem. Int. Ed. 54, 12597–12601 (2015).
2. K. Jähn et al., 'Osteocytes acidify their microenvironment in response to PTHrP *in vitro* and in lactating mice *in vivo*', J. Bone Miner. Res. 32, 1761–1772 (2017).
3. H. Sano et al., 'Intravital bone imaging by two-photon excitation microscopy to identify osteocytic osteolysis in vivo', Bone 74, 134–139 (2015).
4. D. P. Nicolella et al., 'Effects of nanomechanical bone tissue properties on bone tissue strain: implications for osteocyte mechanotransduction', J. Musculoskelet. Neuronal Interact. 8, 330–331 (2008).
5. S. Bajt et al., 'X-ray focusing with efficient high-NA multilayer Laue lenses', Light Sci. Appl. 7, 17162 (2018).

Original publication

'Multimodal X-ray imaging of nanocontainer-treated macrophages and calcium distribution in the perilacunar bone matrix', Scientific Reports 10, 1784 (2020).
DOI: 10.1038/s41598-020-58318-7

Karolina Stachnik[1,2], Martin Warmer[1], Istvan Mohacsi[2], Vincent Hennicke[1,2], Pontus Fischer[1,2], Jan Meyer[1], Tobias Spitzbart[1], Miriam Barthelmess[1,2], Jacqueline Eich[3], Christian David[4], Claus Feldmann[5], Björn Busse[6], Katharina Jähn[6], Ulrich E. Schaible[3] and Alke Meents[1,2]

1. Deutsches Elektronen-Synchrotron DESY, Hamburg, Germany
2. Center for Free-Electron Laser Science (CFEL), DESY, Hamburg, Germany
3. Research Center Borstel – Leibniz Lung Center, Borstel, Germany
4. Paul Scherrer Institute (PSI), Villigen, Switzerland
5. Institute of Inorganic Chemistry, Karlsruhe Institute of Technology (KIT), Karlsruhe, Germany
6. Department of Osteology and Biomechanics, University Medical Center Hamburg-Eppendorf, Hamburg, Germany

Unravelling the secrets of the malaria parasite

PETRA III helps to identify a new kind of protein in *Plasmodium falciparum*

The replication of the protozoan parasite *Plasmodium falciparum* within red blood cells (erythrocytes) and the associated transformation and destruction of these cells is responsible for the clinical symptoms of malaria. With an estimated 228 million cases worldwide in 2018 and more than 400000 deaths, malaria remains an important threat to human health. The dissection of the molecular machinery that the parasite needs for its intracellular replication holds great promise in developing new strategies to combat the infection. In this study, structural analysis using PETRA III was combined with reverse genetics to identify and characterise an essential protein of the malaria parasite belonging to the lipocalin family.

Proteins that are part of the lipocalin family bind to small hydrophobic ligands and are known to be involved in various cellular processes ranging from lipid transport to oxidative-stress responses. Lipocalins have been identified and characterised in mammals, insects, plants and bacteria but their identity and function in unicellular eukaryotes, including important human parasites, remain poorly understood. They have a conserved tertiary structure but show extreme sequence diversity [1].

The genome of the malaria parasite *P. falciparum* contains a single protein (PF3D7_0925900) with a lipocalin signature. To validate the protein as a lipocalin, we determined its crystal structure using X-ray crystallography at the PETRA III synchrotron's P13 beamline. This revealed a tetrameric structure of monomers with a classic lipocalin fold thereby confirming the protein as a lipocalin (Fig. 1). The protein was thus named *P. falciparum* lipocalin (*Pf*LCN). In addition to examining the protein with X-ray crystallography, small-angle X-ray scattering (SAXS) analysis was performed to determine if *Pf*LCN's tetrameric structure was physiologically relevant. The SAXS analysis, conducted at beamline P12 of PETRA III, confirmed that *Pf*LCN also multimerises in solution thereby excluding that this was an artefact of the crystallisation process.

The next step in *Pf*LCN's functional characterisation required determination of its location within the malaria parasite. We thus tagged *Pf*LCN with a green fluorescent protein (GFP) and analysed its location throughout the parasite's life cycle using live-cell fluorescence microscopy techniques available at the Advanced Light and Fluorescence Microscopy core facility within the Centre for Structural Systems Biology (CSSB). We could demonstrate that the protein localises in the so-called parasitophorous vacuole (PV) and the food vacuole (FV) (Fig. 2).

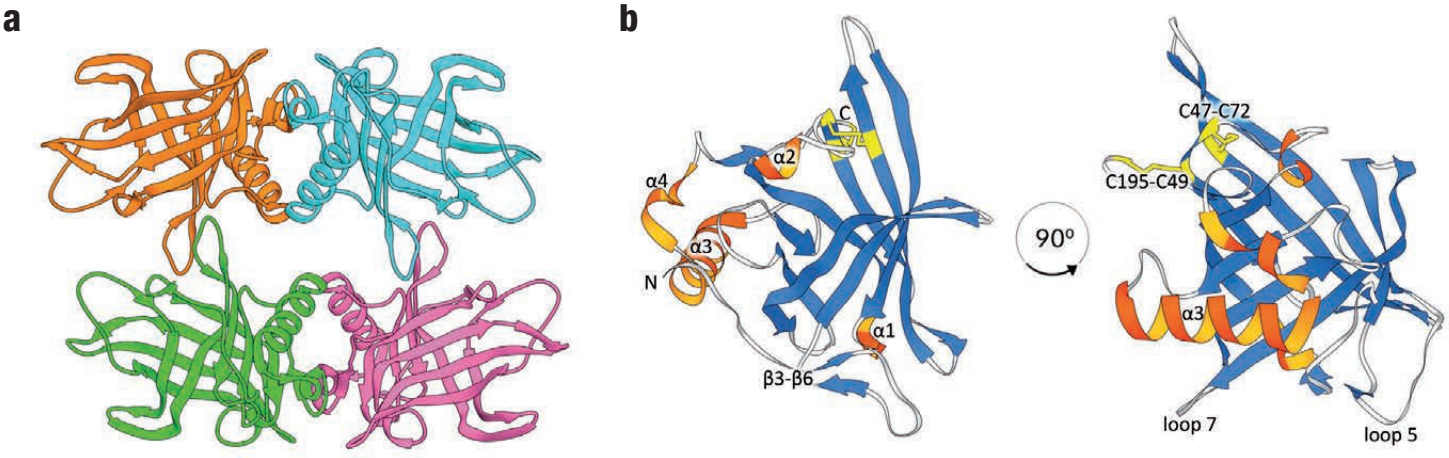

Figure 1

Plasmodium falciparum lipocalin (*Pf*LCN) forms a tetrameric structure of typical lipocalin monomers. (a) Crystal structure of tetrameric *Pf*LCN. (b) Crystal structure of monomeric *Pf*LCN. The N- and C-termini are labelled, as are various structural features including the two disulfide bonds.

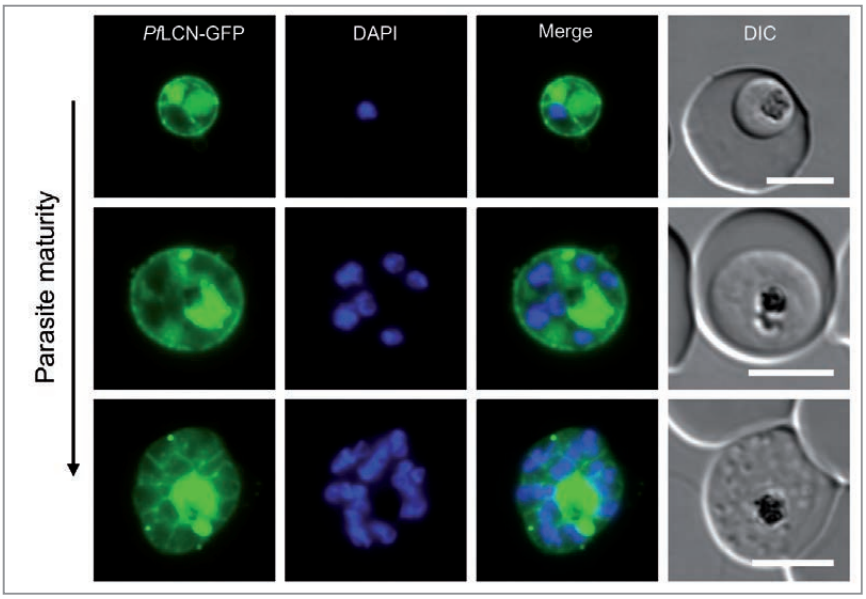

Figure 2

*Pf*LCN localises to the PV and FV of the parasite. Localisation of *Pf*LCN-GFP (green) by live-cell microscopy. Nuclei were stained with DAPI (blue). DIC = Differential interference contrast. Scale bars = 5 µm. Parasites with different stage of maturity are shown.

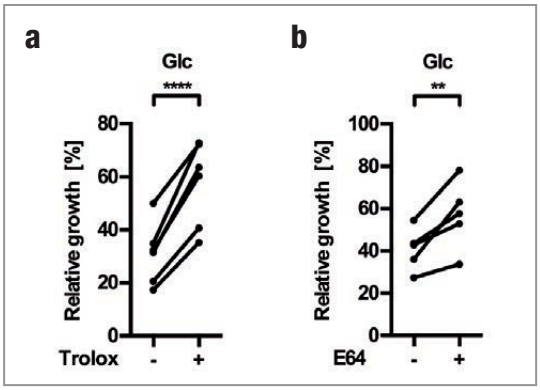

Figure 3

*Pf*LCN is important for parasite growth. Growth analysis of parasites in which *Pf*LCN was conditionally knocked down by addition of glucosamine (Glc) or which were left untreated. Addition of Glc activates a ribozyme in the 3' UTR of *Pf*LCN leading to degradation of its mRNA. The experiment was performed in presence or absence of the radical scavenger Trolox (a) or the protease inhibitor E64 (b). Relative parasitemia values of five to six independent experiments are displayed, which were obtained by dividing the parasitemia of Glc-treated cultures by the parasitemia of the corresponding untreated ones, both in presence or absence of Trolox/E64. For statistical analysis of these experiments a ratio-paired two-tailed t-test was performed. Statistically significant differences are indicated (** $p < 0.01$, **** $p < 0.0001$).

Both compartments are unique parasite-derived structures and have essential roles for parasite growth. The PV is a bubble-like compartment within the host erythrocyte, in which the parasite replicates. The FV is an intra-parasitic structure that is used by the parasite to metabolise host-cell haemoglobin as an important amino-acid source.

After the unambiguous localisation of *Pf*LCN within the infected erythrocyte, we next investigated its function using conditional *Pf*LCN knockdown parasites. Depletion of the protein greatly impaired parasite growth, indicating that the protein fulfils an important function for parasite proliferation (Fig. 3). The first clue for its precise function was given by the localisation of *Pf*LCN to the FV and the fact that the human lipocalin ApoD, to which *Pf*LCN shows high structural similarity, has protective effects against oxidative cell damage [2]. Parasite-mediated degradation of host-cell haemoglobin in the FV is associated with the formation of reactive oxygen species [3]. Protection against oxidative damage is therefore of particular importance for parasite survival, and parasites remain reliant on various detoxification pathways. We thus hypothesised that *Pf*LCN plays a role in oxidative damage control. To test this, we removed *Pf*LCN from the parasite in the presence or absence of the radical scavenger Trolox. Concurrently, we performed a knockdown of *Pf*LCN while temporally inhibiting host-haemoglobin degradation in the FV using the protease inhibitor E64. Interestingly, Trolox treatment as well as inhibition of haemoglobin degradation partially restored the growth phenotype of *Pf*LCN knockdown parasites (Fig. 3), suggesting that *Pf*LCN indeed mediates oxidative cell damage protection.

In conclusion, our study identified *Pf*LCN as a critical protein that the malaria parasite needs to ensure its intracellular replication. Future studies are now necessary to understand *Pf*LCN's anti-oxidative properties in more detail and also to identify possible additional roles of the protein in other processes such as transport of and binding to lipids.

Author contact: Paul-Christian Burda, burda@bnitm.de
Matthias Wilmanns, wilmanns@embl-hamburg.de
Tim-Wolf Gilberger, gilberger@bnitm.de

References

1. D. R. Flower, 'The lipocalin protein family: structure and function', Biochem. J. 318, 1–14 (1996).
2. M. D. Ganfornina, S. Do Carmo, J. M. Lora, S. Torres-Schumann, M. Vogel, M. Allhorn, C. González, M. J. Bastiani, E. Rassart and D. Sanchez, 'Apolipoprotein D is involved in the mechanisms regulating protection from oxidative stress', Aging Cell 7, 506–515 (2008).
3. H. Atamna and H. Ginsburg, 'Origin of reactive oxygen species in erythrocytes infected with *Plasmodium falciparum*', Mol. Biochem. Parasitol. 61, 231–241 (1993).

Original publication

'Structure-based identification and functional characterization of a lipocalin in the malaria parasite *Plasmodium falciparum*', Cell Reports 31,107817 (2020).
DOI: 10.1016/j.celrep.2020.107817

Paul-Christian Burda[1,2,3], Thomas Crosskey[4], Katharina Lauk[1,2,3], Aimo Zurborg[1,2,3], Christoph Söhnchen[1,2,3], Benjamin Liffner[5], Louisa Wilcke[1,2,3], Emma Pietsch[1,2,3], Jan Strauss[1,2,3], Cy M. Jeffries[4], Dmitri I. Svergun[4], Danny W. Wilson[5,6], Matthias Wilmanns[4] and Tim-Wolf Gilberger[1,2,3]

1. Centre for Structural Systems Biology, Hamburg, Germany
2. Bernhard Nocht Institute for Tropical Medicine, Hamburg, Germany
3. Universität Hamburg, Hamburg, Germany
4. European Molecular Biology Laboratory, Hamburg, Germany
5. University of Adelaide, Adelaide, Australia
6. Burnet Institute, Melbourne, Australia

Supramolecular structure of an antimicrobial peptide

Antimicrobial activity via self-assembly into stable helical fibrils of a human-derived peptide

Antimicrobial peptides (AMPs) are a diverse group of molecules that evolved in most living organisms over 2.6 billion years, and can provide new therapeutic venues to combat severe infections, killing cancerous cells and for immunomodulation. Importantly, AMPs are thought to induce less microbial resistance compared to conventional antibiotics. However, their relatively low efficacy and bioavailability, as well as their lack of chemical stability, discouraged development into therapeutic agents. Self-assembly of AMPs is functionally relevant and can enhance antimicrobial activity [1]. Moreover, the formation of supramolecular ordered structures of AMPs can provide immense stability against heat, shear force and chemical and proteolytic degradation.

The human LL-37 antimicrobial peptide (AMP) cleaved from cathelicidin is expressed by various mammalian cells and is considered to play an important role in the first line of defence against pathogens. LL-37 undergoes further proteolytic cleavage by host proteins, microbiome and invading pathogens, to yield numerous derivatives with a diverse array of selectivity against microbial strains and additional functions within the immune system [2]. The LL-$37_{17\text{-}29}$ fragment (amino-acid residue 17-29, 13 residues long), although not detected directly *in vivo*, was suggested to serve as the active core of LL-37, showing a different spectrum of antibacterial activity compared to the full-length LL-37 and other fragments [3]. It generates an amphipathic helix with a large hydrophobic moment of 0.85 and a net charge of +4 (compared to 0.52 and +6, respectively, of the entire LL-37).

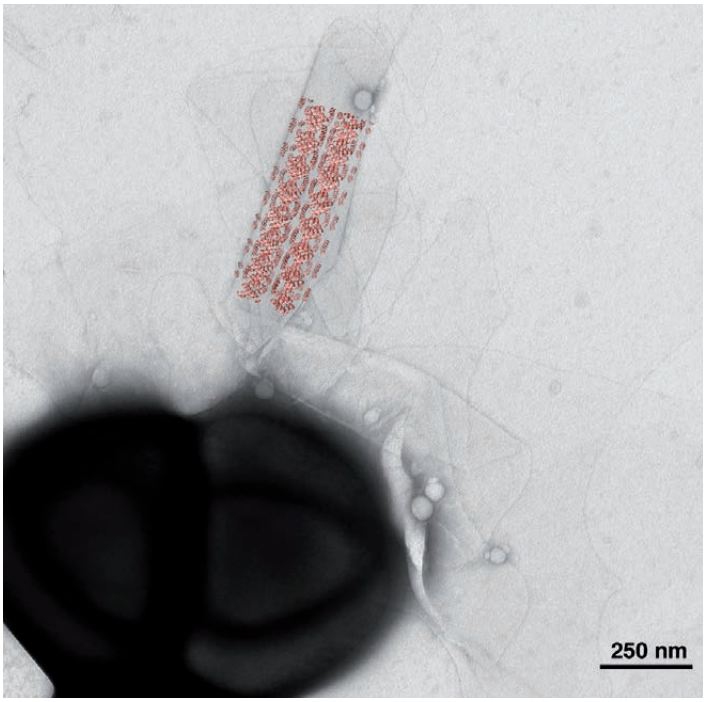

While crystal structures of short helical AMPs are rather rare, we determined the crystal structure of LL-$37_{17\text{-}29}$, at 1.35 Å resolution using X-ray diffraction data collected at EMBL micro-focus beamline P14 at the PETRA III synchrotron (PDB ID 6S6M). Crystals could be only formed under one specific condition among 1440 tested solutions. The crystals diffracted well only when 2-methyl-2,4-pentanediol (MPD) was added before flash freezing. Data processing and refinement were highly challenging but nevertheless rewarding. The structure revealed a novel fibril structure (Fig. 1), composed of self-assembled amphipathic helices into a densely packed and elongated hexameric structure. This fibrillar assembly is comprised of four-helix bundles stabilised by a hydrophobic core, while a network of polar interactions stabilises interactions between bundles. Overall, the fibrillar assembly creates alternating hydrophobic and polar (positively charged) patches on its surface (Fig. 2), suggesting interactions and disruption of negatively charged lipid bilayers such as bacterial membranes.

In accordance with the fibrillar crystal structure, LL-$37_{17\text{-}29}$ formed wide ribbon-like fibrils, which interacted with *M. luteus* bacterial cells (Fig. 2). Structure-guided mutagenesis confirmed the importance of self-assembly to the antibacterial activity. For example, the substitution of the amino-acid residue isoleucine 24, deeply buried within the four-helix

Figure 1

Novel fibrils of the human LL-$37_{17\text{-}29}$ formed around bacterial cells. A transmission-electron micrograph of human LL-$37_{17\text{-}29}$ showing wide fibrils formed around *M. luteus* cells. High-resolution structure of LL-$37_{17\text{-}29}$, illustrated in a salmon-coloured ribbon representation along the fibril.

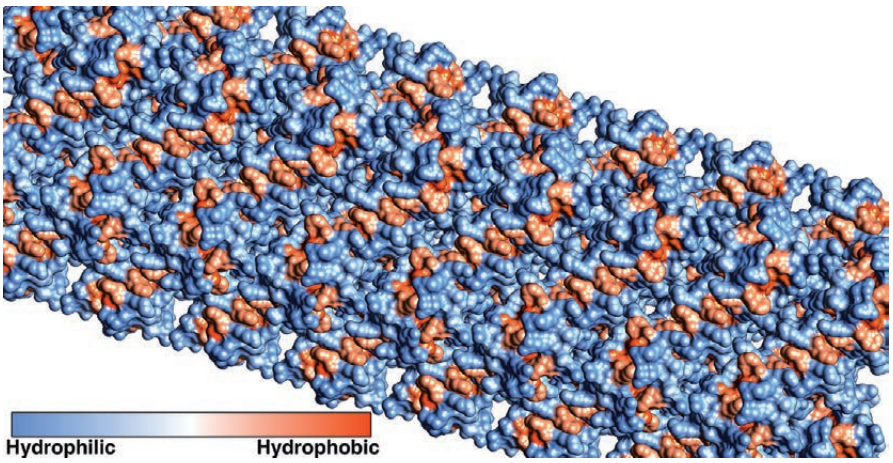

Figure 2

The surface of the LL-37_{17-29} fibril encompasses alternating hydrophobic and positively charged zigzagged belts. A surface representation of the human LL-37_{17-29} fibril, coloured according to hydrophobicity scale. The hydrophobic and hydrophilic (positively charged) zigzagged belts likely underlie interactions with, and subsequent disruption of, negatively charged lipid bilayers such as bacterial membranes.

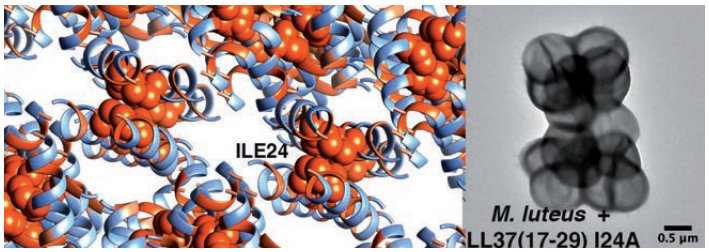

Figure 3

Mutagenesis supported the role of self-assembly in antibacterial activity. On the left, the fibril of human LL-37_{17-29} is coloured according to hydrophobicity scale of Fig. 2. Isoleucine 24 (ILE24), which is deeply buried in the core of the four-helix bundles, is shown as space-filled models. On the right, a transmission electron micrograph image of *M. luteus* incubated with the LL-37_{17-29} I24A mutant peptide indicates no fibril formation around the bacteria, or a lytic process.

bundle, abolished antibacterial activity and the formation of fibrils that interact with the bacterial cells (Fig. 3), despite maintaining the amphipathic nature and total charge. In contrast, a mutation in a relatively exposed position (with minimal inter-helical contacts), despite change in amphipathicity, did not affect activity and showed the formation of nanofibrils and aggregation around the bacteria.

Certain AMPs were suggested to assemble into well-ordered fibrils that resemble amyloids [4], which are proteins associated with neurodegenerative and systemic diseases known to form ultra-stable cross-β fibrils composed of tightly mated β-sheets [5]. Yet LL-37_{17-29} lacks the amyloid continuous sheets and also differs from helical fibrils such as collagen, actin and fibrinogen. Nevertheless, the helical LL-37_{17-29} shares fibril thermostability often observed for β-rich amyloids and remained stable up to 80 °C. Overall, LL-37_{17-29} presents a type of self-assembly which is distinct from other protein fibrils, with a role in direct killing of bacterial cells still to be fully determined.

The findings expose a scaffold for wide-ranging applications in bio and nanotechnology, regenerative medicine and bioengineering, with the invaluable advantage of an inherent antibacterial activity. Links between fibril formation and antimicrobial activity are accumulating [6], and LL-37_{17-29} provides atomic-level insight for such example. Further elucidation of the interplay between antimicrobial activity and fibril formation and morphology will aid the design of AMPs with enhanced potency, selectivity, stability, bioavailability and shelf-life. Successful design of such functional nanostructures with tuneable self-assembly might provide novel antibacterial therapeutics or coating of medical devices, and may target other roles of AMPs in immunomodulation and in killing cancerous cells.

Author contact: Meytal Landau, mlandau@technion.ac.il

References

1. Z. Ye, X. Zhu, S. Acosta, D. Kumar, T. Sang and C. Aparicio, 'Self-assembly dynamics and antimicrobial activity of all L- and D-amino acid enantiomers of a designer peptide', Nanoscale 11, 266–275 (2018).
2. Z. Chen, G. Yang, S. Lu, D. Chen, S. Fan, J. Xu, B. Wu and J. He, 'Design and antimicrobial activities of LL-37 derivatives inhibiting the formation of *Streptococcus mutans* biofilm', Chem. Biol. Drug Des. 93, 1175–1185 (2019).
3. G. Rajasekaran, E. Y. Kim and S. Y. Shin, 'LL-37-derived membrane-active FK-13 analogs possessing cell selectivity, anti-biofilm activity and synergy with chloramphenicol and anti-inflammatory activity', Biochim. Biophys. Acta Biomembr. 1859, 722–733 (2017).
4. M. Landreh, J. Johansson and H. Jornvall, 'Separate molecular determinants in amyloidogenic and antimicrobial peptides', J. Mol. Biol. 426, 2159–2166 (2014).
5. D. Eisenberg and M. Jucker, 'The amyloid state of proteins in human diseases', Cell 148, 1188–1203 (2012).
6. S. J. Soscia, J. E. Kirby, K. J. Washicosky, S. M. Tucker, M. Ingelsson, B. Hyman, M. A. Burton, L. E. Goldstein, S. Duong, R. E. Tanzi and R. D. Moir, 'The Alzheimer's disease-associated amyloid beta-protein is an antimicrobial peptide', PLOS One 5, e9505 (2010).

Original publication

'The human LL-37(17-29) antimicrobial peptide reveals a functional supramolecular structure', Nature Communications 11, 3894 (2020). DOI: 10.1038/s41467-020-17736-x

Yizhaq Engelberg[1] and Meytal Landau[1,2]

1. Department of Biology, Technion – Israel Institute of Technology, Haifa, Israel
2. Centre for Structural Systems Biology (CSSB) and European Molecular Biology Laboratory (EMBL) c/o DESY, Hamburg, Germany

Bone biomineral properties depend on location in human bone

Mapping composition and crystallographic properties in 3D reveals the complex structure of human bone

The structure of bone continues to provide challenges to researchers because bone is a hierarchically structured nanocomposite with structural features ranging from the nanometre to the micrometre scale. This calls for high-resolution methods that afford insights on several length scales at once. In human bone, osteons are particularly important motifs, but the details of their formation mechanisms remain unknown. To address this problem, we conducted X-ray fluorescence computed tomography (XRF-CT) and X-ray powder diffraction computed tomography (XRD-CT) on human bone with a 400 nm diameter X-ray beam. This allowed mapping elements and crystallography in 3D. This showed that the crystallographic properties of bone mineral depend on its location within the osteon.

The structure of bone has been studied for centuries but continues to puzzle and surprise researchers [1-3]. Bone has a remarkable hierarchical structure traversed by cells and can undergo repair through remodelling. In humans and some other animals, remodelling in long bones occurs through formation of osteons: a 100 µm wide channel is carved out and new bone is deposited from the outside in following a winding pattern of mineralised collagen fibrils (Fig. 1). The osteon thus contains lamellae of varying mineral density on the 1–10 µm length scale [4]. The biomineralisation process and the crystallographic properties during osteonal remodelling remain unknown. Because the osteon is formed from the outside in, we hypothesised that spatial/temporal variations in the bone biomineralisation processes could be followed by mapping the bone biomineral structure across an osteon by X-ray diffraction and fluorescence. To resolve the lamellae, a resolution better than 1 µm in 3D is needed. Therefore, we performed tomographic X-ray diffraction (XRD-CT) and X-ray fluorescence (XRF-CT) with a 400 nm diameter 16.5 keV X-ray beam at beamline P06 at PETRA III. In these techniques, the XRD or XRF signal is reconstructed by computed tomography (CT). We measured two samples, one perpendicular to the osteon central canal that we probed by XRF-CT and one ~ 130 µm diameter sample parallel to the osteon axis by XRD-CT (Fig. 1). The XRD-CT data set consists of over 3.6 million voxels, each containing a reconstructed diffraction pattern. For each voxel, we analysed the XRD data by automated Rietveld refinement [5].

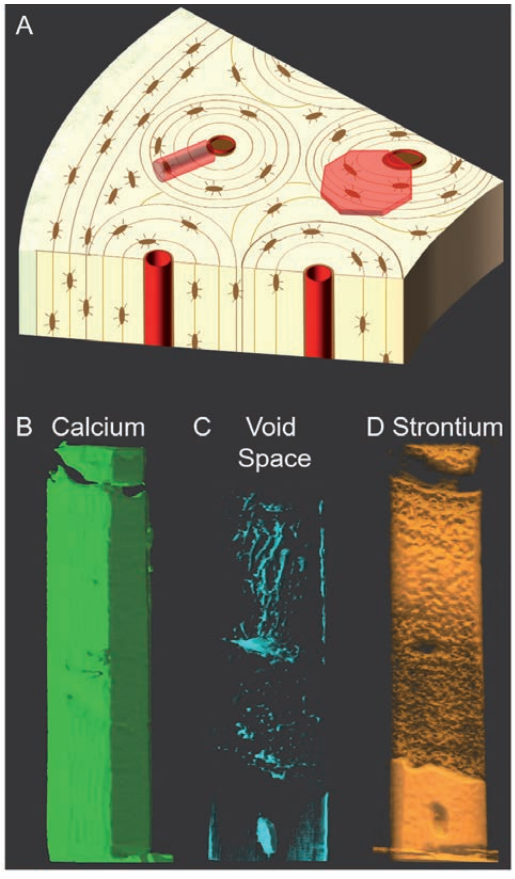

The fluorescence data showed that sub-µm resolution was attained since the imprint left by the cellular network in bone was resolved (Fig. 1c). Additionally, the oligoelement strontium had different concentrations across the osteon and, even more strongly so, inside/outside the osteon (Fig. 1d). The diffraction data allowed mapping the amount of crystalline material, lattice constants and microstructure, the latter through diffraction-peak broadening. We found that most

Figure 1

Bone samples and XRF-CT results. (a) In human bone, osteons are formed by remodeling and traversed by cells (brown). Two samples were cut from the bone, one for XRF cut as thin about 30 µm diameter cylinder perpendicular to osteon axis and another for XRD that was an octagonal column in the plane of the osteon (shown in red). The XRF spectra were reconstructed tomography into maps of elements in 3D. (b) Shows a rendering of the calcium content, while (c) shows the void spaces clearly showing two osteocyte lacunae and part of the canaliculi connecting osteocytes. The strontium content (d) is higher outside the osteon (bottom) and varies within the osteon.

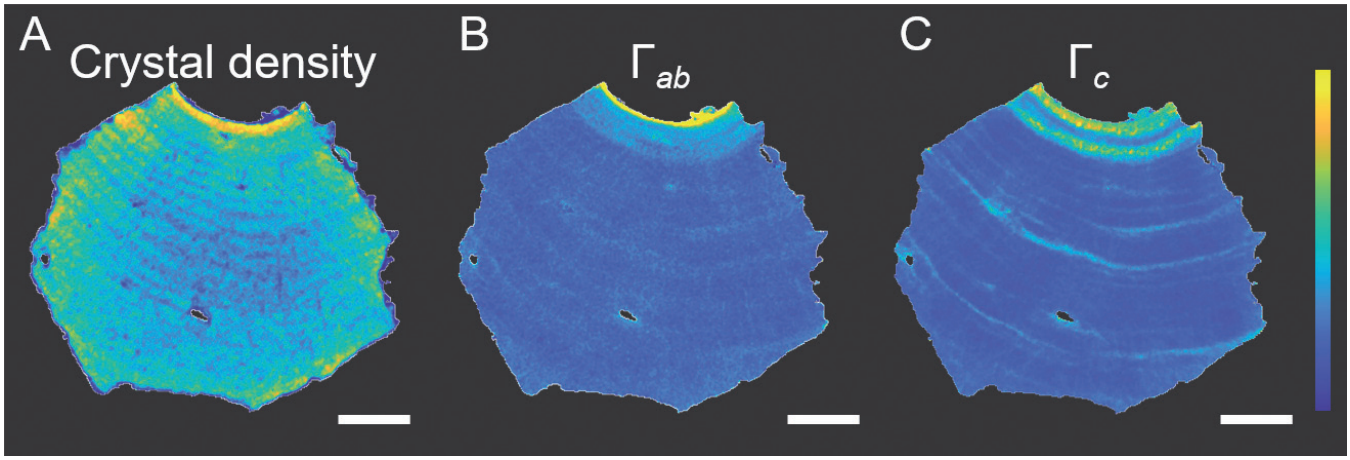

Figure 2

The XRD data were treated by Rietveld refinement in each of the 3.6 million voxels. Here the height-averaged data are shown. The osteon canal is at the top of the sample. The scale bar is 25 µm. (a) The density of crystals in each voxel, as obtained from the scale factor of the crystallographic intensities. Note the variation in crystal density with distance from the osteon canal. (b,c) Width of diffraction peaks reflecting crystallite size with large widths (yellow) indicating small sizes. (b) Shows broadening in the *a,b*-plane of the hexagonal bone biomineral while (c) shows the broadening along the *c*-axis. For clarity, (b) and (c) are shown on their own scales, while in reality crystals are significantly larger along the *c*-axis than perpendicular to it.

crystallographic parameters varied only a little along the 10.4 µm height of the measured volume (parallel to the osteon long axis), which approximately corresponds to the size of a bone-forming cell. This suggests that bone biomineral is uniformly laid down on a cellular length scale. Perpendicular to the osteon long axis, i.e. parallel to the bone on-growth direction, the crystallographic properties varied. Figure 2a shows the crystal density (crystallographic scale factor). The crystal density is banded as a function of distance from the osteon canal as expected from literature [4]. Also, the mineral content is larger close to the osteon canal reflecting a higher degree of mineralisation in this final region of the osteon. A large number of other crystallographic parameters were determined. Here only the microstructure parameters are presented. From the XRD data, the peak broadening along and perpendicular to the crystallographic *c-axis* of the hexagonal bone biomineral was measured (Fig. 2b and 2c). Two main observations were made: First, close to the osteon canal, diffraction peaks are broader than further away reflecting smaller (or more strained) nanocrystals in this region. Second, there are bands of altered peak broadening in specific regions further away and these are not correlated between the two axes. The second observation suggests that the crystal growth along the two crystallographic directions are not completely coupled, while the first observation indicates that biomineralisation close to the osteon canal differs from the osteonal bone further away. We suggest that this results from variation in the local concentration in factors controlling biomineralisation, e.g. non-collagenous proteins or citrate. This idea is supported by the fact that fragments of proteins like osteopontin that are inhibitors of crystallisation are upconcentrated in this area. We propose that they restrict crystal growth resulting in smaller crystals and increased peak broadening. Studies of mice lacking the ability to break down osteopontin agree with this hypothesis: they display accumulation of osteopontin and complete inhibition of mineralisation around blood vessels [6].

In conclusion, this work demonstrated sub-µm XRF-CT and XRD-CT on large samples with over 3.6 million diffraction patterns analysed. This afforded detailed insights into bone structure in osteonal human bone and established that the characteristics of bone mineral depend on the details of the conditions under which they were made.

Author contact: Henrik Birkedal, hbirkedal@chem.au.dk

References

1. N. Reznikov, J. A. M. Steele, P. Fratzl and M. M. Stevens, 'A materials science vision of extracellular matrix mineralization', Nat. Rev. Mater. 1, 16041 (2016).
2. N. Reznikov, M. Bilton, L. Lari, M. M. Stevens and R. Kröger, 'Fractal-like hierarchical organization of bone begins at the nanoscale' Science 360, eaao2189 (2018).
3. T. A. Grünewald, M. Liebi, N. K. Wittig, A. Johannes, T. Sikjaer, L. Rejnmark, M. Rosenthal, M. Guizar-Sicairos, H. Birkedal and M. Burghammer, 'Localized misalign-ment of bone nanostructure and biomineral in human lamellar bone, Sci. Adv. 6, eaba4171 (2020).
4. H. S. Gupta, U. Stachewicz, W. Wagermaier, P. Roschger, H. D. Wagner and P. Fratzl, 'Mechanical modulation at the lamellar level in osteonal bone', J. Mater. Res. 21, 1913–1921 (2006).
5. S. Frølich and H. Birkedal, 'Multiref: software platform for Rietveld refinement of multiple powder diffractograms from *in situ*, scanning or diffraction tomography experiments', J. Appl. Crystallogr. 48, 2019–2025 (2015).
6. B. Hoac, M. Østergaard, N. K. Wittig, T. Boukpessi, D. J. Buss, C. Chaussain, H. Birkedal, M. Murshed and M. D. McKee, 'Genetic ablation of osteopontin in osteomalacic Hyp mice partially rescues the deficient mineralization without correcting hypophosphatemia', J. Bone Miner. Res. 35, 2032–2048 (2020).

Original publication

'Bone biomineral properties vary across human osteonal bone', ACS Nano 13, 12949–12956 (2019). DOI: 10.1021/acsnano.9b05535

Nina K. Wittig[1], Jonas Palle[1], Maja Østergaard[1], Simon Frølich[1], Mie E. Birkbak[1], Kathryn M. Spiers[2], Jan Garrevoet[2] and Henrik Birkedal[1]

1. Department of Chemistry and iNANO, Aarhus University, Aarhus, Denmark
2. Deutsches Elektronen-Syncrotron DESY, Hamburg, Germany

Hydrochloric acid facilitates catalyst characterisation

Analysing the distribution of Ni in active and inactive phases of acid-leached MoS_2 catalysts for hydrodesulfurisation

The production of ultra-low sulfur fuels from crude oil requires hydrotreating processes in the refinery. These processes are performed at high hydrogen pressures over complex mixtures of catalytically active transition-metal sulfides consisting of MoS_2, a Ni/Co-containing MoS_2 phase and a variety of Ni and/or Co sulfides [1,2]. Their catalytic activity is attributed to Co and Ni selectively incorporated in the MoS_2-slab edges. We have combined advanced in-house and synchrotron-based methods (in particular *operando* XAS at PETRA III beamline P65) to elucidate the nature and concentration of the active sites in hydrotreating reactions and the fundamental properties of the catalyst surface.

Today, the vast majority of liquid fuel is produced by hydrotreating of crude oil with Co and Ni-MoS_2 catalysts. However, as low-sulfur crudes are rapidly depleted, highly active and selective hydrotreating catalysts are required to handle feedstocks with increasingly high concentrations of sulfur. In this context, segregated Co- and Ni-sulfides come with a notorious complication: not only do these phases decrease activity by covering active sites and adding inert mass, but they also hinder characterisation and therefore impede the understanding of the catalytic features. In this work, we tackled these problems with an acid-leaching procedure that selectively removes the undesired NiS_x phases from Ni-MoS_2. While kinetic analyses of the resulting materials were performed with model reactants, key structural information was obtained using Ni K-edge EXAFS at beamline P65.

EXAFS of the parent sulfides (Fig. 1a) indicated uniform Ni-S distances (2.26 Å) and coordination numbers (~ 5), close to those found in bulk Ni sulfides, e.g., Ni_3S_2, Ni_9S_8, or NiS. The presence of these phases was confirmed by XRD. After leaching with hydrochloric acid (at pH < 0) the Ni–S coordination number was barely affected, while the Ni–S bond distances decreased significantly and consistently from 2.26 to 2.22 Å. This distance is too short for crystalline Ni sulfides and clearly shows that in the acid-treated catalysts a significant part of the Ni atoms is not located in segregated NiS_x phases, but rather in a promoted Ni-Mo-S phase. The most important change associated with acid treatment was the appearance of a Ni-Mo contribution in the spectra. While the spectra of the parent sulfides could be fully modelled with only one Ni–S and one Ni–Ni scattering path, fitting the spectra of the leached materials required the presence of a Mo scatterer at a distance of 2.86 Å [3]. Analysis of XANES (Fig. 1b) showed further differences between parent and leached sulfides. Both the intensity of the 1s-3d transition (pre-edge feature) and the edge energy were found to qualitatively correlate with the NiS_x content. The pre-edge peak at 8331 eV was most intense in the Ni_3S_2 reference, followed by the parent catalysts, while in the leached catalysts it was barely noticeable. This sequence reflects the fact that tetrahedrally coordinated Ni, such as in Ni_3S_2, typically exhibits a more intense pre-edge peak than Ni-Mo-S. The gradual weakening of the pre-edge peak in the

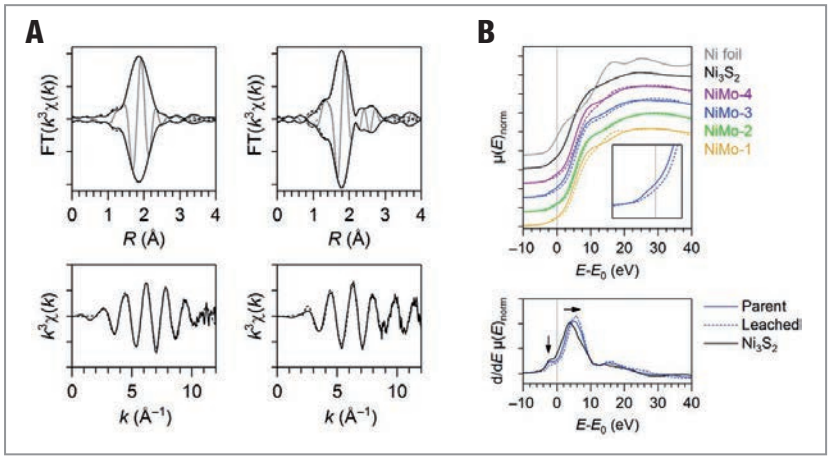

Figure 1

Results of XAS at the Ni K edge measurements: (a) Top row: magnitude (black) and imaginary part (grey) of the Fourier transform before leaching (left) and after leaching (right) with best fit (dashed line). Bottom row: EXAFS and best fit (dashed line) before (left) and after leaching (right). (b) top: normalised XANES of Ni-Mo sulfide catalysts, Ni_3S_2 and Ni metal. The inset shows an enlarged view of the pre-edge. Bottom: derivative of normalised absorption of Ni_3S_2, NiMo-3-p and NiMo-3-L. Continuous and dotted lines correspond to parent and leached samples, respectively.

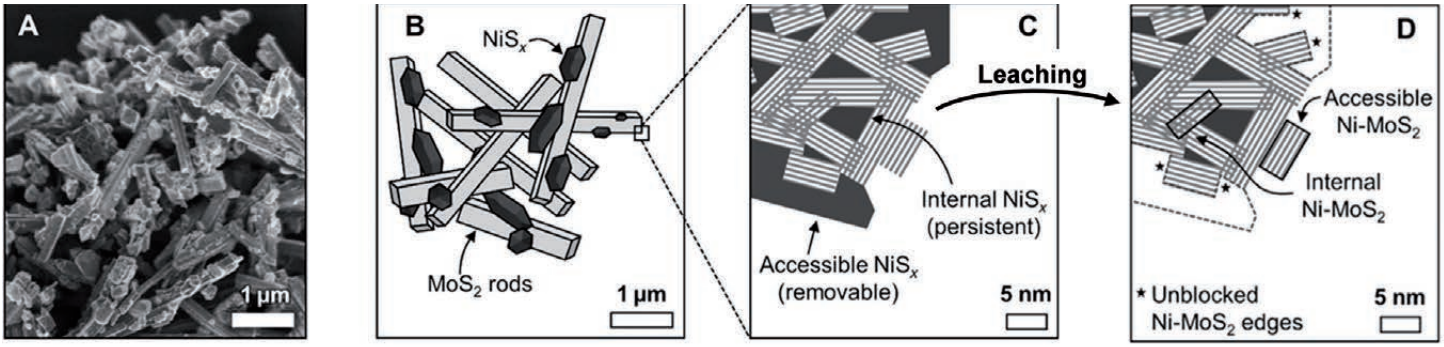

Figure 2

Ni distribution among active and inactive phases: (a) representative SEM micrograph and (b) schematic representation of NiMo-3 before leaching, showing the secondary rod-like MoS_2 phase intermixed with crystalline NiS_x. (c) Enlarged section of the corner of one rod-like particle before leaching and (d) after leaching.

sequence Ni_3S_2 > NiMo-parent > NiMo-leached was accompanied by a shift in the edge energy and points to changes in the overall electron density of Ni. The shift suggests that the average oxidation state of Ni increases as the concentration of Ni atoms incorporated in crystallite edges becomes more and more significant compared to NiS_x.

To analyse the distribution of Ni among active Ni-Mo-S sites and inactive NiS_x phases, the total Ni content was compared to the maximum amount of Ni that could be theoretically incorporated at the crystallite edges. The latter is given by the number of edge metal atoms based on the size of the clusters (determined by TEM) using a geometric model. The analysis of the parent catalysts clearly showed that significantly more Ni was present than the number of potential sites existing at the MoS_2 edges and even after acid treatment, the residual amount of Ni exceeded that of available edge positions. Thus, we conclude that also leached catalysts contain segregated Ni sulfides or small Ni_xS_y clusters, most likely in inaccessible locations (Fig. 2a-d).

Having established that internal NiS_x phases may be present after leaching, the distribution of Ni among the pool of potential species was estimated from a theoretical model of the geometry based on the relation of the amount of edge-incorporated Ni atoms (determined by NO chemisorption) and the total amount of Ni in the catalysts. The results suggest that about 1/3 of the Ni atoms in the leached catalysts were incorporated at the edges of MoS_2, while the remainder existed as inaccessible NiS_x. The partial removal of segregated NiS_x has important implications on the catalytic activity for hydrodesulfurisation (HDS) of dibenzothiophene. Unblocking of active sites, previously covered by Ni sulfides, and the elimination of catalytically inert mass led to a substantial increase in the HDS rates, while the selectivity was not affected at all by acid treatment. This implies that the newly uncovered surfaces exhibit an active-site distribution identical to that of the initially accessible active surface, which can be attributed to the complete preservation of the structural characteristics of the MoS_2 phase throughout acid treatment.

The present study demonstrates that the selective removal of segregated Ni sulfides *via* acid treatment from Ni-Mo sulfide catalysts leads to highly active materials, whose activity depends solely on the concentration of active sites consisting of Ni-Mo-S and SH groups [4]. While most of the Ni after such treatment is incorporated in the Ni-Mo-S phase, the remaining fraction of NiS_x exists in the interior of secondary MoS_2 structures.

Future research employing acid treatment of bulk HDS catalysts focuses on preparing materials that allow for complete elimination of segregated Ni sulfides. The key to a successful description of the structure-activity relations is the combination of advanced in-house and synchrotron-based methods, allowing for *operando* characterisation with X-ray absorption spectroscopy (developed within the BMBF Verbundprojekt MatDynamics for P65 at PETRA III), with detailed micro-kinetic studies. The use of theoretical methods is essential to relate the results from spectroscopy and kinetics to the electronic and structural properties of these multifunctional materials.

Author contact: Andreas Jentys, jentys@tum.de

References

1. R. Prins, 'Hydrotreating'. In: 'Handbook of heterogeneous catalysis', 2nd ed., G. Ertl, H. Knözinger, F. Schüth and J. Weitkamp, Eds. (Wiley VCH Weinheim) Vol.1, 2695–2718 (2008).
2. R. R. Chianelli, G. Berhault and B. Torres, 'Unsupported transition metal sulfide catalysts: 100 years of science and application', Catal. Today 147, 275–286 (2009).
3. S. P. A. Louwers and R. Prins, 'Ni EXAFS studies of the Ni-Mo-S structure in carbon-supported and alumina-supported Ni-Mo catalysts', J. Catal. 133, 94–111 (1992).
4. W. Luo, H. Shi, E. Schachtl, O. Y. Gutierrez and J. A. Lercher, 'Active sites on nickel-promoted transition-metal sulfides that catalyze hydrogenation of aromatic compounds', Angew. Chem. Int. Ed. 57, 14555 (2018).

Original publication

'Enhancing hydrogenation activity of Ni-Mo sulfide hydrodesulfurization catalysts', Science Advances 6, eaax5331 (2020). DOI: 10.1126/sciadv.eaax5331

Manuel F. Wagenhofer[1], Hui Shi[1], Oliver Y. Gutierrez[2], Andreas Jentys[1] and Johannes A. Lercher[1]

1. Technische Universität München, Department of Chemistry and Catalysis Research Center, Garching, Germany
2. Institute for Integrated Catalysis, Pacific Northwest National Laboratory, Richland, WA, USA

Polymorphism in a prototype high-entropy oxide

Highly tuneable lattice distortion induced by high pressure leads to polymorphic transition

High-entropy oxides (HEO) consist of at least five metals that are distributed randomly in a common simple crystal lattice, while their crystal structure can be different from each metal's generic lattice. Their characteristics open an almost infinite compositional space for the exploration of novel materials design and corresponding property engineering for widespread applications, including electrodes in Li-ion batteries and electronic sensors. Lattice distortion caused by the cations' different ionic sizes is believed to be inevitable and is critical to the fundamental understanding of the structure and related properties of HEOs. The complex composition in HEOs, in addition, makes it much more challenging for a comprehensive study compared with conventional materials with simple compositions and thus to understand their structure and properties.

Complex multi-cation compositions were believed to lead to the formation of a mixture of phases with diverse structures and usually useless properties. This stereotype of materials development was broken by recent discoveries. Deliberately incorporating five or more components with equal or near-equal atomic ratios, a material could be stabilised into a single-phase solid solution with a simple structure due to its maximised configurational entropy. This gave rise to a new class of materials, the so-called high-entropy materials. In principle, there is no limit on the number of components to be involved. The high-entropy materials started in the field of high-entropy alloys [1,2] and then quickly expanded into many other systems, including high-entropy oxides [3], carbides [4] and borides [5].

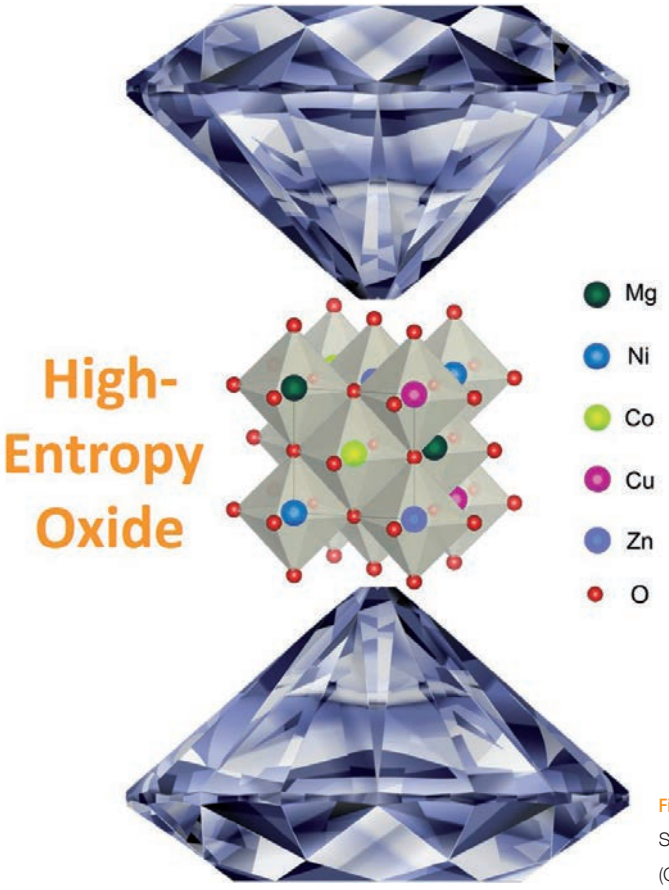

The first HEO with a complex composition of $(Mg_{0.2}Co_{0.2}Ni_{0.2}Cu_{0.2}Zn_{0.2})O$ and a single-phase rock salt structure was synthesised in 2015 [3]. This HEO possesses many remarkable properties, including a huge dielectric constant and a high room-temperature Li-ion conductivity, making it a promising electrode material for Li-ion batteries. As a new class of oxides, understanding their structures and the relationship to properties is considered an important and urgent topic.

With the high-resolution probing capabilities of high-energy synchrotron X-ray diffraction coupled with high-pressure techniques at beamline P02.2 at PETRA III, we could monitor the prototypical HEO $(Mg_{0.2}Co_{0.2}Ni_{0.2}Cu_{0.2}Zn_{0.2})O$ under increasing pressure of up to 43 GPa induced by a portable high-pressure device called a diamond anvil cell (Fig. 1).

Figure 1

Schematic illustration of a diamond anvil cell to generate high pressure on the $(Co_{0.2}Cu_{0.2}Mg_{0.2}Ni_{0.2}Zn_{0.2})O$ HEO for *in situ* synchrotron X-ray probing.

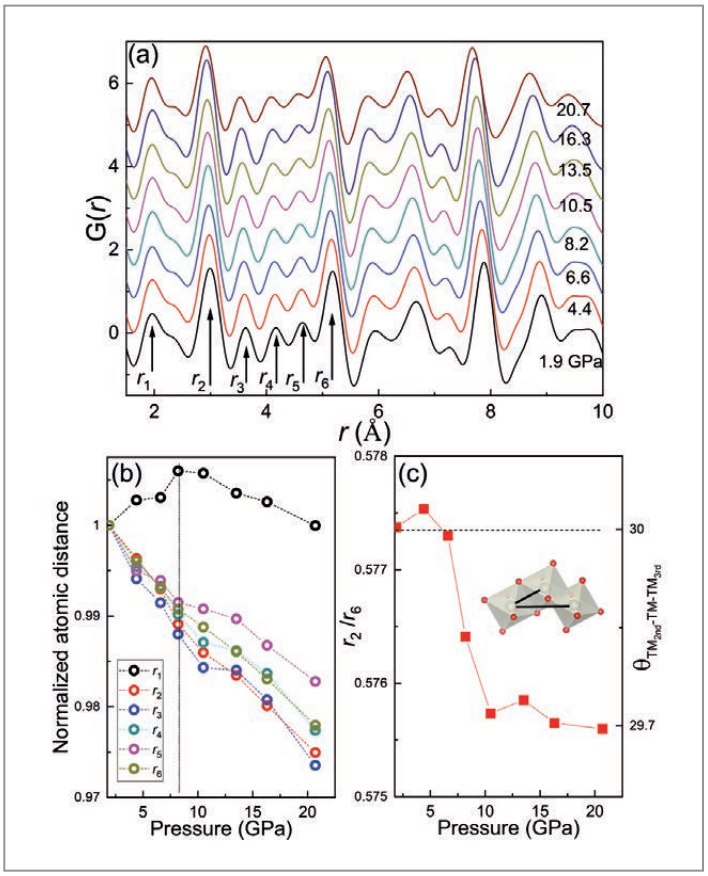

Figure 2

Structure evolution in real space of the $(Co_{0.2}Cu_{0.2}Mg_{0.2}Ni_{0.2}Zn_{0.2})O$ HEO during compression at room temperature. (a) Pair-distribution function of the $(Co_{0.2}Cu_{0.2}Mg_{0.2}Ni_{0.2}Zn_{0.2})O$ HEO at different pressures during compression up to 20.7 GPa. (b) The pressure dependence of the normalised atomic pair distances of the first six peaks denoted as r_1 to r_6 in (a). The black dotted line marks the starting pressure of kinks. (c) The pressure dependence of the r_2/r_6 ratio and the bond angle between a transition-metal (TM) cation and its second and third TM neighbours in $(Co_{0.2}Cu_{0.2}Mg_{0.2}Ni_{0.2}Zn_{0.2})O$ HEO. The inset in (d) is a schematic plot of the bond angle between HEO octahedrons. Below ~ 7 GPa or above ~ 10 GPa, the r_2/r_6 ratio remains almost constant with a sharp drop in between, which manifests distinct low and high-pressure states. The horizontal dashed line marks the ideal values of the r_2/r_6 ratio and bond angle in a standard rock salt structure.

Through Fourier transformation of the carefully corrected diffraction data after subtracting various background signals, the pair-distribution function, $G(r)$, was derived (Fig. 2a). The peaks represent the probability of finding another atom at a distance r in real space from a given atom — that is, the distribution of distances between atom pairs. Therefore, the atomic pair distances (Fig. 2b) and bond angles (Fig. 2c) inside and between transition-metal oxide octahedra can be calculated as a function of pressure by the peak positions in $G(r)$. The result was reproduced and confirmed using different pressure media to rule out the effect of non-hydrostaticity. Diverged atomic pair distance shifting in $G(r)$ and sharp bond angle changes at ~ 10 GPa demonstrate considerably tuned lattice distortion in the initial crystalline rock salt structure, which results in a reversible polymorphic phase transition into a highly distorted phase.

The data obtained enabled us to directly estimate and tune the lattice distortion over a large pressure range, which shed new light on the structural stability and tuneability of HEOs. The observed evidence paves the way for a better understanding of HEO materials, and at the same time it also promotes high-pressure X-ray diffraction as an efficient tool for their exploration and engineering.

Author contact: Qiaoshi (Charles) Zeng, zengqs@hpstar.ac.cn

References

1. J.-W. Yeh, S.-K. Chen, S.-J. Lin, J.-Y. Gan, T.-S. Chin, T.-T. Shun, C.-H. Tsau and S.-Y. Chang, 'Nanostructured high-entropy alloys with multiple principal elements novel alloy design concepts and outcomes', Adv. Eng. Mater. 6, 299–303 (2004).
2. B. Cantor, I.T.H. Chang, P. Knight and A.J.B. Vincent, 'Microstructural development in equiatomic multicomponent alloys', Mater. Sci. Eng. A 375–377, 213–218 (2004).
3. C.M. Rost, E. Sachet, T. Borman, A. Moballegh, E.C. Dickey, D. Hou, J.L. Jones, S. Curtarolo and J.P. Maria, 'Entropy-stabilized oxides', Nat. Commun. 6, 8485 (2015).
4. J. Zhou, J. Zhang, F. Zhang, B. Niu, L. Lei and W. Wang, 'High-entropy carbide: a novel class of multicomponent ceramics', Ceram. Int. 44, 22014–22018 (2018).
5. J. Gild, Y. Zhang, T. Harrington, S. Jiang, T. Hu, M. C. Quinn, W. M. Mellor, N. Zhou, K. Vecchio and J. Luo, 'High-entropy metal diborides: a new class of high-entropy materials and a new type of ultrahigh temperature ceramics', Sci. Rep. 6, 37946 (2016).

Original publication

'Lattice distortion and stability of $(Co_{0.2}Cu_{0.2}Mg_{0.2}Ni_{0.2}Zn_{0.2})O$ high-entropy oxide under high pressure', Materials Today Advances 8, 100102 (2020).
DOI: 10.1016/j.mtadv.2020.100102

Benyuan Cheng[1,2], Hongbo Lou[1], Abhishek Sarkar[4,5], Zhidan Zeng[1], Fei Zhang[1], Xiehang Chen[1], Lijie Tan[1], Konstantin Glazyrin[6], Hanns-Peter Liermann6, Jinyuan Yan[7,8] Liang, Wang[9], Ruzica Djenadic[4], Horst Hahn[4,5] and Qiaoshi Zeng[1,3]

1. Center for High Pressure Science and Technology Advanced Research, Shanghai, People's Republic of China
2. Shanghai Institute of Laser Plasma, Shanghai, People's Republic of China
3. Jiangsu Key Laboratory of Advanced Metallic Materials, School of Materials Science and Engineering, Southeast University, Nanjing, People's Republic of China
4. Joint Research Laboratory Nanomaterials – Technische Universität Darmstadt and Karlsruhe Institute of Technology, Darmstadt, Germany
5. Institute of Nanotechnology, Karlsruhe Institute of Technology, Eggenstein-Leopoldshafen, Germany
6. Deutsches Elektronen-Synchrotron DESY, Hamburg, Germany
7. Advanced Light Source, Lawrence Berkeley National Laboratory, Berkeley, USA
8. Department of Earth and Planetary Sciences, University of California, Santa Cruz, USA
9. School of Materials Science and Engineering, Beijing Institute of Technology, Beijing, People's Republic of China

Tailor-made latex colloids enable functional materials

How nanostructure influences surface wetting

Latex colloids are considered as very promising materials for a broad range of thin-film applications due to their facile surface functionalisation and can coalesce into thin films upon heat treatment. A 'colloid' is a dispersion of small particles in a solution, and a latex colloid is composed of polymeric particles dispersed in water. Even though latex colloids are already used in large-volume applications, it is still challenging to assess the effect the colloids have on film formation and wetting properties. Here, latex colloids were tailor-made by a controlled polymerisation procedure and sprayed onto a substrate. X-ray scattering and real-space imaging techniques allowed for detailed investigations on how the colloids behave on the surface and how the surface properties are affected.

Core-shell colloids composed of a hydrophilic shell (*N,N*-dimethylaminoethyl methacrylate, DMAEMA) and a hydrophobic core (PMMA or PBMA) were synthesised by RAFT-(Reversible-Addition-Fragmentation chain-Transfer) mediated surfactant-free emulsion polymerisation with polymerisation-induced self-assembly (PISA) [1]. The colloids form by self-assembly in situ during the polymerisation; short hydrophilic polymer chains are chain-extended by a hydrophobic monomer and once the hydrophobic block is long enough, the diblock copolymers self-assemble into colloidal particles. The cationically charged hydrophilic part of the polymer chain is located in the shell, stabilising the colloid, while the hydrophobic part of the chains constitutes the core, which makes it favourable for dispersing in water. Two colloids with a low glass-transition temperature (Tg) PBMA core and a high Tg PMMA core with varying chain length of the core polymers were investigated, with a larger chain resulting in larger particles.

Homogeneous sub-monolayer coatings of the core-shell colloids on silicon substrates were obtained by spray deposition (Fig. 1). The corresponding surfaces were analysed by grazing incidence small-angle X-ray scattering (GISAXS) to monitor the film formation and structural evolution during

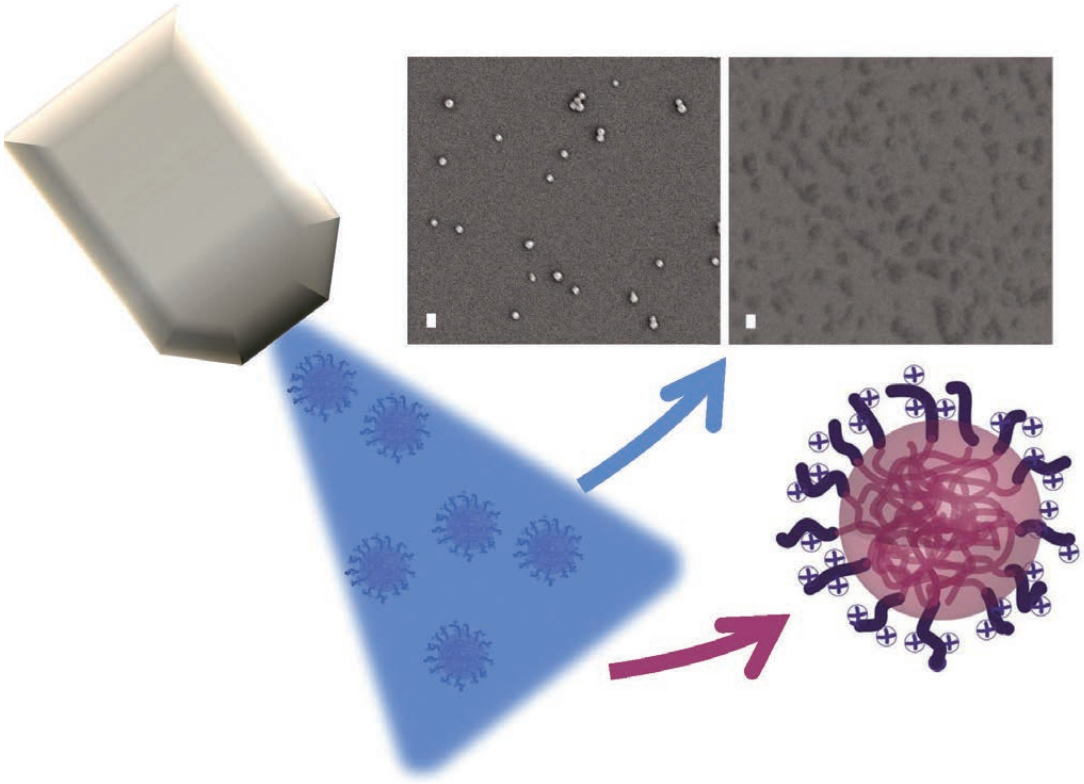

Figure 1

Left side: Sketch of the spray deposition of the core-shell colloids. The less dense shell is depicted as charged water-swollen polymer chains. SEM imaging reveals clear morphological changes between spray-deposited high (left) and low (right) Tg colloids (PMMA (diameter 96 nm) vs. PBMA (diameter 82 nm)). The scale bar is 100 nm.

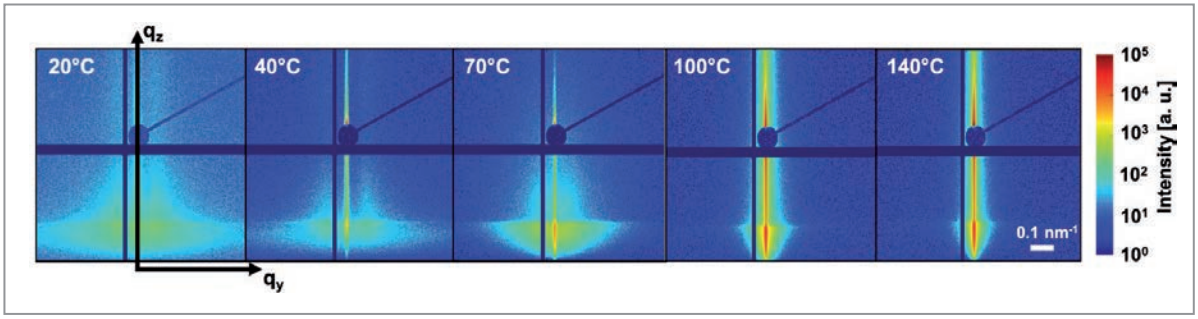

Figure 2
GISAXS pattern for small PMMA colloids deposited on the surface and annealed from room temperature up to 140° C.

annealing (Fig. 2). *Ex situ* analysis of the thin films by contact angle microscopy (CAM), field-emission scanning electron microscopy (FE-SEM) and atomic force microscopy (AFM) was conducted to correlate macroscopic properties with nanoscale changes.

The structural evolution of spray-deposited films during annealing was monitored in real-time by GISAXS at the X-ray beamline P03 at PETRA III. It was evident that the thin films undergo structural evolution during annealing. Unexpectedly, the GISAXS patterns did not change significantly below a temperature of 70 °C, despite the core polymers having different Tg values (PMMA ≈ 126 °C and PBMA ≈ 36 °C as measured by differential scanning calorimetry). We hypothesise that this could be attributed to both core polymers experiencing increased chain mobility at 70 °C. The rapid morphological change above 70 °C can be explained by decreased charge repulsion, due to loss of bound water and partial softening of nanoparticles as observed by Herzog et al. [2]. The GISAXS data were fitted using a spherical form factor on a paracrystal plane, adopted from Schaffer et al. [3]. Fits were conducted based on the assumption that the core-shell colloids were spherical and did not deform during spray deposition. Two distinct spherical domains could be extracted: a smaller domain correlating with the size of the individual colloid and a larger domain size attributed to aggregated or coalesced particles.

The results obtained by GISAXS were complemented by high-resolution real-space imaging. The topographical AFM images showed that, at room temperature, the colloids with PMMA in the core are spherical, whereas the PBMA-cored nanoparticles deformed and aggregated to clusters. FE-SEM was also conducted to further detail the nanoscale surface topography, and the combination of AFM and FE-SEM allowed the distinction of spherical clusters and coalesced particles with distinct disrupted particle boundaries.

Wettability and the ability to control wetting of a surface are crucial properties for functional coatings. CAM was conducted to correlate the structural evolution assessed by GISAXS and high-resolution real-space imaging to wetting properties. CAM was conducted prior to and after annealing at annealing temperatures of 40 and 140 °C. All samples rendered contact angles above 60° despite incomplete surface coverage. It is noteworthy that the film formed only a sub-monolayer, and therefore the roughness dependence can be neglected. The morphological change that occurred at 70 °C, as observed by GISAXS, was found to result in slightly higher contact angles. We hypothesise that the polymer chains align as the nanoparticles coalesce during the annealing and therefore result in a higher contact angle. The low surface coverage and the resulting small changes in contact angles allow for very precise fine-tuning of the wettability. This is of utmost importance for applications where the surface energy results in a small change in contact angles of a few degrees while other physical properties such as light transmission and accessibility of the surface are unaffected.

This fundamental study methodically allowed to correlate the macroscopic tailored functionality (contact angle) to the nanostructural changes of the core-shell colloids. Our results show the high importance of observing the polymer chain mobility in the shell of colloids. In general, our results will impact the use as colloidal inks in the printing industry and additive manufacturing.

Author contact: Eva Malmström, mavem@kth.se
Stephan V. Roth, stephan.roth@desy.de

References

1. J. Engström, F. L. Hatton, L. Wågberg, F. D'Agosto, M. Lansalot, E. Malmström and A. Carlmark, 'Soft and rigid core latex nanoparticles prepared by RAFT-mediated surfactant-free emulsion polymerization for cellulose modification – a comparative study', Polym. Chem. 8, 1061–1073 (2017).
2. G. Herzog, M. M. Abul Kashem, G. Benecke, A. Buffet, R. Gehrke, J. Perlich, M. Schwartzkopf, V. Körstgens, R. Meier, M. A. Niedermeier, M. Rawolle, M. A. Ruderer, P. Müller-Buschbaum, W. Wurth and S. V. Roth, 'Influence of nanoparticle surface functionalization on the thermal stability of colloidal polystyrene films', Langmuir 28, 8230–8237 (2012).
3. C. J. Schaffer, C. M. Palumbiny, M. A. Niedermeier, C. Jendrzejewski, G. Santoro, S. V. Roth and P. Müller-Buschbaum, 'A direct evidence of morphological degradation on a nanometer scale in polymer solar cells', Adv. Mater. 25, 6760–6764 (2013).

Original publication

'Core–shell nanoparticle interface and wetting properties', Advanced Functional Materials 30, 1907720 (2020). DOI: 10.1002/adfm.201907720

Joakim Engström[1,2], Calvin J. Brett[1,2,3], Volker Körstgens[4], Peter Müller-Buschbaum[4,5], Wiebke Ohm[3], Eva Malmström[1,2] and Stephan V. Roth[1,2,3]

1. KTH Royal Institute of Technology, Stockholm, Sweden
2. Wallenberg Wood Science Center, Stockholm, Sweden
3. Deutsches Elektronen-Synchrotron DESY, Hamburg, Germany
4. Technische Universität München, Garching, Germany
5. Heinz Maier-Leibnitz Zentrum, Garching, Germany

Unravelling the spatial distribution of unconventional lattices in a gold bipyramid

Scanning X-ray diffraction microscopy of a five-fold twinned Au bipyramid

Gold is known to crystallise in the face-centred cubic (fcc) lattice and is extremely difficult to stabilise in other lower symmetry lattices. Here, we show that Au can be stabilised in unconventional lattices with ~ 92% of the crystallite volume and the rest in fcc. Scanning X-ray diffraction microscopy (SXDM) has the potential to decipher the multi-phase or strained region within a nanostructure without dissecting. The spatial distribution of the lattices was unraveled using SXDM in a 1.36 µm long and 230 nm thick bipyramidal crystallite.

Au, noblest of all metals, crystallises in the face-centred cubic (fcc) lattice and possesses extraordinary stability under high pressure and temperature [1–3]. Recently, Au has been stabilised in body-centred orthorhombic (bco) and body-centred tetragonal (bct) mixed lattices, together known as bc(o,t) lattices in the form of microcrystallites, mostly of bipyramidal shape [4], as shown in Fig. 1a,b. The bipyramids are ~ 3 µm in length with a penta-twinned geometry (inset, Fig. 1a). Geometrical constraint-induced stresses in the bipyramid cause stabilisation of the bc(o,t) lattices, as high as 92% of the entire crystallite volume (see XRD pattern in Fig. 1c). The crystallites hosting the unconventional lattices exhibit strong catalytic performance in a reduction reaction [5] and are nobler than fcc Au in harsh chemicals such as Hg and aqua regia [6]. Therefore, separating the spatial distribution of the different lattices in the crystallite volume is interesting. The crystallites are 200–400 nm thick and not suitable for study by high-resolution transmission electron microscopy (HRTEM). SXDM with a nanobeam, in contrast, offers a great opportunity in this regard.

A 100 nm X-ray beam (15 keV) at beamline P06 at PETRA III was used to scan in steps over the crystallite, and the diffraction volume contributing towards diffraction was located. The crystallite was rotated around its long axis by 42°, and within the rotational frame, 14 diffraction spots appeared (Fig. 2). The spots were widespread and asymmetric in nature. The assignment of the spots reveals the presence of both fcc and bco lattices. From the assignment, the orientation of the unit cells was derived and it was found that the crystal growth directions were bco<010> and fcc<110>. Intriguingly, within the 42° rotation, all symmetry reflections appeared. The diffraction spot c appearing at 0° was retained up to a rotation of the crystal of 10° (Fig. 3a). The diffracting volume contributing towards spot c appeared from the top tip at 0° and, while rotating, the volume followed a translation along the length of the crystallite from the top tip to the bottom (Fig. 3b). This translation of the diffraction volume with rotation indicates the presence of a twist of ~ 6° in total from the top tip to the bottom tip of the crystallite.

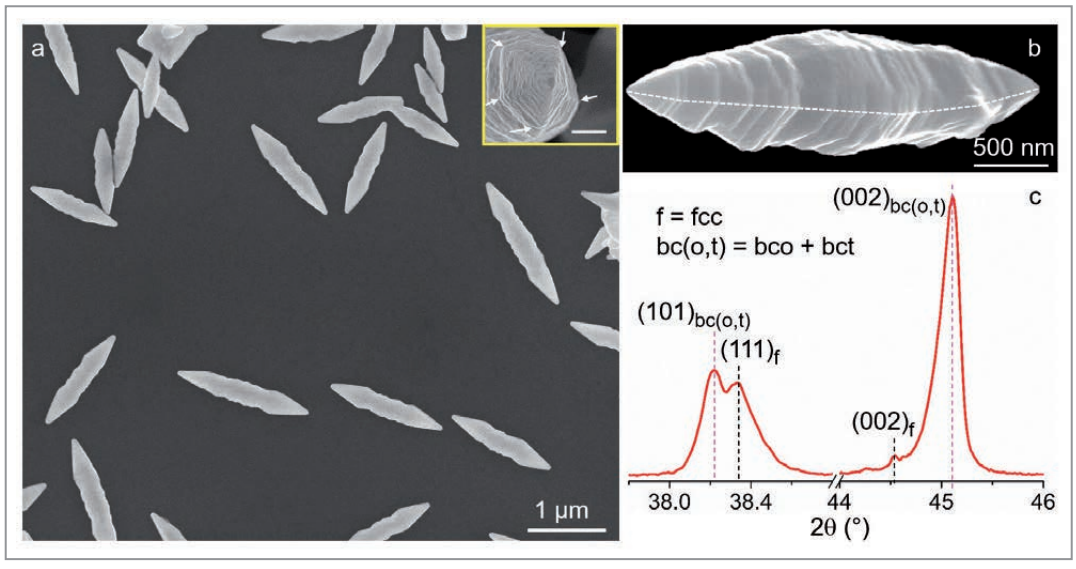

Figure 1

SEM images of (a) a collection of Au microcrystallites and (b) a single bipyramid in the tilted view. The inset in (a) shows the presence of a penta-twinned tip, where the white arrows denote the twinned boundaries. Scale bar 200 nm. A white dotted line is drawn in (b) showing a twin boundary. (c) XRD pattern of the bc(o,t) Au microcrystallite; bc(o,t) refers to a mixture of body-centred orthorhombic (bco) and body-centred tetragonal (bct) lattices. (Adapted with permission. Copyright (2020) American Chemical Society)

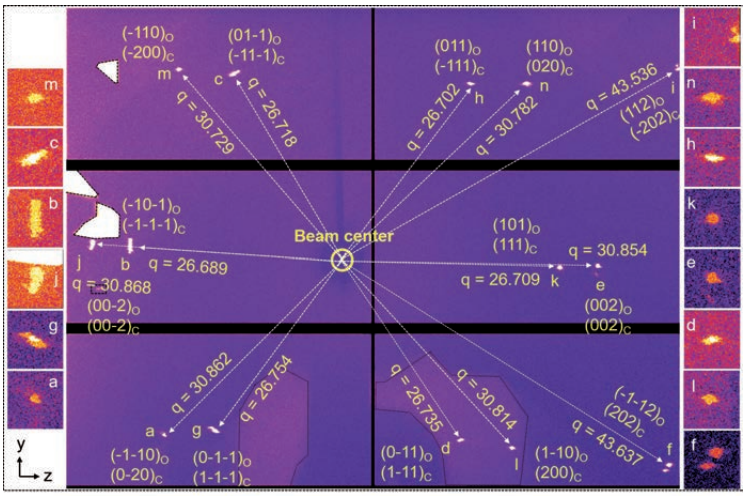

Figure 2

Integrated diffraction spots on the detector; *q*-values are given in nm^{-1}. The 14 reflections (a-n) have been assigned to a combination of fcc (C) and bco (O). Within the 42° rotation, all symmetry spots appear. The magnified views of the spots are shown in the left and right rectangular boxes. (Reprinted with permission. Copyright (2020) American Chemical Society)

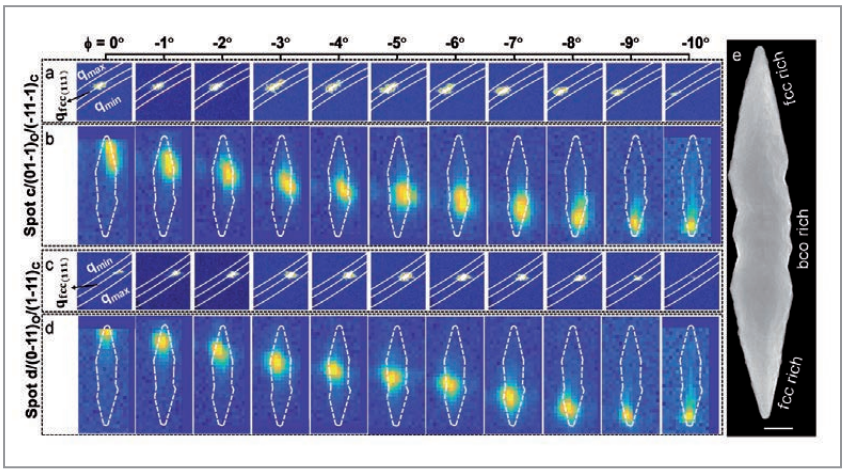

Figure 3

Diffraction spots and the corresponding diffraction maps. (a,c) With the rotation angle in the top row, the signals of the mirror reflection spots c and d grow and decay. The spots are shown enclosed between q_{min} and q_{max} circles (white) obtained by considering the intensity spread of the spot in various frames, including those of the symmetry-related ones with the circle corresponding to the *q*-value of fcc(111) passing in between. (b,d) Diffraction maps in real space for different rotations (4° to –37°). The contour of the crystallite is drawn as white dashed line to visualise the relative position of the diffracting region. Note that spots (c) and (d) appear from longitudinally opposite halves of the crystallite. (e) SEM image of the crystallite demonstrating the spatial distribution of various lattices. The scale bar is 200 nm long. (Adapted with permission. Copyright (2020) American Chemical Society)

The mirror reflection of spot c is spot d, which also appears within a similar rotational range (Fig. 3c). The nature and location of the diffraction spots c and d are different. Whereas spot c appears on the right-hand side of the crystal, spot d shows up on the left side (Fig. 3b and 3d). The appearance of the mirror reflections can be understood by considering the presence of twin boundaries. The examined crystallite accommodates a penta-twinned geometry (Fig. 1b, the white dotted line) and therefore explains the presence of symmetry reflections without a 180° rotation.

It also can be noted from the experiment that the spots reappear after a rotation of around 33–40°, which can be attributed to the presence of a five-fold symmetry along the crystal axis. From the spread of the spots, the spatial distributions of the lattices were unveiled, i.e., the tips are rich in the fcc phase, whereas the body mainly contains the bco phase (Fig. 3e). The study demonstrates the presence of both, compression and expansion (-6.06% and +4.21%, respectively). The distribution of the lattices explains the more noble behaviour of bc(o,t) Au in harsh chemical environments in contrast to conventional fcc gold.

Author contact: Chaitali Sow, sow.chaitali325@gmail.com
Abhisakh Sarma, abhisakh.sarma@desy.de
Thomas F. Keller, thomas.keller@desy.de
Milan K. Sanyal, milank.sanyal@saha.ac.in

References

1. L. Dubrovinsky, N. Dubrovinskaia, W. A. Crichton, A. S. Mikhaylushkin, S. I. Simak, I. A. Abrikosov, J. S. De Almeida, R. Ahuja, W. Luo and B. Johansson, 'Noblest of all metals is structurally unstable at high pressure', Phys. Rev. Lett. 98, 045503 (2007).
2. R. Briggs, F. Coppari, M. G. Gorman, R. F. Smith, S. J. Tracy, A. L. Coleman, A. Fernandez-Pañella, M. Millot, J. H. Eggert and D. E. Fratanduono, 'Measurement of body-centered cubic gold and melting under shock compression', Phys. Rev. Lett. 123, 045701 (2019).
3. S. M. Sharma, S. J. Turneaure, J. M. Winey, Y. Li, P. Rigg, A. Schuman, N. Sinclair, Y. Toyoda, X. Wang, N. Weir, J. Zhang and Y. M. Gupta, 'Structural transformation and melting in gold shock compressed to 355 GPa', Phys. Rev. Lett. 123, 045702 (2019).
4. G. Mettela, M. Bhogra, U. V Waghmare and G. U. Kulkarni, 'Ambient stable tetragonal and orthorhombic phases in penta-twinned bipyramidal Au microcrystals', J. Am. Chem. Soc. 137, 3024 (2015).
5. G. Mettela, N. Mammen, J. Joardar, S. Narasimhan and G. U. Kulkarni, 'Non-fcc rich Au crystallites exhibiting unusual catalytic activity', Nano Res. 10, 2271 (2017).
6. G. Mettela, S. Kouser, C. Sow, S. T. Pantelides and G. U. Kulkarni, 'Nobler than the noblest: noncubic gold microcrystallites', Angew. Chem. Int. Ed. 57, 9018 (2018).

Original publication

'Unraveling the spatial distribution of catalytic non-cubic Au phases in a bipyramidal microcrystallite by X-ray diffraction microscopy', ACS Nano 14, 9456–9465 (2020).
DOI: 10.1021/acsnano.0c02031

Chaitali Sow[1], Abhisakh Sarma[2], Andreas Schropp[2], Dmitry Dzhigaev[2,†], Thomas F. Keller[2,3], Christian G. Schroer[2,3], Milan K. Sanyal[4] and Giridhar U. Kulkarni[1]

1. Chemistry and Physics of Materials Unit, Jawaharlal Nehru Centre for Advanced Scientific Research (JNCASR), Bangalore, India
2. Deutsches Elektronen-Synchrotron DESY, Hamburg, Germany
3. Physics Department, Universität Hamburg, Hamburg, Germany
4. Saha Institute of Nuclear Physics, Kolkata, India

† Current Address: Division of Synchrotron Radiation Research, Department of Physics, Lund University, Lund, Sweden

Reaction-driven restructuring of Pt-Rh nanoparticles

Bragg coherent diffraction imaging during gas–surface reactions

Platinum-group metals and alloys are among the most important catalysts for organic and electrochemical reactions [1,2]. For this reason, the structure-activity relationships of the platinum alloy nanoparticles have been a focus of extensive studies. Some studies [3,4] even suggested that the core–shell compositions of nanoparticles can dynamically change depending on gas reaction environments. Until now, however, there was no direct evidence for such dynamic restructuring because so far there was no *in situ* experimental technique that could directly image the internal alloy compositions. The situation changed recently because new coherent X-ray imaging techniques emerged and advanced rapidly.

Recent breakthroughs in several coherent X-ray techniques have enabled nanoscale imaging in many areas of science and technology. In particular, the new Bragg Coherent Diffraction Imaging (BCDI) technique enabled visualisation of unprecedented details of nanoparticle structures such as internal elastic-strain distribution [5]. A BCDI image is composed of 3D complex numbers where the amplitudes show the mass densities and the phases represent lattice displacements. It turns out that the phase images are much more reliable and precise than the amplitude images. The extreme sensitivity of the phase to the lattice makes the technique unique and the visualisation of elastic strain possible. In this work, the sensitivity to the lattice was reformulated to be applicable to the composition strain instead of the elastic strain [6]. Now, the 'amplitude' of the image is proportional to the internal mass density and the 'phase' of the image — more precisely the derivative of the phase — is proportional to the composition deviation of a binary-alloy nanoparticle.

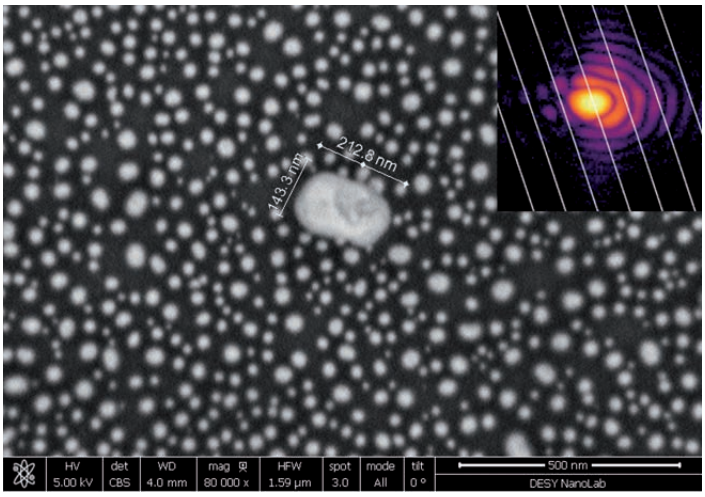

Figure 1

An SEM image of the $Pt_{2/3}$-$Rh_{1/3}$ alloy nanoparticle. The size of the particle is marked to be 212.8 nm × 143.3 nm. The smaller nanoparticles of several nm are pure Rh particles. (inset) A 2D coherent diffraction pattern of the (111) Bragg reflection from the particle on a logarithmic intensity colour scale. The white equi-2θ lines indicate the expected Bragg-reflection maximum for every 10% change in the mean Rh composition of the particle and the diffraction angle of the average position is used for the particle average composition. A stack of such patterns forms a 3D set of Bragg diffraction intensity that was inverted to reconstruct the real-space image.

A scanning electron microscopy (SEM) image (Fig. 1) shows a $Pt_{2/3}$-$Rh_{1/3}$ particle among the scattered, smaller pure Rh particles. The sample was prepared by depositing a Rh layer at 630 °C over Pt nanoparticles dewetted on an Al_2O_3(0001) substrate. Hierarchical fiducial markers were used to identify the same particle with SEM in the DESY NanoLab and with a

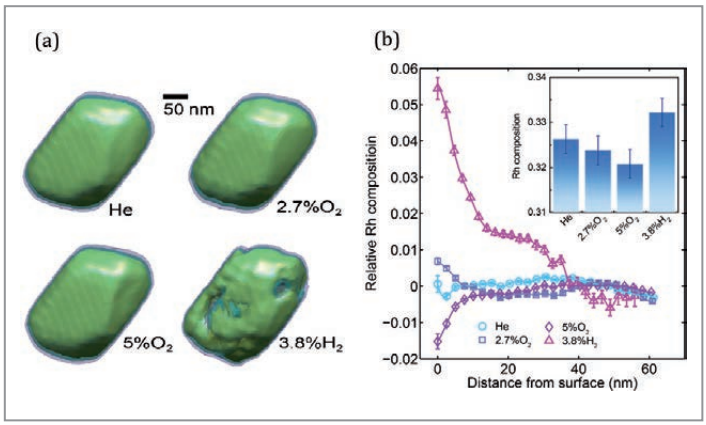

Figure 2

(a) BCDI images of the Pt/Rh alloy nanoparticle under different gas environments reveal changes in the 3D particle morphology. (b) The redistributions of the radially averaged Rh composition within the particle under oxidizing and reducing environments. The surface Rh composition (distance at 0 nm) changes sensitively to the exposed gas at the reaction temperature (550° C). The inset shows the particle average compositions of Rh determined from the Bragg angles.

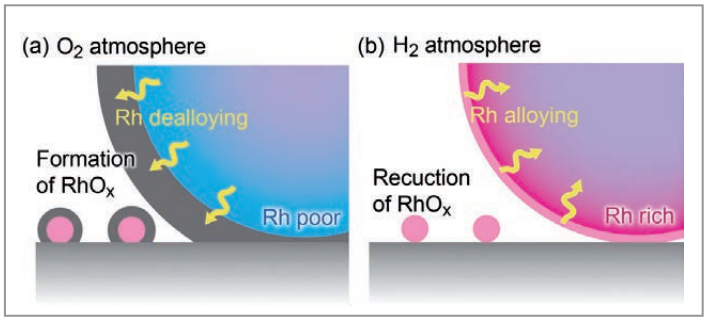

Figure 3

Schematics of alloying and dealloying processes in O_2 and H_2 environments. The large sphere indicates the Pt-Rh particle and the small ones do Rh nanoparticles. (a) In O_2, the Rh-oxide layer grows faster because Rh is more oxophilic than Pt, which induces the Rh migration to the surface. (b) In H_2, the Rh-oxide layer reduces, which increases the Rh compositions at the surface (Fig. 2b).

confocal microscope at the X-ray beamline. The 2D intensity pattern (inset of Fig. 1) of the (111) Bragg reflection of the particle is also shown as an example for diffraction patterns. 3D Bragg intensities, a collection of such 2D patterns, were obtained during surface reactions in various gases at 550 °C and inverted to reconstruct the 3D real-space images of complex numbers using an iterative phase-retrieval algorithm [5].

The 3D amplitude images (Fig. 2a), confirming the SEM image, do not change during the exposure to oxygen and helium. However, we can clearly see that the particle shape deforms during the exposure to hydrogen. The deformation suggests qualitatively that the surface Rh composition may increase, thereby decreasing the mass density of the surface under hydrogen exposure. The quantitative analyses of the 3D phase images show that the radial composition redistributes, depending on the surface–gas reactions (Fig. 2b), even though the apparent shape of the particle changes little during the reactions. In a 5% O_2 environment, the Pt-rich (Rh-poor) region appeared at the surface whereas the composition was relatively flat in He and in 2.7% O_2. At the same time, the average Rh composition (inset) decreased slightly under the 2.7% O_2 atmosphere, and even more under the 5% O_2. On the other hand, the H_2 atmosphere yielded a 6% *increase* of Rh-composition due to Rh segregation at the surface as well as a considerable increase of the average Rh composition.

The observation has a rather simple explanation. When the particle is heated in O_2 atmosphere, Rh, being more oxophilic than Pt, forms oxides faster and thicker than Pt does (Fig. 3a). This thermodynamic force causes Rh dealloying from the surface of the particle by forming Rh oxides, which does not diffract to the (111) Bragg peak. This Rh oxidation eventually yields the Rh-poor, Pt-rich region on the surface by decreasing the surface Rh composition. In the H_2 atmosphere, the reverse reaction is expected. The Rh oxide is reduced and Rh atoms are incorporated into the particle (Fig. 3b). In addition, Rh atoms migrate from the neighbouring Rh nanoislands surrounding the $Pt_{2/3}$-$Rh_{1/3}$ particle. The Rh migration explains the Rh-rich surface and the increases of the overall Rh composition (see inset of Fig. 2b), which could not have happened without Rh migration. The continuous Rh migration from the Rh nanoislands explains the overall slope of the gradual decrease of Rh concentration from the surface to the core. However, it is also possible that it is driven thermodynamically towards the truncated surface, which requires further theoretical clarification.

The redistributions of metals observed in alloy nanoparticles as large as 100 nm offers an insight into the dynamic nature of the generally much smaller nanoparticle catalysts in practical usages for gas-phase catalysis and fuel-cell catalysts operating at elevated temperatures. Such dynamic reconfiguration can be much more significant for smaller nanoparticles for the simple reason of the larger surface-to-bulk ratio. This suggests that the active compositional segregation, redistribution and other structural dynamics must be taken into account for rational design of new catalysts and electrocatalysts.

Author contact: Hoydoo You, you@anl.gov
Thomas F. Keller, thomas.keller@desy.de
Ivan Vartaniants, ivan.vartaniants@desy.de
Andreas Stierle, andreas.stierle@desy.de

References

1. G. A. Somorjai and Y. Li, 'Introduction to surface chemistry and catalysis' (Wiley, 2010).
2. G. Ertl, 'Reactions at Solid Surfaces' (Wiley, 2009).
3. F. Tao et al., 'Reaction-driven restructuring of Rh-Pd and Pt-Pd core-shell nanoparticles', Science 322, 932–935 (2008).
4. P. Müller, U. Hejral, U. Rütt and A. Stierle, 'In situ oxidation study of Pd–Rh nanoparticles on $MgAl_2O_4(001)$', Phys. Chem. Chem. Phys. 16, 13866–13874 (2014).
5. I. Robinson and R. Harder, 'Coherent X-ray diffraction imaging of strain at the nanoscale', Nature Mater. 8, 291–295 (2009).
6. T. Kawaguchi et al., Proceedings to the 15th Int'l Conf. on Surface X-ray and Neutron Scattering (SXNS15), J. Korean Phys. Soc. 75, 528–533 (2019).

Original publication

'Gas-induced segregation in Pt-Rh alloy nanoparticles observed by in-situ Bragg coherent diffraction imaging', Physical Review Letters, 123, 246001 (2019).
DOI: 10.1103/PhysRevLett.123.246001

Tomoya Kawaguchi[1,6], Thomas F. Keller[2,3], Henning Runge[2,3], Luca Gelisio[2], Christoph Seitz[2], Young Y. Kim[2], Evan R. Maxey[4], Wonsuk Cha[4], Andrew Ulvestad[1], Stephan O. Hruszkewycz[1], Ross Harder[4], Ivan A. Vartanyants[2,5], Andreas Stierle[2,3] and Hoydoo You[1]

1. Materials Science Division, Argonne National Laboratory, Argonne, Illinois , USA
2. Deutsches Elektronen-Synchrotron DESY, Hamburg, Germany
3. Physics Department, Universität Hamburg, Hamburg, Germany
4. Advanced Photon Source, Argonne National Laboratory, Argonne, Illinois, USA
5. National Research Nuclear University MEPhI, Moscow, Russia
6. Institute for Materials Research, Tohoku University, Sendai, Japan

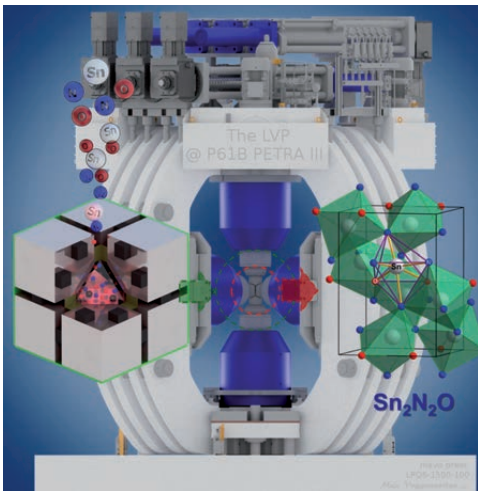

A roadmap for high-pressure synthesis of novel nitrides

The discovery of tin oxynitride

As opposed to conventional chemical synthesis, high-pressure methods are very well suited for the synthesis of novel materials with unusual crystal structures and properties. A large volume press (LVP) can generate high pressure (over 100000 atm) and high temperature (over 2000 °C) environments in sample volumes of several cubic mm to form new compounds, potentially metastable at room pressure. Known examples are synthetic diamond and cubic BN, the hardest materials in the world. Currently, research in nitrides is particularly popular due to their optoelectronic properties for use in, for example, solar cells and LEDs. Therefore, the new compound tin oxynitride (Sn_2N_2O), stabilised with high pressure, is an exciting discovery.

The elements Si, Ge and Sn, belonging to group 14 of the periodic table, form nitrides with exceptional thermo-mechanical and optoelectronic properties. Low compressibility and high hardness have been reported for spinel-type Si_3N_4 and Ge_3N_4. These materials and their solid solutions are predicted to form a new family of wide direct gap semiconductors [1,2]. Adding oxygen brings even more versatility to search for novel materials. Interestingly silicon oxynitride (Si_2N_2O), named ‘sinoite’, was discovered in a meteorite in 1964, at the same time of its first synthesis from silicon and quartz powder above 1500 °C in nitrogen atmosphere [3]. Sinoite proved to be one of the most stable, oxidation resistant refractory nitrides. The isotypic Ge_2N_2O has also been synthesised at ambient pressure, however, a corresponding tin oxynitride was unknown so far. Failure of standard synthesis routes may be caused by metastability of phases and kinetic hinderances to reach a stability field in the phase diagram. Thus, extreme pressure and temperature is needed to overcome the activation energy barrier. We have reported the synthesis of such a metastable compound, namely a novel Sn_2N_2O (SNO) at high-pressure high-temperature (HP-HT) conditions, using a LVP.

An oxygen-bearing Sn_3N_4 precursor was synthesised at TU Darmstadt from the molecular compound $Sn[NMe_2]_4$, via a two-stage chemical process in an ammonia atmosphere. This precursor was subjected to HP-HT conditions in a Hall-type 6-ram LVP installed at the P61B beamline at PETRA III (Fig. 1). At a pressure of ~ 20 GPa (200000 times atmospheric pressure), and in a temperature range of 1200–1500 °C, the reaction produced the novel Sn_2N_2O in crystalline form. Controlled heating in this temperature range, made possible by the LVP with resistive heating, was necessary to acquire this new compound.

The samples were recovered after HP-HT treatment and appeared dense and fine-grained. Synchrotron X-ray diffraction was performed at the high-resolution powder-diffraction beamline P02.1 at PETRA III. The high-quality XRD pattern showed a novel phase, which seemed to be cubic with lattice parameter a = 7.831(2) Å. However, the true symmetry must be lower than cubic, hidden below overlapping reflections. Here the limitations of powder diffraction were reached. The evaluation of the crystal structure of this novel phase was not

Figure 1

High-pressure synthesis of a tin oxynitride Sn_2N_2O (SNO).

(a) Photograph and (b) schematic drawing of the LVP (Max Voggenreiter GmbH, mavo press LPQ6-1500-100) installed at PETRA III beamline P61B is presented along with the high-pressure anvil assembly for extreme conditions. The SNO crystal structure (space group: *Pbcn*) of Rh_2S_3-type with all Sn atoms in six-fold coordination is also highlighted (Credit: Stefan Sonntag, Shrikant Bhat, DESY).

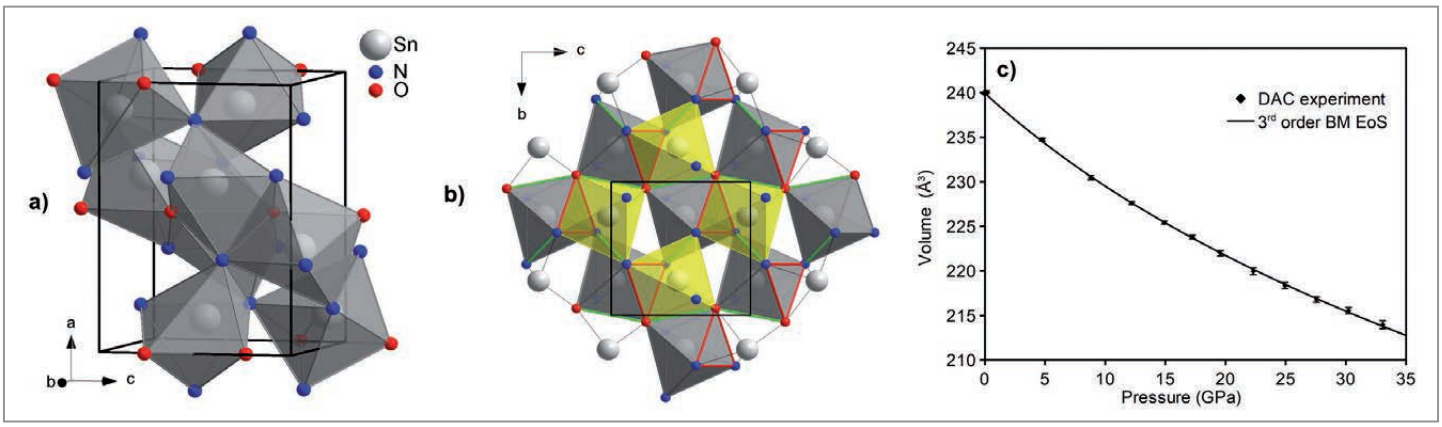

Figure 2

(a) Unit cell of SNO, showing the distorted octahedral coordination of Sn. (b) Crystal structure of SNO: view along the a-axis, showing grey and yellow coloured octahedra sharing faces (indicated as red triangles). Additional edge sharing (indicated as green lines) connects octahedra into chains running along the b-axis. (c) Pressure dependence of the unit cell volume of SNO and the 3rd order Birch-Murnaghan EoS fitted to the data.

straightforward, but needed the cooperation of different methods on different length scales, from XRD (µm) over electron diffraction (nm) to *ab initio* structure calculations (individual atoms).

The method of choice was transmission electron microscopy, namely automated diffraction tomography (ADT) at the Johannes Gutenberg-Universität Mainz [4]. Single-crystal structure determination from a ~200 nm sized crystal, using ADT, revealed the true symmetry of SNO as orthorhombic with space group *Pbcn* and two of the lattice parameters by a factor of √2 smaller than the cubic one with deviations of less than 0.2%. The crystal structure is of the Rh_2S_3 type, which is known as a high-pressure modification of several oxide structures like Rh_2O_3, Al_2O_3 or Fe_2O_3. All Sn atoms are six-fold coordinated by nitrogen and oxygen, whereas the sinoite structure shows only four-fold coordination (Fig. 2a,b).

From the dense-packed structure, a low compressibility of SNO was expected. Indeed, a bulk modulus of B_0 = 193(5) GPa with pressure derivative B' = 6.9(7) was determined from the pressure dependence of the unit cell volume by fitting a 3rd order Birch-Murnaghan equation of state (EoS) (Fig. 2c). The pressure dependence of the unit cell volume of SNO was measured in a diamond-anvil cell using synchrotron radiation at the Extreme Conditions Beamline P02.2 at PETRA III.

Ab initio structure calculations using density functional theory (DFT) in collaboration with the University of Texas at Arlington, USA, confirmed the ordered N/O distribution of the crystal structure and predicted a bulk modulus comparable with that analysed experimentally. Moreover, the SNO structure model (Fig. 2a,b) was calculated to be stable above 12 GPa and to remain the most favourable one up to 95 GPa.

The synthesised tin oxynitride may be considered for applications, for example, in the field of low bandgap semiconductors. It is also the first evidence for the existence of a crystalline ternary oxynitride of tin and complements and extends the well-known group 14 element oxynitrides of silicon and germanium. This work demonstrates the potential of high-pressure synthesis routes to access novel materials and would not have been successful without the research collaboration within DESY (three different beamlines at PETRA III) and the cooperation of four different national / international partners.

Author contact: Shrikant Bhat, shrikant.bhat@desy.de
Leonore Wiehl, leonore.wiehl@tu-darmstadt.de
Robert Farla, robert.farla@desy.de
Ralf Riedel, ralf.riedel@tu-darmstadt.de

References

1. A. Zerr, G. Miehe, G. Serghiou, M. Schwarz, E. Kroke, R. Riedel, H. Fueß, P. Kroll and R. Boehler, 'Synthesis of cubic silicon nitride', *Nature* 400, 340–342 (1999).
2. T. D. Boyko, A. Hunt, A. Zerr and A. Moewes, 'Electronic structure of spinel-type nitride compounds Si_3N_4, Ge_3N_4, and Sn_3N_4 with tunable band gaps: application to light emitting diodes', Phys. Rev. Lett. 111, 097402 (2013).
3. C. A. Andersen, K. Keil and B. Mason, 'Silicon oxynitride: a meteoritic mineral', *Science* 146, 256–257 (1964).
4. U. Kolb, E. Mugnaioli and T. E. Gorelik, 'Automated electron diffraction tomography – a new tool for nano crystal structure analysis', Cryst. Res. Technol. 46, 542–554 (2011).

Original publication

'A novel high-pressure tin oxynitride Sn_2N_2O', Chemistry–A European Journal 26, 2187–2194 (2020). DOI: 10.1002/chem.201904529

Shrikant Bhat[1], Leonore Wiehl[2], Shariq Haseen[3], Peter Kroll[3], Konstantin Glazyrin[1], Philipp Gollé-Leidreiter[2], Ute Kolb[2,4], Robert Farla[1], Jo-Chi Tseng[1], Emanuel Ionescu[2], Tomoo Katsura[5] and Ralf Riedel[2]

1. Deutsches Elektronen-Synchrotron DESY, Hamburg, Germany
2. FB Material- und Geowissenschaften, Technische Universität Darmstadt, Germany
3. Department of Chemistry and Biochemistry, The University of Texas at Arlington, USA
4. Institut für Physikalische Chemie, Johannes Gutenberg-Universität Mainz, Germany
5. Bayerisches Geoinstitut, University of Bayreuth, Germany

Watching excitons through the eyes of core levels

Core-*cum*-conduction photoelectron spectroscopy reveals an ultrafast excitonic Mott transition

Optoelectronic properties of semiconductors are largely governed by two types of excitations: excitons, the bosonic quasiparticles comprised of an electron and a hole bound by Coulomb interaction, and quasi-free carriers (QFCs) of single-particle character. The process of breaking excitons into QFCs, i.e. an excitonic Mott transition, has been quite elusive to observe due to its ultrafast nature. A novel approach of studying the interaction between core electrons and excited carriers has enabled distinguishing excitons from QFCs and tracking the evolution of an excitonic Mott transition on a femtosecond time scale using photoelectron spectroscopy.

Static X-ray photoelectron spectroscopy (XPS) has been a workhorse of surface science by driving the understanding of catalytic processes, chemical states of interfaces and functional materials [1]. The emitted photoelectron distribution is proportional to the created core-hole spectral function and carries information about the many-body interactions such as Auger scattering, electron–phonon coupling, plasmonic excitations and local screening [2]. The XPS line shape of metals is usually asymmetric with characteristic tails towards higher binding energy originating from core-hole screening by conduction electrons. In contrast, the core-level line shapes in semiconductors are typically symmetric. Upon optical excitation and the formation of excited carriers, a semiconductor becomes partially metallic and one can expect a change of the core-level line shapes. This opens the possibility of studying non-equilibrium dynamics with XPS. Recently, technological advances of femtosecond X-ray sources [3] and photoelectron detectors [4] have made time-resolved XPS (trXPS) experiments possible.

This work presents the results of core-*cum*-conduction trXPS experiments, i.e. the simultaneous measurement of the ultrafast dynamics of core-level and conduction-band electrons, using the free-electron laser FLASH in a pump-probe measurement scheme at the PG2 beamline. The layered semiconductor WSe_2 was optically excited with femtosecond laser pulses of 1.6 eV photon energy such that so-called A-excitons were formed [5]. A time-of-flight momentum microscope was used as the photoelectron analyser, which enabled to simultaneously probe a ~40 eV broad spectral window including the excited states, valence band and the highest core levels of tungsten and selenium. Schematics of the setup as well as a model conduction band and core energy level diagram are shown in Fig. 1. The observed time-dependent XPS spectra of W $4f_{5/2}$ shown in Fig. 2a exhibit distinct dynamics

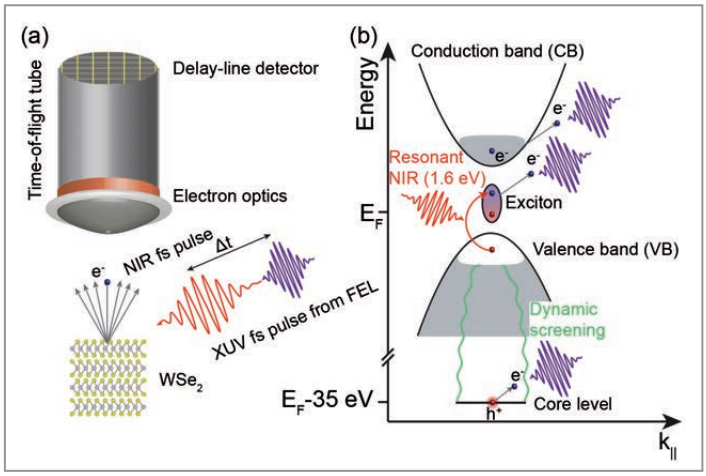

Figure 1

(a) Sketch of the experimental setup for pump-probe trXPS on WSe_2 using a momentum microscope, which enabled the simultaneous analysis of core, valence and conduction electrons. The sample was excited with a near-infrared (NIR) pulse and probed with an extreme ultraviolet (XUV) pulse. (b) Energy-band diagram of the photoexcited WSe_2: the NIR pulse (red) resonant with the exciton energy generates excited carrier populations in the valence (h^+) and conduction (e^-) bands. Transient conduction-band population as well as the induced renormalisation of the screened core-hole spectral function are probed by the XUV pulse (violet).

after optical excitation, namely changes of the position, width and shape (skewness) of the core-level photoemission signal. Simultaneously, a transient population of excited carriers responsible for the core-hole line shape modifications was observed.

A theoretical model based on Green's function formalism [6] has been developed to understand the induced core-level spectral changes. The model includes a dynamic screening of the core hole due to the presence of excited carriers, as

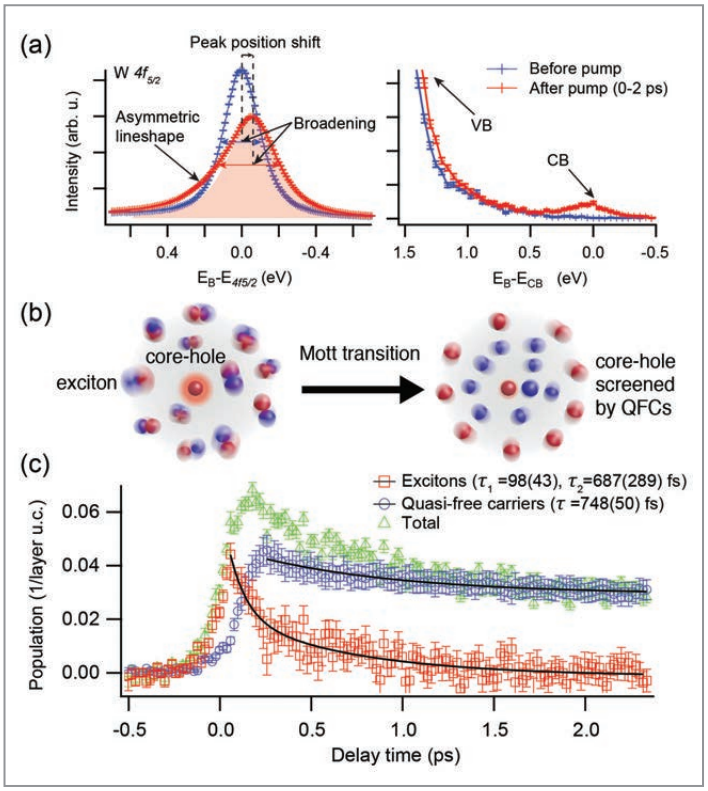

Figure 2

(a) Core-*cum*-conduction trXPS spectra showing W $4f_{5/2}$ (left) and momentum-integrated conduction-band (right) regions, before (blue) and after the excitation (red). Coloured arrows indicate corresponding full-width at half maximum of the spectra and the shaded area is the symmetric part of the lineshape, illustrating its asymmetry. (b) Illustration of the effect of excitons and QFCs on the core-hole line shape. Charge-neutral electron–hole pairs only weakly screen the core holes and have a negligible effect on its spectral function (left). In contrast, single-particle-like QFCs more effectively screen the localised charge residing in the core hole, resulting in a renormalisation of the photoemission line shape (right). (c) Decomposition of the dynamics of excitons (red squares), QFC (blue circles) and total excited carriers (green triangles). Black lines present fitted double exponential and single exponential decay for excitons and QFC, respectively.

shown in Fig. 2b. The results of this model are in excellent agreement with the experimental findings, and enable us to effectively disentangle the contributions of excitons and QFCs (Fig. 2c). The experiment revealed that the initial stage of dynamics is dominated by excitons which subsequently break into QFCs within the first picosecond. The results shed new light into the ultrafast dynamics of the excitonic Mott transition and are indicative of a continuous phase transition with coexisting phases of excitons and QFCs.

The possibility of disentangling the dynamics of excitons and QFCs by trXPS is quite surprising due to the small energy difference between these two phases, typically 50 meV, in comparison to the characteristic core-state energy scale of tens of electron volt. Discrimination of excitons and QFCs is based on the different screening of the core-hole created during the photoemission process, as illustrated in Fig. 2b. This can be understood quite intuitively: excitons, being localised charge-neutral quasiparticles, are expected to interact much weaker with the suddenly created core-hole potential than delocalised, charged QFCs. Our results support the continuous phase-transition scenario of the excitonic Mott transition in transition metal dichalcogenide materials. The detailed interpretation of these results relies on the proposed theoretical model which, we believe, is readily applicable to further ultrafast studies of many-body states as well as electronic phase transitions. The advantage of the trXPS approach over optical spectroscopy techniques is element-specific information. This seems to be especially appealing in combination with hard X-ray photoemission due to its larger probing depth, providing access to buried interfaces in realistic semiconducting devices or heterostructures.

Author contact: Maciej Dendzik, dendzik@kth.se
Ralph Ernstorfer, ernstorfer@fhi-berlin.mpg.de

References

1. G. Ertl and N. Thiele, 'XPS studies with ammonia synthesis catalysts', Appl. Surf. Sci. 3, 99–112 (1979).
2. P. H. Citrin, G. K. Wertheim and Y. Baer, 'Many-body processes in X-ray photoemission line shapes from Li, Na, Mg, and Al metals', Phys. Rev. B 16, 4256–4282 (1977).
3. W. Ackermann, G. Asova, V. Ayvazyan et al., 'Operation of a free-electron laser from the extreme ultraviolet to the water window', Nat. Photon. 1, 336–342 (2007).
4. G. Schönhense, K. Medjanik and H.-J. Elmers, 'Space-, time- and spin-resolved photoemission', J. Electron Spectros. Relat. Phenom. 200, 94–118 (2015).
5. D. Kutnyakhov, R. P. Xian, M. Dendzik et al., 'Time- and momentum-resolved photoemission studies using time-of-flight momentum microscopy at a free-electron laser', Rev. Sci. Instrum. 91, 013109 (2020).
6. G. Stefanucci and R. van Leeuwen, 'Nonequilibrium many-body theory of quantum systems: a modern introduction', Cambridge University Press (2013).

Original publication

'Observation of an excitonic Mott transition through ultrafast core-*cum*-conduction photoemission spectroscopy', Physical Review Letters 125, 096401 (2020).
DOI: 10.1103/PhysRevLett.125.096401

Maciej Dendzik[1,2], R. Patrick Xian[1], Enrico Perfetto[3,4], Davide Sangalli[3,5], Dmytro Kutnyakhov[6], Shuo Dong[1], Samuel Beaulieu[1], Tommaso Pincelli[1], Federico Pressacco[7], Davide Curcio[8], Steinn Ymir Agustsson[9], Michael Heber[6], Jasper Hauer[1], Wilfried Wurth[6,7], Günter Brenner[6], Yves Acremann[10], Philip Hofmann[8], Martin Wolf[1], Andrea Marini[3], Gianluca Stefanucci[4,11], Laurenz Rettig[1] and Ralph Ernstorfer[1]

1. Fritz Haber Institute of the Max Planck Society, Berlin, Germany
2. Department of Applied Physics, KTH Royal Institute of Technology, Stockholm, Sweden
3. CNR-ISM, Division of Ultrafast Processes in Materials (FLASHit), Monterotondo Scalo, Italy
4. Department of Physics, Tor Vergata University of Rome, Rome, Italy
5. Department of Physics, University of Milan, Milan, Italy
6. Deutsches Elektronen-Synchrotron DESY, Hamburg, Germany
7. Center for Free-Electron Laser Science (CFEL), DESY, Hamburg, Germany
8. Department of Physics and Astronomy, Interdisciplinary Nanoscience Center (iNANO), Aarhus University, Aarhus, Denmark
9. Institute of Physics, Johannes Gutenberg University Mainz, Mainz, Germany
10. Department of Physics, Laboratory for Solid State Physics, ETH Zürich, Zürich, Switzerland
11. INFN, Sezione di Roma Tor Vergata, Rome, Italy

Two-flavoured superconductivity

X-ray diffraction reveals a bipartite phase competition between charge order and superconductivity

Besides the high-temperature superconductivity, copper-oxide (or cuprate) materials have a unique set of phenomenology such as strange metal behaviour, nematicity, pseudogap and density waves. A charge density wave, a periodic modulation of the electron density, is commonly discovered in the cuprate family before the superconductivity emerges at lower temperature. We performed X-ray diffraction experiments to systematically study the interplay between the CDW and superconducting order. The competition was controlled by the application of a magnetic field. We found that two different types of CDW compete with the superconductivity in different ways. Our result provides a new insight into the inhomogeneous two-flavoured nature of superconductivity.

Many theories and experiments point to an inhomogeneous nature of superconductivity of high-temperature cuprate superconductors. Indeed, inhomogeneity that results from an interplay of superconductivity and a charge density wave (CDW) may be at the heart of cuprate superconductivity. In this context, $YBa_2Cu_3O_{6+x}$ (YBCO), the material in which superconductivity above the liquid-nitrogen temperature was first discovered, is an important model system where both superconducting and CDW order coexist at relatively high temperature. Previous X-ray diffraction experiments revealed a competing relationship between the two [2]. At zero magnetic field, the intensity of the CDW peak is suppressed below the superconducting transition temperature. However, when superconductivity is partially suppressed by application of a magnetic field, the CDW intensity is vastly enhanced. The application of a magnetic field introduces vortices into the superconducting state and tips the energy balance in favour of CDW order. Thus, the magnetic field is a parameter which can control the competing relationship between the two orders. In addition, X-ray free-electron laser diffraction under a pulsed magnetic field revealed that a new CDW peak appears at high magnetic field [3,4].

CDW order in YBCO manifests itself as weak satellite reflections at fractional positions in reciprocal space, reflecting the additional periodicity of the electronic density. Figure 1a shows a CDW satellite reflection measured at a magnetic field of 14 T at beamline P07 of PETRA III. The CDW reflection is peaked at an in-plane position k near 4-1/3, and an out-of-plane position ℓ of 1/2. In other words, the CDW has a periodicity of three and two unit cells, in the in-phase and out-of-phase direction, respectively. As the strength of the magnetic field was further increased, a strong peak emerged at an integer out-of-plane position (Fig. 1b), with the same in-plane maximum position. Therefore, two different but intimately related CDW ordering tendencies are realised. These correspond to different ordering patterns of the CDW along the out-of-plane axis (the c-axis) of the crystal. The magnetic field induces regions of an in-phase CDW (ferro-coupled, F-CDW) (Fig. 1b) on top of the original out-of-phase CDW (antiferro-coupled, AF-CDW) order (Fig. 1a).

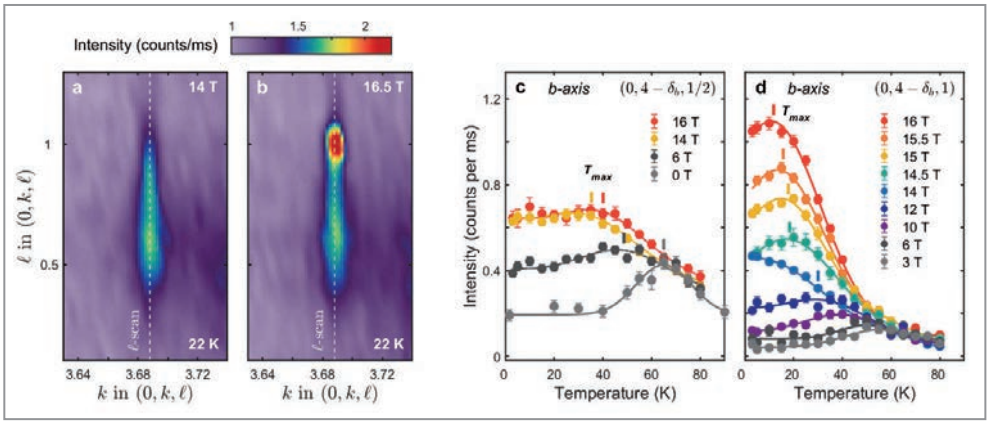

Figure 1

Two charge density wave orders in YBCO. (a) AF-CDW order measured by X-ray diffraction at 14 T. (b) F-CDW order emerges at high magnetic field ~16.5 T at reciprocal position $\ell = 1$. Temperature dependence of (c) AF-CDW and (d) F-CDW measured at different magnetic fields reveal different competition strength with superconductivity.

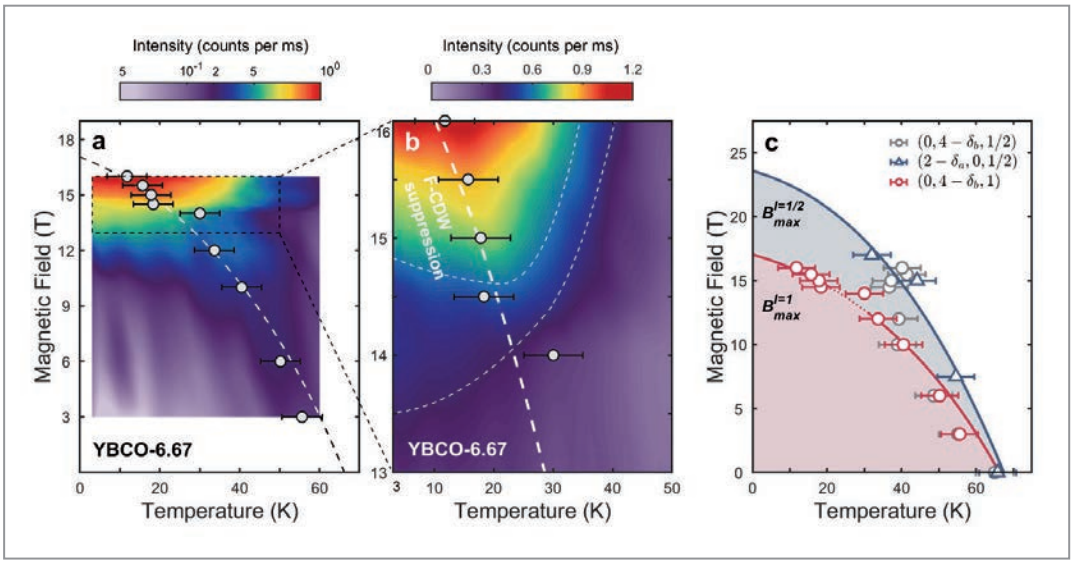

Figure 2

Inhomogeneous competition between superconductivity and charge density waves. (a) Two-dimensional intensity map of F-CDW. (b) Same, but zoomed in on the high field region. (c) Competition temperature scale of AF-CDW (blue, $\ell=1/2$) and F-CDW (red, $\ell=1$) reveals an inhomogeneous nature of competition between superconductivity and charge density waves.

To elucidate the relationship between two CDW orders and superconductivity, we further investigated how both AF-CDW and F-CDW order evolved as the magnetic field and temperature changed. Surprisingly, the temperature dependence of two CDW intensities showed a considerable difference. The intensity of F-CDW is strikingly enhanced above 15 T, whereas that of AF-CDW remains unaffected at high magnetic fields (Figs. 1c,d). In addition, we extracted the characteristic temperatures below which the respective CDW correlations were suppressed. They were significantly different at high magnetic fields, where the AF-CDW correlation length becomes large, and the F-CDW correlations are suppressed at a significantly lower temperature (Fig. 2c). These different temperatures indicate where superconducting order becomes strong enough to influence the F-CDW and AF-CDW correlations. Two-dimensional intensity maps of the F-CDW as a function of temperature and magnetic field traces its evolution from low magnetic fields (Figs. 2a,b).

Thus, in a magnetic field, two CDW orders with different ordering tendencies coexist and superconductivity is far more suppressed by the CDW in the F-CDW regions. In this fashion, inhomogeneous superconductivity emerges due to competition with CDW correlations which are locally different. Consequently, regions with weaker, more fragile superconductivity are created [5]. Our results suggest that F-CDW order in YBCO plays an important role for both the electronic structure and in rendering superconductivity into an inhomogeneous state that includes a more fragile flavour. Together with our series of experiments previously performed at DESY [2,4], X-ray diffraction experiments have been playing an indispensable role in elucidating the nature of charge density waves and providing new insights into their relationship with high-temperature superconductivity.

Author contact: Jaewon Choi, jaewon.choi@diamond.ac.uk
Oleh Ivashko, oleh.ivashko@desy.de

References

1. E. Fradkin, S. A. Kivelson and J. M. Tranquada, 'Colloquium: Theory of intertwined orders in high-temperature superconductors', Rev. Mod. Phys. 87, 457-482 (2015).
2. J. Chang, E. Blackburn, A. T. Holmes, N. B. Christensen, J. Larsen, J. Mesot, R. Liang, D. A. Bonn, W. N. Hardy, A. Watenphul, M. v. Zimmermann, E. M. Forgan and S. M. Hayden, 'Direct observation of competition between superconductivity and charge density wave in $YBa_2Cu_3O_{6.67}$', Nat. Phys. 8, 871-876 (2012).
3. S. Gerber et al., 'Three-dimensional charge density wave order in $YBa_2Cu_3O_{6.67}$ at high magnetic field', Science 350, 949-952 (2015).
4. J. Chang, E. Blackburn, O. Ivashko, A. T. Holmes, N. B. Christensen, M. Hücker, R. Liang, D. A. Bonn, W. N. Hardy, U. Rütt, M. v. Zimmermann, E. M. Forgan and S. M. Hayden, 'Magnetic field controlled charge density wave coupling in underdoped $YBa_2Cu_3O_{6+x}$', Nat. Commun. 7, 11494 (2016).
5. Y. Yu and S. A. Kivelson, 'Fragile superconductivity in the presence of weakly disordered charge density waves', Phys. Rev. B 99, 144513 (2019).

Original publication

'Spatially inhomogeneous competition between superconductivity and the charge density wave in $YBa_2Cu_3O_{6.67}$', Nature Communications 11, 990 (2020).
DOI: 10.1038/s41467-020-14536-1

Jaewon Choi[1], Oleh Ivashko[1,2], Elizabeth Blackburn[3,4], Ruixing Liang[5,6], Doug A. Bonn[5,6], Walter N. Hardy[5,6], Alexander T. Holmes[7], Niels B. Christensen[8], Markus Hücker[9], Simon Gerber[10], Olof Gutowski[2], Uta Rütt[2], Martin von Zimmermann[2], Edward M. Forgan[3], Stephen M. Hayden[11] and Johan Chang[1]

1. Physik-Institut, Universität Zürich, Zürich, Switzerland
2. Deutsches Elektronen-Synchrotron DESY, Hamburg, Germany
3. School of Physics and Astronomy, University of Birmingham, Birmingham, United Kingdom
4. Department of Physics, Lund University, Lund, Sweden
5. Department of Physics & Astronomy, University of British Columbia, Vancouver, Canada
6. Canadian Institute for Advanced Research, Toronto, Canada
7. European Spallation Source ERIC, Lund, Sweden
8. Department of Physics, Technical University of Denmark, Lyngby, Denmark
9. Department of Condensed Matter Physics, Weizmann Institute of Science, Rehovot, Israel
10. Laboratory of Micro and Nanotechnology, Paul Scherrer Institut, Villigen, Switzerland
11. H. H. Wills Physics Laboratory, University of Bristol, Bristol, United Kingdom

Competing interactions in a honeycomb magnet

Determining the magnetic moment direction in $RuCl_3$ with resonant X-rays

The two-dimensional honeycomb magnet $RuCl_3$ is a prime candidate to experimentally realise an exotic state of matter, known as the Kitaev quantum spin liquid (QSL). This theoretically predicted phase of matter would support unusual electronic excitations that could provide a basis for quantum memory and computation [1]. There has therefore been an intense search for materials with the type of magnetic interaction required to realise the Kitaev QSL. $RuCl_3$ has emerged at the forefront of this research, with mounting evidence of a substantial Kitaev-type magnetic interaction alongside other competing interactions. The magnetism of $RuCl_3$ is currently the topic of intense research, with the goal of quantifying all magnetic interactions and fully explaining the unusual magnetism of this material.

Over the past few years, the magnetism of $RuCl_3$ has been closely studied using a wide variety of experimental techniques. The results of this research have brought to light several unusual phenomena, thought to be signatures of Kitaev QSL physics. Neutron-diffraction measurements have uncovered a continuum of magnetic excitations, resembling those expected for the Kitaev QSL state [2]. In a magnetic field, $RuCl_3$ also shows a half-integer quantum thermal Hall effect, characteristic of unusual topologically protected edge states [3]. These findings are all the more remarkable considering that the material actually has strong secondary magnetic interactions competing with the anisotropic Kitaev interaction. These secondary interactions include isotropic Heisenberg interactions as well as a second anisotropic term known as the Gamma term. Intense work is ongoing to quantify all of these interactions, and arrive at a complete and accurate description of magnetism in $RuCl_3$.

This task of quantifying the magnetic interactions has been made more challenging by the presence of multiple competing interactions in $RuCl_3$. Minimal models typically include 3 or 4 different interactions, which gives a large possible 'parameter space' to explore. Models of this kind have been used to successfully fit a variety of experimental data sets, using various different values for the magnetic interactions [4]. These test models have used different magnitudes, and even different signs for the Kitaev term and for other competing interactions. In light of this, it is clear that stronger experimental evidence for constraining the values of the interaction strengths will be needed to simplify the search for the correct description of $RuCl_3$.

In this work, we have been able to provide such a constraint, with a careful measurement of the magnetic moment direction using resonant elastic X-ray scattering at beamline P09 at PETRA III [5]. This measurement made use of the newly commissioned complete in-vacuum beam path, minimising air absorption and scattering and maximising the magnetic signal. The moment direction, measured in the low-temperature magnetically ordered phase, is known to encode information about the magnetic interactions. It has been shown theoretically that the sign and relative sizes of the Kitaev and Gamma terms can be deduced directly from such a measurement [6]. These anisotropic interaction terms are closely connected with the magnetic moment direction,

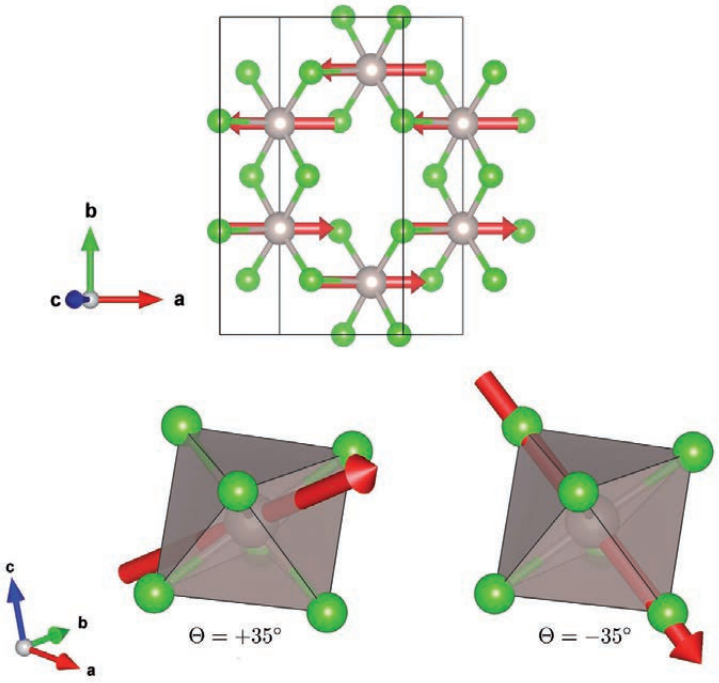

Figure 1

Crystal structure and proposed magnetic-moment directions in $RuCl_3$. The magnetic moment angle of +35° corresponds to a negative Kitaev term as well as a large positive Gamma interaction.

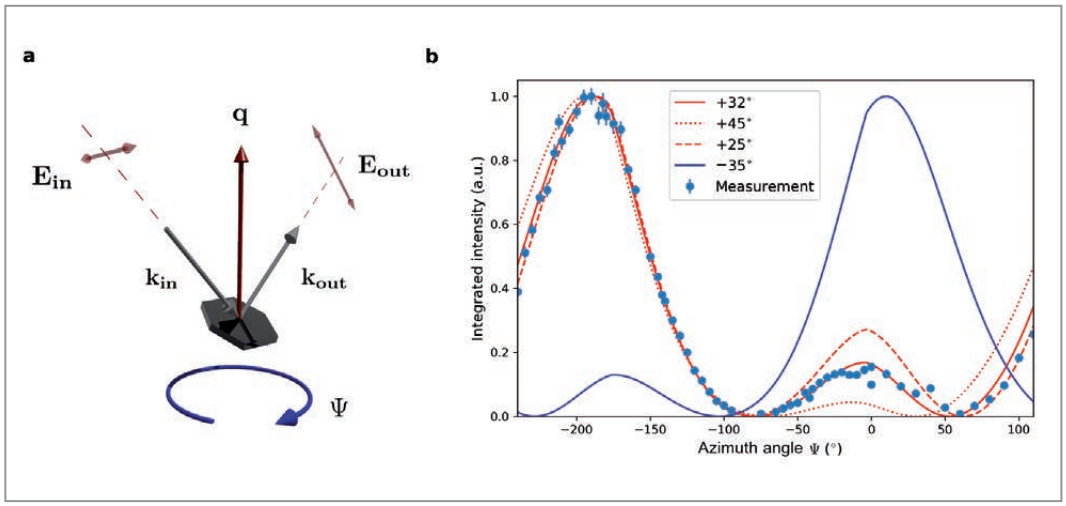

Figure 2

Resonant elastic X-ray scattering geometry and measurement results. (a) Schematic showing the scattering geometry for the azimuthal scan. The vectors $\mathbf{k}_{in}$ and $\mathbf{k}_{out}$ are the incoming and scattered beams, and $\mathbf{E}_{in}$ and $\mathbf{E}_{out}$ denote the electric field polarisation of the respective beams. During the azimuthal-dependent measurement, the scattered intensity was measured while the sample was rotated about the scattering vector $\mathbf{q}$. (b) Azimuthal dependence of the magnetic diffraction intensity, compared with modeled intensity for the two proposed magnetic structures.

which is expected to depend strongly on sign and strength of the Kitaev or Gamma terms. Prior to this work, the precise moment direction had not been determined, although the magnetic structure had been investigated using neutron diffraction [7]. Rather, two possible structures had been proposed corresponding to very different values of the magnetic interactions (Fig. 1). Our measurement has resolved this ambiguity.

The resonant X-ray scattering technique that we have applied to determine the magnetic moment direction makes use of the particular form of the magnetic X-ray scattering process. The intensity of the diffracted beam is expected to depend on the angle between the magnetic moment and scattered beam, with the highest intensity when the moment is aligned parallel to the scattered beam direction. In this measurement, known as an azimuthal-dependent scan, we rotated the sample about the scattering vector as shown in Fig. 2a. This rotation has the effect of moving the magnetic moment in and out of alignment with the scattered beam, and results in a scan with a modulated sinusoidal shape as shown in Fig. 2b. A comparison with the modelled intensities for the two proposed magnetic moment directions shows that this measurement can readily distinguish between these structures. The angle of the magnetic moment direction was also refined based on our data, giving a value of 32°, in close agreement with the one of the two candidate structures shown in Fig. 1 (magnetic moment angle of +35°).

Our solution of the magnetic moment direction shows that the moment is pointing towards the face of the $RuCl_6$ octahedron found within the honeycomb layers of the crystal. By comparing this with the calculation reported in the literature, we conclude that the Kitaev magnetic interaction must be negative to explain this moment direction. Further, we find that the competing Gamma interaction must be positive and with a magnitude comparable to that of the Kitaev term. This result has also provided a natural explanation for one of the unusual features of magnetism in $RuCl_3$: the pronounced anisotropy in the response to a magnetic field. Our modelling reveals that the presence of a large Gamma interaction can cause this anisotropy, without the need for anisotropy at the atomic level.

The results of our measurement have therefore allowed us to impose an unambiguous and experimentally derived constraint on the magnetic interactions in $RuCl_3$. The azimuthal-dependent measurement provides a simple and elegant way to pinpoint the magnetic moment direction — information that allows the anisotropic interactions to be greatly constrained. These findings not only give direct insight into the magnetic anisotropy of $RuCl_3$, but will also form a crucial foundation for further work modelling magnetism in this material. These constraints on dominant magnetic interactions will guide the search for the correct theoretical model, and pave the way for understanding the exotic magnetic phenomena observed in $RuCl_3$.

Author contact: Young-June Kim, yjkim@physics.utoronto.ca

References

1. A. Kitaev, 'Anyons in an exactly solved model and beyond', Ann. Phys. 321, 2–111 (2006).
2. A. Banerjee et al., 'Proximate Kitaev quantum spin liquid behavior in a honeycomb magnet', Nat. Mater. 15, 733–740 (2016).
3. Y. Kasahara et al., 'Majorana quantization and half-integer thermal quantum Hall effect in a Kitaev spin liquid', Nature 559, 227–231 (2018).
4. C. Eichstaedt et al., 'Deriving models for the Kitaev spin-liquid candidate material α-$RuCl_3$ from first principles', Phys. Rev. B 100, 075110 (2019).
5. J. Strempfer et al., 'Resonant scattering and diffraction beamline P09 at PETRA III', J. Synchrotron Rad. 20, 541–549 (2013).
6. J. Chaloupka and G. Khaliullin, 'Magnetic anisotropy in the Kitaev model systems Na_2IrO_3 and $RuCl_3$', Phys. Rev. B 94, 064435 (2016).
7. H. B. Cao et al., 'Low-temperature crystal and magnetic structure of α-$RuCl_3$', Phys. Rev. B 93, 134423 (2016).

Original publication

'Ferromagnetic Kitaev interaction and the origin of magnetic anisotropy in α-$RuCl_3$', Nature Physics 16, 837–840 (2020). DOI: 10.1038/s41567-020-0874-0

Jennifer A. Sears[1], Li Ern Chern[2], Subin Kim[2], Pablo J. Bereciartua[1], Sonia Francoual[1], Yong Baek Kim[2] and Young-June Kim[2]

1. Deutsches Elektronen-Synchrotron DESY, Hamburg, Germany
2. Department of Physics, University of Toronto, Toronto, Canada

Efficient light emission from silicon-germanium

A game changer for the silicon industry

Traditionally, both silicon (Si) and silicon-germanium (SiGe) have a cubic crystal structure. Silicon is extremely successful in the electronics industry and has provided the basis for electronic devices like personal computers and smartphones. However, cubic silicon is not able to emit light, meaning it cannot be used for fabricating light-emitting diodes or lasers for optical communication. We have succeeded in fabricating Si and SiGe with a hexagonal crystal structure, known as hex-SiGe. The hexagonal crystal structure is the key to transforming SiGe into a very efficient light-emitting semiconductor for germanium compositions above 65%. Taking advantage of synchrotron radiation, we could measure the crystalline properties of the hex-SiGe polytypes for the first time.

Silicon has long been the basis for the majority of electronic devices, but it is incapable of emitting light since it does not have a direct bandgap. As a consequence, developing a silicon-compatible light emitter has, for years, been regarded as something of a 'holy grail' for researchers the world over. So far, the way around this has been to use other semiconductor materials for light emission, such as gallium arsenide (GaAs), indium phosphide (InP) or gallium nitride (GaN).

Theoretical calculations show that the hexagonal polytypes of SiGe, for Ge compositions above 65% up to pure Ge [1], are direct bandgap semiconductors. The reason is that the hexagonal unit cell is twice as large as the cubic unit cell. The unit cell of hex-SiGe in reciprocal space is, therefore, half the size of the reciprocal unit cell for cubic SiGe, implying that the L-minimum of the cubic unit cell is folded back towards the Γ-point. Thus, a direct gap-band alignment becomes possible for sufficiently high Ge contents. We have grown hex-SiGe by growing SiGe as a shell around a hexagonal (Wurtzite) GaAs nanowire core. In this growth method, the hexagonal crystal structure is transferred from the core towards the SiGe shell [2]. A high-resolution transmission electron micrograph of the of GaAs–hex-Ge core–shell structure shows the ABAB stacking sequence, which is

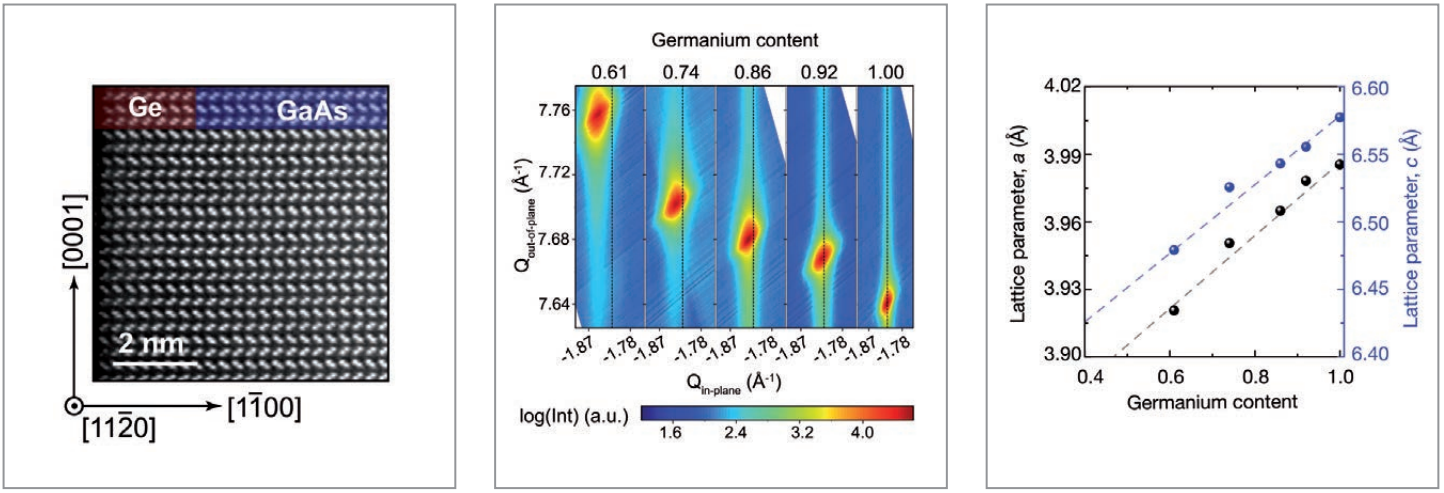

Figure 1

(a) Aberration-corrected high angular annular dark field scanning transmission electron microscopy (HAADF-STEM) image of the interface of GaAs/Ge structure obtained in the [11$\bar{2}$0] zone axis, displaying the ABAB stacking along [0001] of the hexagonal crystal structure. (b) X-ray diffraction reciprocal space maps showing the logarithmic scattering intensity (Int) of $Q_{out\text{-}of\text{-}plane}$ and $Q_{in\text{-}plane}$ in arbitrary units (a.u.), around the hexagonal ($\bar{1}$018) nanowire reflections for five different Ge fractions ranging from 0.61 to 1. (c) Plot of the hex-Si_{1-x} Ge_x in-plane lattice parameter *a* and out-of-plane lattice parameter *c* as a function of the Ge fraction. Reprint by permission from Springer Nature: Nature 'Direct-bandgap emission from hexagonal Ge and SiGe alloys', Fadaly, E. M. T. et al., Copyright (2020).

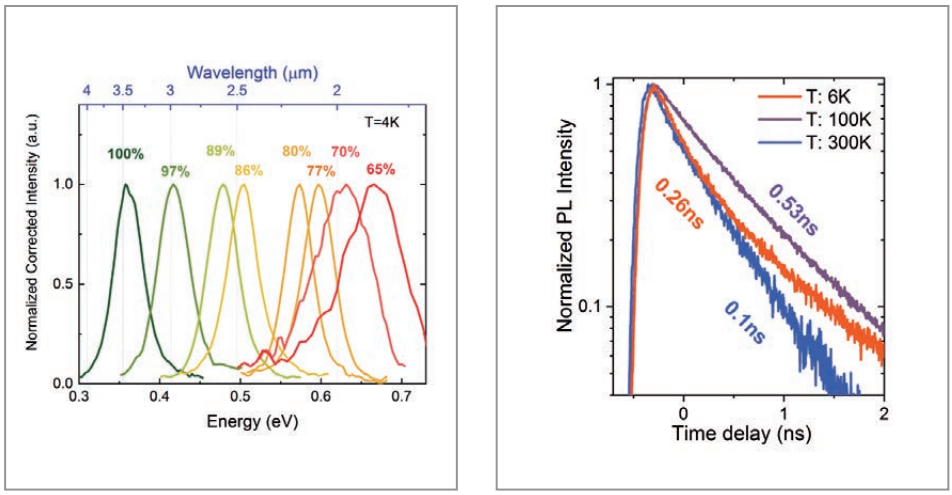

Figure 2

(a) Tuneability of the photoluminescence spectra for different compositions. The spectra were recorded at 4 K at an excitation density of 2 kW cm^{-2} on ensembles of as-grown samples. (b) Photoluminescence lifetime measurements of hex-$Si_{0.2}Ge_{0.8}$ recorded from a single wire for different temperatures. All decay traces show a single exponential decay and are vertically shifted for clarity.

typical for the hexagonal polytype (Fig. 1a). The crystal quality and the unit-cell parameter, for various Ge concentrations, have been studied by high-resolution X-ray diffraction measurements at beamline P08 of PETRA III. The position of the ($\bar{1}$018) Bragg reflection shifts as a function of the Ge content (Fig. 1b). The chosen type of Bragg reflection, ($\bar{1}$01L), is a unique fingerprint for hex-SiGe, since they are exclusively allowed in the hexagonal crystal system. The information on the hexagonal unit cell (Fig. 1c), gained from the X-ray diffraction experiments, set the basis for precise band-structure calculations which are in excellent agreement with the experimental results.

Furthermore, we subsequently performed photoluminescence measurements of our hex-SiGe crystals, observing bright photoluminescence at low temperature, shifting from 3.5 μm for pure hex-Ge towards 1.8 μm for hex-$Si_{0.2}Ge_{0.8}$ (Fig. 2a). Thus, we can show that hex-SiGe features a broad tuneability in the near and mid-infrared, which is very promising for both inter and intra-chip optical communications as well as for optical sensors in the molecular fingerprint region. In addition, we performed photoluminescence lifetime measurements for hex-$Si_{0.2}Ge_{0.8}$ samples (Fig. 2b). The measurements show a sub-nanosecond recombination lifetime, which is a clear indication for a direct bandgap semiconductor. A more detailed analysis revealed that hex-$Si_{0.2}Ge_{0.8}$ remains in the radiative limit up to room temperature, at an excitation density of about 30 kW cm^{-2}, showing that the optical quality of hex-SiGe is comparable to other III/V semiconductors.

In conclusion, hex-SiGe shows exciting optical properties, opening a promising path towards optical communications as well as for infrared optical sensors, both on a Si basis. It is expected that silicon photonics will penetrate towards board to board, chip to chip and finally to intra-chip communication. The closer photonics approaches the chip level, the more urgent becomes the demand for a silicon compatible light source. In addition, replacing the state-of-the-art copper wiring with optical links powered by integrated hex-SiGe emitters would significantly reduce energy consumption.

Author contact: Erik P. A. M. Bakkers, e.p.a.m.bakkers@tue.nl

References

1. C. Rödl et al.,'Accurate electronic and optical properties of hexagonal germanium for optoelectronic applications', Phys. Rev. Mater. 3, 034602 (2019).
2. H. I. T. Hauge et al., 'Hexagonal silicon realized', Nano Lett. 15, 5855–5860 (2015).

Original publication

'Direct-bandgap emission from hexagonal Ge and SiGe alloys', Nature 580, 205–209 (2020).
DOI: 10.1038/s41586-020-2150-y

Elham M. T. Fadaly[1], Alain Dijkstra[1], Jens Renè Suckert[2], Dorian Ziss[3], Marvin A. J. van Tilburg[1], Chenyang Mao[1], Yizhen Ren[1], Victor T. van Lange[1], Ksenia Korzun[1], Sebastian Kölling[1,6], Marcel A. Verheijen[1,4], David Busse[5], Claudia Rödl[2], Jürgen Furthmüller[2], Friedhelm Bechstedt[2], Julian Stangl[3], Jonathan J. Finley[5], Silvana Botti[2], Jos E. M. Haverkort[1] and Erik P. A. M. Bakkers[1]

1. Department of Applied Physics, Eindhoven University of Technology, Eindhoven, Netherlands
2. Institut für Festkörpertheorie und -optik, Friedrich-Schiller-Universität Jena, Jena, Germany
3. Institute of Semiconductor and Solid-State Physics, Johannes Kepler University, Linz, Austria
4. Eurofins Materials Science Netherlands, Eindhoven, The Netherlands
5. Physik Department & Walter-Schottky-Institut, Technische Universität München, Garching, Germany
6. Department of Engineering Physics, École Polytechnique de Montréal, Montreal, Québec, Canada

Revealing secrets of the 'magic film' on duplex stainless steel

Mapping of lateral variations in the passive film using HAXPEEM

Stainless steel is stainless because a 'magic' passive film spontaneously forms on its surface, which protects the steel from rapid corrosion like the rusting of iron. Duplex stainless steel (DSS), having a ferrite-austenite dual-phase microstructure with grains of different orientations, exhibits excellent corrosion resistance despite its intricate microstructure. Lateral variation in the passive film on DSS has been debated for a long time. We have performed a detailed analysis of the passive film on a commercial DSS by hard X-ray photoemission electron microscopy (HAXPEEM). The measurement revealed lateral variations in thickness and composition of a native passive film on the DSS. The protocol enabled one-to-one correlation with individual grains and thus grain mapping.

In air and aqueous environments, most metals spontaneously form a thin (1-3 nm thick) oxidic layer on the surface that hinders further interactions with the surrounding. This oxidic layer is called passive film, acting as a 'magic film' that changes active metals to a passive state so they can be used in practical applications. Stainless steels are Fe-based alloys containing Cr and other alloying elements. Passive films of stainless steels consist mostly of Cr and Fe oxidic species and in some cases also a minor amount of Mo oxides. Duplex stainless steel contains a ferrite phase (enriched in Cr and Mo) and an austenite phase (enriched in Ni and N) in a microstructure which gives excellent mechanical strength. It is a mystery why DSS exhibits high corrosion resistance in spite of its intricate heterogeneous microstructure. Passive films have been studied extensively, however there has been a debate over whether the passive film on DSS is homogenous [1]. To investigate lateral variations of the passive film on DSS, a few attempts were made in recent years, including local sputtering [2], etching [3] and single phase materials [4], all involving manipulation of the samples.

In our approach, we used HAXPEEM in combination with electron backscatter diffraction (EBSD) to analyse the passive film on a commercial DSS without manipulation of the sample. A 10×10×1 mm^3 sample of DSS was prepared by grinding and polishing. Three fiducial Pt markers were deposited on the surface to identify the region of interest (ROI) for the analyses. The makers also allowed relocation and analysis of the ROI after *ex situ* electrochemical polarization. Figure 1 displays the image showing the analysed grains (numbered from 1 to 58) of the ferrite (red) and austenite (blue) phases (Fig. 1a) and the grain orientations in the inverse pole figure (Fig. 1b).

HAXPEEM is an energy-filtered full-field imaging technique which creates image stacks from which X-ray photoelectron spectra (XPS) of the analysed elements can be extracted for specific surface areas. Our HAXPEEM measurement was conducted at beamline P22 at PETRA III, at a photon energy of 4 keV and with field-of-view of 90 × 90 µm^2. This photon energy is high enough to create photoelectrons with sufficiently high kinetic energies to probe the entire oxidic layer without the need to remove the surface carbon contamination that is commonly present on real sample surfaces. The experimental procedures are illustrated in Fig. 2. The mea-

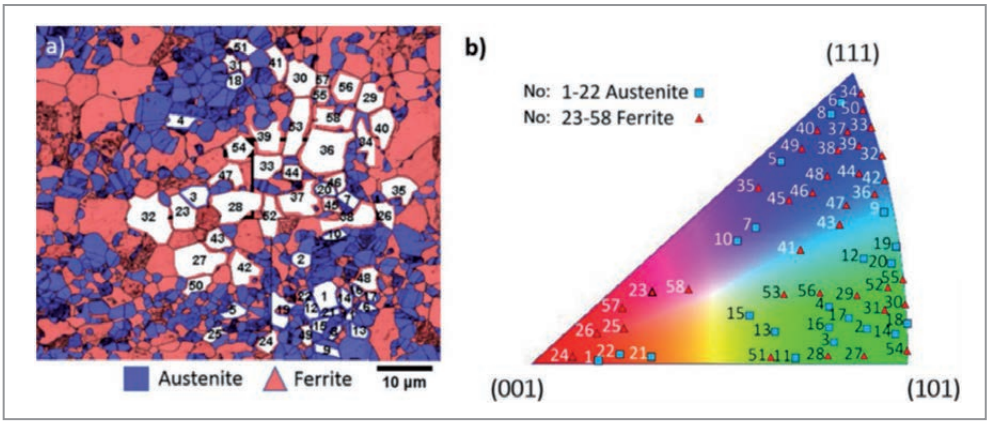

Figure 1

(a) EBSD image showing the analysed austenite grains in blue and ferrite grains in red. The grains selected for analysis are numbered and marked in white. (b) Inverse pole figure showing the crystallographic orientation of each grain with respect to the sample surface.

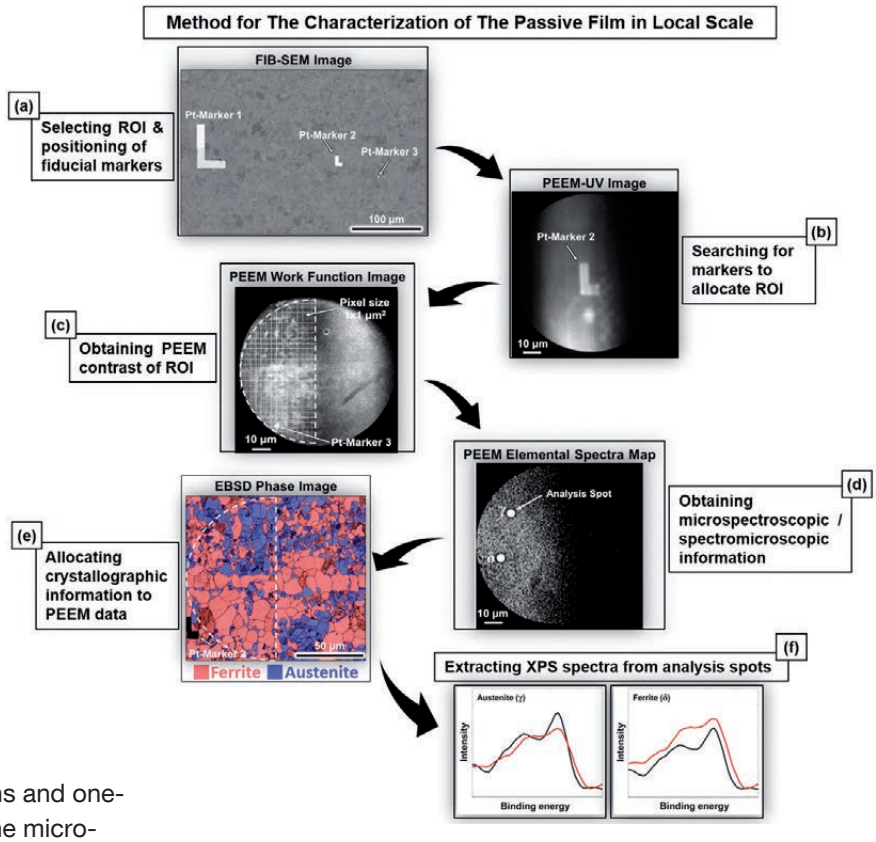

Figure 2

Overview of the method used to analyse the local composition and thickness of the passive film of DSS. The steps were: (a) Mark ROI in a FIB-SEM. (b) Find the ROI in the chamber using UV light. (c) Make a work-function image of the ROI. (d) Elemental scan of elements of interest. (e) Identify the ROI and the phases, the grains and grain orientations in EBSD. (f) Combine the work function image, the elemental scans and the EBSD image to extract XPS spectra from specific areas, which enables XPS mapping over the analysed region.

surement protocol enabled analysis of single grains and one-to-one correlation between the passive film and the microstructure features. The measurement provided information on the composition and thickness of the passive film of individual grains, as well as averages for each grain orientation and for each phase of the DSS [5].

The quantitative analysis was focused on the data from Cr and Fe that are the major components in the passive film. The composition and thickness of the passive film were calculated using a two-layer model and established methods reported in literature [4,5]. The results were evaluated in two ways: i) calculations based on the summed signal intensities of each grain orientation and each phase, respectively; ii) calculations based on the mean values of individual grains and grain orientations, respectively, which gave standard deviations of the data. The results showed that, on a global level, the passive film is 2.1±0.4 nm thick and contains 80% Cr oxide species. On a phase level, the thickness is similar for the two phases, but the outer layer of the film on ferrite contains more Cr oxidic species. On grain level the ferrite-(111) grains have a lower content of Cr oxidic species in the outer layer. In summary, there are small but detectable lateral variations in the passive film at the microscopic scale.

The HAXPEEM measurements presented in this investigation show a way for future studies of complex materials such as advanced alloys. The approach is particularly useful to study chemical phenomena with lateral variations on the micron scale, such as phase transformations, grain boundary segregation and the fate of the passive film upon heating.

Author contact: Jinshan Pan, jinshanp@kth.se
Carsten Wiemann, c.wiemann@fz-juelich.de
Marie Långberg, langberg@kth.se

References

1. J. Pan, 'Studying the passivity and breakdown of duplex stainless steels at micrometer and nanometer scales – the influence of microstructure', Front. Mater. 7, 133 (2020).
2. V. Vignal, O. Delruea, O. Heintz and J. Peultier, 'Influence of the passive film properties and residual stresses on the micro-electrochemical behavior of duplex stainless steels', Electrochim. Acta 55, 7118–7125 (2010).
3. Y. Wang, X. Cheng and X. Li, 'Electrochemical behavior and compositions of passive films formed on the constituent phases of duplex stainless steel without coupling', Electrochem. Commun. 57, 56–60 (2015).
4. E. Gardin, S. Zanna, A. Seyeux, A. Allion-Maurer and P. Marcus, 'Comparative study of the surface oxide films on lean duplex and corresponding single phase stainless steel by XPS and ToF-SIMS', Corros. Sci. 143, 403–413 (2018).
5. M. Långberg, C. Örnek, F. Zhang, J. Cheng, M. Liu, E. Grånäs, C. Wiemann, A. Gloskovskii, Y. Matveyev, S. Kulkarni, H. Noei, T. F. Keller, D. Lindell, U. Kivisäkk, E. Lundgren, A. Stierle and J. Pan, 'Characterization of native oxide and passive film on austenite/ferrite phases of duplex stainless steel using synchrotron HAXPEEM', J. Electrochem. Soc. 166, C3336-C3340 (2019).

Original publication

'Lateral variation of the native passive film on super duplex stainless steel resolved by synchrotron hard X-ray photoelectron emission', Corrosion Science 174, 108841 (2020).
DOI: 10.1016/j.corsci.2020.108841

Marie Långberg[1,2], Fan Zhang[1], Elin Grånäs[3], Cem Örnek[4], Jie Cheng[1], Min Liu[1], Carsten Wiemann[5], Andrei Gloskovskii[3], Thomas F. Keller[3,6], Christoph Schlueter[3], Satishkumar Kulkarni[3], Heshmat Noei[3], David Lindell[2], Ulf Kivisäkk[7], Edvin Lundgren[8], Andreas Stierle[3,6] and Jishan Pan[1]

1. Division of Surface and Corrosion Science, KTH Royal Institute of Technology, Stockholm, Sweden
2. SWERIM, Kista, Sweden
3. Deutsches Elektronen-Synchrotron DESY, Hamburg, Germany
4. Department of Metallurgical and Materials Engineering, Istanbul Technical University, Istanbul, Turkey
5. Peter Grünberg Institute (PGI-6), Research Center Jülich, Jülich, Germany
6. Physics Department, Universität Hamburg, Hamburg, Germany
7. AB Sandvik Materials Technology, Sandviken, Sweden
8. Division of Synchrotron Radiation Research, Lund University, Lund, Sweden

How do extreme plasmas absorb light?

Shedding new light on quantum mechanisms of free-free absorption in warm dense matter

The interaction of light with free electrons at high densities is a fundamental quantum process, the study of which lies on the boundary between plasma and condensed matter physics. As the electron density is increased, it tests our fundamental understanding of correlated many-body systems, but is also needed to understand the radiative properties of high energy-density plasmas, including transport in stellar interiors and in fusion energy research. The unique capabilities of the FLASH free-electron laser allowed this complex process to be investigated in a novel way, and enabled the first experimental measurement of how the ability of a dense plasma to absorb extreme ultraviolet (XUV) photons changes as the electrons are heated to temperatures exceeding 100000 K.

There are several ways in which matter can absorb light, depending primarily on the wavelength of the light in question and on the 'type' of electron involved in the interaction. For electrons that are not bound to specific atoms, the process is thought to be well-described by the classical inverse bremsstrahlung theory of the early 1960s [1]. This free-free absorption, as it is often called in plasma physics, is an important part of energy transport in highly ionised systems where there are few or no bound electrons: stellar interiors, highly ionised laser-produced plasmas and inertial confinement fusion implosions. Understanding this process and how it is affected by temperature at high densities is thus of broad interest.

While recreating stellar matter in a laboratory comes with some significant challenges, the same physics can be studied in a surprisingly simple proxy system: simple metals. In metals, the conduction electrons are known to form a near-free electron gas which is quantum-degenerate. The interactions of these electrons with photons in the XUV regime is normally dominated by the free-free opacity. However, it has been known for some time that the classical inverse bremsstrahlung theory breaks down at the high densities present in a typical metal [2]. The difficulty is down to the quantum nature of the electrons: interaction with light becomes a fully fledged quantum many-body problem. It is interesting to note that the detailed solution, even for ground-state metals, remains challenging and was addressed for aluminium only recently [3].

To study the free-free opacity in conditions relevant to various astrophysical applications, one needs to heat the electrons to temperatures comparable to the Fermi energy. For typical metals this is around 10 eV, or just above 100000 K, a regime commonly known as warm dense matter. In stark contrast to the classical prediction, quantum calculations indicate that the free-free opacity at these temperatures actually increases, before eventually falling off at even higher temperatures [3-6]. However, there remain considerable discrepancies in the predicted size, shape, extent and explanation of this important effect. While theory abounds, little is known experimentally about this process at all.

To attempt to address this, we turned to FLASH, a light source capable of producing bright XUV pulses suited to probe the free-free plasma opacity. The FLASH pulse was split in two, as shown in Fig. 1: the first pulse was used to heat a thin, few hundred nanometre aluminium sample, while the second was deployed as a XUV probe, to measure the opacity. The heated warm dense samples we can create in this manner are very small, only a few microns across, and also very short lived. However, even within these microscopic samples, substantial gradients in temperature remain inevitable

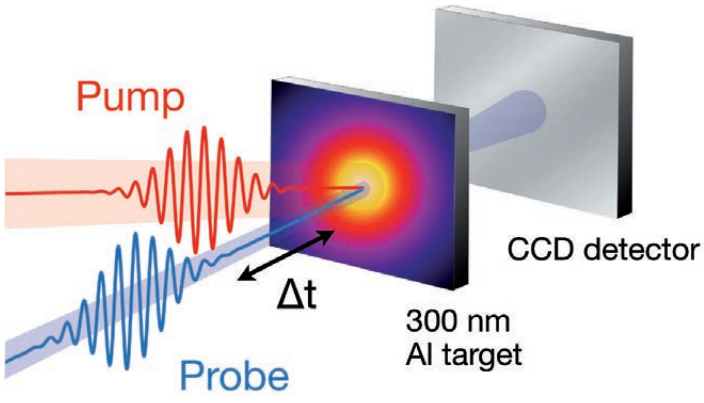

Figure 1

Schematic of the experiment: the FLASH pulse was split into two, with the first pulse creating a warm dense transient system and the second probing its free-free opacity in transmission.

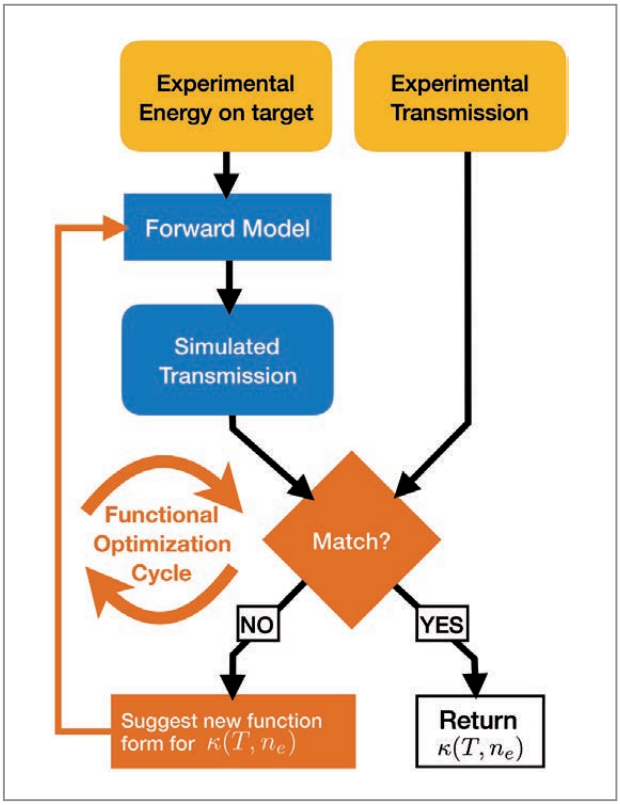

Figure 2
Schematic representation of the machine learning functional exploration approach developed to extract the opacity as a function of electron temperature and density by constraining it to best fit the dataset of integrated transmission measurements.

on the nanoscale, and measuring them directly is beyond our current capabilities.

Instead of trying to find a way to measure the complex spatial distribution of temperatures, we decided to approach the problem differently. We first constructed a heating model that would predict, given some form of the free-free opacity, and given the characteristics of the FLASH pulse, how the pulse would propagate through the sample, heat it and be absorbed. We then collected over 5000 experimental transmission measurements across a broad range of heating conditions. We fed both the data and the model into a machine learning functional exploration algorithm, schematically shown in Fig. 2. We tasked it with trying to deduce what form of the temperature-dependent opacity best matched our data. Bayesian inference was also used to quantify how reliable this extracted opacity was and how confident we were in its validity. Fortunately, the results were found to be robust to the various experimental uncertainties, and a free-free opacity could be extracted reliably from the data. What might seem surprising is that this approach allows us to deduce a temperature-dependent opacity from the measurements, yet without ever having to measure — or even know — how the temperature is distributed within the sample.

Our results confirmed that the opacity does indeed rise as the electrons are heated and that it peaks at temperatures around the Fermi energy. Interestingly, we found the peak to be even more pronounced than predicted by current state-of-the-art theories and that the hot opacities were significantly larger than we thought. For once, the ball is now in the theorists' court!

Author contact: Sam Vinko, sam.vinko@physics.ox.ac.uk

References

1. J. Dawson and C. Oberman, 'High–frequency conductivity and the emission and absorption coefficients of a fully ionized plasma', Phys. Fluids 5, 517–524 (1962).
2. K. Sturm, E. Zaremba and K. Nuroh, 'Core polarization and the dielectric response of simple metals', Phys. Rev. B 42, 6973–6992 (1990).
3. P. Hollebon et al., '*Ab initio* simulations and measurements of the free-free opacity in aluminum', Phys. Rev. E 100, 043207 (2019).
4. S. M. Vinko et al., 'Free–free opacity in warm dense aluminum', High Energy Density Phys. 5, 124–131 (2009).
5. C. A. Iglesias, 'XUV absorption by solid-density aluminum', High Energy Density Phys. 6, 311–317 (2010).
6. N. Shaffer et al., 'Free-free opacity in dense plasmas with an average atom model', High Energy Density Phys. 23, 31–37 (2017).

Original publication

'Time-resolved XUV opacity measurements of warm dense aluminum', Physical Review Letters 124, 225002 (2020). DOI: 10.1103/PhysRevLett.124.225002

Sam Vinko[1], Vojtěch Vozda[2,3], Jakob Andreasson[4,5], Saša Bajt[6], Johan Bielecki[7], Tomáš Burian[3], Jaromír Chalupský[3], Orlando Ciricosta[1], Michael Desjarlais[8], Holger Fleckenstein[9], Janos Hajdu[4,10], Věra Hajková[3], Patrick Hollebon[1], Libor Juha[3], Muhammad Kasim[1], Emma McBride[11], Kerstin Mühlig[10], Thomas Preston[7], David Rackstraw[1], Sebastian Roling[12], Sven Toleikis[6], Justin Wark[1] and Helmut Zacharias[12]

1. Department of Physics, University of Oxford, Oxford, United Kingdom
2. Faculty of Mathematics and Physics, Charles University, Prague, Czech Republic
3. Institute of Physics, Czech Academy of Sciences, Prague, Czech Republic
4. ELI Beamlines, Czech Academy of Sciences, Prague, Czech Republic
5. Department of Physics, Chalmers University of Technology, Göteborg, Sweden
6. Deutsches Elektronen-Synchrotron DESY, Hamburg, Germany
7. European XFEL GmbH, Schenefeld, Germany
8. Sandia National Laboratories, Albuquerque, NM, USA
9. Center for Free-Electron Laser Science (CFEL), DESY, Hamburg, Germany
10. Laboratory of Molecular Biophysics, Uppsala University, Uppsala, Sweden
11. SLAC National Accelerator Laboratory, Menlo Park, CA, USA
12. Universität Münster, Münster, Germany

The Scream and its fading yellow

Moisture, but not light, is the main cause of deterioration of cadmium yellows in *The Scream*

The degradation of cadmium yellow paints in *The Scream* (ca. 1910) by Edvard Munch (Munch Museum, Oslo) is a little-understood phenomenon. A combination of non-invasive *in situ* spectroscopy techniques at the macroscale with synchrotron radiation X-ray methods at the sub-microscale allowed us to establish that moisture, but not light, is the main cause of degradation. Overall, our findings contribute to optimising preventative conservation strategies of this masterpiece.

The Scream, realised in different versions by Edvard Munch between 1893 and 1916, is one of the most well-known series of masterpieces of the modern era. The two most popular versions are the two paintings made in 1893 and ca. 1910, which belong to the National Gallery and the Munch Museum in Oslo, Norway, respectively. In both artworks, Munch made use of a wide range of newly synthesised pigments. One of these, however, is causing problems for long-lasting preservation.

The investigated ca. 1910 version of *The Scream* (Fig. 1a) shows noticeable signs of degradation in a few regions where cadmium sulfide (CdS)-based pigments, also known as cadmium yellows, have been employed. In the cloudy sky and in the neck area of the middle character, some yellow brushstrokes have turned off-white; in the lake region, a thickly applied opaque yellow paint is flaking. The extent of painting degradation over time is attributable to a number of causes: the manufacturing process and chemical properties of the yellow pigments used, the storage environment and the theft of the painting in 2004, when the masterpiece vanished for about two years. Since its return, this version of *The Scream* has been kept in a private storage room of the museum under controlled conditions of lighting, temperature (~ 18 °C) and relative humidity (RH ~ 50%).

Previous investigations of paint micro-samples of *The Scream* revealed that cadmium carbonate ($CdCO_3$) is a main ingredient of the paler yellow paints of the sky and neck of the middle character. In the lake region, the same component had been detected as part of a mixture with variable abundances of sulfur-, chlorine- and sodium-containing species. Such compounds are generally associated with residues of the starting reagents employed for manufacturing the cadmium yellow [1]. These findings, however, still leave some questions unanswered: (i) Is there any link between the extent of degradation of the cadmium yellow paint and its chemical composition? (ii) Into which compound(s) had the cadmium yellow transformed? (iii) What are the key factors for the alteration of the yellow paint? To answer these questions, we studied a selection of CdS-based paints from *The Scream* by non-invasive *in situ* spectroscopy methods. In addition, we analysed a set of paint micro-flakes (Fig. 1b), collected by scraping off a spot of the flaked yellow surface of the lake area, and a series of artificially aged oil paint mock-ups (Fig. 2a) by micro-

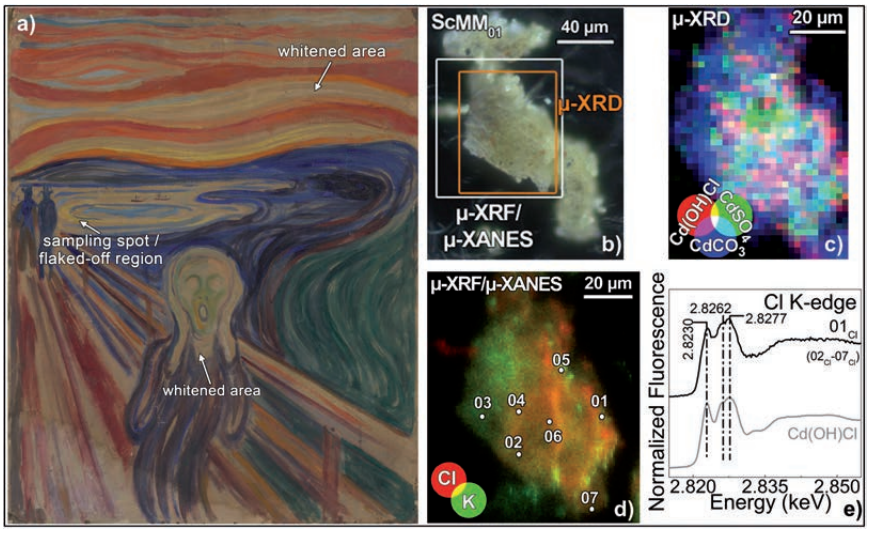

Figure 1

(a) Photograph of *The Scream* (ca. 1910) (Munch Museum, Oslo) with indication of the sampling spot and degraded cadmium yellow paint areas. (b) Photomicrograph of one of the paint's micro-flakes analysed by SR X-ray methods at beamline ID21 of ESRF. (c) µ-XRD distribution of $Cd(OH)Cl/CdSO_4/CdCO_3$. (d) µ-XRF maps of Cl/K. (e) Selection of a Cl K-edge spectrum (black) compared to that of Cd(OH)Cl reference (grey), acquired from the spots indicated in (d).

focussed X-ray diffraction (μ-XRD), fluorescence (μ-XRF) and absorption near-edge structure spectroscopy (μ-XANES). Such measurements were performed at beamline P06 of PETRA III and at beamline ID21 of the ESRF.

μ-XRD mapping of micro-flakes showed that they are composed of poorly crystalline hexagonal CdS and contain considerable abundances of $CdCO_3$ (Fig. 1b,c). Sulfate agglomerates made up of Na_2SO_4 and varying amounts of $CdSO_4$ along with minor abundances of sulfites (Na_2SO_3) were identified inside the CdS-paint. The local presence of Cd(OH)Cl was revealed by Cl K-edge μ-XANES analysis (Fig. 1d,e) and μ-XRD (Fig. 1c) along with NaCl and KCl particles.

To extrapolate the causes that trigger degradation of cadmium yellows, the study of the painting was complemented with investigations of artificially aged oil paint mock-ups having a similar composition to the lake yellow region (Fig. 2a). The thermal ageing at a RH ≥ 95% of the mock-up prepared using an early 20th century cadmium yellow pigment powder (called '7914') resulted in a highly relevant phenomenon: the formation of S^{VI}-rich aggregates within the hexagonal-CdS/$CdCO_3$-based matrix (Fig. 2b,c). The aggregates were mainly composed of $CdSO_4$/$CdSO_4 \cdot n H_2O$ (Fig. 2d) and lower amounts of the same compounds were occasionally present in the CdS-based matrix. In the S^{VI}-rich aggregates, sulfites were detected and were likely formed as intermediates of the pigment's oxidation process. Neither sulfates nor sulfites were identified by μ-XRD, possibly due to their amorphous nature. It is remarkable that the results also reveal the colocalised presence of Cd(OH)Cl and cadmium sulfates: Cd(OH)Cl is mainly localised in the S^{VI}-rich aggregate that formed *in situ* during ageing (Fig. 2b-e). This suggest that the original Cd(OH)Cl may have dissolved, migrated and recrystallised, possibly simultaneously with the oxidation of CdS to $CdSO_4$.

Overall, the results on *The Scream* micro-flakes combined with those obtained from artificially aged paint mock-ups lead us to conclude that sulfates and sulfites can be interpreted as degradation products of the paint. As the most important finding of this study, we proved that in high-moisture conditions and in the presence of cadmium chlorides, the original CdS is oxidised to $CdSO_4$. This occurs even in the absence of light and does not take place on chlorine-free oil paint mock-ups aged under similar conditions [2]. Under exposure to moisture, secondary reactions, involving dissolution, migration through the paint and recrystallisation of water-soluble phases, e.g., Na_2SO_4 and Cd(OH)Cl, may have further favoured the formation of $CdSO_4$ and different chloride compounds. The identification of such phases may contribute to explaining the instability and flaking of the yellow paint in the lake area of the painting.

The findings are expected to have important implications for the preventive conservation of *The Scream*. To stop or slow down the degradation of cadmium yellow paints, the artworks should be kept to RH levels lower than 45%, while lighting conditions should be maintained at standard values foreseen for light-fast painting materials.

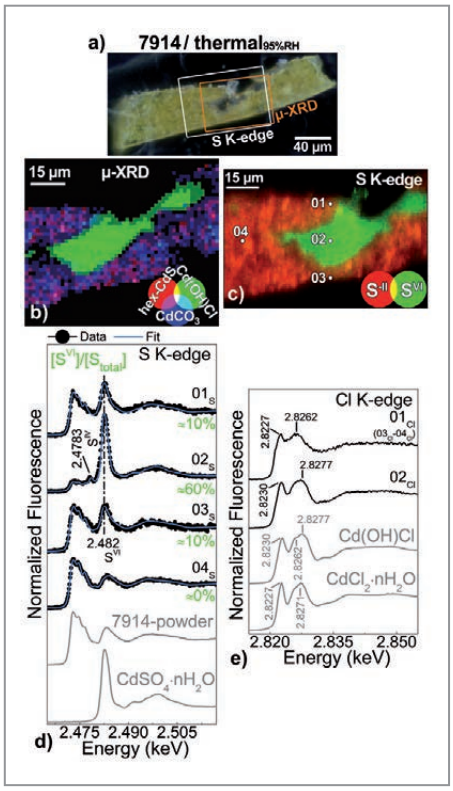

Figure 2

(a) Photomicrograph of a thin section obtained from the thermally aged early 20th century cadmium yellow oil mock-up (7914). (b) μ-XRD images of hexagonal-CdS/Cd(OH)Cl/$CdCO_3$ recorded at P06. (c) μ-XRF maps of S^{-II}/S^{VI} and selection of μ-XANES spectra at (d) S K-edge and (e) Cl K-edge obtained from the points indicated in (c) and linear combination fit results (cyan) of different S-based reference compounds. In (d,e) the spectral profiles of selected reference compounds are reported in grey colour for comparison. Data of (c-e) were acquired at ID21.

Author contact: Letizia Monico, letizia.monico@cnr.it
Costanza Miliani, costanza.miliani@cnr.it
Koen Janssens, koen.janssens@uantwerpen.be
Gerald Falkenberg, gerald.falkenberg@desy.de

References

1. 'Public paintings by Edvard Munch and his contemporaries: change and conservation challenges', T. Froysaker, N. Streeton, H. Kutzke, F. Hanssen-Bauer and B. Topalova-Casadiego (Eds), Archetype Publications Ltd, London, pp. 3–35, 52–71, 204–216, 294–324 (2015).
2. L. Monico, A. Chieli, S. De Meyer, M. Cotte, W. De Nolf, G. Falkenberg, K. Janssens, A. Romani and C. Miliani, 'Role of the relative humidity and the Cd/Zn stoichiometry in the photooxidation process of cadmium yellows (CdS/$Cd_{1-x}Zn_xS$) in oil paintings', Chem. Eur. J. 24, 11584–11593 (2018).

Original publication

'Probing the chemistry of CdS paints in *The Scream* by *in situ* noninvasive spectroscopies and synchrotron radiation X-ray techniques', Science Advances 6, eaay3514 (2020).
DOI: 10.1126/sciadv.aay3514

Letizia Monico[1,2,3], Laura Cartechini[1,2], Francesca Rosi[1,2], Annalisa Chieli[1,2], Chiara Grazia[1,2], Steven De Meyer[3], Gert Nuyts[3], Frederik Vanmeert[3], Koen Janssens[3,4], Marine Cotte[5,6], Wout De Nolf[5], Gerald Falkenberg[7], Irina Anca Sandu[8], Eva Storevik Tveit[8], Jennifer Mass[9,10], Renato Pereira de Freitas[1,11], Aldo Romani[1,2] and Costanza Miliani[1,2,12]

1. Istituto di Scienze e Tecnologie Chimiche 'Giulio Natta', Consiglio Nazionale delle Ricerche (CNR-SCITEC), Perugia, Italy
2. SMAArt Centre and Department of Chemistry, Biology and Biotechnology, University of Perugia, Perugia, Italy
3. AXES Research Group, NANOlab Centre of Excellence, University of Antwerp, Antwerp, Belgium
4. Rijksmuseum, Amsterdam, The Netherlands
5. European Synchrotron Radiation Facility (ESRF), Grenoble, France
6. Laboratoire d'archéologie moléculaire et structurale (LAMS), CNRS UMR 8220, Sorbonne Université, Paris, France
7. Deutsches Elektronen-Synchrotron DESY, Hamburg, Germany
8. Munch Museum, Oslo, Norway
9. Bard Graduate Center, New York, NY, USA
10. Scientific Analysis of Fine Art, LLC, Berwyn, PA, USA
11. LISComp Laboratory, Federal Institute of Rio de Janeiro, Brazil
12. Istituto di Scienze del Patrimonio Culturale, Consiglio Nazionale delle Ricerche (CNR-ISPC), Napoli, Italy

Stressed out metal 3D printing

Laser-induced internal stresses revealed during printing

Additive manufacturing, also known under the term 3D printing, covers a wide range of some of the most interesting manufacturing technologies to date. Its popularity is driven by the potential of nearly unlimited geometric design opportunities for prototyping, medicine technology, aviation and more. To produce metallic parts, laser powder bed fusion is amongst the most promising approaches, with residual stress being one of the major obstacles for its widespread application. These stresses are generated by steep thermal gradients, solidification shrinkage and repeated heating and cooling cycles during the manufacturing process. *In situ* diffraction experiments at PETRA III have elucidated the generation of these stresses and helped us to better understand the process.

Laser powder bed fusion (LPBF) is an additive manufacturing technology where a powder bed is selectively exposed with a highly focused laser beam. A wide range of metallic materials are suited for use with this relatively young manufacturing process. However, some refinements are still necessary for a widespread adoption of LPBF in industrial applications and to meet the safety and quality standards required by industries such as aerospace and medicine. LPBF suffers from process-induced defects, porosity and residual internal stress, which lead to distortions and crack formation.

Researchers and companies worldwide devote large amounts of time, money and energy to mitigate these process-related problems. A deeper understanding of the underlying mechanisms during laser–matter interaction is one piece to this puzzle. Our aim is to illuminate the generation of internal stresses in LPBF during the process by the means of high-energy synchrotron radiation diffraction.

A unique experimental setup for LPBF was developed and built at the Technische Universität Berlin, allowing experiments to be performed at the High Energy Materials Science (HEMS) beamline P07 at PETRA III. The custom LPBF machine closely represents an industrial machine with the added transparency for X-rays [1], ensuring the transferability of the gained knowledge. With this setup, shown in Fig. 1a, we were able to manufacture basic thin geometries and simultaneously observe any desired part of the sample as it is being built using a combination of the internal linear axes in the process chamber and the heavy-load hexapod available at P07.

For our investigation, the nickel-base superalloy Inconel 625 was used. Laser processing parameters applied industrially were used in the *in situ* experiments. The laser beam was directed over the powder bed with a speed of 760 mm/s to melt it with a nominal laser power of 275 W. Since the laser beam was focused on a spot size of only 60 µm in diameter, high laser intensities act on the thin powder layer with a thickness of 50 µm. This highly dynamic and localised energy input ensures rapid melting and solidification of the metallic powder, but at the same time induces high temperature gradients that cause non-uniform solidification conditions. Thereby, residual stresses are created, the origin and development of which were observed. We distinguish between the assumed principle stress directions, the transversal direction

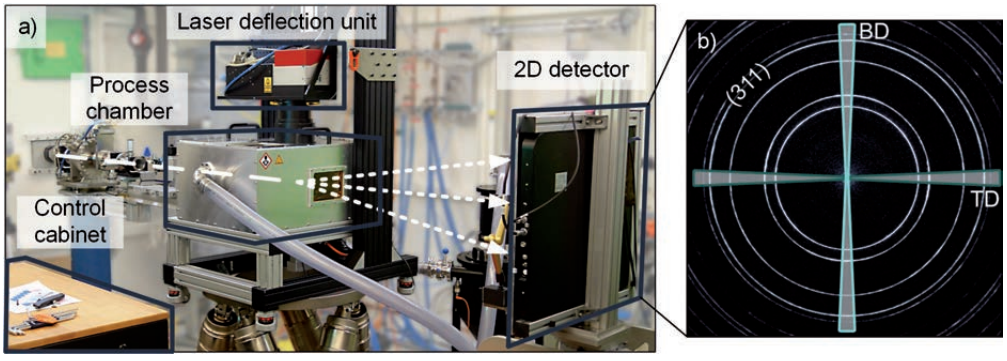

Figure 1

In situ experiments during laser powder bed fusion: (a) experimental setup at P07 EH3, (b) Inconel 625 diffractogram for strain evaluation.

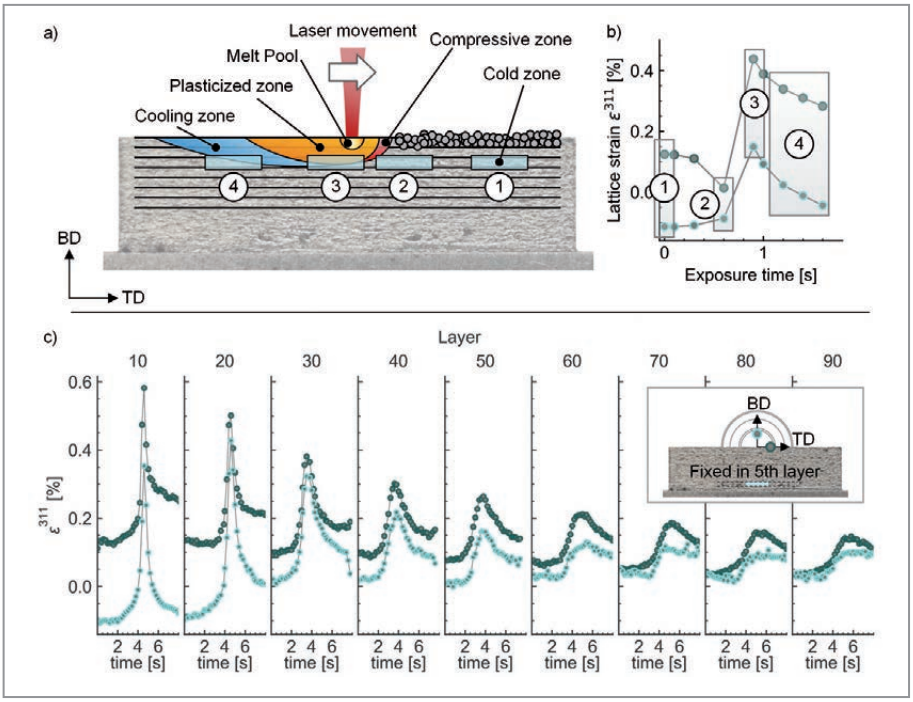

Figure 2

Dynamic strain progression during laser powder bed fusion: (a) schematic of the stress zones surrounding the heat-affected zone, (b) lattice strain progression along TD (dark green) and BD (bright green) of one layer, (c) strain progression over manufacturing process in a fixed gauge volume.

(TD) and the building direction (BD). The corresponding lattice spacings for subsequent strain and stress analysis were calculated from the diffraction patterns' angular sections as illustrated in Fig. 1b.

The results provide insights in a number of stress-related phenomena during laser metal interaction. In-plane strain was found to be generally higher than out-of-plane strain, with tensile stress in TD resulting in a transverse contraction along BD. The localised heat input induces a complex stress field that involves an outer halo of compressive stresses, which was experimentally detected in TD. A model of the heat affected zone surrounding the melt pool is given in Fig. 2a, while the corresponding lattice strain progression is shown in Fig. 2b. Four distinct zones were identified as a result of the lattice strain progressions of various sets of manufacturing parameters. Furthermore, a thermal gradient mechanism model, applied to LPBF by Mercelis et al. [2], was confirmed and extended by directional differences in the emerging stress field. During the laser exposure, the combination of high temperature, the associated low strength and the hindered expansion resulted in a plastic compression of the material. The material cooled down after laser exposure, while shrinkage was hindered by the underlying material. The hindered contraction had a much higher impact in the plane of the layer (TD) than out-of-plane (BD). Therefore, the tensile stresses described by the model were induced in TD. Subsequently, BD was compressed due to transverse contraction, thus explaining that the strains in TD are generally higher than in BD.

During LPBF, the stress state of the sample was altered by the laser up to the very last layer. Figure 2c shows the lattice strain progression of a sample manufactured with a reduced laser power of 55 W for ten layers. The same gauge volume in the centre of the 5th layer was observed for the whole process. Even in the later stages of the process, an increase in the lattice strain is visible, despite there being about 4.5 mm of material between the gauge volume and the top surface exposed to the heat source.

The same data contained significant information regarding texture development, which is currently being analysed. The results show the feasibility of *in situ* X-ray diffraction experiments for multilayer samples in LPBF, based on a custom-built process chamber for an industrial-scale machine, and provide information on strain and stress development during LPBF manufacturing.

Author contact: Felix Schmeiser, felix.schmeiser@tu-berlin.de

References

1. E. Uhlmann, E. Krohmer, F. Schmeiser, N. Schell and W. Reimers, 'A laser powder bed fusion system for *in situ* X-ray diffraction with high-energy synchrotron radiation', Rev. Sci. Instrum. 91, 075104 (2020).
2. P. Mercelis and J.-P. Kruth, 'Residual stresses in selective laser sintering and selective laser melting', Rapid Prototyp. J. 12, 254–265 (2006).

Original publication

'Experimental observation of stress formation during selective laser melting using *in situ* X-ray diffraction', Additive Manufacturing 32, 101028 (2020).
DOI: 10.1016/j.addma.2019.101028

Felix Schmeiser[1], Erwin Krohmer[2], Norbert Schell[3], Eckart Uhlmann[2] and Walter Reimers[1]

1. Institute for Materials Science and Technology, Metallic Materials, Technische Universität Berlin, Berlin, Germany
2. Institute for Machine Tools and Factory Management, Technische Universität Berlin, Berlin, Germany
3. Institute of Materials Research, Helmholtz-Zentrum Geesthacht, Geesthacht, Germany

Superheating liquid water above 170 °C

Sub-µs dynamics of soft matter probed at European XFEL

Dynamics and kinetics in soft-matter physics, biology, and nanoscience frequently occur on submicrosecond timescales which are difficult to probe experimentally. With its X-ray pulse repetition rate of up to 4.5 MHz, the European XFEL enables such experiments down to atomic length scales by taking series of diffraction patterns with microsecond resolution. To obtain the dynamics of nanoparticles dispersed in water, µs X-ray Photon Correlation Spectroscopy (XPCS) has been performed. By fine-tuning the fluence of the XFEL pulses, different degrees of non-linear heating have been observed. At fluences above 50 µJ/mm², superheated water states above 170 °C are reached that persist at least for 100 µs.

Hard X-ray Free-Electron Lasers (FELs) have opened new research directions during the last years. In particular, these machines hold great promise for exploring equilibrium and non-equilibrium processes via XPCS [1]. Limited by the coherent X-ray flux and detector readout, real-time dynamics between milliseconds and hours are typically probed in XPCS experiments at storage-ring sources, covering atomic to nanometre length scales. At pulsed sources such as a hard X-ray FELs, the accessible timescale in XPCS experiments is defined by the pulse repetition rate. The unique pulse scheme at the European XFEL consists of trains of up to 2700 pulses at a spacing of 222 ns that are generated every 100 ms, enabling the study of submicrosecond dynamics in XPCS experiments. These temporal regimes are the natural time of diffusion processes of nanoparticles and biological macromolecules in their native aqueous environment. We explored this timescale by studying dynamics of charge-stabilised colloidal nanoparticles as a model for nanoscale materials.

The scheme of the experiment performed at the SPB instrument [2] is shown in Fig. 1. Pulse trains of 120 X-ray pulses of 9.3 keV, a size of 3.6 µm × 4.4 µm and with a repetition rate of 1.128 MHz (corresponding to a time difference of 886 ns) hit a fresh spot of the colloidal sample every 100 ms. The coherent diffraction patterns — so-called speckle patterns — were measured by the AGIPD detector. The fluence per pulse was controlled by introducing different silicon slides upstream of the sample location to attenuate the beam.

XPCS as a coherent X-ray scattering technique relies on the coherence properties of the X-ray pulses. The sample dynamics are obtained from intensity–intensity correlation functions from subsequent X-ray pulses given by

$$g_2(q,\tau) = \frac{\langle I(q,t_e)\cdot I(q,t_e+\tau)\rangle_{t_e}}{\langle I(q,t_e)\rangle^2}$$

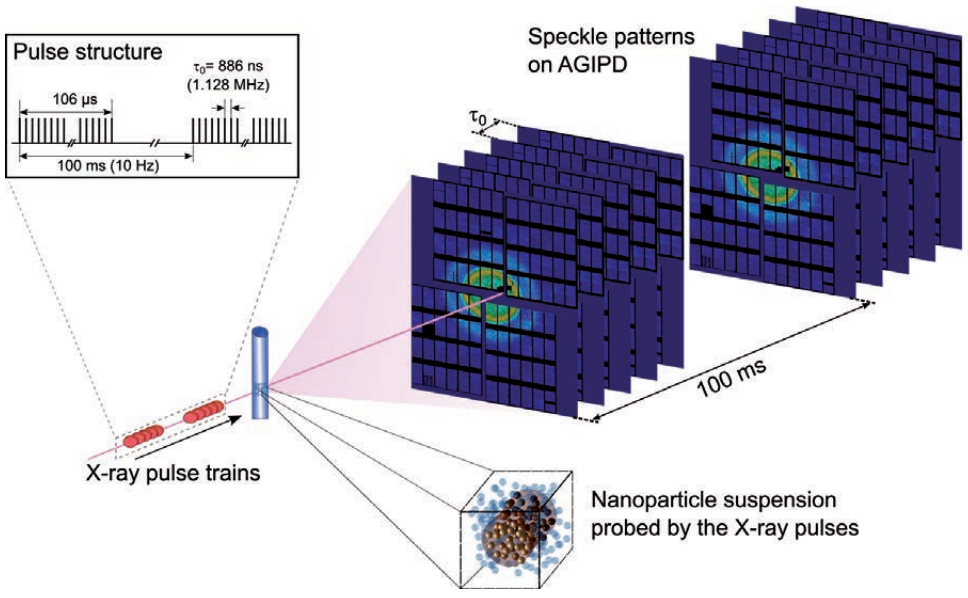

Figure 1

Sketch of the experiment at the SPB instrument of the European XFEL. The X-ray pulse trains scatter from the sample filled in quartz capillaries. The speckle patterns were recorded in small-angle scattering geometry 5.5 m downstream of the sample by the AGIPD. The pulse trains containing 120 pulses were generated at a 10 Hz repetition rate. Within the train, consecutive pulses were separated by 886 ns (1.128 MHz).

for wave-vector transfers q and averaged over experimental time t_e. For the systems studied in this work, g_2 is quantified by

$$g_2(q,\tau) = 1 + \beta_C \exp(-2Dq^2\tau),$$

with the contrast β_c and the Stokes–Einstein diffusion coefficient D. In XPCS experiments, correlations are calculated from different X-ray pulses, therefore pointing stability during the pulse train is of utmost importance. Pulse-to-pulse pointing fluctuations at FEL sources based on self-amplified spontaneous emission have been observed [3,4], challenging the performance of XPCS at FELs including the European XFEL. The degree of such fluctuations can be quantified by a comparison of the speckle contrast β_s from single-pulse speckle patterns given by the intensity-normalised variance of intensity and the contrast β_c obtained from the intensity–intensity correlation function. We found that both values match, which shows that the European XFEL provides unprecedented beam stability within a pulse train.

The XPCS experiments have been performed on colloidal silica particles with a radius of 69 nm that are dispersed in water. We studied different X-ray fluences between 1.3 and 56.8 mJ/mm² per single pulse. At low fluences, the measured diffusion coefficients resemble the results from theory. With increasing fluence, the particle dynamics speed up. Due to the exceptionally high intensity of the XFEL pulses, the sample volume that was exposed to the beam heats up instantaneously and its temperature subsequently relaxes back towards the previous conditions. While the scenario of full equilibration before the subsequent pulse hits has been observed at LCLS and SACLA [3,4], it is not fully valid in our case because the temperature relaxation time is longer than the pulse repetition time [1]. Consequently, the next pulse impinges on the non-equilibrated sample, resulting in a stepwise increase of temperature and thus speeding up of the sample dynamics.

In order to quantify this heating process, we performed a pulse-resolved XPCS analysis extracting the diffusion coefficients which gave access to the effective temperature after each pulse (Fig. 2). At the highest fluence studied (56.8 mJ/mm²), the effective temperature crosses the boiling point of water at 1 bar and rises to superheated states at about 445 K at the end of the train while still in the liquid phase, evidenced by the diffusive dynamics of the nanoparticles. This non-linear heating exceeds the pure heating of water (dashed lines) and could be modelled taking into account heat relaxation of the solvent and convective heat transfer between the nanoparticles and the solvent (solid lines). Both models fail at short times and large T_{eff} which suggests a breakdown of the Stokes–Einstein relation where the nanoparticles move faster than expected. This motivates further theory and simulation studies on heat transfer at the nanoscale to fully understand the emergence of non-equilibrium dynamics of liquids and soft matter probed at MHz XFEL sources.

Author contact: Felix Lehmkühler, felix.lehmkuehler@desy.de

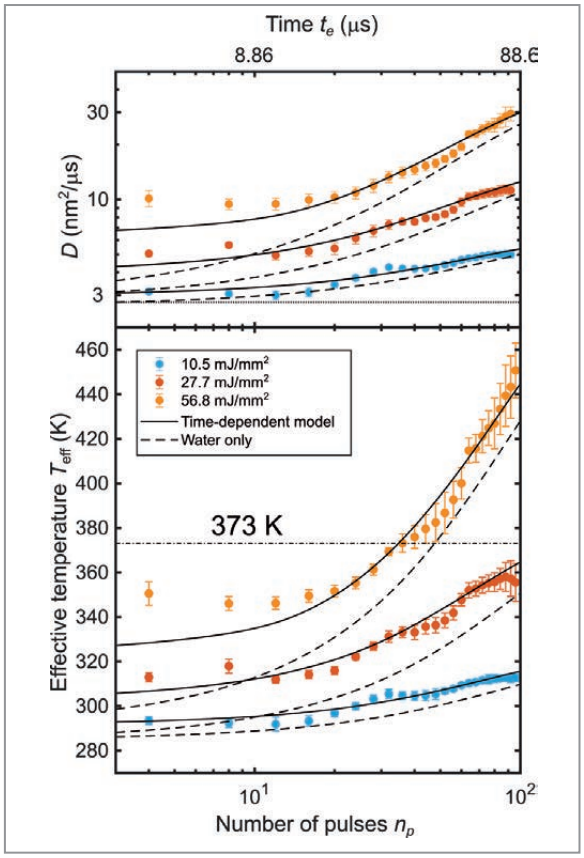

Figure 2

Diffusion coefficient D (top) and temperature T_{eff} (bottom) as a function of pulse number in the pulse train, n_p, for different fluences. The dotted line (top) is the equilibrium diffusion coefficient probed at lower fluences. The black lines (bottom) represent the time-dependent heating model, the dashed lines the heating of water as solvent only. The boiling temperature of water at 1 bar is given by the horizontal dashed-dotted line.

References

1. G. Grübel, G. B. Stephenson, C. Gutt, H. Sinn and T. Tschentscher, 'XPCS at the European X-ray free electron laser facility', Nucl. Instrum. Meth. B 262, 357–367 (2007).
2. A. P. Mancuso et al., 'The single particles, clusters and biomolecules and serial femtosecond crystallography instrument of the European XFEL: initial installation', J. Synchrotron Rad. 26, 660–676 (2019).
3. J. Carnis et al., 'Demonstration of feasibility of X-ray free electron laser studies of dynamics of nanoparticles in entangled polymer melts', Sci. Rep. 4, 6017 (2014).
4. F. Lehmkühler et al., 'Sequential single shot X-ray photon correlation spectroscopy at the SACLA free electron laser', Sci. Rep. 5, 17193 (2015).

Original publication

'Emergence of anomalous dynamics in soft matter probed at the European XFEL', Proc. Natl. Acad. Sci. USA 117, 24110–24116 (2020). DOI: 10.1073/pnas.2003337117

Felix Lehmkühler[1,2], Francesco Dallari[1], Avni Jain[1], Marcin Sikorski[3], Johannes Möller[3], Lara Frenzel[1,2], Irina Lokteva[1,2], Grant Mills[3], Michael Walther[1], Harald Sinn[3], Florian Schulz[2,4], Michael Dartsch[1,2], Verena Markmann[1], Richard Bean[3], Yoonhee Kim[3], Patrik Vagovic[1,3], Anders Madsen[3], Adrian P. Mancuso[3,5] and Gerhard Grübel[1,2]

1. Deutsches Elektronen-Synchrotron DESY, Hamburg, Germany
2. The Hamburg Centre for Ultrafast Imaging (CUI), Hamburg, Germany
3. European X-ray Free-Electron Laser, Schenefeld, Germany
4. Universität Hamburg, Hamburg, Germany
5. La Trobe University, Melbourne, Australia

Shining light on mechanochemical reactions

Switching reaction trajectories and polymorphism in mechanochemical reactions

The use of X-ray powder diffraction to monitor mechanochemical reactions *in situ* offers unique opportunities to improve the fundamental understanding of these solid-state transformations. Real-time monitoring provides direct information on the underlying reaction mechanisms, and enables the discovery of new reactivity and materials. Time-resolved experiments have now shown that the choice of the milling assembly can be used to control the results of mechanochemical cocrystallisation, enabling the discovery of new phases and selective synthesis of cocrystal polymorphs.

Mechanochemistry, i.e. the use of mechanical force to induce and sustain chemical transformations, is a rapidly emerging technique for solvent-free synthesis of a wide range of materials. This includes alloys, coordination polymers, solid electrolytes, as well as cocrystals: multi-component crystalline solids with a well-defined stoichiometry [1]. Milling reactions are typically performed at room temperature by either grinding reactants alone or with small amounts of liquid additives. These can have a catalytic effect on the reaction [2], as well as steering the polymorphic outcome [3].

Here, we present a hitherto unexplored effect of the choice of milling jars and media on the mechanism and outcome of the reaction. Mechanochemical syntheses of a model pharmaceutical cocrystal of nicotinamide (nic) and adipic acid (adi), as well as of a ternary halogen-bonded ionic cocrystal adopting a supramolecular interwoven Borromean topology [4], were followed *in situ* using powder X-ray diffraction (PXRD). Real-time monitoring was conducted at the PETRA III beamline P02.1 using a shaker mill and X-ray transparent poly(methyl methacrylate) (PMMA) milling jars.

The observed reaction pathways were unexpectedly sensitive to the choice of milling media, i.e. number and size of milling balls. In the cocrystallisation of nic and adi, three different reaction designs were studied, using: (A) two or (B) four steel balls of 1.4 g weight each, as well as (C) two zirconia balls of 2.8 g weight. In all cases, the reactions proceeded via the

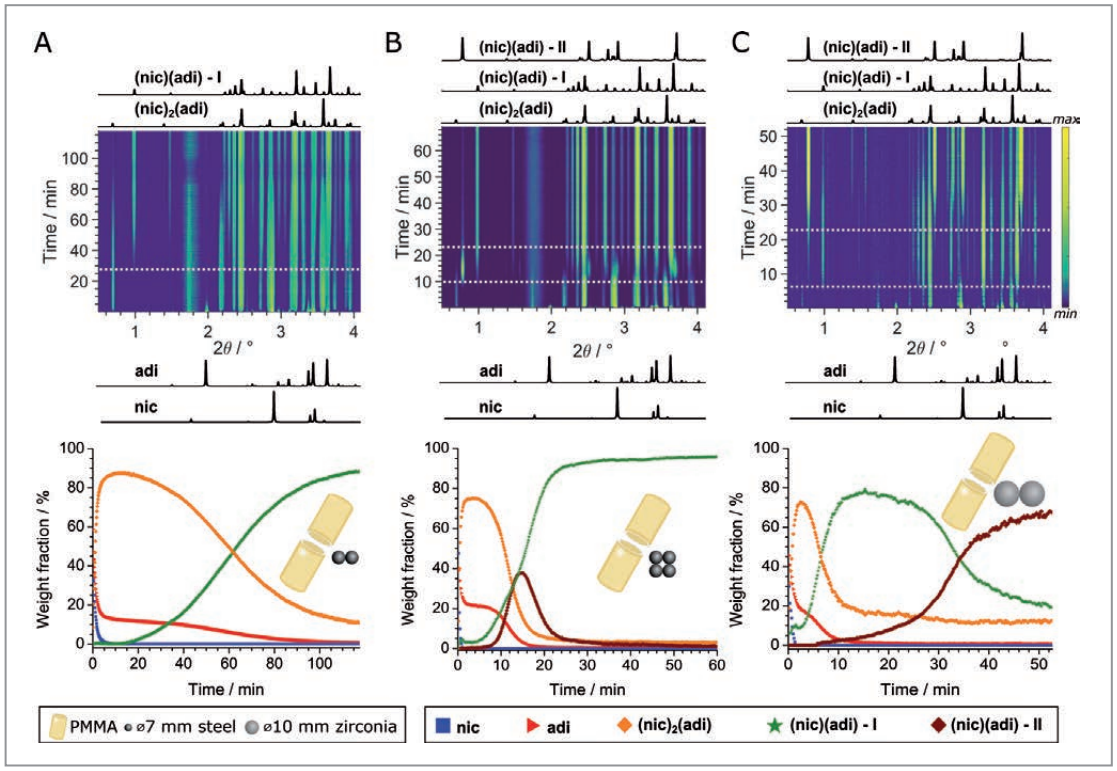

Figure 1

Mechanochemical cocrystallisation of nic and adi using either (A) two or (B) four small steel and (C) two larger zirconia balls. The top row shows the time evolution of the PXRD signal. The corresponding analyses yielding the phase composition are given below.

cocrystal intermediate $(nic)_2(adi)$. In experiment (A), this intermediate transformed within 90 minutes of milling into the (nic)(adi) polymorph Form I as the final product (Fig. 1A). However, doubling the number of steel balls led to the brief appearance of a different polymorph (Form II) of (nic)(adi) in the reaction trajectory (Fig. 1B), indicating that $(nic)_2(adi)$ can convert into Form I via two competing pathways. Surprisingly, although the overall ball weight in experiments (B) and (C) was almost identical, the use of zirconia balls in the latter led to a change in reaction pathway, with Form I now being the intermediate phase and Form II the final product. This observation was unexpected, as previous work on metal-organic frameworks had indicated that mechanochemical reactions should follow Ostwald's rule of stages: from metastable to increasingly more stable products. In contrast, this *in situ* study has shown that changes in milling media can lead to reaction pathways that are either in line or against Ostwald's rule of stages.

Thermal and long-term stability measurements have shown that (nic)(adi) Form I is thermodynamically more stable compared to the enantiotropically related high-temperature Form II, with a small energy difference of ~2 kJ/mol between the two forms. Surprisingly, milling of the pre-assembled Form I or Form II in different jars (PMMA or steel) under otherwise identical conditions enabled the reversible polymorph interconversion: Form I transformed into Form II by milling in steel jars, while using PMMA jars enabled the transformation of Form II into Form I (Fig. 2A). These observations provide a new route for controlling polymorphism in molecular solids, and we explain them by a difference in the efficiency of mechanical energy input due to different elastic properties of the milling assembly materials.

Altering the reaction pathway by modification of milling media appears to be a more general phenomenon: real-time monitoring of the mechanosynthesis of the halogen-bonded Borromean structure revealed that the choice of milling balls can lead to a switch in the supramolecular reaction trajectory. Whereas milling the reactants using one 2.9 g steel ball led to the interwoven Borromean structure, milling with two 1.4 g steel balls unexpectedly led to the exclusive formation of a polymorph based on an open-structure halogen-bonded network (Fig. 2B). In contrast to the (nic)(adi) case, the two phases do not reversibly interconvert by milling. Instead, the open-network polymorph was found to unidirectionally convert into the Borromean structure upon heating (Fig. 2).

In conclusion, real-time X-ray diffraction enabled us to observe and analyse a so far unexplored effects of the milling assembly on reaction trajectories. These findings can pave the way for the controlled solvent-free synthesis of novel materials and properties.

Author contact:
Luzia S. Germann, luzia.germann@mail.mcgill.ca
Pierangelo Metrangolo, pierangelo.metrangolo@polimi.it
Tomislav Friščić, tomislav.friscic@mcgill.ca

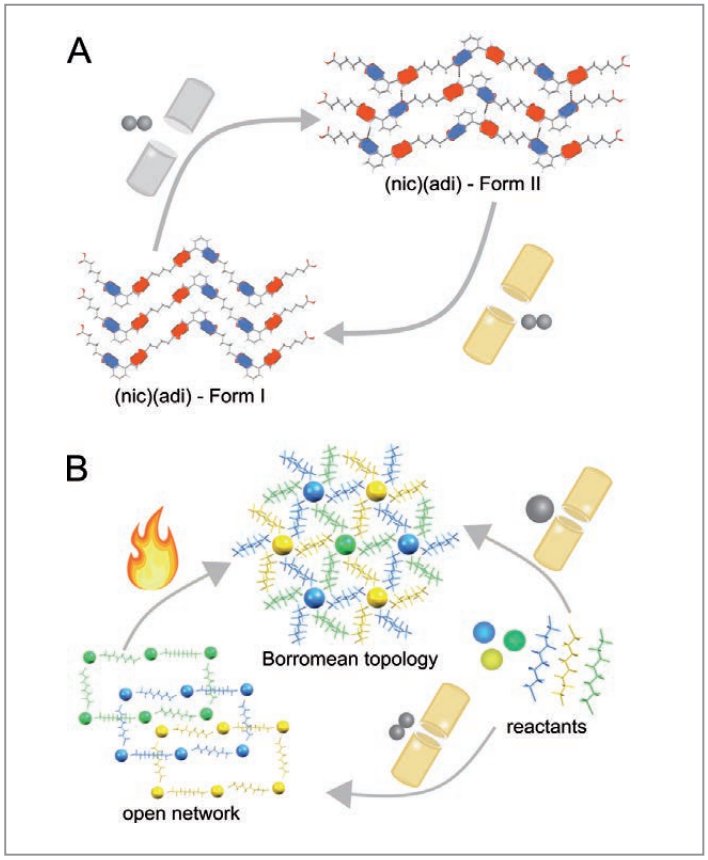

Figure 2

(A) Reversible mechanochemical polymorph interconversion between (nic)(adi) Form I and Form II by changing the material of milling jar (PMMA and steel) and (B) interplay between milling conditions (ball sizes), heating and the open halogen-bonded network and the Borromean structure.

References

1. T. Friščić, C. Mottillo and H. M. Titi, 'Mechanochemistry for synthesis', Angew. Chem. Int. Ed. 59, 1018–1029 (2020).
2. P. A. Julien, L. S. Germann, H. M. Titi, M. Etter, R. E. Dinnebier, L. Sharma, J. Baltrusaitis and T. Friščić, 'In situ monitoring of mechanochemical synthesis of calcium urea phosphate fertilizer cocrystal reveals highly effective water-based autocatalysis', Chem. Sci. 11, 2350–2355 (2020).
3. D. Hasa, E. Miniussi and W. Jones, 'Mechanochemical synthesis of multicomponent crystals: one liquid for one polymorph? A myth to dispel', Cryst. Growth Des. 16, 4582–4588 (2016).
4. R. Liantonio, P. Metrangolo, T. Pilati and G. Resnati, 'Fluorous interpenetrated layers in a three-component crystal matrix' Cryst. Growth Des. 3, 355–361 (2003).

Original publications

'Challenging the Ostwald rule of stages in mechanochemical cocrystallisation', Chemical Science 11, 10092–10100 (2020). DOI: 10.1039/D0SC03629C
Luzia S. Germann[1,2], Mihails Arhangelskis[2,3], Martin Etter[4], Robert E. Dinnebier[1] and Tomislav Friščić[2]

'Open vs. interpenetrated: switchable supramolecular trajectories in mechanosynthesis of a halogen-bonded Borromean network', Chem, in press (2020). DOI: 10.1016/j.chempr.2020.10.022
Luzia Luca Catalano[5], Luzia S, Germann[1,2], Patrick A. Julien[2], Mihails Arhangelskis[3], Ivan Halasz[6], Krunoslav Užarević[6], Martin Etter[4], Robert E. Dinnebier[1], Maurizio Ursini[5], Massimo Cametti[5], Javier Martí-Rujas[5], Tomislav Friščić[2,6], Pierangelo Metrangolo[5], Giuseppe Resnati[5] and Giancarlo Terraneo[5]

1. Max Planck Institute for Solid State Research, Stuttgart, Germany
2. McGill University, Montreal, Canada
3. University of Warsaw, Warsaw, Poland
4. Deutsches Elektronen-Synchrotron DESY, Hamburg, Germany
5. Politecnico di Milano, Milano, Italy
6. Ruđer Bošković Institute, Zagreb, Croatia

Observation of photoion backward emission

Light can attract atoms and molecules by photoionisation

Every photon carries a linear momentum, and light that is absorbed or reflected from an object exerts a forward-directed radiation pressure. In photoionisation of single atoms and molecules, the emitted photoelectron might receive a larger momentum in light direction than the photon supplies. By means of momentum conservation, this entails that the atom or molecule (photoion) is accelerated towards the light source. This counter-intuitive effect was predicted almost a century ago, but lacked experimental confirmation until recently.

In one of the earliest photoionisation studies, performed in 1927, Auger and Perrin were puzzled by the observation that the average forward shift of photoelectron momenta was 'more than 50% higher than the momentum of the photon' [1]. Consequently, as first formulated by Sommerfeld and Schur in 1930 [2], photoionisation might accelerate single atoms or molecules towards the light source. The photoion is essentially the system's centre of mass and, from intuition, one would arguably expect that the radiation pressure pushes it away from the light source. The effect received no further attention until recently, when explicit energy-dependent scaling rules were presented in 2014 [3]. These scaling rules predict that the mean value of the photoion momentum along the light axis equals $-3/5$ times the photon momentum, whereas for photoelectrons it is $+8/5$ times the photon momentum.

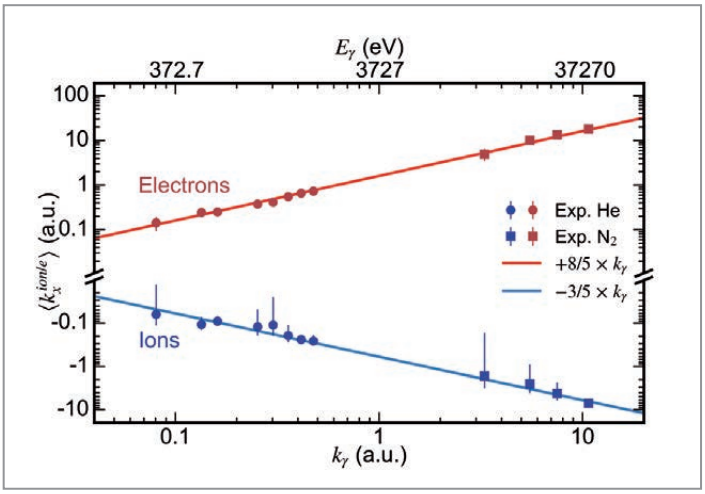

Figure 1

Mean value of electron (red) and ion (blue) momenta along the light propagation axis after photoionisation as functions of photon momentum ($k_\gamma = E_\gamma/c$, bottom scale) and photon energy (E_γ, top scale). The lines show the scaling rules from [3]. The error bars are asymmetric because the *y*-axis is logarithmic.

In our recent work, we were able to confirm this effect experimentally for the first time. We studied the momentum distributions of photoelectrons and photoions generated in one-photon single ionisation in a photon-energy range of 300–40000 eV. One experiment used He as a target and was performed at the PIPE end station of beamline P04 at PETRA III using circularly polarised light. The second experiment, targeting N_2, was performed at ESRF in Grenoble. Both experiments employed a cold-target recoil ion momentum spectroscopy (COLTRIMS) reaction microscope to measure the momentum distributions.

Figure 1 summarises the results of our study. Shown are the measured mean values of ion and electron momenta in the direction of light propagation as functions of photon energy (top scale) and photon momentum (bottom scale). Negative values correspond to backward emission, i.e. against the photon propagation direction. The agreement between experiment and prediction [3] is excellent and the results yield direct experimental confirmation of backward-directed ion emission in photoionisation.

A more detailed view of the momentum distributions underlying the mean value clearly visualises the physics origin of the observed ion backward emission. Figure 2 shows the measured photoion momentum distributions for photoionisation of He by 300, 600, 1125 and 1775 eV photons. The horizontal axis is the momentum component parallel to the photon; the vertical axis is the momentum perpendicular to the photon. The measured ion momenta do not accumulate on rings

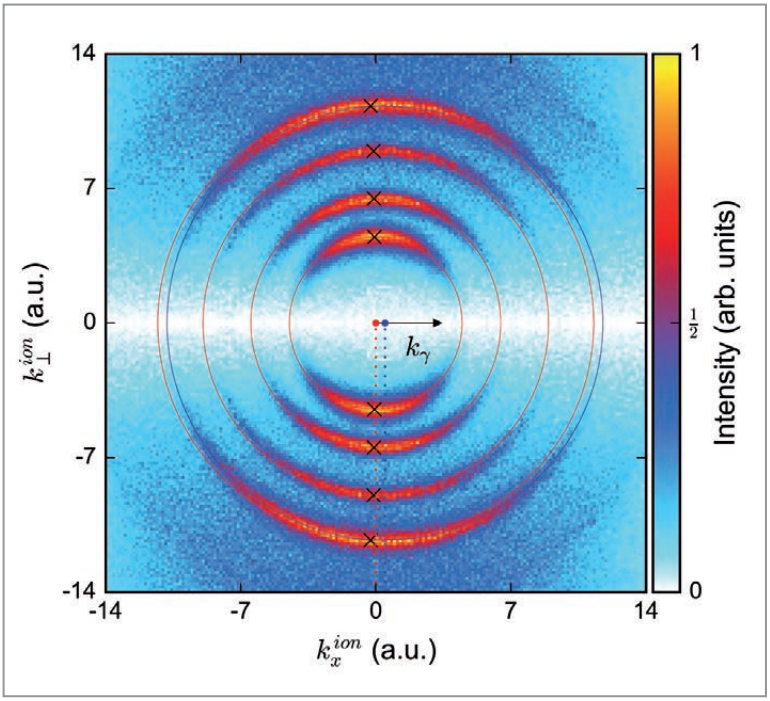

Figure 2

Momentum distributions of He^+ ions after photoionisation by photons with E_γ = 300, 600, 1125 and 1775 eV. The red circles are centred at the origin with a radius of the photoelectron momentum. The blue outer circle is forward shifted by the corresponding photon momentum k_γ = 0.476 a.u. The data from the different photon energies are arbitrarily normalised to match the colour scale.

centred on the origin of momentum space (red circles), but are shifted forward in direction of photon propagation. This is most clearly visible at the outermost ring corresponding to 1775 eV photon energy. The shift of the experimental distributions corresponds to the respective photon momentum. To guide the eye, the blue circle is shifted forward by the photon momentum of a 1775 eV photon (0.476 a.u.). Consequently, the measured ion momentum distributions show that the photon momentum is transferred to the photoion.

Besides the forward shift of photoions in momentum space, the distribution of counts on the red rings (Fig. 2) also changes with photon energy. This distribution is tilted more towards the backward hemisphere upon increase of the photon energy. By means of momentum conservation, the ion's final momentum is the photon momentum (causing the forward shift of the sphere) minus the photoelectron momentum. Therefore, the distribution of the ions on the shifted sphere in momentum space is a direct mirror image of the angular distribution of the photoelectrons in the laboratory frame. The angular distribution of a photoelectron indicates the angular momentum in the final state. If the initial state is He(1s), the leading angular momentum term in the final state is a dipole due to the photon spin. However, the photon momentum brings in additional orbital angular momentum that leads to a forward tilt of the electron angular distribution. This tilt causes the average forward shift of the photoelectron momenta as shown in Fig. 1. The forward-directed mean momentum of the electron is balanced by a backward-directed momentum transfer to the ion which overcompensates for the forward-directed photon momentum transfer.

The experiment confirmed the 90 year old prediction of atoms and molecules being accelerated towards the light source after photoionisation. We have shown that the radiation pressure pushes the ion away from the light source, but that this pressure is overcompensated by the recoil of photoelectron emission.

Author contact:
Sven Grundmann, grundmann@atom.uni-frankfurt.de
Till Jahnke, jahnke@atom.uni-frankfurt.de
Florian Trinter, florian.trinter@desy.de
Reinhard Dörner, doerner@atom.uni-frankfurt.de

References

1. P. Auger and F. Perrin, 'La répartition dans l'espace des directions d'émission des photoélectrons', J. Phys. Radium 8, 93–112 (1927).
2. A. Sommerfeld and G. Schur, 'Über den Photoeffekt in der K-Schale der Atome, insbesondere über die Voreilung der Photoelektronen', Ann. Phys. 4, 409–432 (1930).
3. S. Chelkowski, A. D. Bandrauk and P. B. Corkum, 'Photon momentum sharing between an electron and an ion in photoionization: from one-photon (photoelectric effect) to multiphoton absorption', Phys. Rev. Lett. 113, 263005 (2014).

Original publication

'Observation of photoion backward emission in photoionization of He and N_2',
Physical Review Letters 124, 233201 (2020). DOI: 10.1103/PhysRevLett.124.233201

Sven Grundmann[1], Max Kircher[1], Isabel Vela-Perez[1], Giammarco Nalin[1], Daniel Trabert[1], Nils Anders[1], Niklas Melzer[1], Jonas Rist[1], Andreas Pier[1], Nico Strenger[1], Juliane Siebert[1], Philipp V. Demekhin[2], Lothar Ph. H. Schmidt[1], Florian Trinter[3,4], Markus S. Schöffler[1], Till Jahnke[1] and Reinhard Dörner[1]

1. Institut für Kernphysik, Goethe-Universität, Frankfurt am Main, Germany
2. Institute of Physics and CINSaT, University of Kassel, Kassel, Germany
3. Deutsches Elektronen-Synchrotron DESY, Hamburg, Germany
4. Molecular Physics, Fritz-Haber-Institut, Berlin, Germany

Quantum billiards with photons

First kinematically complete measurement of Compton scattering on gas-phase helium

On the billiard table, our eyes can simultaneously follow the motion of the cue ball and the balls which are hit by it. In Compton scattering at isolated gas-phase atoms, such 'kinematically complete' observation of the process is challenging. It requires determining the energy and direction of the scattered photon, the knocked-out electron and the left-behind ion. We succeeded with the first such measurement with 2.1 keV photons scattering off electrons bound in helium. The energy of these photons is so low that even for backscattering of the photon the momentum transfer does not correspond to an energy high enough to overcome the ionisation threshold. Hence, in this energy regime, ionisation by Compton scattering is an intriguing quantum phenomenon explored in the presented work.

The cross section of Compton scattering is in the range of 10^{-24} cm^2, six orders of magnitude lower than typical photoabsorption cross sections at the respective threshold. This proves to be a major challenge for kinematically complete coincidence measurements, since a gas-phase target is necessary for such a measurement. The low target density and low cross section can be compensated for by a highly efficient detection method and high photon flux. In our work, we used the cold target recoil ion momentum spectroscopy (COLTRIMS) [1] end station at beamline P04 of the synchrotron PETRA III. The beamline was operated in pink-beam mode, in which the full energy spectrum of light from the undulator is used without a frequency selection by the monochromator. With the COLTRIMS technique, we measured the momenta of the helium ions and the Compton electrons at the reaction time. Knowing the momentum of the initial photon, exploiting momentum conservation allowed us to determine the momentum of the scattered photon. With this approach, we were able to detect the He^+ ion and the electrons with energies up to 25 eV with 4π collection solid angle.

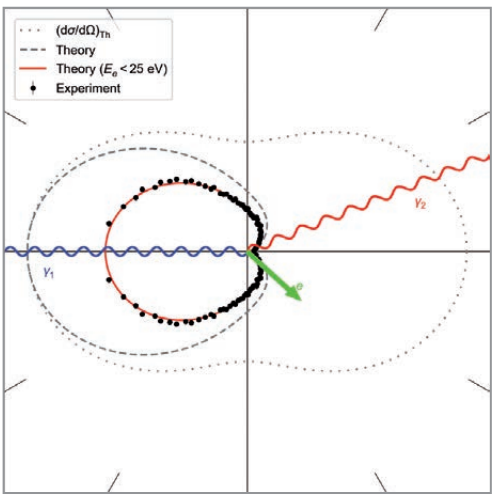

Figure 1

Photon angular distribution of Compton scattering at helium. The wavy blue line resembles the incoming photon, the wavy red line the outgoing photon. The green arrow depicts the momentum of the emitted electron. The dotted line is the Thomson cross section, the dashed and red line are theoretical predictions for the photon angular distributions for all electron energies and for electrons below 25 eV, respectively. The black dots are the experimental photon angular distribution integrated over all electron emission angles and electron energies below 25 eV. The data is mirrored at the *x*-axis.

Ionisation by Compton scattering does not set in abruptly, but emerges slowly with increasing photon energy. It fades out once the energy related to the momentum transfer for backscattering of the photon at an electron is below the binding energy of the electron. In this threshold region, Compton scattering is an intriguing quantum phenomenon. In the often-invoked impulse approximation, the ionic core of the helium atom is only a passive spectator of the Compton reaction. The binding energy of the electron is ignored, but its initial momentum distribution is taken into account. In the impulse approximation, the ionic core only compensates for that initial momentum. This approximation is only valid if the energy of the Compton electron is high compared to its binding energy, which is not the case at $h\nu$ = 2.1 keV. The maximum momentum transfer onto an electron is, to a very good approximation, two times the initial photon momentum (backscattering). If we consider an electron at rest, this means that, for helium with a binding energy of 24.6 eV, the minimal photon energy must be 2.5 keV; otherwise, the respective maximum momentum transfer onto the electron at rest would not be enough to overcome the ionisation threshold. With our chosen energy of 2.1 keV, we are well below this threshold, i.e., outside the validity of the impulse approximation.

Figure 1 shows the angular distribution of the scattered photon. It differs significantly from the Thomson cross section, which would describe the angular distribution of a low-energy photon scattering at a free electron at rest.

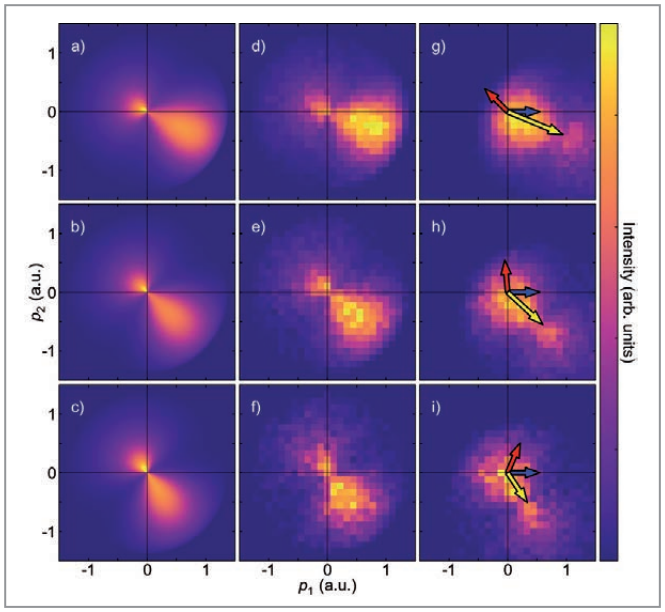

Figure 2

Electron and ion momentum distributions in the scattering plane for different magnitudes of the momentum transfer. Here, p_1 is the momentum component in direction of the incoming photon, p_2 is the component perpendicular to that within the scattering plane. The fixed momentum configuration of the incoming (blue) and outgoing (red) photon is depicted by the arrows in the last panel of each row. The resulting momentum transfer is depicted by the yellow arrows. The first column shows the electron distribution obtained from modelling within the A^2 approximation, the second column the experimental electron momentum distribution and the third column the experimental He^+ momentum distribution.

Forward-scattering angles are especially strongly supressed. Only events resulting in the ionisation of helium are detected, and as Fig. 1 shows, the majority of ionisation is a result of backscattering photons. The dashed and the red lines in Fig. 1 are theoretical calculations within the so-called A^2 approximation, which is in excellent agreement with our experimental data.

For a better understanding of the underlying mechanisms facilitating the ionisation process, it is helpful to visualise the electron and ion momenta in the scattering plane. This plane is defined by the incoming and outgoing photon momentum vectors $\mathbf{k}_1$ and $\mathbf{k}_2$, with the vector $\mathbf{k}_1$ pointing forward, $\mathbf{k}_2$ pointing into the upper half plane, resulting in the momentum transfer $\mathbf{Q} = \mathbf{k}_1 - \mathbf{k}_2$, i.e., the 'kick' of the photon, pointing into the lower right quadrant. Figure 2 shows the electron and He^+ momentum distributions in this coordinate frame. The different rows of subpanels are different momentum configurations of the photon, as depicted in the last column (Fig. 2g-i). Focusing on the electron distribution (Fig. 2d-f), we see a bimodal momentum distribution, with lobes in forward and backward directions separated by a node. The relative intensity of the lobes depends on the scattering angle of the photon. Figure 2a-c shows the theoretical electron momentum distributions in excellent agreement with our experiment.

The forward lobe points in the direction of the momentum transfer and the backward lobe in the opposite direction. These distributions resemble momentum distributions known from different contexts, e.g., ionisation from electron impact (e,2e) [2] or ion impact [3]. There, the forward lobe was termed binary peak and the backward lobe recoil peak, hinting at their underlying mechanisms. The binary peak results from the binary encounter of the photon and the electron, resulting in the electron momentum following the momentum transfer, whereas the recoil peak results from the electron recoiling off the remaining ionic core into the opposite direction. The mirrored ion momentum distributions support this model.

The process of ionisation by Compton scattering can be described in a two-step model, referred to as the A^2 approximation. First, a photon scatters at an electron, described by the Thomson cross section, determining the direction and magnitude of the approximate momentum transfer. The second step is the response of the electronic wave function to this sudden kick. The kick displaces the bound electron wave function in momentum space, which then relaxes onto the electronic eigenstates of the He^+ ion. The displaced wave function has some overlap with the Coulomb continuum, and this overlap leads to ionisation and is observed experimentally.

Author contact: Max Kircher, kircher@atom.uni-frankfurt.de
Florian Trinter, florian.trinter@desy.de
Till Jahnke, jahnke@atom.uni-frankfurt.de
Reinhard Dörner, doerner@atom.uni-frankfurt.de

References

1. J. Ullrich, R. Moshammer, A. Dorn, R. Dörner, L. Ph. H. Schmidt and H. Schmidt-Böcking, 'Recoil-ion and electron momentum spectroscopy: reaction-microscopes', Rep. Prog. Phys. 66, 1463–1545 (2003).
2. H. Ehrhardt, K. Jung, G. Knoth and P. Schlemmer, 'Differential cross sections of direct single electron impact ionization', Z. Phys. D – At. Mol. Clusters 1, 3–32 (1986).
3. D. Fischer, R. Moshammer, M. Schulz, A. Voitkiv and J. Ullrich, 'Fully differential cross sections for the single ionization of helium by ion impact', J. Phys. B: At. Mol. Opt. Phys. 36, 3555–3567 (2003).

Original publication

'Kinematically complete experimental study of Compton scattering at helium atoms near the threshold', Nature Physics 16, 756–760 (2020). DOI: 10.1038/s41567-020-0880-2

Max Kircher[1], Florian Trinter[2,3], Sven Grundmann[1], Isabel Vela-Perez[1], Simon Brennecke[4], Nicolas Eicke[4], Jonas Rist[1], Sebastian Eckart[1], Salim Houamer[5], Ochbadrakh Chuluunbaatar[6,7,8], Yuri V. Popov[6,9], Igor P. Volobuev[9], Kai Bagschik[2], M. Novella Piancastelli[10,11], Manfred Lein[4], Till Jahnke[1], Markus S. Schöffler[1] and Reinhard Dörner[1]

1. Institut für Kernphysik, J. W. Goethe Universität, Frankfurt, Germany
2. Deutsches Elektronen-Synchrotron DESY, Hamburg, Germany
3. Molecular Physics, Fritz-Haber-Institut der Max-Planck-Gesellschaft, Berlin, Germany
4. Institut für Theoretische Physik, Leibniz Universität Hannover, Hannover, Germany
5. LPQSD, Department of Physics, Faculty of Science, University Sétif-1, Setif, Algeria
6. Joint Institute for Nuclear Research, Dubna, Russia
7. Institute of Mathematics and Digital Technologies, Mongolian Academy of Sciences, Ulaanbaatar, Mongolia
8. Peoples' Friendship University of Russia (RUDN University), Moscow, Russia
9. Skobeltsyn Institute of Nuclear Physics, Lomonosov Moscow State University, Moscow, Russia
10. Sorbonne Universités, CNRS, Laboratoire de Chimie Physique Matière et Rayonnement, Paris, France
11. Department of Physics and Astronomy, Uppsala University, Uppsala, Sweden

Electrons' waltz with molecules

New tool for unravelling electron dynamics

Imaging the structure of a molecule and capturing its dynamics with atomic resolution is one of the holy grails for unravelling chemistry in real time. We investigated the interaction between a molecule fixed in space and a very intense laser field, and captured the photoionisation process and subsequent electronic dynamics of a molecule for the first time. We followed the electrons as they were ejected and then danced around the molecules in the strong laser field. Surprisingly, we observed that it is the molecule itself that sets the rhythm and the pace of the electrons' waltz. These results redefine the seminal statements of strong-field molecular physics and open new ways to image molecules with unprecedented spatio-temporal resolution.

The interaction of strong laser fields with matter intrinsically provides a powerful tool for imaging transient dynamics. In the prototypical strong-field interaction, a driving field extracts a valence electron from the target through tunnel ionisation, accelerates the free electron and drives it back to the parent ion. The rescattered portion of this electron wavepacket is exploited in laser-induced electron diffraction (LIED) experiments [1] as a coherent diffraction pattern of the target. In our work, we experimentally and computationally studied molecular-frame photoelectron spectroscopy of strongly aligned molecules. We demonstrated how the molecular frame governs the rescattering time for the photoelectron and consequently its final momentum.

Figure 1 depicts the experiment. An ensemble of carbonyl sulfide (OCS) molecules was strongly aligned using a linearly polarised 800 nm laser pulse, in two different configurations:

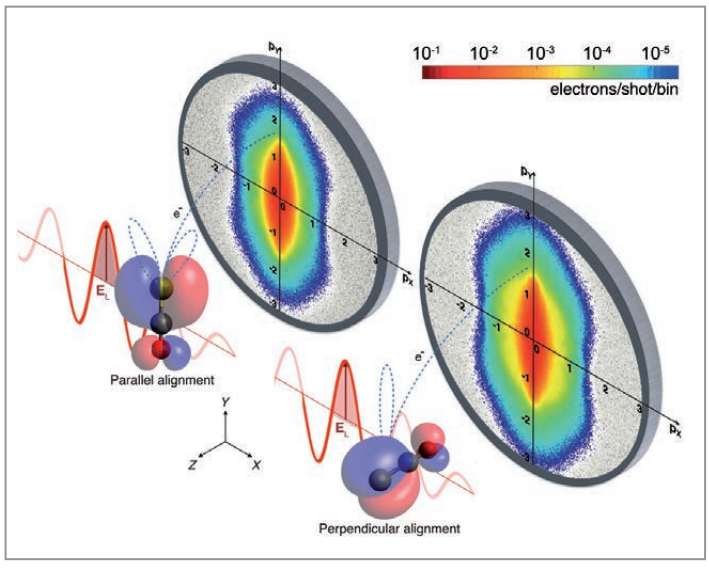

parallel and perpendicular to the *Y* axis. A second short and intense laser pulse, centred at a wavelength of 1300 nm and also linearly polarised along the *Y* axis, was used to singly ionise the OCS molecules. The resulting molecular-frame photoelectron-momentum distributions (MF-PEMD) were measured in a velocity map imaging spectrometer. The two MF-PEMD plots show that the longitudinal momenta p_Y for parallel alignment (left) drop around 2.5 atomic units (a.u.), while they extend up to 3 a.u. for perpendicular alignment (right). According to the strong-field approximation, the cut-off of the photoelectron momentum is expected to only depend on the laser-field properties [2]. Surprisingly, our data showed a clear dependence of the cut-off on the molecular frame.

To elucidate the experimental observations, state-of-the-art calculations were performed using both time-dependent density-functional theory (TDDFT) [3] and semi-classical molecular trajectory simulations based on the Ammosov–Delone–Krainov (ADK) tunnelling theory [4] in conjunction with a simple man propagation (SM) [5]. With the TDDFT calculation, we unravelled the relevance of the dynamical electron–electron interaction in the photoionisation. With the ADK-SM model, we retrieved the dynamics of the freed photoelectron in the presence of the laser and the molecular potential. Figure 2 shows the final photoelectron momenta as a func-

Figure 1

Sketch of the experiment and the observed images. OCS molecules (O in red, C in black, S in yellow) were aligned in the laboratory frame, parallel (left) and perpendicular (right) to the polarisation axis of the ionising laser electric field (E_L). The molecular-frame photoelectron-momentum distributions were projected onto a 2D detector in a velocity map imaging spectrometer. The alignment-dependent photoelectron trajectories are pictorially shown (blue dashed lines), as well as the corresponding shape of the ionising orbital (blue and red lobes).

tion of the recollision phase for both alignments, calculated with ADK-SM. They consist of peaks appearing every half cycle of the electric field at phases close to $(k + 1/2)\pi$, where k is a positive integer.

In this framework, the largest absolute momentum for perpendicular alignment, Fig. 2a, comes from the first rescattering event at a phase around $3\pi/2$. It yields the largest momentum, 3.15 a.u, as expected from the classical theory [2]. However, in the case of parallel alignment, Fig. 2b, most of the large-momentum electrons come from the third revisit at a phase of $7\pi/2$. As a result, the momentum cut-off is smaller, around 2.9 a.u. This is in good agreement with the reduced cut-off experimentally observed for parallel alignment. The dynamics is mainly driven by the molecular potential: the node of the highest occupied molecular orbital along the molecular axis, which in this case is along the laser polarisation direction, imprints an angle on the electron emission at tunnelling. This angle prevents the electron from rescattering at the first revisit. However, the Coulomb attraction by the parent molecular ion keeps the electron nearby, leading to recollisions at multiple revisits.

Furthermore, the photoelectron cut-off in the molecular frame carries crucial time information. While the cut-off for perpendicular alignment is strongly shaped by electrons recolliding 3/4 of an optical cycle after ionisation, as usually assumed, the cut-off for parallel alignment is dominated by electrons revisiting the molecule much later, e.g., after one or two full optical cycles. Since the time spent by the photoelectron before rescattering is employed as the elementary delay step for time-resolved LIED [1], our results indicate that the previous interpretation of LIED experiments should be reconsidered. In the conventional strong-field approximation, the electron dynamics is governed mostly by the external laser field. Our analysis, however, demonstrates that the molecule has a crucial role: it not only defines the initial direction of the ejected electron, but it also pulls the electron towards itself multiple times and sets the recollision time. This molecular-frame clock for electron recollision could be exploited to disentangle the structural dynamics even with sub-femtosecond temporal resolution. Our work allows for a deeper understanding of strong-field ionisation in molecules and for tracking the molecular potential in real time.

Author contact: Andrea Trabattoni, andrea.trabattoni@desy.de
Jochen Küpper, jochen.kuepper@cfel.de.

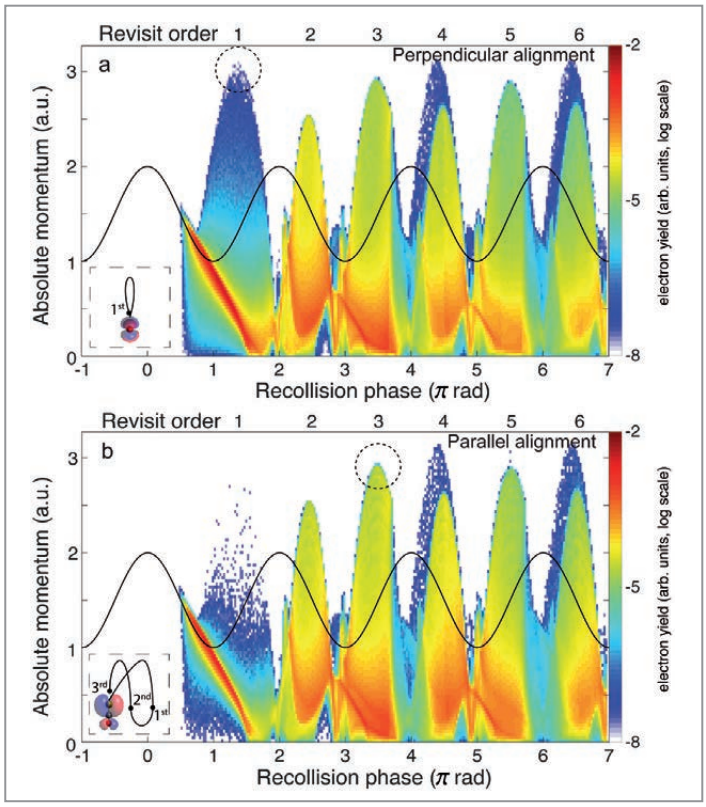

Figure 2

Final absolute photoelectron momentum as a function of the recollision phase (bottom axis) and revisit order (top axis) for (a) perpendicular and (b) parallel alignment, calculated with ADK-SM. The colour scale maps the electron counts at every momentum-phase point. The dashed black circles highlight the largest-momentum electrons at the most probable revisit order for the two alignments. The solid black line depicts the external electric field. The insets give pictorial representations of molecular-frame electron trajectories, with the order of revisits indicated.

References

1. C. I. Blaga et al., 'Imaging ultrafast molecular dynamics with laser-induced electron diffraction', Nature 483, 194–197 (2012).
2. G. G. Paulus, W. Becker, W. Nicklich and H. Walther, 'Rescattering effects in above-threshold ionization: a classical model', J. Phys. B. 27, L703–L708 (1994).
3. M. A. L. Marques, N. T. Maitra, F. Nogueira, E. K. U. Gross and A. Rubio (Eds.), 'Fundamentals of time-dependent density functional theory', Springer Verlag (2012).
4. M. V. Ammosov, N. B. Delone and V. P. Kraĭnov, 'Tunnel ionization of complex atoms and of atomic ions in an alternating electromagnetic field', J. Exp. Theor. Phys. 64, 1191–1194 (1986).
5. J. Wiese, J. Onvlee, S. Trippel and J. Küpper, 'Strong-field ionization of complex molecules', submitted (2020); arXiv:2003.02116 [physics].

Original publication

'Setting the photoelectron clock through molecular alignment', Nature Communications 11, 2546 (2020). DOI: 10.1038/s41467-020-16270-0

Andrea Trabattoni[1,2], Joss Wiese[1,3], Umberto De Giovannini[4], Jean-François Olivieri[1], Terry Mullins[1], Jolijn Onvlee[1], Sang-Kil Son[1,2], Biagio Frusteri[5], Angel Rubio[4,6,7], Sebastian Trippel[1,2] and Jochen Küpper[1,2,3,7]

1. Center for Free-Electron Laser Science (CFEL), DESY, Hamburg, Germany
2. The Hamburg Centre for Ultrafast Imaging (CUI), Universität Hamburg, Hamburg, Germany
3. Department of Chemistry, Universität Hamburg, Hamburg, Germany
4. Max Planck Institute for the Structure and Dynamics of Matter (MPSD) and Center for Free-Electron Laser Science (CFEL), Hamburg, Germany
5. Dipartimento di Fisica e Chimica, Universitá degli Studi di Palermo, Palermo, Italy
6. Center for Computational Quantum Physics (CCQ), The Flatiron Institute, New York, New York, USA
7. Department of Physics, Universität Hamburg, Hamburg, Germany

Ultrafast birth of free radicals in water

Femtosecond hole dynamics following photoionisation directly observed using X-ray absorption spectroscopy

Water is the main component of biological tissue and vital for human life. The elementary processes following photoionisation of liquid water are fundamental for understanding radiation–matter interaction in biology and chemistry. With absorption spectroscopy, using femtosecond soft X-ray pulses from the LCLS XFEL, we tracked the ultrafast hole dynamics following the creation of a valence hole by strong-field ionisation. We recorded the decay of the H_2O^+ cation during the primary proton transfer reaction and witnessed the birth of the OH free radical. Simulations revealed that the X-ray spectra are sensitive to structural dynamics at the ionisation site.

Liquid water is composed of individual molecules, where nuclear and electron dynamics unfold within femtoseconds. These ultrafast dynamics are the starting point for biological and chemical processes that follow on much longer time scales. One way such dynamics are induced in water is photoionisation, which may be caused by either natural radiation exposure or radiation-based medical treatments. Photoionisation creates a photoelectron and the unstable water cation H_2O^+, which undergoes a series of decay processes [1]. Ultimately, these lead to the formation of highly reactive free radicals that cause radiation damage to biological tissue.

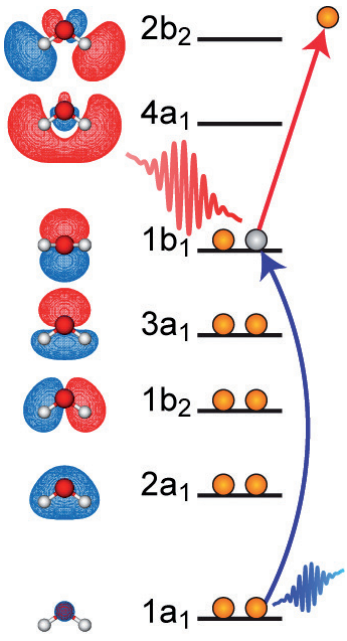

Figure 1

Strong-field ionisation removes an electron from a water valence orbital. X-ray absorption spectroscopy probes the hole by promoting an oxygen core electron to fill the vacancy.

The fastest process following the photoionisation of liquid water is the proton transfer reaction [2],

$$H_2O^+ + H_2O \rightarrow OH + H_3O^+.$$

The end products of the proton transfer reaction, as well as the dynamics of the ejected photoelectron, have been studied extensively [1]. The short-lived H_2O^+ cation, however, had so far not been observed directly.

Photoionisation creates a hole in the water molecule by removing an electron. The proton transfer reaction is directly related to the ultrafast dynamics of this hole: first the hole localises on the H_2O^+, and once the proton transfer is completed, it remains on the OH [2]. In the experiment presented here, we used strong-field ionisation with an intense optical laser to create a valence hole in liquid water. The evolution of the hole is then probed by transient X-ray absorption spectroscopy (Fig. 1), where an oxygen core electron is promoted

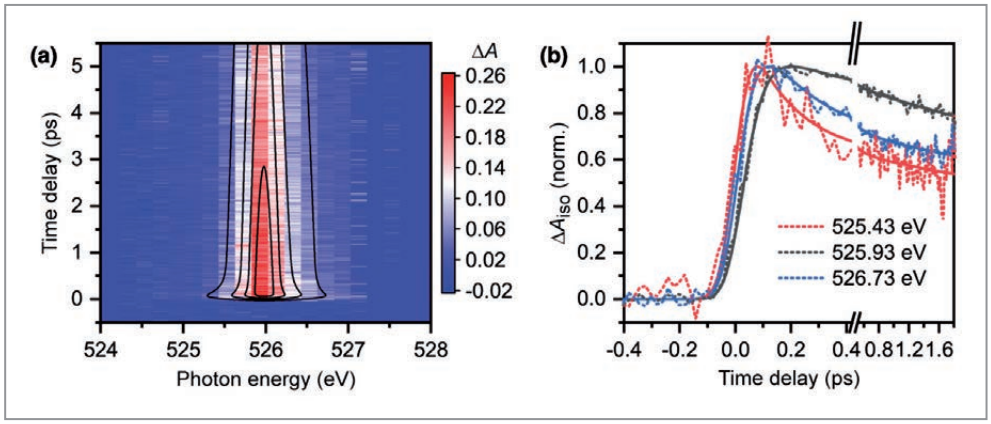

Figure 2

Experimental X-ray absorption spectrum. (a) Full time-dependent X-ray spectrum. (b) Selected time traces show the energy dependence of peak rise times.

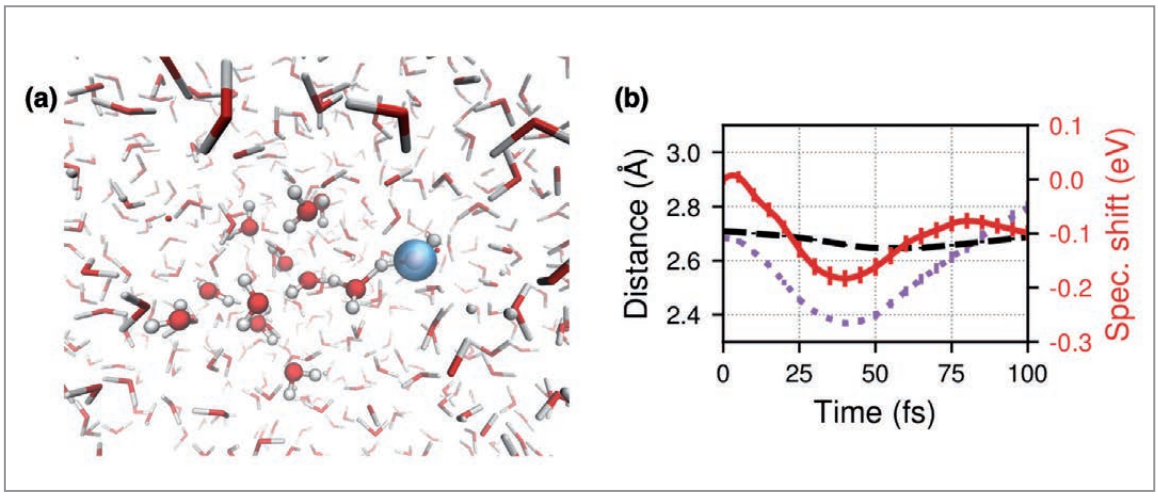

Figure 3

Molecular dynamics simulations. (a) View of the water cluster at the verge of OH formation, including the hole orbital. (b) Time-dependent peak position of the X-ray absorption spectrum (red) along with the distance of H_2O^+/OH to the next neighbouring oxygen atom (violet) and average distance of oxygens not involved in proton transfer (black).

to fill the hole. This transition at about 526 eV is clearly separated from the water background and is distinguishable for the two main involved species, H_2O^+ and OH. The required ultrashort, intense pulses in the soft X-ray region are available at X-ray free-electron lasers.

Using femtosecond X-ray pulses from the Linac Coherent Light Source (LCLS), we obtained the time-dependent X-ray absorption spectrum (Fig. 2a) and additional time traces at three selected photon energies (Fig. 2b). Combined, the variation of the spectral peak position and width allows us to identify three characteristic time scales for ultrafast processes. The fastest process takes place within 46±10 fs. It is associated with the formation of OH in a vibrationally excited state. This is followed by equilibration of the OH within 180±20 fs. Ultimately, OH and the photoelectron recombine within 14.2 ps, leading to a loss of the respective signal.

This interpretation of the experimental spectrum is informed by theoretical work we performed at DESY. Simulations provide valuable insight into the complex relation between the changes in the spectrum and the underlying ultrafast molecular dynamics. To describe liquid water, we extended our in-house electronic structure software XMOLECULE [3]. A cluster of 12 water molecules is treated quantum mechanically. It is immersed in a larger sphere of water molecules treated classically, at much lower computational cost (Fig. 3a). Non-Born-Oppenheimer effects are incorporated by the quantum-classical surface-hopping method.

Within this framework, we were able to capture the proton transfer reaction in our simulations and calculate the expected X-ray absorption spectrum. We focus on the most prominent feature of this spectrum, the shift in its peak position (Fig. 3b). We realised that it is clearly related to changes in the chemical environment of the hole. As the proton transfer reaction starts, the distance between the hole and the next-neighbouring oxygen atom shrinks. This is due to electrostatic interaction between the positively charged hole and the partially negatively charged oxygen. Consequently, the orbital energy levels shift slightly and the resonance peak shifts. As proton transfer progresses, the excess charge is separated from the hole [2]. The spectrum peak shifts back to its original position, with good agreement to the time scale of the fastest process in the experiment. This correlation shows that X-ray absorption spectroscopy is indirectly sensitive to the proton transfer reaction: it can be used to trace the chemical environment of the hole in real time.

With the combination of *ab initio* molecular dynamics simulations and a challenging experiment, we were able to resolve the very first processes following the photoionisation of liquid water. Future experiments with increased time resolution are expected to resolve the proton transfer reaction more clearly.

Author contact: Caroline Arnold, caroline.arnold@desy.de
Robin Santra, robin.santra@cfel.de

References

1. J. Li, Z. Nie, Y. Y. Zheng, S. Duo and Z.-H. Loh, 'Elementary electron and ion dynamics in ionized liquid water', J. Phys. Chem. Lett. 4, 3698–3703 (2013).
2. O. Marsalek, C. G. Elles, P. A. Pieniazek, E. Pluhařová, J. VandeVondele, S. E. Bradforth and P. Jungwirth, 'Chasing charge localization and chemical reactivity following photoionization in liquid water', J. Chem. Phys. 135, 224510 (2011).
3. Y. Hao, L. Inhester, K. Hanasaki, S.-K. Son and R. Santra, 'Efficient electronic structure calculation for molecular ionization dynamics at high X-ray intensity', Struct. Dyn. 2, 041707 (2015).

Original publication

'Observation of the fastest chemical processes in the radiolysis of water', Science 367, 179–182 (2020). DOI: 10.1126/science.aaz4740

Zhi-Heng Loh, Gilles Doumy, Caroline Arnold, Ludvig Kjellsson, Stephen H. Southworth, Andre Al Haddad, Yoshiaki Kumagai, Ming-Feng Tu, Phay J. Ho, Anne Marie March, Richard D. Schaller, Muhamamd Shafiq Bin Mohd Yusof, Tushar Debnath, Marc Simon, Ralph Welsch, Ludger Inhester, Khadijeh Khalili, Kaushik Nanda, Anna I. Krylov, Stefan Moeller, Giacomo Coslovich, Jake Koralek, Michael P. Minitti, William F. Schlotter, Jan-Erik Rubensson, Robin Santra and Linda Young

Affiliation details at
https://science.sciencemag.org/content/367/6474/179

Time-of-flight momentum microscopy at FLASH

Three in one: merged time-resolved photoelectron spectroscopy techniques in a single instrument

Being the world's first free-electron laser in the soft X-ray range, FLASH at DESY generates ultrashort laser pulses of extremely high intensity, offering a multitude of experimental opportunities in physics, chemistry and biology. Now, a new generation of time-resolved photoemission spectroscopy experiments at FLASH can probe condensed matter systems like low-dimensional materials, molecular systems and quantum materials in unprecedented detail. The high-energy X-ray time-of-flight (HEXTOF) spectrometer is a versatile instrument that enables time-resolved momentum microscopy, time-resolved X-ray photoelectron spectroscopy and time-resolved X-ray photoelectron diffraction combined in a single setup.

With the HEXTOF instrument shown in Fig. 1, a so-called 'momentum microscope', the two momentum components of photoelectrons parallel to the sample surface, as typically emitted from valence and conduction bands of materials, can be measured simultaneously together with their energy. Furthermore, it is possible to record core-level spectra (X-ray photoelectron spectroscopy, XPS) as well as core-level diffraction patterns (X-ray photoelectron diffraction, XPD). Traditionally, these measurements have been carried out using separate instruments. Now, all three photoemission techniques have been successfully integrated within one setup and extended into the time domain at the PG2 beamline of FLASH via optical pump–FEL probe-type experiments, thus combining the time-of-flight momentum microscope with the free-electron laser's multiple capabilities.

HEXTOF features full-field momentum-resolved imaging and time-of-flight energy recording for direct mapping of multi-dimensional electronic structures. The overall performance

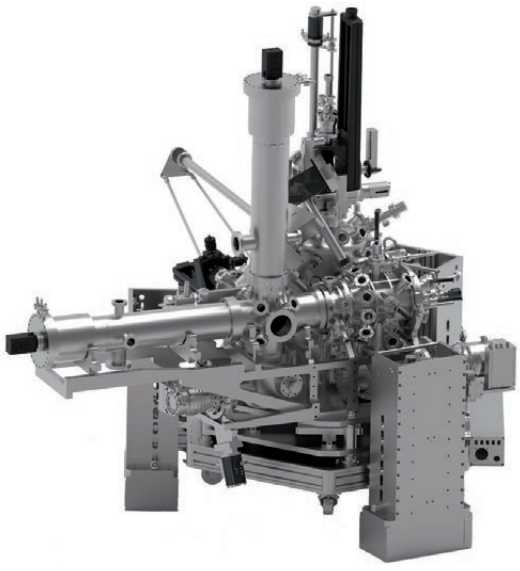

Figure 1
The HEXTOF setup as installed at the PG2 beamline at FLASH or used in the lab.

was demonstrated by investigating the carrier dynamics in the layered semiconductor WSe_2. An experimental energy resolution of 130 meV, a momentum resolution of 0.06 $Å^{-1}$ and a system response function of 150 fs have been achieved. Figure 2a shows a typical time and momentum-integrated photoemission spectrum of WSe_2 (1D data) as recorded with 109.5 eV FEL pulses (with the FEL tuned to 36.5 eV selecting the 3rd harmonic radiation of FLASH by the PG2 monochromator). The W 4f and Se 3d core levels lie about 33 eV and 55 eV below the Fermi level, respectively.

The direct and parallel recording in 3D parameter space (k_x, k_y, E) yields a more complete characterisation of the excited-state electron distribution, while requiring only a fraction of the measurement time compared with conventional spectrometers. Thus, a large portion of energy–momentum space can be accessed in an ultra-efficient manner and without any sample manipulation. By performing pump-probe experiments, photo-induced excited-state dynamics above the Fermi level (Fig. 2b) become accessible. Utilising the full four-dimensional information content of the photoemission signal leads to the case of time-resolved momentum microscopy (trMM). Example data from WSe_2 is shown in Fig. 2c before and after (pump off/on) optical excitation with femtosecond pulses of 1.6 eV photon energy. Here, all data from valence and conduction bands within 2 ps of the optical excitation was integrated. We were able to observe and compare the conduction-band carrier distribution in the non-equivalent conduction-band maxima (K or K') and corresponding minima upon direct excitation of the *A*-exciton at room temperature.

Moreover, the use of spectral tuneability of the FEL radiation provides additional access to core levels giving information on transient excited-state distributions through trXPS (Fig. 2d) [1] and structural dynamics through trXPD [2] as shown for the W $4f_{7/2}$ core level of WSe_2 in Fig. 2e. The combined dynamics

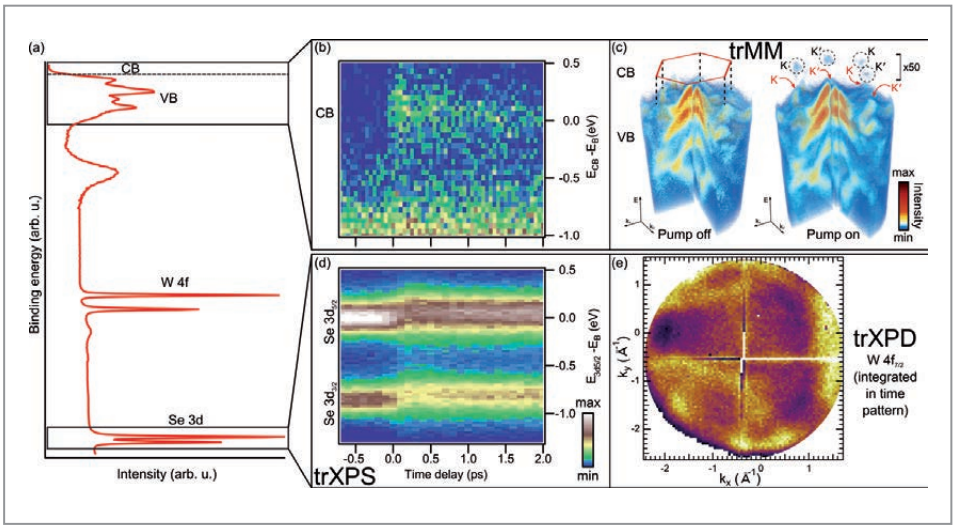

Figure 2

Time-resolved dynamics over a broad energy range of the photoemission spectrum of WSe_2. (a) Momentum-integrated photoemission spectrum. Time-resolved measurements showing concurrent dynamics in (b) the WSe_2 conduction band and (d) Se 3d core-level doublet. (c) Momentum-resolved photoemission data of WSe_2 as a volumetric rendering of the conduction band-mapping measurement outcome before (pump off) and after (pump on) the optical excitation (data from one quadrant cut out to reveal dispersive electronic bands on the inside). (e) Time-integrated XPD pattern of W $4f_{7/2}$ core-level emission from WSe_2.

of the excited-state and core-level signals clearly revealed a delayed core hole change due to screening by excited quasi-free carriers resulting from an excitonic Mott transition [1].

In order to process and analyse the large amount of data acquired with HEXTOF, we have developed a distributed analysis workflow, based on efficient interaction with single-event data and compatible with data acquisition schemes at both 3rd and 4th generation light sources, respectively, as well as tabletop laser sources. In addition, we have defined the corresponding format for data storage and reuse, and compared visual representations pertaining to the band-mapping data [3,4].

In conclusion, we have realised a novel setup combining full-field momentum imaging and time-of-flight energy recording (3D data recording architecture) with a flexible sample preparation chamber and additional characterisation tools. The HEXTOF instrument is the ideal tool for time-consuming pump-probe photoemission experiments with femtosecond-pulsed XUV/soft X-ray radiation from the high repetition rate FEL FLASH. Furthermore, it is routinely used together with a tabletop high-harmonic laser source in the Center for Free-Electron Laser Science (CFEL) to perform either sample pre-characterisation before beamtimes or independent research activities. With the present setup and available light sources, it thus becomes possible to investigate in unprecedented detail the ultrafast electronic, chemical and structural dynamics of a wide range of chemical and physical systems. Moreover, the simultaneous detection of the electronic, spin and geometric structure in the time domain with femtosecond resolution opens a new avenue for the direct determination of the couplings between these degrees of freedom that give rise to fascinating emergent properties of quantum materials.

Author contact: Dmytro Kutnyakhov, dmytro.kutnyakhov@desy.de

References

1. M. Dendzik et al., 'Observation of an excitonic Mott transition through ultrafast core-cumconduction photoemission spectroscopy', Phys. Rev. Lett. 125, 096401 (2020).
2. D. Curcio et al., 'Imaging of coherent phonons in Bi_2Se_3 probed by time-resolved photoelectron diffraction' (to be submitted).
3. R. P. Xian et al., 'An open-source, end-to-end workflow for multidimensional photoemission spectroscopy', Sci. Data 7, 442 (2020).
4. R. P. Xian et al., 'A machine learning route between band mapping and band structure', arXiv:2005.10210.

Original publication

'Time- and momentum-resolved photoemission studies using time-of-flight momentum microscopy at a free-electron laser', Review of Scientific Instruments 91, 013109 (2020). DOI: 10.1063/1.5118777

Dmytro Kutnyakhov[1], Rui Patrick Xian[2], Maciej Dendzik[2], Michael Heber[1], Federico Pressacco[3,4], Steinn Ymir Agustsson[5], Lukas Wenthaus[1], Holger Meyer[3], Sven Gieschen[3], Giuseppe Mercurio[3], Adrian Benz[3], Kevin Bühlman[6], Simon Däster[6], Rafael Gort[6], Davide Curcio[7], Klara Volckaert[7], Marco Bianchi[7], Charlotte Sanders[8], Jill Atsuko Miwa[7], Søren Ulstrup[7], Andreas Oelsner[9], Christian Tusche[10,11], Ying-Jiun Chen[10,11], Dmitrii Vasilyev[5], Katerina Medjanik[5], Günter Brenner[1], Siarhei Dziarzhytski[1], Harald Redlin[1], Bastian Manschwetus[1], Shuo Dong[2], Jasper Hauer[2], Laurenz Rettig[2], Florian Diekmann[12], Kai Rossnagel[1,12,13], Jure Demsar[5], Hans-Joachim Elmers[5], Philip Hofmann[7], Ralph Ernstorfer[2], Gerd Schönhense[5], Yves Acremann[6] and Wilfried Wurth[1,3]

1. Deutsches Elektronen-Synchrotron DESY, Hamburg, Germany
2. Fritz Haber Institute of the Max Planck Society, Berlin, Germany
3. Physics Department and Center for Free-Electron Laser Science (CFEL), Universität Hamburg, Hamburg, Germany
4. The Hamburg Centre for Ultrafast Imaging (CUI), Hamburg, Germany
5. Institut für Physik, Johannes Gutenberg-Universität Mainz, Mainz, Germany
6. Laboratorium für Festkörperphysik, ETH Zürich, Zürich, Switzerland
7. Department of Physics and Astronomy, Interdisciplinary Nanoscience Center (iNANO), Aarhus University, Aarhus, Denmark
8. Central Laser Facility, STFC Rutherford Appleton Laboratory, Harwell, United Kingdom
9. Surface Concept GmbH, Mainz, Germany
10. Forschungszentrum Jülich GmbH, Peter Grünberg Institut (PGI-6), Jülich, Germany
11. Fakultät für Physik, Universität Duisburg-Essen, Duisburg, Germany
12. Institut für Experimentelle und Angewandte Physik, Christian-Albrechts-Universität zu Kiel, Kiel, Germany
13. Ruprecht-Haensel-Labor, Christian-Albrechts-Universität zu Kiel, Kiel, Germany

Finding crystals in living cells

Synergistic application of SAXS and XRPD enables rapid detection of protein microcrystals in living cells

Protein crystallisation in living cells holds the potential to develop into an exciting approach that complements established *in vitro* crystallisation techniques. However, the cellular environment renders the detection of *in cellulo* crystals challenging. This limitation is overcome by a synergistic application of small-angle X-ray scattering (SAXS) and X-ray powder diffraction (XRPD). Based on the presence of Bragg reflection fingerprints in the scattering curves, SAXS-XRPD screening allows us to prove if diffracting crystalline structures are present in at least a low percentage of cells within a culture. The whole detection procedure requires only a few seconds, for which no other established methods can compete. Moreover, more detailed insights into the *in cellulo* crystallisation process can be obtained.

X-ray crystallography is a well-established technique to obtain high-resolution structural information of proteins. Diverse strategies to crystallise recombinant proteins in artificial chambers have been established, but there is still no guarantee of success. A novel approach is to exploit the intrinsic ability of living cells to form intracellular protein crystals. Next to native crystallisation events, the formation of '*in cellulo* crystals' has been observed for a growing number of recombinant proteins, predominantly produced in mammalian and baculovirus-infected insect cells [1]. Thanks to the developments in serial crystallography at X-ray free-electron lasers (XFELs) and synchrotron sources during the past decade, protein crystals in the low micrometre or even the nanometre size range can now be used for structure determination [2], which enabled the extraction of high-resolution structural information from *in cellulo* crystal diffraction [1]. Crystallisation in a cell does not require optimisation of protein purification and extensive crystallisation screening steps, but provides quasi-native conditions for crystal growth, and the opportunity to identify native co-factors present in the natural reservoir of compounds [3].

The development of a versatile screening strategy for *in cellulo* protein crystallisation as an alternative complementary to conventional crystallisation techniques does not require only a more detailed understanding of the involved

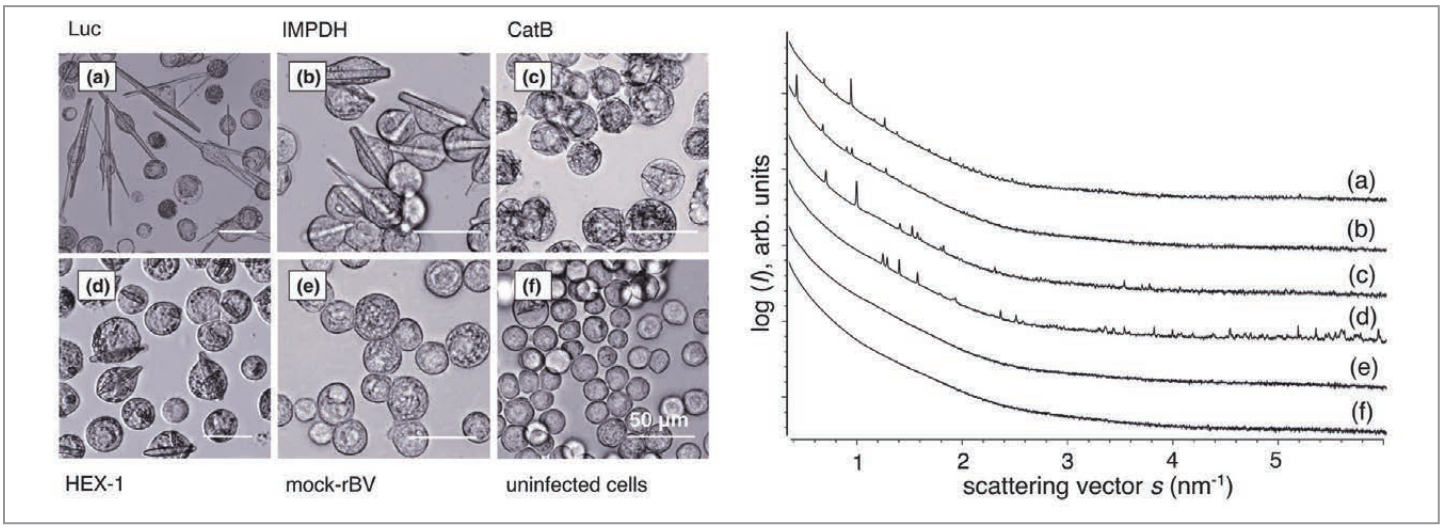

Figure 1

Left panels: light-microscopic images of insect cells four days after infection with recombinant baculoviruses encoding (a) *P. pyralis* luciferase, (b) *T. brucei* inosine monophosphate dehydrogenase, (c) *T. brucei* cathepsin B, as well as (d) *N. crassa* HEX-1. (e) shows mock-rBV infected cell and (f) shows unifected cells. Right panel: 1D radially averaged X-ray scattering data of the insect cells containing intracellular crystals of the target proteins.

Figure 2

1D radially averaged X-ray scattering data of insect cells containing intracellular crystals of *T. brucei* cathepsin B. The percentage of crystal-containing cells within the entire culture of each sample, as determined by light microscopy, is presented next to the scattering curves.

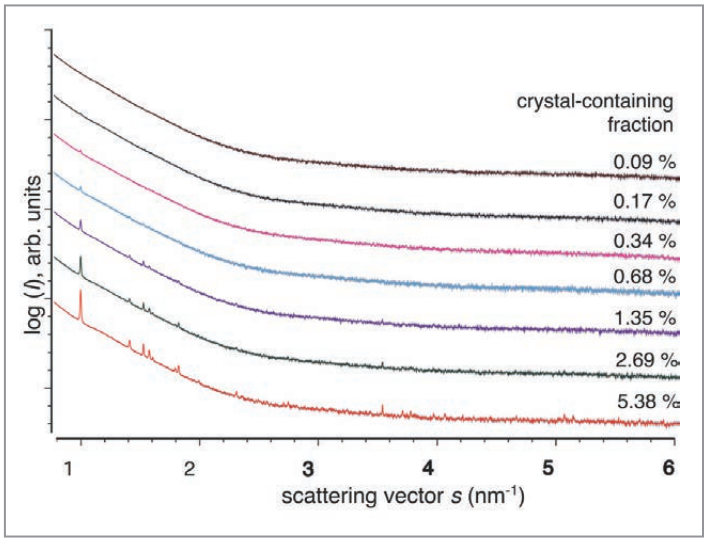

cellular processes, but also the reliable detection of crystals inside living cells. During recent years, diverse methods have been optimised to identify even nanometre-sized protein crystals in crystallisation setups [4], but the environmental challenges imposed by the living cells prevent an application to *in cellulo* crystals. Moreover, the proportion of crystal-containing cells within the entire culture can be less than one percent, rendering the detection of successful *in cellulo* crystallisation into a laborious and time-consuming effort.

A direct proof for the presence of crystallites is given by the detection of specific Bragg reflections of X-rays from a sample. Therefore, we established a synergistic approach of SAXS and XRPD for a rapid and sensitive detection of intracellular protein crystals. Dense suspensions of insect cells containing crystals of four test proteins (Fig. 1a-f) were automatically loaded with a robotic sample changer into a quartz capillary for X-ray diffraction at the high-brilliance and low-background P12 bioSAXS beamline [5] of EMBL at the PETRA III storage ring. Summation of the detector frames, subtraction of the buffer signal and radial averaging resulted in scattering curves exhibiting clear peaks after a measurement time of only 4 seconds per sample (right panel in Fig. 1). The lack of peaks indicate the absence of crystalline structures within the cells. These peaks represent the Debye-Scherrer rings that result from the orientational average of the Bragg reflections from the many small crystals randomly oriented in the cell suspension, a typical observation during XRPD measurements. The intensity of the peaks depends on the overall scattering capability of the irradiated part of the sample and reliably indicates the presence of intracellular crystalline structures. Depending on the individual protein, the peaks were detected even when only a tiny amount (0.3–6%) of cells in the culture contained crystals (Fig. 2). However, the peak intensity on its own does not represent a suitable measure to compare the number and/or the size of different crystallites in the living cells.

SAXS-XRPD screening has the potential to overcome current limitations in the reliable detection of intracellular crystals. A further increase in peak brilliance, e.g. by using a fourth-generation synchrotron or an XFEL, will allow the detection of smaller crystals or even lower the detection limit in the future. High-throughput SAXS-XRPD screening of potentially crystal-containing samples can be directly linked to serial diffraction data collection at a crystallography beamline to streamline the structure determination. Moreover, the dependence of the Bragg reflection positions on the unit-cell composition offers the possibility of investigating the influence of growth conditions, e.g. stress, temperature, starvation and cellular compartmentalisation, on the size and formation of *in cellulo* crystals. This could contribute to more detailed insights into the *in cellulo* crystallisation process.

Author contact:
J. Mia Lahey-Rudolph, mia.lahey-rudolph@th-luebeck.de
Robert Schönherr, schoenherr@biochem.uni-luebeck.de
Cy M. Jeffries, cy.jeffries@embl-hamburg.de
Lars Redecke, redecke@biochem.uni-luebeck.de

References

1. R. Schönherr, J. M. Rudolph and L. Redecke, 'Protein crystallization in living cells', Biol. Chem. 399, 751–772 (2018).
2. J. Standfuss and J. Spence, 'Serial crystallography at synchrotrons and X-ray lasers', IUCrJ 4, 100–101 (2017).
3. K. Nass et al., '*In cellulo* crystallization of *Trypanosoma brucei* IMP dehydrogenase enables the identification of genuine co-factors', Nat. Commun. 11, 620 (2020).
4. M. Becker, D. J. Kissick and C. M. Ogata, 'Locating and visualizing crystals for X-ray diffraction experiments', Methods Mol. Biol. 1607, 143–164 (2017).
5. C. E. Blanchet et al., 'Versatile sample environments and automation for biological solution X-ray scattering experiments at the P12 beamline (PETRA III, DESY)', J. Appl. Cryst. 48, 431–443 (2015).

Original publication

'Rapid screening of *in cellulo* grown protein crystals via a small-angle X-ray scattering/X-ray powder diffraction synergistic approach', Journal of Applied Crystallography 53, 1169–1180 (2020). DOI: 10.1107/S1600576720010687

Janine Mia Lahey-Rudolph[1,2], Robert Schönherr[1,3], Cy M. Jeffries[4], Clément E. Blanchet[4], Juliane Boger[1], Ana Sofia Ferreira Ramos[1], Winnie Maria Riekehr[1], Dimitris-Panagiotis Triandafillidis[5], Alexandros Valmas[5], Irene Margiolaki[5], Dmitri Svergun[4] and Lars Redecke[1,3]

1. Institute of Biochemistry, University of Lübeck, Lübeck, Germany
2. Center for Free-Electron Laser Science (CFEL), DESY, Hamburg, Germany
3. Deutsches Elektronen Synchrotron DESY, Hamburg, Germany
4. European Molecular Biology Laboratory (EMBL) c/o DESY, Hamburg, Germany
5. Department of Biology, Section of Genetics, Cell Biology and Development, University of Patras, Patras, Greece

New method turns high-power picosecond lasers into femtosecond sources

Record compression delivers ultrashort laser pulses

Ultrashort, femtosecond laser pulses are nowadays employed in many different fields. Their very short pulse duration is the key to unravelling the fastest processes observable within atoms, molecules or solids and enables reaching high electrical field strengths that can be used for particle acceleration, strong-field physics, extreme nonlinear optics and more. However, ultrashort pulse femtosecond lasers have in the past only been available with an average power of typically a few watts. In particular, laser-driven accelerators demand high laser repetition rates and thus much higher average power. In contrast to femtosecond lasers, industrial-scale picosecond lasers can nowadays easily generate several kilowatts of average power. A new method turns high-average power picosecond pulses into the femtosecond regime with very high efficiency.

The workhorse within ultrafast femtosecond laser technology was, and still is to some extent, the titanium-sapphire (Ti:sapphire) laser. While Ti:sapphire-based amplifiers can easily reach pulse durations below 30 fs, their average power is typically limited to a few watts. In contrast, ytterbium-based amplifiers are easily power-scalable into the kilowatt range, however, their output pulse duration is limited to a few 100 fs or even 1 ps. External spectral broadening methods employing fibres or waveguides followed by post-compression offer the possibility to combine ultrashort pulse durations and high repetition rates with millijoule-level pulse energies. A new spectral broadening technique, which relies on Herriott-type multi-pass cells [1,2] is currently expanding the limits of laser post-compression, offering high throughput, large compression ratios and excellent beam quality.

We have demonstrated multi-pass post-compression reaching the few-cycle regime directly driven with 1.2 ps pulses. Using a single multi-pass cell, we broadened and compressed 2 mJ pulses at 200 W in-burst average power down to 32 fs, followed by a second broadening and compression stage yielding 13 fs at a reduced pulse energy. These results demonstrate few-cycle pulse generation via direct post-compression of picosecond pulses for the first time, opening a route towards high average-power few-cycle laser sources driven by commercial kilowatt-class picosecond

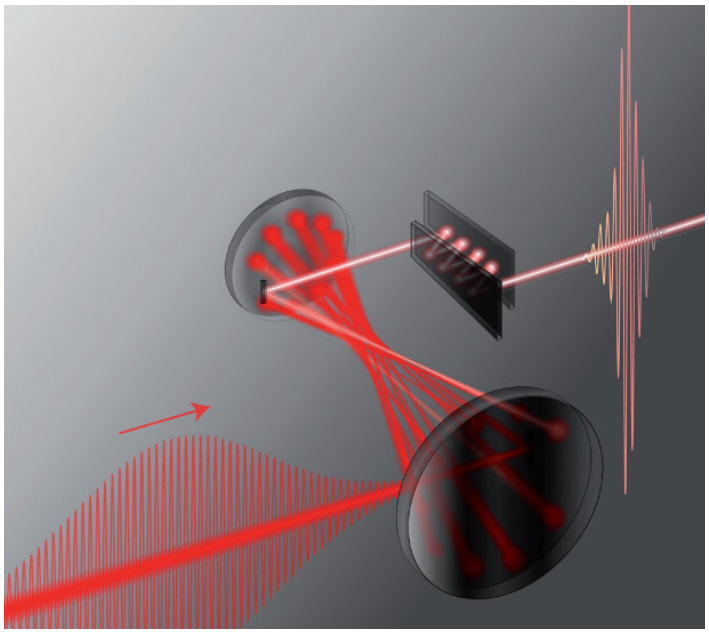

Figure 1

Illustration of laser pulse post-compression using a Herriott-type multi-pass cell: an intense laser pulse enters a gas-filled multi-pass cell undergoing spectral broadening via nonlinear self-phase modulation. Consecutively, chirped mirrors are used to compress the pulses in time reaching a compression ratio of about 40.

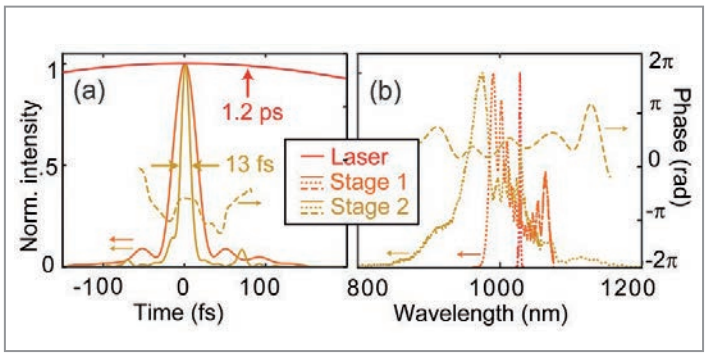

Figure 2

a) Reconstructed temporal pulse profile and (b) output spectra of laser and post-compression stage 1 and 2. The dashed lines indicate the reconstructed phase of the 13 fs pulse.

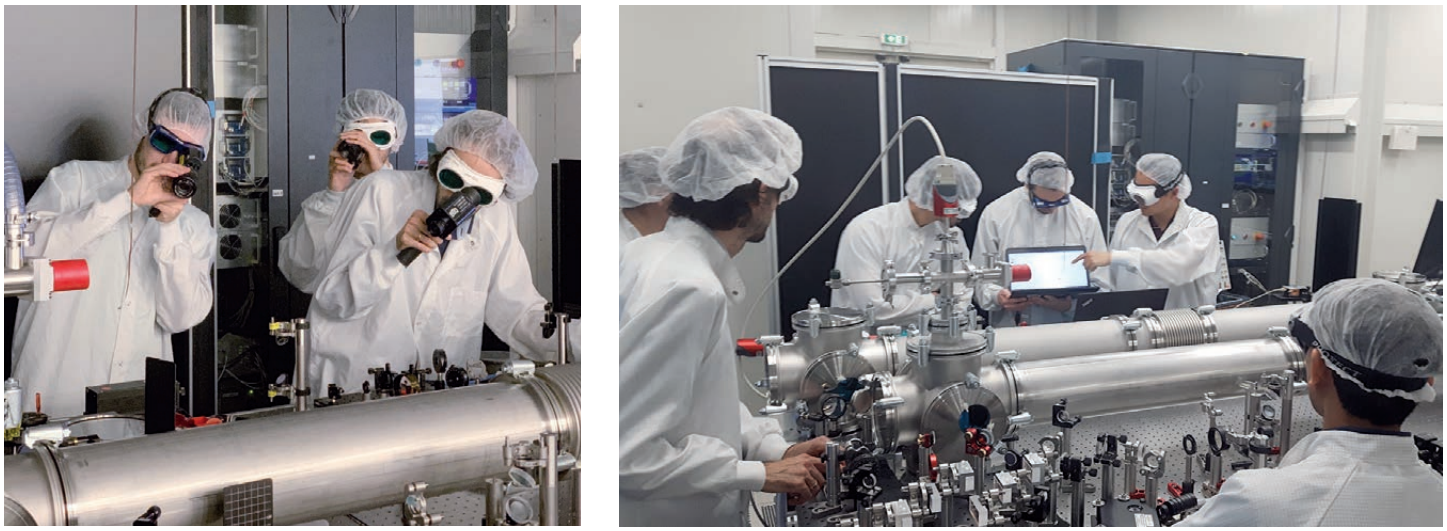

Figure 3

Work at the ongoing experiment in the FLASH2 laser hutch at DESY (end of 2019). Left: Experiment in progress: researchers equipped with infrared viewers control the alignment of the system. Right: Ongoing work at the experimental setup consisting of two gas-filled multi-pass cells placed inside two steel tube chambers.

lasers. Moreover, we pushed the single-stage compression factor to about 40 with more than 80% efficiency for millijoule-level post compression, surpassing latest records achieved using stretched hollow-core fibers [3] and multi-pass cells [4].

The experimental setup is shown schematically in Fig. 1. An intense laser pulse with 1.2 ps duration entered a multi-pass cell placed inside a chamber filled with krypton gas. The laser pulse underwent spectral broadening induced by nonlinear self-phase modulation. Afterwards, chirped mirrors were used to compress the pulses in time reaching a compression ratio of almost 40, yielding a pulse duration of 32 fs. Cascading this scheme by adding a second multi-pass cell allowed us to compress the pulses down to 13 fs, pushing the total compression factor to about 90. Experimental data are shown in Fig. 2 and a photograph of the experiment in Fig. 3.

As the demonstrated spectral broadening method is based on nonlinear pulse propagation in gases, the pulse energy is fully scalable [5] and limited mainly by the mirrors' damage thresholds. Ultimately, pulse energy up-scaling at a given mirror damage threshold leads to geometric scaling of the setup determining its size. Average power limitations are expected solely due to thermal effects on the mirrors and chamber windows, thus promising great prospects for average power scalability far into the kilowatt regime. Pump-probe laser systems based on the multi-pass post-compression method described here are currently being installed in the framework of ongoing FLASH2020+ upgrades at DESY [6]. Moreover, a further ultrashort pulse laser system using this method is currently being set up for plasma acceleration applications at DESY.

Author contact: Christoph M. Heyl, christoph.heyl@desy.de

References

1. J. Schulte, T. Sartorius, J. Weitenberg, A. Vernaleken and P. Russbueldt, 'Nonlinear pulse compression in a multi-pass cell', Opt. Lett. 41, 4511–4514 (2016).
2. M. Hanna, X. Délen, L. Lavenau, F. Guichard, Y. Zaouter, F. Druon and P. Georges, 'Nonlinear temporal compression in multipass cells: theory', J. Opt. Soc. Am. B 34, 1340–1347 (2017).
3. T. Nagy, S. Hädrich, P. Simon, A. Blumenstein, N. Walther, R. Klas, J. Buldt, H. Stark, S. Breitkopf, P. Jójárt, I. Seres, Z. Várallyay, T. Eidam and J. Limpert, 'Generation of three-cycle multi-millijoule laser pulses at 318 W average power', Optica 6, 1423–1424 (2019).
4. M. Kaumanns, V. Pervak, D. Kormin, V. Leshchenko, A. Kessel, M. Ueffing, Y. Chen and T. Nubbemeyer, 'Multipass spectral broadening of 18 mJ pulses compressible from 1.3 ps to 41 fs', Opt. Lett. 43, 5877–5880 (2018).
5. C. M. Heyl, H. Coudert-Alteirac, M. Miranda, M. Louisy, K. Kovacs, V. Tosa, E. Balogh, K. Varjú, A. L'Huillier, A. Couairon and C. L. Arnold, 'Scale-invariant nonlinear optics in gases', Optica 3, 75–81 (2016).
6. A.-L. Viotti, S. Alisauskas, A. Bin Wahid, P. Balla, N. Schirmela, B. Manschwetus, I. Hartl and C. M. Heyl, '60 fs, 1030 nm FEL pump-probe laser based on a multi-pass post-compressed Yb:YAG source', J. Synchrotron Rad. 28 (2021).

Original publication

'Postcompression of picosecond pulses into the few-cycle regime', Optics Letters 45, 2572–2575(2020). DOI: 10.1364/OL.388665

Prannay Balla[1,2,3], Ammar Bin Wahid[1], Ivan Sytcevich[4], Chen Guo[4], Anne-Lise Viotti[1,4], Laura Silletti[1,5], Andrea Cartella[6], Skirmantas Alisauskas[1], Hamed Tavakol[1], Uwe Grosse-Wortmann[1], Arthur Schönberg[1,2,3], Marcus Seidel[1], Andrea Trabattoni[1,5], Bastian Manschwetus[1], Tino Lang[1], Francesca Calegari[1,5,6,7], Arnaud Couairon[8], Anne L'Huillier[4], Cord L. Arnold[4], Ingmar Hartl[1] and Christoph M. Heyl[1,2,3]

1. Deutsches Elektronen-Synchrotron DESY, Hamburg, Germany
2. Helmholtz-Institute Jena, Jena, Germany
3. GSI Helmholtzzentrum für Schwerionenforschung GmbH, Darmstadt, Germany
4. Department of Physics, Lund University, Lund, Sweden
5. Center for Free-Electron Laser Science (CFEL), DESY, Hamburg, Germany
6. The Hamburg Centre for Ultrafast Imaging (CUI), Universität Hamburg, Hamburg, Germany
7. Institut für Experimentalphysik, Universität Hamburg, Hamburg, Germany
8. Centre de Physique Théorique, CNRS, Ecole Polytechnique, Institute Polytechnique de Paris, Palaiseau, France

Ultracompact 3D microfluidics for time-resolved structural biology

X-ray tomography confirms fast 'mix-and-inject' serial crystallography

Macromolecular serial crystallography has recently emerged as a new technique for structural biology. It has the ability to obtain room-temperature macromolecular structures from microcrystals in suspension, with short exposure times that allow brief snapshots of the macromolecular changes that occur during a reaction. The temporal precision of these time-resolved crystallography experiments depend on how fast and accurate reactions can be initiated. Using high resolution 3D printing, we created microfluidic structures with geometries which were not previously possible, to enable 'mix-and-inject' experiments with millisecond time resolution. The mixing speed and efficiency of our devices were confirmed by high-speed microscopy and *operando* X-ray tomography at the PETRA III beamline P05.

Serial crystallography was first introduced as a new approach to use the powerful yet destructive femtosecond pulses of X-ray free-electron lasers (FEL) [1]. Such pulses overcome the problem of radiation damage by the premise of 'diffraction before destruction', where the exposure is recorded before the effects of the ensuing vaporisation and explosion of the sample are seen at the atomic scale. Since the object is destroyed in this encounter, measurements must be carried out while microcrystals are constantly being replenished into the X-ray beam. Tens of thousands of single-pulse diffraction patterns of tiny crystals can then be recorded in a short time using a high frame-rate detector matched to the X-ray pulse scheme of the FEL. A particularly suitable way to feed fresh crystals into the X-ray beam is using a liquid microjet, formed by a process of flow focusing the crystals suspension with a nozzle. This depends upon robust microfluidic devices which enable continuous mix-and-inject measurements to capture structural kinetics of proteins in crystals while reacting with a particular reagent.

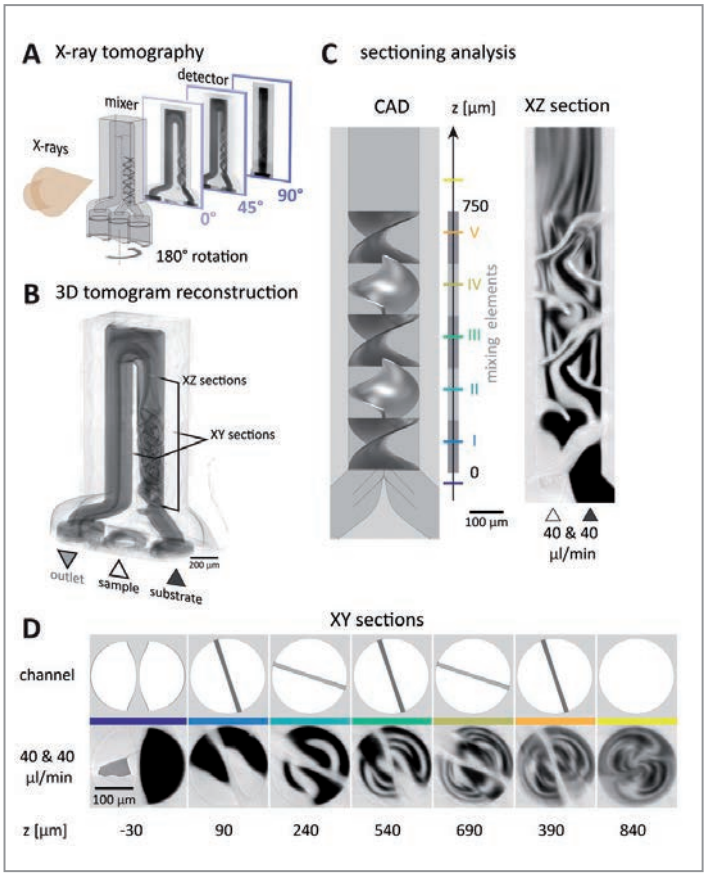

Time-resolved mix-and-inject serial crystallography [2] can be used to reveal the structural kinetics of macromolecules. This method helps us to understand their role in catalysis, long-range structural interaction pathways, induced fit and selectivity in ligand binding and allosteric control of conformational entropy. When a suspension of crystals is mixed with a solution containing a binding ligand, the ligand must diffuse throughout the crystal solution and into the crystal to initiate a reaction. The timescales for these steps are shorter for small crystals. To achieve millisecond time resolution, crystals smaller than about 3 µm width are needed. This is the timescale of many enzymatic reactions and allosteric transitions in proteins, as well as the timescale on which most pharmaceu-

Figure 1

Static 3D mixers for time-resolved mix-and-inject serial crystallography. A) X-ray microtomography was carried out while potassium iodide contrast agent flowed through the 3D-printed micromixer at a constant flow rate. B) This radiograph series was then reconstructed into a 3D X-ray tomogram. Sections of the 3D tomogram volume in C) vertical XZ slices and D) horizontal XY slices reveal quantitative liquid flow and mixing through the five mixing elements highlighted in the CAD drawing. The cross section through the mixer blade is shown in the top row of D).

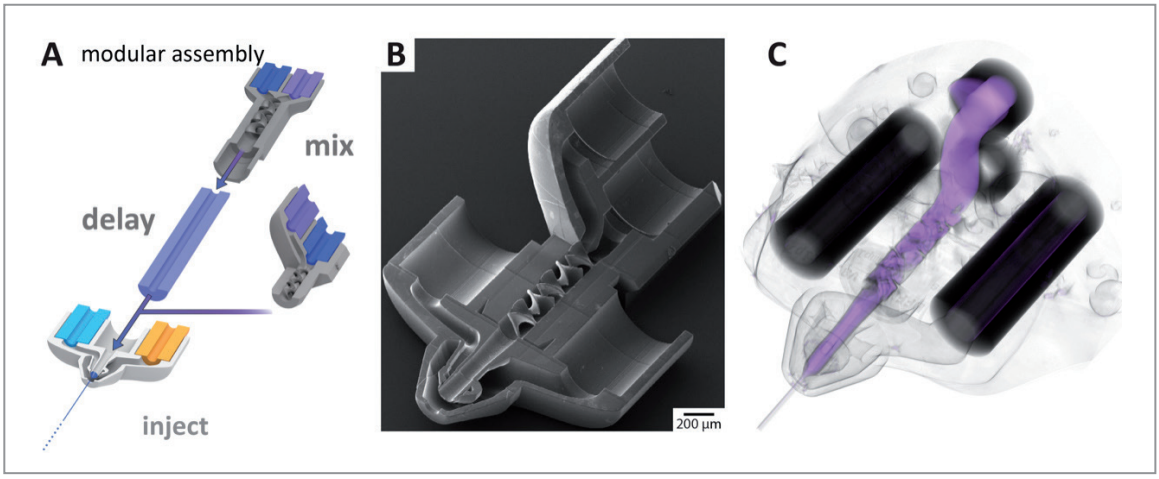

Figure 2
Modular mixer assembly. A) Reaction times are set by adjusting the delay time between reaction initiation and X-ray diffraction measurement. B) Scanning electron microscope image of a mixer directly inserted into a nozzle for a 3 ms time delay. C) Tomographic reconstruction of this 3D mixing-nozzle assembly.

tical compounds bind to biological macromolecules. Since serial crystallography builds up diffraction signals from many individual crystals — tens or hundreds of thousands of them — the weak diffraction from protein crystals of this size can be well measured, even without a FEL, at synchrotron radiation facilities such as PETRA III [3]. However, there are other constraints that limit the ability to achieve high-quality data at fast mixing times. For example, when the two solutions are brought together in a microfluidic T-junction, the laminar flow of the fluids leads to a slow and inefficient mixing that again is dictated by diffusion. Previous serial crystallographic mixing experiments could only realise a time precision on the order of a second, or required high dilution ratios and high flow rates of the fluids that wasted a lot of sample.

We vastly improved the microfluidic mixing speeds and efficiencies by including three-dimensional structures that stir or fold the fluids so that there is less travel needed for diffusive equilibration. Our mixer is a miniaturised adaptation of the static 'Kenics mixer', which consists of a series of five 180° turn helical elements that divide and rotate the flow alternately in clockwise and counterclockwise directions. The 150 µm long elements are stacked inside a 200 µm diameter channel as shown in Fig. 1. Unlike conventional 2D microfluidic chips that can be characterised in an optical fluorescence microscope, it is challenging to confirm the speed at which mixing occurs in our 3D devices. We solved this problem by using X-ray microtomography at the PETRA III beamline P05. Water (white in the tomogram, low X-ray absorption) was mixed with aqueous potassium iodide (KI) as contrast agent (black in the tomogram, high X-ray absorption), while recording a radiographic rotation series at a resolution of 1.1 µm at a photon energy of 11 keV. The mixing efficiency can be tracked directly and quantitatively in the tomograms from the KI density. Depending on the flow rates and concentration of the reagent, a mixing time as low as 10 ms could be achieved.

A time-resolved experiment has been performed by measuring diffraction patterns at various delay times after the mixing. The X-ray beam intersected the crystals in a free jet formed by a micro nozzle. This nozzle, too, was made by super-resolution two-photon polymerisation 3D printing and our modular design allowed the mixer to be fixed directly to the nozzle or with delay lines (capillaries) mounted in between. The modular design is shown in Fig. 2. We recorded X-ray tomograms of the device for the shortest delay which was found to be 3 ms.

Our microfluidic devices have been used in a number of serial crystallography experiments at LCLS, PETRA III, ESRF and the European XFEL. The 3D printing offers an unrivalled fabrication precision to create jets that exceed 100 m/s as needed when measuring with megahertz pulse trains at the European XFEL [4]. This system enables new time-resolved experiments to elucidate mechanisms of antibiotic resistance and drug binding.

Author contact: Juraj Knoška, juraj.knoska@desy.de
Michael Heymann, michael.heymann@bio.uni-stuttgart.de

References

1. H. N. Chapman et al., 'Femtosecond X-ray protein nanocrystallography', Nature, 470, 73–77 (2011).
2. M. Schmidt, 'Mix and inject: reaction initiation by diffusion for time-resolved macromolecular crystallography', Adv. Cond. Matt. Phys. 10, 167276 (2013).
3. K. Beyerlein et al., 'Mix-and-diffuse serial synchrotron crystallography', IUCrJ 4, 769–777 (2017).
4. M. Wiedorn et al., 'Megahertz serial crystallography', Nat. Commun. 9, 4025 (2018).

Original publication

'Ultracompact 3d microfluidics for time-resolved structural biology', Nature Communications 11, 657 (2020). DOI: 10.1038/s41467-020-14434-6

J. Knoška[1,2], L. Adriano[3], S. Awel[1,4], K. R. Beyerlein[1], O. Yefanov[1], D. Oberthuer[1], G. E. Peña Murillo[1,2], N. Roth[1,2], I. Sarrou[1], P. Villanueva-Perez[1], M. O. Wiedorn[1,2], F. Wilde[5], S. Bajt[3], H. N. Chapman[1,2,4] and M. Heymann[1,6]

1. Center for Free-Electron Laser Science (CFEL), DESY, Hamburg, Germany
2. Department of Physics, Universität Hamburg, Hamburg, Germany
3. Deutsches Elektronen-Synchrotron DESY, Hamburg, Germany
4. Center for Ultrafast Imaging (CUI), Universität Hamburg, Hamburg, Germany
5. Helmholtz-Zentrum Geesthacht (HZG), Institut für Werkstoffforschung, Geesthacht, Germany
6. Institut für Biomaterialien und Biomolekulare Systeme (IBBS), Universität Stuttgart, Stuttgart, Germany

Sub-cycle pulse synthesis for attosecond science

Creation of intense tailored waveforms lasting less than one optical cycle

The generation of ultrashort and intense laser pulses is a major quest in contemporary laser science. Especially intriguing are pulses with tailored light-field oscillations and durations below one single optical cycle ('sub-cycle waveforms'), as they allow driving an isolated event of strong-field light–matter interaction. For instance, the process of high-harmonic generation driven by such sub-cycle waveforms can produce single pulses up to the soft X-ray range with pulse durations of attoseconds. The ultra-broad optical bandwidth and energy required to create such intense sub-cycle waveforms can be achieved via combination of different optical parametric amplifiers. This novel technology allows unprecedented control of the generated attosecond pulses and higher brightness, which is a major advantage for future attosecond science experiments.

Tailored sub-cycle optical waveforms allow studying and controlling light–matter interactions in the strong-field regime with remarkable degrees of freedom. In such interactions, the trajectories of the driven charges are determined by the exact evolution of the optical waveform. The coherent combination among pulses emerging from different optical parametric amplifiers allows shaping the synthesised waveforms by controlling the carrier-envelope phase and relative phase while achieving excellent shot-to-shot stability.

In our synthesiser setup (Fig. 1), the optical parametric amplifiers (OPAs) are pumped by a Ti:Sapphire laser system with 20 mJ pulse energy at 1 kHz repetition rate. We prepare broadband and carrier-envelope phase-stable seed pulses in

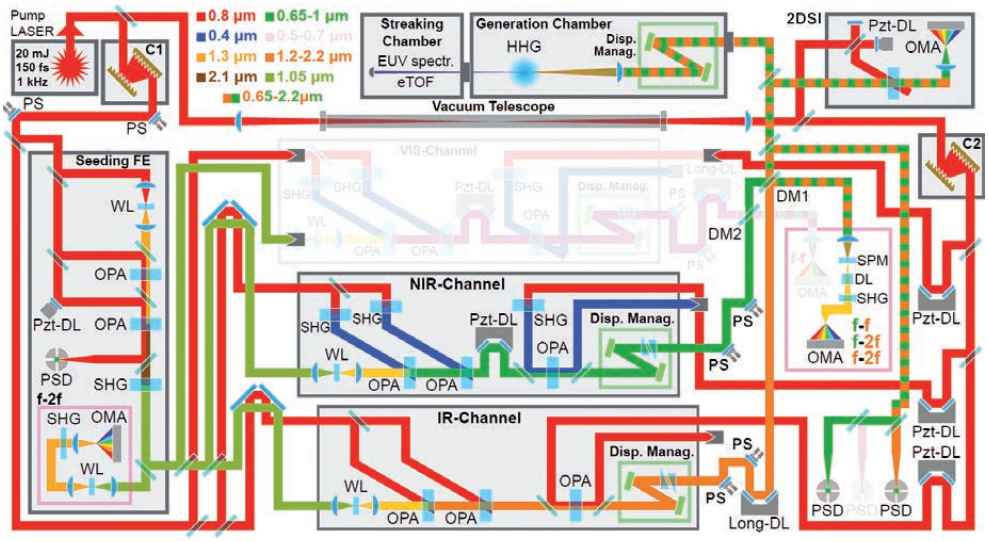

Figure 1

Schematic of the parametric waveform synthesiser. A Ti:Sapphire laser (top left) is used as pump laser for the system. First a CEP-stable seed is prepared in the seeding front end, which then undergoes spectral broadening via white-light generation. This broadband seed is amplified in the different spectral channels (VIS, NIR, IR) and coherently combined afterwards. At this synthesis point, a multi-phase meter is measuring the phase parameters and actively stabilises the synthesised waveform by moving appropriate actuators. The main output is then directed to our attosecond beamline to perform experiments.

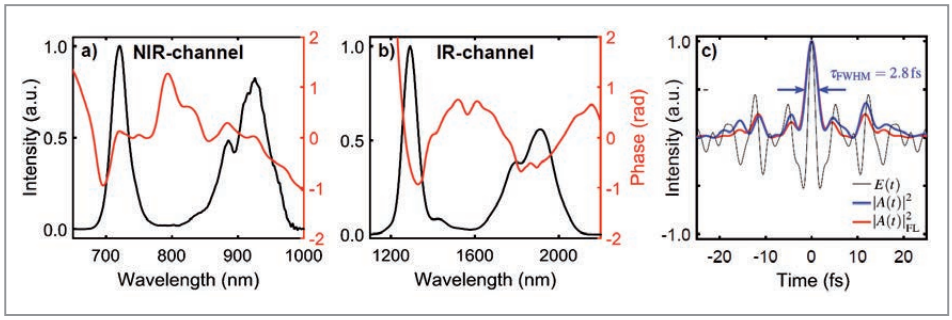

Figure 2

(a,b) Spectral intensity (black) and spectral phases (red) of the NIR and IR channel. The phases were measured via two-dimensional spectral shearing interferometry. Both spectral channels generate already few-cycle pulses with 6 fs and 8 fs, respectively. (c) If these pulses are coherently combined, optical transients with durations of down to 2.8 fs FWHM (0.6 optical cycles) are generated.

our seeding front end by employing several optical techniques. Those weak but ultra-broadband pulses are amplified in the different spectral channels of our setup.

In these spectral channels, broadband OPAs were used in a 3-stage amplification chain to raise the initial seed-pulse energies up to hundreds of microjoule. Currently, we are operating an infrared (IR) spectral channel (600 µJ, 1.2–2.2 µm, 8 fs) and a near infrared (NIR) spectral channel (150 µJ, 650–1000 nm, 6 fs, see Fig. 2a,b). After amplification, these pulses are coherently combined to synthesise the output pulse. A multi-phase detection system tracks the carrier-envelope phase (CEP) and the relative phase which are the most crucial synthesis parameters. The stabilisation and control of those synthesis parameters is performed by a high-speed feedback system driving various delay lines within our system. The synthesised waveform, whose spectrum spans from 650 to 2200 nm, can be set to be as short as 2.8 fs corresponding to just 0.6 optical cycles at 1.4 µm centre wavelength (see Fig. 2c). The synthesised pulses are guided to our attosecond beamline to drive high-harmonic generation (HHG) in a gas cell.

With suitable synthesis settings, we can generate broadband as well as tuneable narrowband isolated attosecond pulses. With such isolated attosecond pulses we can measure the evolution of the sub-cycle optical field (Fig. 3) by means of attosecond streaking.

The ability to perform attosecond streaking proves the remarkable pulse-to-pulse stability of the synthesised sub-cycle transients. After implementing a high-pressure HHG gas cell, this source will be primarily used to produce intense attosecond pulses in the spectral range of the so-called water window (282–533 eV). The central wavelength of 1.4 µm is a sweet spot for generating water-window radiation balancing out the photon cut-off energy and conversion efficiency. With the unique ability to customise the waveform and generate non-sinusoidal field evolutions, we expect an additional significant increase in the HHG conversion efficiency. Soon, the system will be further extended with a third spectral channel in the visible (500–700 nm, ~ 150 µJ) to yield even higher customisability of the waveform.

These intense and tailored attosecond pulses in the water window will be used in conjunction with a synthesised pulse replica or a secondary attosecond pulse to perform truly attosecond resolved pump-probe experiments. Recently, for instance the radiolysis of water was studied using free-electron laser (FEL) pulses with ~ 100 fs temporal resolution [2]. The FEL pulses were too long to sufficiently resolve the dynamics of this reaction. However, precisely tuned attosecond pulses from our synthesiser are able to resolve them. In an initial experiment, we intend to use a thin sheet of water [3] as target sample and the synthesised sub-cycle pulses to precisely observe the temporal dynamics during radiolysis, when a water molecule yields a proton to the H_2O^+ cation from neighbouring molecules.

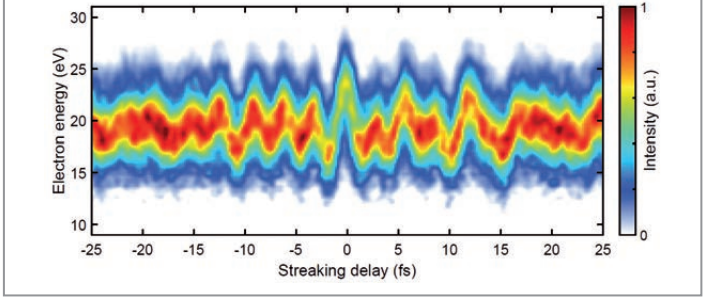

Figure 3

By means of attosecond streaking the synthesised optical pulse can be measured directly in the time domain. A generated attosecond pulse is used to instantly release electrons from a thin gas while being superimposed with a delayed replica of the synthesised pulse. The kinetic energy of the generated photoelectrons is modulated depending on the time delay between the release and the arrival of the pulse replica.

These novel pulses have the potential to also break new ground in other fields, ranging from chemical bond making to the generation, acceleration and manipulation of charged particle beams. Additionally, the demonstrated scheme of passive CEP stability exploited in the seeding front end, parallel synthesis based on multi-stage parametric amplifiers and the implemented attosecond synchronisation scheme proves that this technology can produce stable and well-controlled sub-cycle pulses. The underlying parametric technology easily allows further scaling of these sources: in bandwidth by the addition of another spectral channel, in pulse energy by adding additional amplification stages and, moreover, in repetition rate, as the system does not show significant heat-up. Different laser technologies can be adapted to pump the OPAs, such as novel Yb-based high-power laser sources that could potentially even allow increasing the intensity of these sub-cycle-tailored waveforms to make them even useful for laser driven wakefield acceleration.

Author contact: Roland E. Mainz, roland.mainz@desy.de

References

1. P. D. Keathley et al., 'Volkov transform generalized projection algorithm for attosecond pulse characterization', New J. Phys. 18, 073009 (2016).
2. Z.-H. Loh et al., 'Observation of the fastest chemical processes in the radiolysis of water', Science 367, 179–182 (2020).
3. J. D. Koralek et al., 'Generation and characterization of ultrathin free-flowing liquid sheets', Nat. Commun. 9, 1353 (2018).

Original publication

'Sub-cycle millijoule-level parametric waveform synthesizer for attosecond science', Nature Photonics 14, 629–635 (2020), DOI: 10.1038/s41566-020-0659-0

Giulio Maria Rossi[1,2], Roland E. Mainz[1,2], Yudong Yang[1,2], Fabian Scheiba[1,2], Miguel A. Silva-Toledo[1,2], Shih-Hsuan Chia[1,2], Phillip D. Keathley[3], Shaobo Fang[1,2], Oliver D. Mücke[1,2], Cristian Manzoni[4], Giulio Cerullo[4], Giovanni Cirmi[1,2] and Franz X. Kärtner[1,2]

1. Center for Free-Electron Laser Science (CFEL), DESY, Hamburg, Germany
2. Physics Department and The Hamburg Centre for Ultrafast Imaging (CUI), Universität Hamburg, Hamburg, Germany
3. Research Laboratory of Electronics, Massachusetts Institute of Technology, Cambridge, MA, USA
4. IFN-CNR, Dipartimento di Fisica, Politecnico di Milano, Milan, Italy

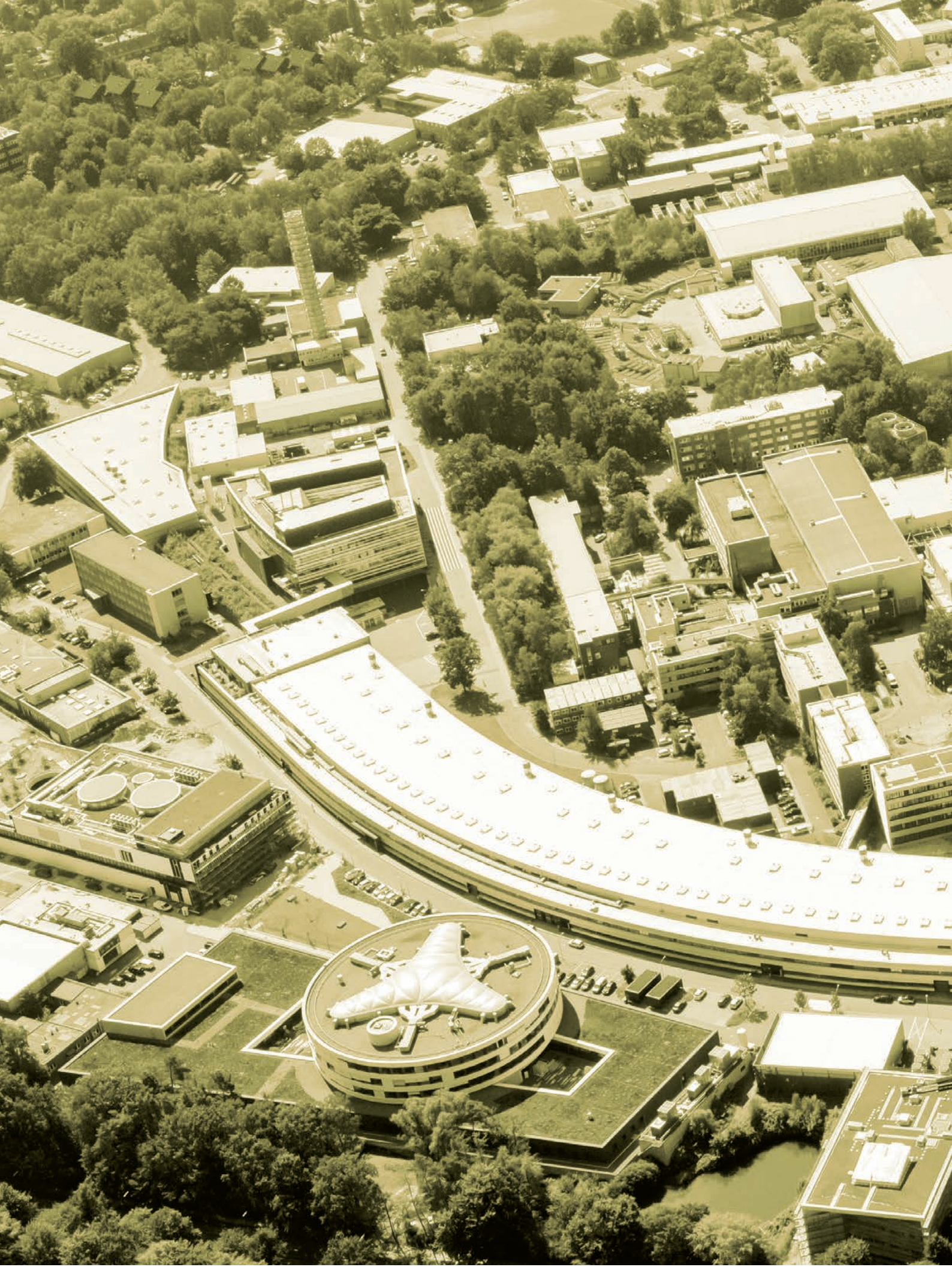

Light Sources

FLASH

Keeping the pace in challenging times

Figure 1

Measurements at the FLASH beamline PG2 with users from abroad participating via video conference during the Covid-19 pandemic.

User operation under Covid-19 boundary conditions

In the first half of 2020, we were able to successfully finish 'User Block 1', which was directly followed by the Covid-19-related lockdowns forcing us to stop FLASH operation and cancel the remaining User Blocks 2 and 3. While we originally planned for about 4600 hours of user beamtime in six 'User Blocks', this reduced it to a bit more than 3000 hours in 4 blocks in 2020.

After having established all necessary measures for safely and efficiently running experiments at FLASH during the pandemic (Fig. 1), we were — with the improving situation – able to restart user operation in the beginning of August and to continue with User Blocks 4 to 6 up to the end of the year. Despite the worldwide challenging situation due to the pandemic, we managed to successfully and safely conduct a total of 19 user experiments in 2020, while we had to postpone another 17 experiments, i.e. almost half a year of user beamtimes, to 2021.

Notwithstanding all the Corona-related restrictions, the user feedback from the second half of 2020 was very positive. FLASH was running very reliably, and due to the new weekly schedule, where each experiment is conducted five or six days in a row, the experiments could continuously take data with very few interruptions. Hence, they all ended up with good data statistics and very satisfied users and local teams. At the time of writing, 27 publications were already published in 2020, with three further papers in press and a long list of submitted manuscripts where we are looking forward to their publication in 2021.

Assuming that the pandemic situation improves in 2021 and that FLASH experiments with core teams from abroad can then be performed as well, we hope to be able to complete the postponed 17 plus 15 new experiments from the most recent review (deadline 1 April 2020) in 2021.

Two FLASH calls for proposals with deadlines on 1 October 2020 and 1 April 2021, have been cancelled. The first one was cancelled due to Covid-19 and the many postponed experiments, the second one due to the first shutdown of our FLASH2020+ upgrade program. The start of this major (~ 9 months) shutdown for FLASH2020+ was shifted from July to mid November 2021. This provides sufficient time for all postponed and recently approved experiments and also accounts for delays in the technical preparation of this shutdown.

New pump probe laser system for the FLASH1 beamlines PG1 and PG2

Most of the experiments performed at FLASH are pump-probe experiments where often the dynamic temporal evolution of a sample is studied. Typically, a femtosecond laser in the UV to NIR spectral region is used to excite the reaction. For this purpose, a pulse train laser system matched to the pulse structure of FLASH has been in operation in the FLASH1 experimental hall 'Albert Einstein' since 2005. This system has slowly been reaching the end of its life, and in

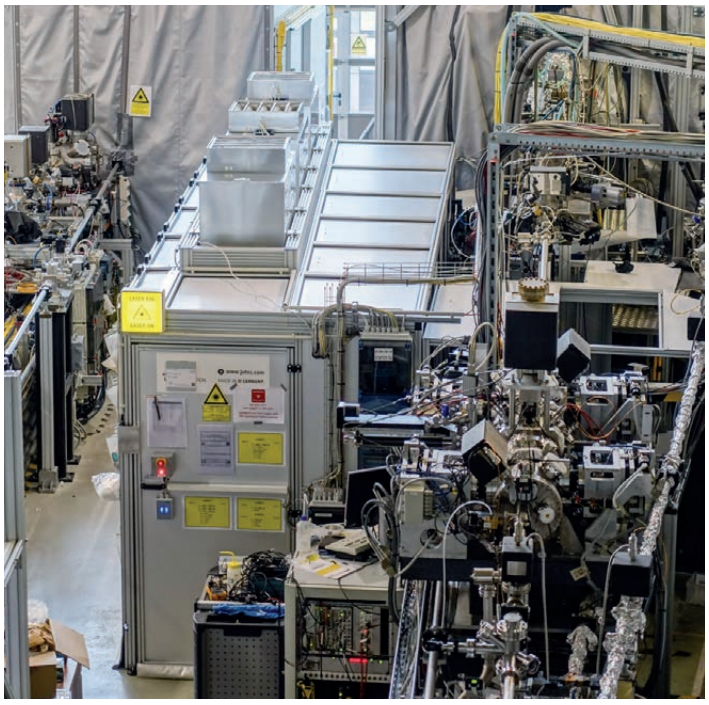

Figure 2

Hutch for the new pulse train laser (in the centre), with the FLASH1 beamlines PG2 at right and (in the background) the experimental hutches for BL1 (CAMP) at left and PG2 at right. On the roof of the laser hutch, laminar flow boxes with fine particle filters are mounted which blow filtered air onto the laser table inside.

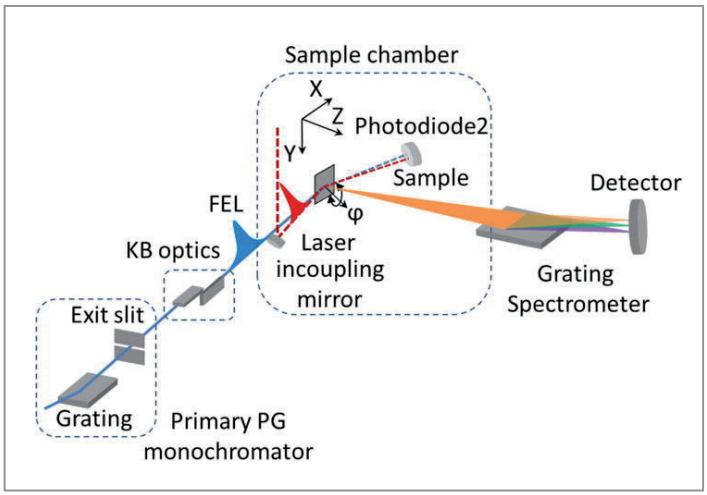

Figure 3

Schematic overview of the TRIXS end station including the monochromator beamline PG1 and its focusing optics. The grating spectrometer is sketched omitting its focusing optics.

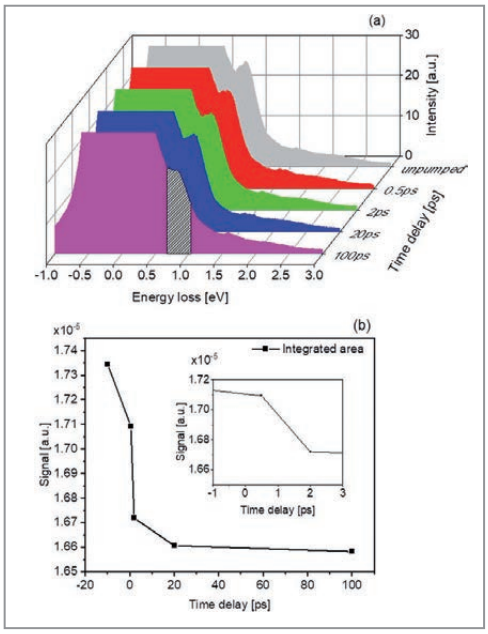

Figure 4

Time-resolved Co M-edge RIXS spectrum of cobalt oxide pumped at 400 nm (a), and the evolution of the d-d excitation peak integrated over the shaded area (b). The inset in (b) demonstrates the sub-picosecond dynamics of the d-d excitation upon optical pumping.

October 2020 it was replaced with a new laser system developed by the DESY laser group FS-LA (Fig. 2).

The new laser system provides a 1 MHz train of 75 fs, 20 µJ pulses during 800 µs bursts at 10 Hz burst repetition frequency from a spectrally broadened Yb:fiber / Yb:YAG amplifier chain. Its central wavelength is 1030 nm. This laser system has recently been commissioned and is now available for experiments with the FEL at the plane-grating monochromator beamlines PG1 and PG2 at FLASH. For laser–FEL pump–probe experiments excellent timing is required. Therefore, the laser system is stabilised to the facility-wide pulsed-timing system via a balanced cross-correlator. In addition, group-delay drifts in the amplifier chain and at the spectral broadening stage are corrected.

The old pulse train laser system, which beside PG1 and PG2 served the beamlines BL1–3 as well, will be decommissioned in winter 2020/21. Hence, only the 10 Hz single pulse laser system can be provided for experiments at beamlines BL1 and BL3 in the next years. Note that, due to the reduced demand and in view of the FLASH2020+ upgrades, beamline BL2 has been decommissioned in autumn 2020 and is being disassembled as well. Removing it will also provide space for further state-of-the-art laser installations.

TRIXS – the end station for time-resolved RIXS studies at PG1

Resonant inelastic X-ray scattering (RIXS) is a powerful spectroscopic technique which is very well suited to study a vast variety of elementary excitations, such as plasmons and magnons in strongly correlated systems like transition metal oxide complexes or rare-earth element compounds, and and RIXS, for example, also allows one to study charge transfer processes in bio-inorganic molecules with a metal centre. Therefore, we have recently upgraded our RIXS end station at the PG1 beamline for femtosecond time-resolved RIXS (TRIXS) experiments. Using monochromatised, ultrashort femtosecond soft X-ray photon pulses in combination with the synchronised optical laser pulses in a pump–probe scheme, the TRIXS end station allows one to measure almost transform limited, high-resolution RIXS spectra with sub-picosecond (< 250 fs) time-resolution on solid samples [1]. The instrument (Fig. 3) covers the energy range from 35 eV to 210 eV with an energy resolution of 35–160 meV over the entire spectral range. In the course of the last year, several time-resolved RIXS experiments have been successfully performed at TRIXS and demonstrated sub-picosecond dynamics of the elemental excitations of interest, for instance on cobalt oxide (Fig. 4). The high repetition rate of FLASH (up to 5000 pulses/second), in combination with the high intensity per pulse at the sample and an optimised spectrometer throughput permits the acquisition of highly-resolved RIXS spectra with sufficient signal levels to enable time-resolved studies within a few hours per spectrum. In order to extend the capabilities of the end station, a new experimental sample chamber has been designed and will be installed in 2021. The new chamber will then allow to not only perform RIXS but also X-ray absorption and X-ray reflectivity measurements, with sample cooling capabilities down to 20 K.

One year of THz streaking at FL21

In the FLASH2 experimental hall ‘Kai Siegbahn’, the special photon diagnostic beamline FL21, meant to establish novel diagnostic tools, has meanwhile been in operation for more than a year. The beamline consists of two branches that can be operated simultaneously. Utilising a ‘cutting mirror’, partially inserted into the beamline, part of the beam can be reflected to a dedicated XUV pulse length measurement setup, while the remaining part of the beam can be used at an open-port beamline end. Here the commissioning and development of new photon diagnostic devices, such as wavefront sensors and pulse energy metres, takes place. In 2021, this open-port branch will be upgraded with the focusing ellipsoidal mirror formerly used at beamline BL2, delivering a 20 µm focal spot.

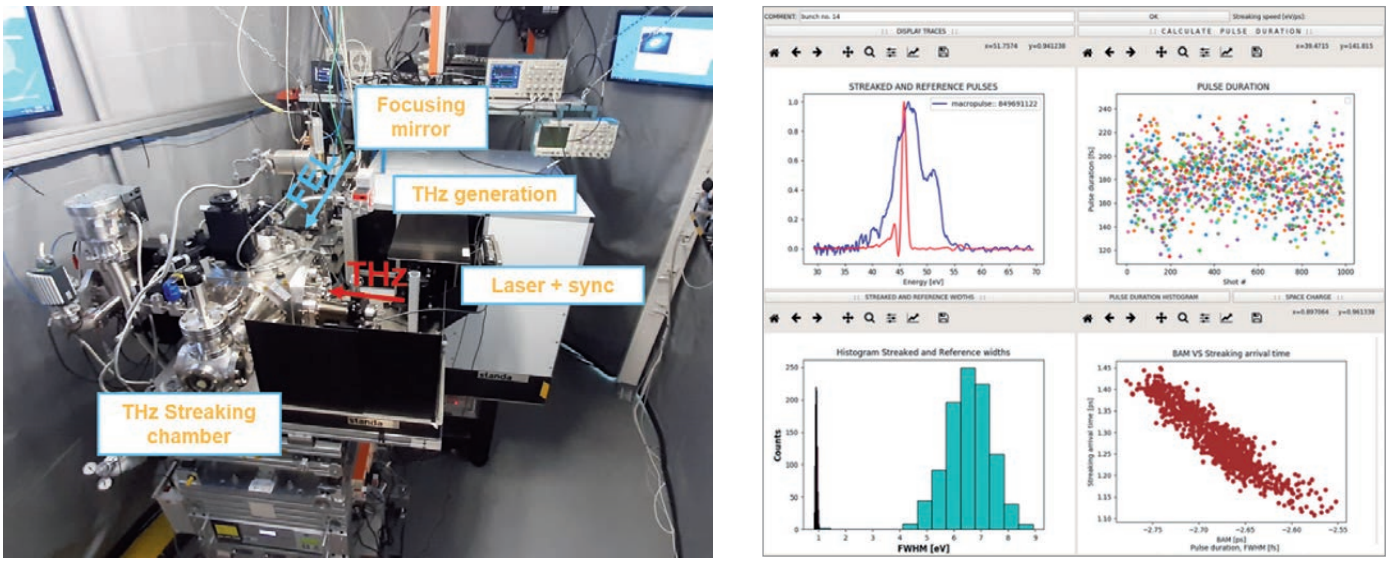

Figure 5

View into the THz-streaking lab, containing the optical laser, the THz production as well as the interaction chamber. The picture on the right shows an example of the online data analysis.

In the second branch, a laser-based THz streaking setup [2] is located (Fig. 5), consisting of a permanently installed interaction chamber and a dedicated laser system, which was built by the group of F. Kärtner from DESY-CFEL. In more than a year of operation (together with experience gained at FLASH1), a wide range of different FEL parameters, with pulse durations ranging from very short (~ 10 fs) to rather long (350 fs) XUV pulses at various wavelengths has been studied. Along with that, the main sources of measurement uncertainties have been determined and all that has been summarised in a recent publication [3]. In addition, a large amount of pulse-resolved data for the different operation points of the FEL were collected, allowing studies of correlations between different parameters such as pulse duration, spectral distribution, arrival time and pulse energy of SASE XUV pulses. With the aid of simulations, one can derive scaling laws for the fluctuations of these parameters and disentangle the statistical SASE fluctuations from accelerator-based parameter fluctuations and measurement uncertainties. This detailed understanding of the presence or absence of correlations between different pulse parameters is important for the analysis of experimental data to avoid spurious correlations in the data [4]. A python-based online analysis of the recorded spectra has been developed as well. Besides the study of the SASE process and further development of THz streaking techniques, the setup is used to determine the XUV pulse duration delivered for user experiments at FLASH2.

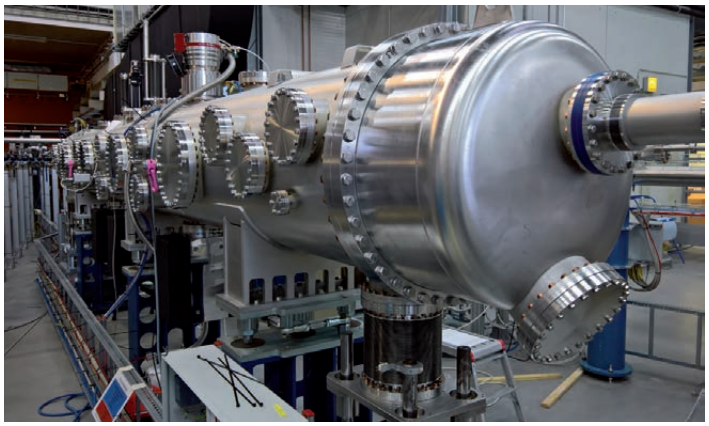

Figure 6

The split-and-delay unit in the FLASH2 experimental hall 'Kai Siegbahn'. The vacuum vessel with its total length of about 7m is located at the beginning of the FL24 branch, close to the main laser hutch in the background.

New split-and-delay unit at FL24

A new 'split-and-delay unit' (SDU) has been successfully installed (Fig. 6) and commissioned at FLASH2. The SDU has been funded as a collaborative research project by the German Federal Ministry of Education and Research (BMBF), and its design and realisation has been led by the University of Münster (Helmut Zacharias et al.) [5].

The SDU covers the entire photon energy range of FLASH, including harmonics, up to 1500 eV and allows X-ray pump–X-ray probe experiments at beamline FL24 as well as at the adjacent future monochromator beamline FL23. The setup relies on wavefront beam splitting at grazing incidence angles. To optimise transmission over the wide spectral range, two different beam paths with different mirror coatings have been realised (Fig. 7 bottom). Ni-coated mirrors provide a total transmission between T = 79% at 30 eV, and T = 30% at 800 eV, while Pt-coated mirrors in the other beam path offer for the higher photon energies a total transmission between T = 19% at 800 eV and T = 13% at 1500 eV.

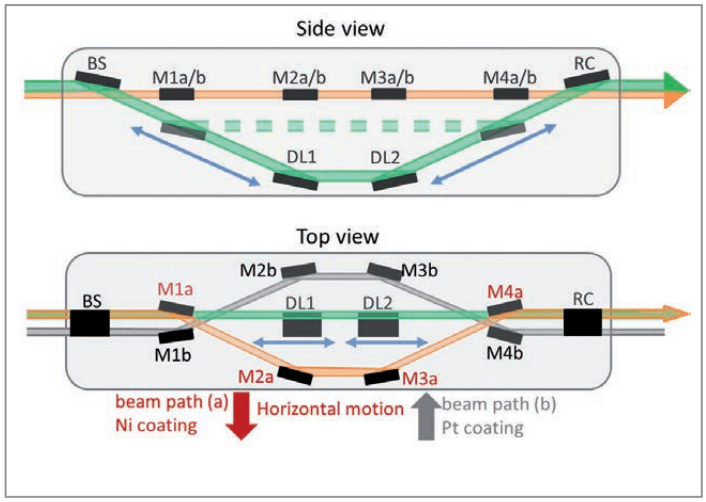

Figure 7

Basic principle of the split-and-delay unit. The beamsplitter (BS) splits the beam geometrically into two parts, both directed in different paths (green, orange). The part reflected to the bottom (green) can be delayed by moving the mirrors DL1 and DL2 along the beam path direction. Recombination of the two partial beams occurs at the recombining mirror (RC) at the end of the SDU. Mirror sets with different reflective coatings can be selected by just translating the optical bench inside the SDU horizontally to the position of the respective beam path (orange or grey).

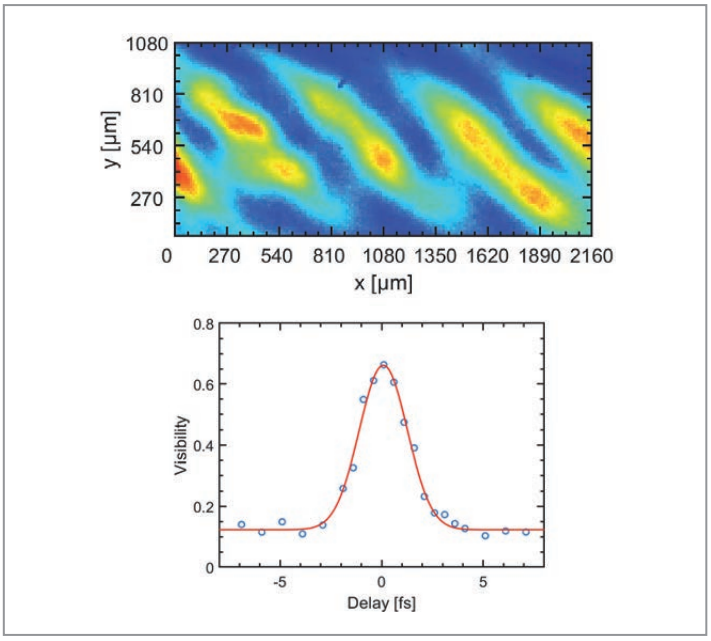

Figure 8

(top) Interference fringes obtained by crossing both partial beams with zero delay at a wavelength of 10 nm. (bottom) Temporal coherence at 10 nm. The visibility measurement at 10 nm indicates a coherence time of 1.4 fs (HWHM).

A temporal delay is achieved by moving both interferometrically controlled mirrors DL1 and DL2 along the beam path. The accessible delay ranges from –5 ps up to 18 ps with sub-femtosecond jitter and resolution. Therefore, X-ray pump–X-ray probe experiments even with shortest pulses available at FLASH2 can be carried out basically jitter-free to achieve an optimum temporal resolution. In addition, a non-invasive partial beam intensity monitoring device as well as filter stages with Zr and Pd-filters have been implemented.

During the commissioning, while establishing the zero delay position, longitudinal coherence measurements of FLASH2 have been taken in the wavelength range from 4.5 nm up to 48 nm. They yield for instance a temporal coherence of 1.4 fs (HWHM) at 10 nm (Fig. 8).

The future of FLASH – status of the FLASH2020+ upgrade project

Within the FLASH2020+ upgrade project, substantial improvements to the photon beam quality are planned and ongoing, as highly requested by the user community. FLASH2020+ was initiated and coordinated by Wilfried Wurth, the scientific head of FLASH, until his sudden death in 2019. The conceptual design report (CDR) [6], which was published at the beginning of 2020, is dedicated to his memory.

In July 2020, Enrico Allaria, who had coordinated the development of the seeded FERMI FEL at Elettra in Trieste (Italy), joined DESY as the leader of the FLASH2020+ project. Along with his start, the project went into the technical design phase, accompanied by first hardware implementations. Individual work packages have been defined and organisational structures established. In 2021, the technical design report (TDR) will be compiled, while at the same time the first major shutdown is prepared for end of the year. In this first shutdown, it is planned to replace two old accelerator modules by new ones, reaching higher gradients. That way, the maximum machine energy will be raised from 1.25 GeV to about 1.35 GeV. In parallel, the installation of an APPLE III undulator as 'afterburner' at FLASH2 will take place, enabling us to generate FEL radiation with variable, in particular circular polarisation, well suited for magnetic studies, e.g. at the L-edges of Fe, Co and Ni.

Furthermore, a 'transverse deflecting structure' (TDS) will be installed this winter (2020/21) in the FLASH2 electron beamline to allow a precise determination of the electron bunch length with a resolution of 5 fs.

A second major shutdown, currently anticipated for 2024, will then focus on the FLASH1 FEL line and is foreseen to implement high repetition rate external seeding with APPLE III undulators providing also here variable gap and polarisation. The FLASH2020+ upgrade project will make FLASH brighter, faster and more flexible.

Contact: Rolf Treusch, rolf.treusch@desy.de

References

1. S. Dziarzhytski et al., 'The TRIXS end-station for femtosecond time-resolved resonant inelastic x-ray scattering experiments at the soft x-ray free-electron laser FLASH', Struct. Dyn. 7, 054301 (2020).
2. R. Ivanov et al., 'FLASH free-electron laser single-shot temporal diagnostic: terahertz-field-driven streaking', J. Synchrotron Rad. 25, 26–31 (2018).
3. R. Ivanov et al., 'Single-shot temporal characterization of XUV pulses with duration from ~10 fs to ~350 fs at FLASH', J. Phys. B 53, 184004 (2020).
4. I. Bermudez et al., 'Study of temporal, spectral, arrival time and energy fluctuations of SASE FEL pulses', submitted (2020).
5. S. Roling, M. Rollnik, M. Kuhlmann, E. Plönjes, F. Wahlert and H. Zacharias, 'A soft x-ray split-and-delay unit for FLASH II, Proc. SPIE 10237, 1023712 (2017).
6. 'FLASH2020+ Conceptual Design Report' (CDR), DESY (2020), DOI: 10.3204/PUBDB-2020-00465.

PETRA III

Successful operation, new installations and the upgrade project PETRA IV

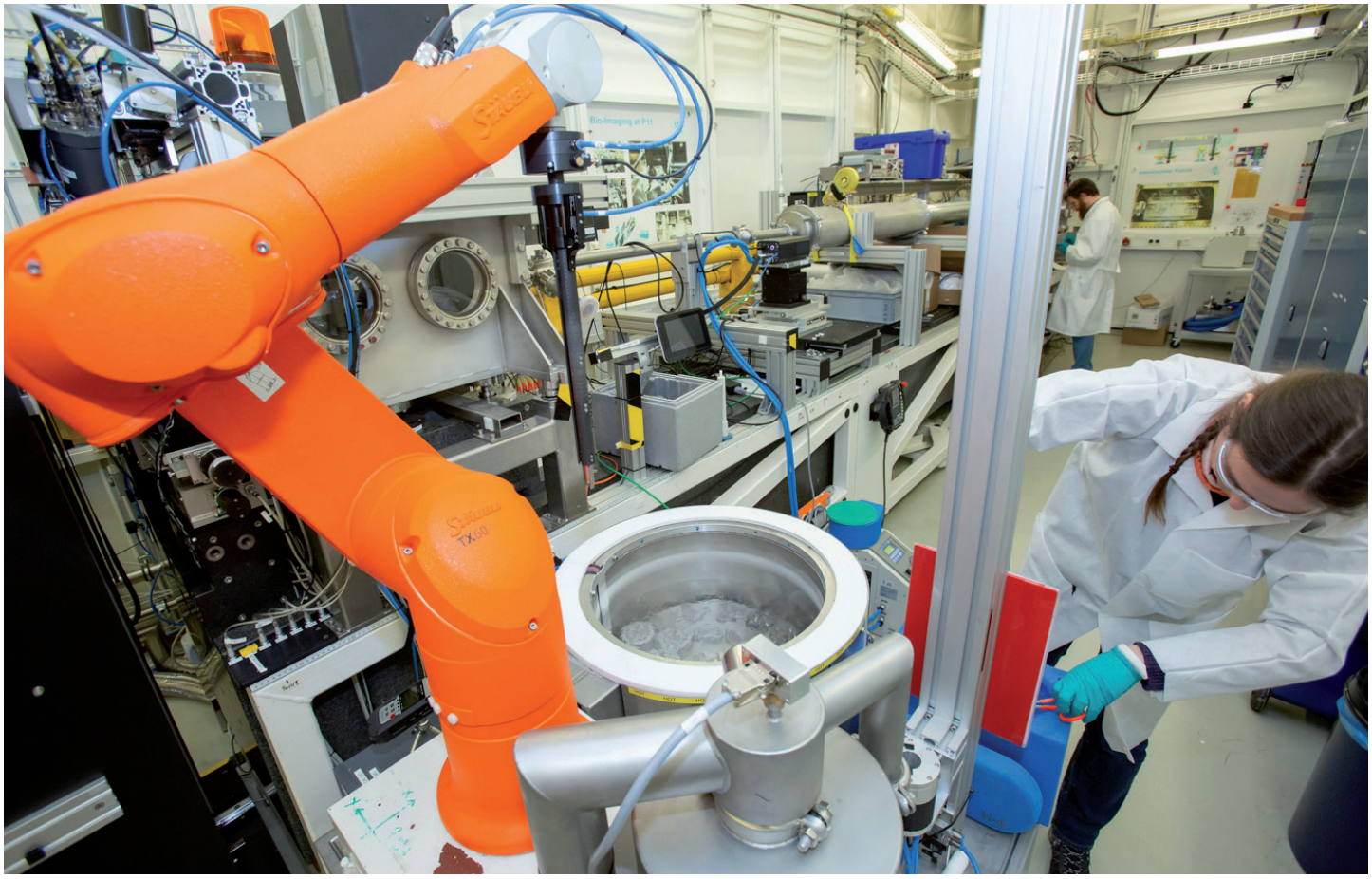

Figure 1

Corona-related research at the PETRA III beamline P11. Final preparations of involved scientists in the experiment hutch: the robot arm (in orange) will later automatically grab a sample from the liquid nitrogen tank (in the foreground) for the measurement series in the X-ray beam.

During the year 2020 the operation of PETRA III for users and the construction of beamlines were strongly affected by the worldwide SARS-CoV-2 pandemic. It is remarkable that PETRA III was operated almost as originally planned with only a few adaptations to the schedule in spring. However, the execution of experiments was strongly influenced by national regulations and travel restrictions which made it difficult to prepare samples in the users' home institutions or to travel to DESY. Nearly 2000 individual users performed experiments at PETRA III beamlines, roughly 30% less than in recent years. The reduction was also necessary due to a limitation of persons allowed on-site.

As usual, the operation time of PETRA III was split in two run periods: one from beginning of March until beginning of July and a second from beginning of August until end of December 2020. Only the first run had to be adapted due to the conditions during the pandemic, i.e., the user run was completely halted between 21–30 March. Between 31 March and 3 May, the user run was resumed for urgent studies related to Covid-19 (Fig. 1). On 4 May standard user operation was resumed for users who were allowed to travel, mainly from Germany.

In total, 4569 hours the of scheduled beamtime for users were provided at PETRA III, 600 hours of them exclusively for high-priority Covid-19-related studies and also DESY research. About 3300 hours were available for proposals of users at 23 beamlines: P01–P14 in the PETRA III experimental hall 'Max von Laue', P21.1–P24 in the hall 'Ada Yonath' and P61–P65 in the hall 'Paul Peter Ewald'. However, the scheduling of beamtimes turned out to be challenging, in particular for users from foreign countries. Beamtimes were shifted and rescheduled multiple times to match with the availability of the users. This flexibility could be achieved by omitting the usual call for proposals in September 2020 for most of the beamlines and thereby stretching the overall PETRA III run period for proposals originally scheduled in 2020 until mid of 2021.

PETRA III – user access made possible during the coronavirus pandemic

The operation for users of PETRA III started on 2 March 2020. It soon became clear that the coronavirus pandemic was spreading, resulting in unknown risks for all involved in the operation of PETRA III. Therefore, PETRA III operation was stopped on 21 March. Since many experiments at PETRA III have eminent impact, not only on coronavirus-related research, but also on the work of the scientific community in general, it was quickly decided that PETRA III needs to be operational. Consequently, rules were developed, allowing PETRA III to further operate, which specify the number of users per experiment, contact restrictions, hygienic measures, etc. (Fig. 2). Already on 31 March PETRA III restarted operation for experiments of DESY groups and for coronavirus-related experiments prioritised by the DESY directorate. After having extended and refined the rules and by reallocating beamtime according to travel options of users, PETRA III regained regular user operation on 4 May. End of September, with rising infection numbers throughout Europe, it became apparent that the existent rules need to be adapted for the rest of the year. Therefore, since 26 October the access rules have been significantly reinforced, e.g., by requesting users to present negative PCR tests for SARS-CoV-2 prior to the experiment.

Since 21 March the beamline staff is partially working from home offices, according to DESY's safety rules during the pandemic, which makes operation even more challenging. Furthermore, almost all PETRA III beamlines are offering mail-in services: users can send samples with instructions of how the measurements should be performed by the beamline staff. All these activities create significant extra workload for involved on-site personnel, therefore, the number of mail-in experiments is limited to-date, except for the DESY and EMBL beamlines P11, P12, P13 and P14 which have mail-in and remote-controlled MX and SAXS experiments available as standard methods.

The biggest challenge was to reschedule user beamtimes cancelled in March and April, to shift beamtimes of users who were affected by travel restrictions and, in turn, to fill gaps arising from users' cancellations. To reschedule cancelled beamtimes or shift planned experiments, the actual run period in the second half of the year (II-2020) was extended from 31 December 2020 until 7 July 2021. While this generated sufficient flexibility for the reallocation procedure, it was often problematic and sometimes impossible to fill gaps arising from short-notice users' cancellations. The buffer of proposals needed to fill the extended schedule was insufficient for seven beamlines altogether. Therefore, a call

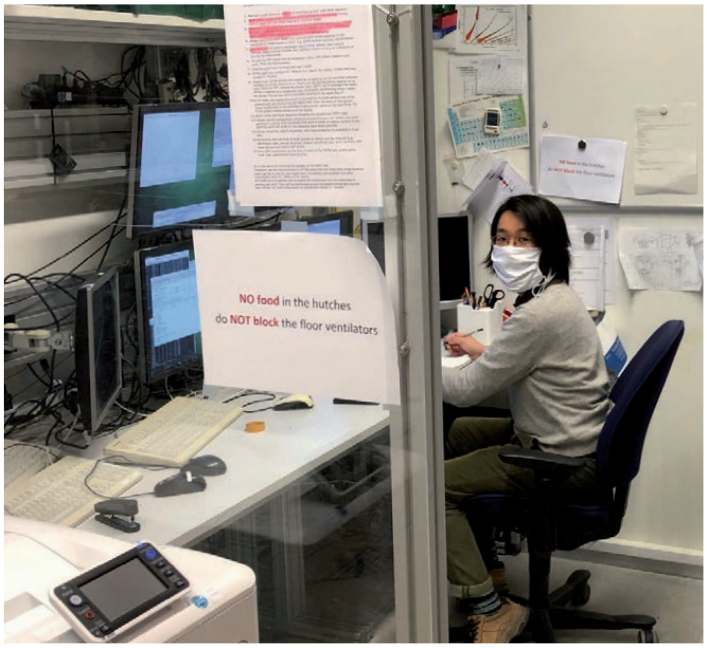

Figure 2

Experiment control at the PETRA III beamline P08 during the Covid-19 pandemic.

for proposals for P01, P05, P09, P11, P24, P61-HZG and P65 has been held for the run period I-2021. Roughly 150 proposals were submitted, enabling DESY to continuously operate also these beamlines for users in I-2021.

PETRA III – priority experiments for coronavirus-related research

A specific call for rapid access proposals with focus on fighting the coronavirus pandemic was launched by the DESY directorate. 13 successful proposals were submitted, proposing research at various beamlines. The first to start was a comprehensive molecular crystallography screening campaign aiming at identifying possible drugs to inactivate the main protease of the SARS-CoV-2 virus. For further information on these and other projects please refer to the 'Corona Special' section of this Annual Report.

PETRA III – machine operation

In 2020 the availability of the PETRA III storage ring was 98.89% with a mean time between failures of 78 hours (as of 10 December 2020). Thus, the PETRA III machine was performing excellently during the pandemic.
As in the previous years, two different bunch filling modes were offered in the PETRA III storage ring: a 'time resolved' mode with 40 bunches and a 'continuous' mode with 480 bunches, both with approximately the same share. This

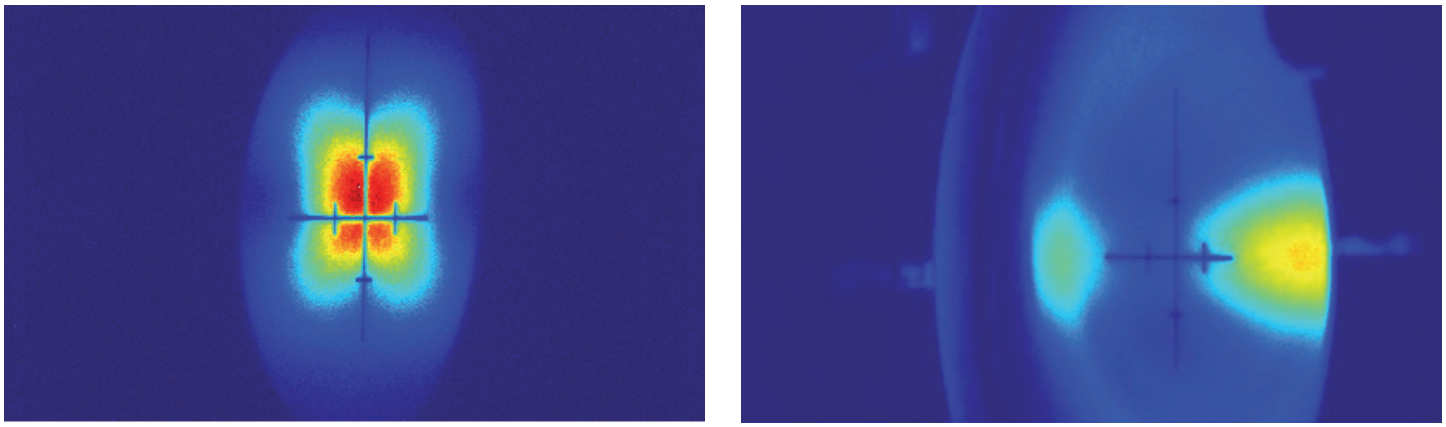

Figure 3

(left) First undulator beam at beamline P62. (right) First light from the bending magnet in the front end of beamline P25. The undulator is still missing.

bunch mode distribution has proven to be an optimal scenario to provide a maximum number of 'timing mode' shifts while minimising the radioactive activation of ring components as well as radiation damage of undulators.

The shutdown period in January and February of 2020 was used to install a bypass connection to the accelerator 'PIA' which is part of the pre-accelerator installations of PETRA III. To-date electrons are accelerated with the linear accelerator 'LINAC II' and then accumulated in the PIA ring before injecting them into the synchrotron 'DESY II', the actual PETRA III pre-accelerator. Originally, PIA was used to accumulate positrons and is still used to reshape the time structure of the electron bunches to match DESY II and PETRA III. However, after an upgrade, foreseen in the upcoming shutdown in winter 2020/21, LINAC II will be able to directly inject electron bunches into DESY II. This direct injection scheme requires a PIA bypass which was installed in the winter of 2019/20.

Installation of the undulator for beamline P62 has successfully been completed. The first undulator beam (Fig. 3) has been recorded after the 'Easter service week' in 2020. Also, the front end of beamline P25 has been finalised with first beams from the bending magnet available in the front end. However, no undulator has been installed so far.

The planned work to complete the vacuum chamber, the front end and the mirror chamber of P66 — VUV fluorescence spectroscopy beamline — is delayed due to the impact of the pandemic on the delivery of the parts. It is now foreseen for summer 2021.

PETRA III – collaborations

In 2020 several new strategic collaborations were initiated with PETRA III being an essential partner: on a European level the project 'CREMLINplus' has become active. This project is a cooperation between the EU and Russia on new mega-science projects in Russia. On the European side PETRA III, together with the light sources ESRF (Grenoble, France) and MAX IV (Lund, Sweden), is leading the activity around the new beamlines planned related to the future 4th generation synchrotron radiation source 'USSR4'. The kick-off meeting of CREMLINplus was held in May 2020. In 2020, the European project 'LEAPS-INNOV' was approved as well, which was initiated to foster cooperation between the European accelerator-based light sources, in particular on topics with innovational aspects. Here, the PETRA III team is leading the activity to develop a generic concept for hardware and software synchronisation of ultrafast X-ray experiments with complex sample environment.

Two new national DESY collaborations were initiated this year, with PETRA III being one of the main players: the collaboration with the Institut für Kristallzüchtung (IKZ) in Berlin focusing on the development of novel types of monochromator crystals for PETRA IV and the collaboration with the TU Bergakademie Freiberg focusing on generating synergies in materials sciences at PETRA III.

PETRA III – beamlines and experiments

The coronavirus pandemic has prevented progress on some projects, mostly due to delays in the work flow of external companies, sometimes also due to DESY internal rules according to the national regulations. Nevertheless, many projects are on time or only moderately delayed.

In the PETRA III hall 'Max von Laue', new laboratories are going to be installed: laboratories for vacuum applications, cryogenic instrumentation, setups with lasers, as well as a number of general laboratories. The laboratories are under the responsibility of the 'PETRA III sample environment' team and will be operated to support beamline teams and users with dedicated infrastructure. Furthermore, a dedicated laboratory for an Auger microscope will be operated by the DESY NanoLab. The construction of these labs is split into three phases. In 2020, the installation of the

Figure 4

Completed design of the new hutches EH2 and CH2 to add hierarchical imaging capabilities to the PETRA III beamline P23. (Drawing: Design by KIT, Karlsruhe, Germany)

general laboratories was finalised. In 2021, the construction of all other laboratories will follow, except for the laser laboratory which will be built later. In the frame of reorganising the infrastructure, responsibility for general chemistry, biology and clean room user laboratories in the PETRA III and FLASH experimental halls has been shifted from the technical infrastructure group to the PETRA III group in 2020.

In the PETRA III hall 'Ada Yonath', the biggest activity is the upgrade of the *in situ* diffraction beamline P23 with an imaging end station for hierarchical imaging. This is a joint project of Karlsruhe Institute of Technology (KIT) in cooperation with DESY, and is funded by the Helmholtz Association of German Research Centres (HGF) with the scope to transfer the novel hard X-ray microscope 'MIQA', originally constructed for the ANKA 'XMIC' beamline to PETRA III. At PETRA III, this instrument, now called 'HIKA', will complement the already existing imaging techniques by hierarchical imaging methods for materials research in life sciences and semiconductor research which are hardly covered at PETRA III to-date. In 2020, the planning of the new experimental hutch was completed (Fig. 4). The actual construction work has started in December 2020 with preparations for removing parts of the roof of the 'Ada Yonath' hall in order to fit through the large HIKA instrument.

In the PETRA III hall 'Paul Peter Ewald', construction of the new beamline P62 (Fig. 5) for small angle X-ray scattering (SAXS) for materials research with options of anomalous scattering and SAXS CT is delayed due to the pandemic, in particular with respect to parts provided by external companies, such as the monochromator. The undulator was installed in January 2020, the interlock was finalised in September. Delivery of the monochromator was delayed by more than 12 months, finally arriving in December 2020. Also, parts of the SAXS flight tube could not be delivered, whereas both detectors, the in-vacuum Eiger2X 9M SAXS detector and the in-air Eiger2X 4M-DESY for WAXS have already arrived. The optics will be finalised in January and February 2021 and first monochromatic X-rays are planned for spring 2021 followed by first experiments with 'friendly' users.

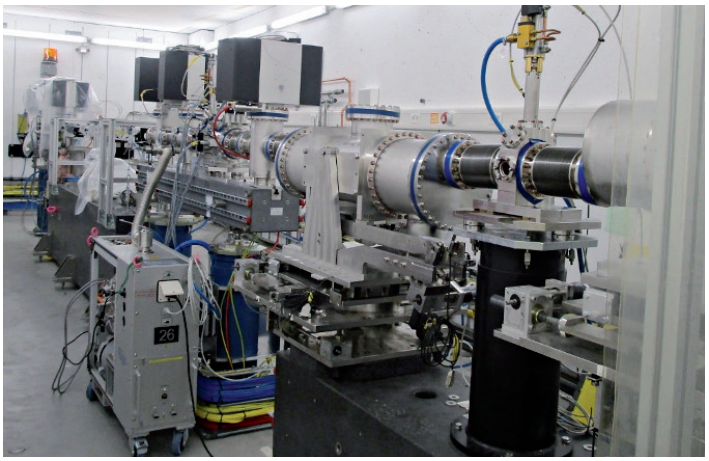

Figure 5

View into the optics hutch of the PETRA III beamline P62.

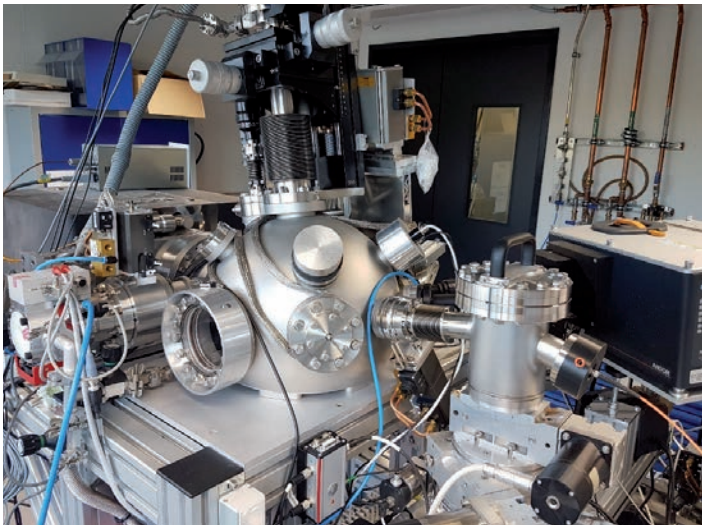

Figure 6

Sample chamber ready to be installed at the PETRA III beamline P66.

Figure 7

Artist's view of the planned curved PETRA IV experimental hall (left of the tennis courts). The new hall will be mostly underground and covered with lawn to fully integrate it in the surrounding park landscape next to DESY in Hamburg.

PETRA III – outlook

The beamline P66 for luminescence spectroscopy will be operating in the ultraviolet (UV) to vacuum ultraviolet (VUV) spectral region. The primary 2 m normal incidence monochromator in 15° Mc Pherson mounting covers a spectral range from 3.7 eV to 40 eV. Applications are in the fields of VUV fluorescence spectroscopy, photon-stimulated desorption and time-resolved spectroscopy. Whereas the hutch and the spectrometer are already in place, the installation of the mirror and the front end parts (Fig. 6) are delayed due to the pandemic. This work is planned in the summer shutdown 2021.

At beamline P23 the construction of the laboratory and control hutches for the hierarchical imager 'HIKA' will be done in 2021. Moreover, infrastructure work and the extension of the beamline vacuum to the new hutch will be started. First beam in the new hutch is expected for 2022.

In the PETRA III experimental hall 'Ada Yonath', the currently empty beamline P25 will be used as a PETRA IV test beamline with the additional capability of serving users and customers from industry with fully automated pharmaceutical powder diffraction and medical imaging. This beamline is planned for accommodation of white and monochromatic X-rays. It is funded by the DESY 'Innovation and Technology Transfer' (ITT) group. The front end of P25 has already been finalised in summer 2020. The first undulator beam is expected at the end of 2022.

PETRA IV

PETRA IV – the TDR phase has started

The PETRA IV project at DESY develops an ultra-low emittance storage ring for hard X-ray radiation that will yield three-dimensional images of matter with up to 100 times higher spatial and up to 10000 times higher temporal resolution in comparison with today. This goal will be achieved by an upgrade of the existing PETRA III facility with recent pioneering developments in accelerator and undulator technologies. The gain in brightness, which is the key parameter to characterise the quality of X-ray beams, will be a factor of 100 for hard X-rays at 10 keV and a factor of almost 1000 at high energy photons up to 150 keV. The high spatial coherence provided by the source, particularly at high photon energies, will allow for true diffraction-limited focusing capabilities without severe losses of photon flux. This will result in

high sensitivity and high spatial and temporal resolution *operando* and *in situ* studies of complex systems.

The conceptual design report (CDR) of the PETRA IV project was successfully finalised in November 2019 and the technical design report (TDR) phase has started at the beginning of this year. Dedicated work package groups have commenced their work tackling specific aspects of photon-beam delivery and transport, as well as sample environment and labs, technical infrastructure, scientific computing and experiment control, ultra-precision mechanics, and detectors. Competence teams, meeting structures, etc. were established in order to facilitate the exchange of information between different DESY groups and to tackle key issues related to the entire PETRA IV project structure.

In 2020, colleagues from the DESY accelerators division worked on the final details of the magnet structure — the envisioned hybrid seven-bend achromat (H7BA) lattice cell — of the PETRA IV storage ring, as well as on the necessary upgrades of the pre-accelerator chain including LINAC II and the new booster synchrotron DESY IV. As many different parts of the DESY infrastructure will be affected by the PETRA IV project, careful strategies were developed for the integration of all necessary components. Discussions on different scenarios for the logistics of the project and the assembly of components have started. The novel H7BA machine lattice planned for PETRA IV allows for ultra-low emittances of $\varepsilon < 20$ pmrad in the brightness mode and $\varepsilon < 50$ pmrad in the timing mode. In order to achieve this goal, the current PETRA III canting schemes of undulators are not possible anymore. Due to the longer cell length of the new PETRA IV lattice, 26.2 m compared to the current 23 m in the 'Max-von-Laue' hall, fewer beamline sectors per hall can be realised. Therefore a dismanteling relocation of all existing PETRA III beamlines is required. However, the new lattice structure of the storage ring will allow for 5 m long insertion devices for the beamlines and much more space for labs and infrastructure compared to PETRA III. In the storage ring section upstream of each experimental hall, after a long straight section, even up to 10 m insertion devices will be possible.

To compensate the space for beamlines which have to move out of the experimental hall 'Max von Laue', and to be able to extend the beamline portfolio, an additional experimental hall in the west of PETRA is planned. Since the PETRA tunnel in the west, at the adjacent 'Lise-Meitner Park', is mainly below ground, the new experimental hall has to be integrated into the park landscape (Fig. 7). The new PETRA IV hall will offer space for up to 16 beamlines. Hence, at PETRA IV 30 beamlines are planned in total. Five of these beamlines will be so-called 'flagship' beamlines and can be operated with a 10 m insertion device. The flagship beamlines will be designed to make optimal use of the extreme brightness of the source and will be selected during the TDR phase of PETRA IV. However, with the current design of the PETRA IV storage ring, all beamlines will gain substantially both in brightness and in photon flux, as the electron-beam emittance is significantly reduced.

In May 2020, the user community and all national and international partners of PETRA III were invited to submit 'scientific instrumentation proposals' (SIPs) until December 2020 to sketch their ideas of how the experimental stations at the beamlines shall look like in the future. The idea of the SIPs is to survey the needs of the user community and to look for experiments which will benefit most from the ultimate brightness and spatial coherence of the new source. The SIPs will be used for the development of the PETRA IV beamline portfolio. PETRA and its partners, supported by the German 'Committee Research with Synchrotron Radiation' (KFS), organised a series of PETRA IV workshops in October and November 2020, in order to discuss draft ideas of SIPs and to support the user community with the process. These workshops were intended to foster the scientific exchange among different user communities and to bring together current and future users working in all fields of science. These scientific workshops in an online format, with a total number of 1342 registrations and 230 speakers, were well-received and led to fruitful discussions about science cases across all scientific fields, potential experiments at PETRA IV and associated scientific and technical requirements.

PETRA IV – outlook

After the deadline in December 2020, a technical and scientific review of the SIPs will follow. The outcome of both reviews as well as further information about the already existing PETRA III beamlines will be used to develop a preliminary version of the PETRA IV beamline portfolio together with the present PETRA III beamline staff and DESY partners. In April 2021, the PETRA IV beamline portfolio draft will be submitted to the DESY Photon Science Committee (PSC). With the advice and recommendations given by the PSC, the draft version of the PETRA IV beamline portfolio will be refined during the next year.

Contact (PETRA III): Oliver Seeck, oliver.seeck@desy.de
Hans-Christian Wille, hans.christian.wille@desy.de
Contact (PETRA IV): Kai Bagschik, kai.bagschik@desy.de
Stephan Klumpp, stephan.klumpp@desy.de

Campus and Collaborations

Campus and Collaborations – Overview

DESY Photon Science is part of a worldwide collaborative network. The collaboration landscape at DESY Photon Science is diversified and involves local as well as national and international partners. Cooperation creates new scientific and technological opportunities at DESY's facilities, increases the pool of talents and is also indispensable to further coordinate of research roadmaps and agendas.

Interdisciplinary research platforms

The Center for Free-Electron Laser Science (CFEL) as a joint enterprise of DESY, the Max-Planck-Institute for the Structure and Dynamics of Matter (MPSD) and the Universität Hamburg is designed to advance science with next generation light sources and lasers.

Within the Centre for Structural Systems Biology (CSSB) — a cooperation of ten partner institutions — scientists use a novel approach which combines integrative structural biology with systems biology to advance our understanding of the molecular mechanisms of some of the world's most widespread infectious diseases.

Five partner institutions will be working together at the Centre for X-ray and Nano Science (CXNS): the Helmholtz Centre Geesthacht (HZG), Christian-Albrechts-Universität zu Kiel (CAU), the Leibniz-Institut für Kristallzüchtung (IKZ), the Technische Universität Hamburg (TUHH) and DESY. In addition to several research groups, the building will house the DESY NanoLab.

Further centres in the planning phase are the Centre for Molecular Water Science (CMWS), the Centre for Data and Computing in Natural Science (CDCS), and the Wolfgang-Pauli-Centre (WPC) for theoretical physics.

Universities

DESY collaborates with universities through joint professorships, graduate schools, collaborative research centres (SFBs) and in the frame of the Excellence Strategy of Federal and State Governments. German universities are closely involved at PETRA III and FLASH, for example, via BMBF-funded collaborative research.
A strong connection to the Universität Hamburg (UHH) is established through the 'Partnership for Innovation, Education and Research' (PIER). This structural cooperation has provided the ground for a joint graduate school (PIER Helmholtz Graduate School, PHGS), joint professorships and a seed fund facility for research projects.

DESY within user consortia at the European XFEL

Besides being responsible for the construction and the operation of the European XFEL linear accelerator, DESY plays an important role as user of the European XFEL. DESY is partner in several user consortia. The three largest of these are the Serial Femtosecond Crystallography (SFX) user consortium; the Helmholtz International Beamline for Extreme Fields (HIBEF) and the Heisenberg Resonant Inelastic X-ray Scattering (hRIXS) user consortium. Moreover, DESY scientists are developing lasers and detectors for usage at the European XFEL.

European Molecular Biology Laboratory (EMBL) Hamburg

At EMBL Hamburg, scientists investigate the structure of challenging molecules that impact human health. The Hamburg site's service teams develop methods and software to support scientists from around the world in every step of biological structure determination. EMBL runs three beamlines at PETRA III: one for small-angle X-ray scattering experiments and two for macromolecular crystallography.

Helmholtz-Zentrum Geesthacht (HZG)

The German Engineering Materials Science Centre (GEMS) is a user platform of HZG for the complementary research with photons and neutrons with an outstation at DESY. GEMS research groups work in X-ray diffraction and imaging on the DESY campus. HZG operates several beamlines and end stations at PETRA III, focusing on research in the field of engineering materials science.

Innovation and Technology Transfer

With support of the DESY department for Innovation and Technology Transfer (ITT), scientists from DESY Photon Science contribute to the DESY innovation strategy, including the transfer of knowledge and technology from the laboratory to industry.

International cooperation

DESY is engaged in international cooperation and user consortia, for example, to leverage new resources and contributions to DESY facilities and installations. Significant examples for DESY Photon Science in that respect are the international contributions to PETRA III by Sweden in connection to the Röntgen-Ångström-Cluster (RAC) and by India via the India@DESY collaboration.

Cooperation for research and education

News from partner universities

Figure 1

Entrance area of the new HARBOR building.

Universität Hamburg (UHH)

On the occasion of the annual meeting of Hamburg's Cluster of Excellence 'CUI: Advanced Imaging of Matter' (AIM), the Mildred Dresselhaus Prize 2020 has been awarded to Caterina Vozzi and Giulia Fulvia Mancini. Vozzi of the Institute of Photonics and Nanotechnology (CNR-IFN) in Milan, an expert in attosecond physics, received the senior prize. The junior award winner, Mancini of the University of Pavia, performs cutting-edge ultrafast electron diffraction and small-angle scattering at X-ray facilities. The prize, dedicated to female scientists, will give both awardees the opportunity of an extended research stay in Hamburg in 2021.

In June 2020 the new building for the 'Hamburg Advanced Research Centre for Bioorganic Chemistry' (HARBOR) was completed on the Bahrenfeld site (Fig. 1). Here, around 120 scientists from the University's Faculty of Mathematics, Informatics and Natural Sciences will be conducting research on molecular biological systems. A large part of the scientific programme is embedded in the Cluster of Excellence AIM. Members of the centre conduct experiments at DESY's X-ray facilities, for example at the T-REXX station at beamline P14 of PETRA III, where data with particular relevance for time-resolved structural biology are acquired.

Yet another important new building, 'Haus der Lehre - Light & Schools', was handed over in June to the Department of Physics and AIM. About 600 m^2 of floor space at the Bahrenfeld campus are now available for the physics school laboratory 'Light & Schools' of the Universität Hamburg and for the advanced practical training of physics students. In the 'Light and Schools' labs, small groups of young pupils are invited to explore the marvels of nature in real experiments with modern photonic tools like lasers.

In order to bring together and further expand their computing capabilities, the Universität Hamburg, DESY and Technische Universität Hamburg founded the Center for Data and Computing in Natural Science (CDCS). At the interface between computer science and the natural sciences, modern solutions shall be developed for tackling the current and future computational challenges in astro and particle physics, photon science, structural systems biology and accelerator physics. A close collaboration is envisaged with the DASHH (Data Science in Hamburg – Helmholtz Graduate School for the Structure of Matter).

In November, the national Women Physics Conference 2020 took place in a digital format for the first time. Hosted by the Universität Hamburg, together with DESY, the Clusters of Excellence AIM and 'Quantum Universe' and the Hochschule für Angewandte Wissenschaften Hamburg, the conference served to promote scientific exchange and networking among women in physics at all career stages. Various opportunities were offered to build networks, to present one's own work as poster or lecture, to hear keynote speakers talking about their career and to make contacts with the industry. Hamburg's Second Mayor Katharina Fegebank took over the patronage.

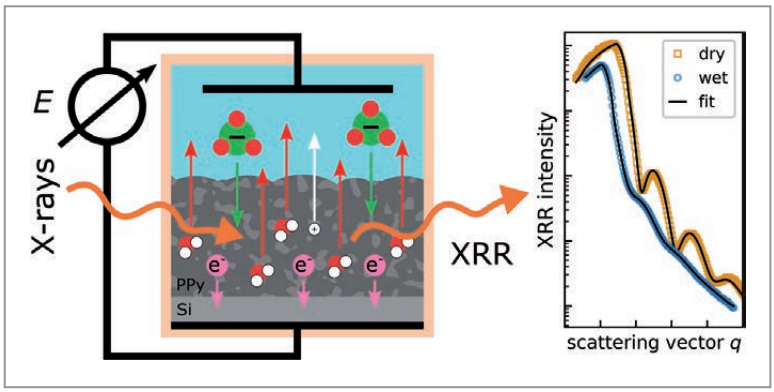

Figure 2

In situ X-ray reflectivity at the PETRA III beamline P08 was used simultaneously with electrochemical analysis to probe the electrical potential induced swelling and the electrolyte transfer in a semiconducting polypyrrole film on silicon. Investigation of the incorporation mechanism in this planar system helps to understand the electrolyte imbibition into polypyrrole-filled nano-porous silicon. Such biocompatible soft polypyrrole filler – stiff silicon matrix composite material could be used in the future for bioactuoric applications like artificial muscles. (Image from [1], Copyright ACS, DOI: 10.1021/acs.langmuir.0c02068)

Christian-Albrechts-Universität zu Kiel (CAU)

The joint appointment of Holger Sondermann as Lead Scientist at the Centre for Structural Systems Biology (CSSB) will strengthen the collaboration between Christian-Albrechts-Universität zu Kiel and DESY. The established cooperation also continues to flourish through the Ruprecht Haensel Laboratory. The BMBF-funded projects QM-MBE-SXPES (design and *in situ* characterisation of novel quantum materials) and XFEL-k-Spin-multi-D (understanding and controlling ultrafast dynamics of quantum matter) are progressing well. The 'momentum and spin resolving photoelectron spectrometer' ASPHERE was successfully upgraded to a photoemission micro-spectroscope and is now permanently installed at PETRA III beamline P04. While at P08, the 'liquid interfaces scattering apparatus' (LISA) continues to provide opportunities to study and understand ultrafast dynamics of water interfaces and cell membranes. The project 'High-energy surface X-ray scattering for electrocatalysis and energy science' (HESEC) is on good track to make atomic structural changes to electrodes for fuel cells and electrolytic hydrogen production visible using high-energy X-ray beams.

Georg-August-Universität Göttingen (GAU)

This very unusual year 2020 has also led to a scientific reflection on possible scientific contributions in the fight of the pandemic within the GAU-DESY bridge. Cooperative studies included the nano-structural and real-time observation of the chemical dynamics of drugs for Covid-19 treatment by *in situ* GISAXS experiments at PETRA III beamline P03. Furthermore, the biophysical and structural characterisation of coronavirus-infected cells by 3D synchrotron tomography, which augments optical histology, was performed at PETRA III beamline P10. The parenchymal architecture of unstained lung tissue from patients, who succumbed to Covid-19, was investigated with GINIX. Diffuse alveolar damage has been visualised and distribution and density of lymphocytes infiltrating the tissue has been quantified in 3D. Based on the dynamic X-ray studies, novel approaches were developed for low-dosing medication of active ingredients with dangerous side effects. Details can be found in the highlight section and the 'Corona Special' section of this Annual Report.

In addition to these successful efforts regarding Covid-19-related research, Sadia Bari, who is a member of the GAU-DESY joint research group, successfully applied for Helmholtz funding of first-time professorial appointments with her research focus of 'probing the dynamical local structure of isolated to solvated proteins'.

Technische Universität Hamburg (TUHH)

There are several joint research projects of scientists at DESY Photon Science and TUHH. In 2020, the DESY NanoLab has continued its fruitful cooperation with the materials science departments of the TUHH within two projects in the SFB 986 'Tailor-made Multi-scale Material Systems', funded by the German Science Foundation (DFG). Its aim is a better understanding of structure – functionality relations in bottom-up fabricated materials (for a science example, see Fig. 2).

The application for the third funding period of the SFB was approved in December 2020. To further deepen their cooperation in the field of materials science, the TUHH and DESY have jointly submitted a Hamburg X proposal together with UHH and HZG for a Center for Integrated Multiscale Materials Systems (CIMMS) which receives funding from the City of Hamburg. The goal of CIMMS is the development and production of sustainable, multi-functional composite materials, so-called multiscale hybrid and integrated material systems out of self-arranging nano particles via 3D-print. Within CIMMS, TUHH and DESY decided to support long-term funding of a W3 professorship for high resolution X-ray analytics of materials which has been filled by Patrick Huber from the TUHH. The new CIMMS group will be located at the CXNS.

Contact:
Markus Drescher, UHH, markus.drescher@uni-hamburg.de
Bridget Murphy, CAU, murphy@physik.uni-kiel.de
Simone Techert, GAU and DESY, simone.techert@desy.de
Christian Schroer, UHH and DESY, christian.schroer@desy.de
Andreas Stierle, UHH and DESY, andreas.stierle@desy.de

Reference

1. P. H. Lakner et al., Langmuir 36, 13448 (2020).

Center for Free-Electron Laser Science CFEL

Three institutions working successfully together

CFEL is a joint enterprise of DESY, Universität Hamburg (UHH) and the Max-Planck-Institute for the Structure and Dynamics of Matter (MPSD) and the fruitful cooperation results in outstanding research, of which a few highlights are presented in the following.

Imaging the structure of a molecule and capturing its dynamics during a chemical reaction with atomic resolution and in real time is one of the holy grails for unravelling chemistry. An interdisciplinary team of CFEL scientists from DESY and MPSD took a crucial step forward in this direction [1]. The researchers were able to capture the details of the strong-field photoionisation process where an electron is ejected from a molecule by ultra-intense light and the subsequent intricate electronic dynamics of the molecule in real time. The researchers investigated the interaction between carbonyl sulfide molecules, which were fixed in space using laser alignment, and a very intense laser field – applying the method of laser-induced electron diffraction. Here, the strong laser field extracts an electron from the molecule, accelerates it, and then makes this electron recollide with the molecule itself at high energy. The scattered electrons create a diffraction pattern that allows for the extraction of the molecule's structure with very high spatial and temporal resolution (Fig. 1). A combined experimental, theoretical, and computational approach enabled the team to follow the electrons as they danced around the molecules in the strong laser field. Details can be found in the highlight section of this report.

X-ray lasers can reveal the spatial structures of biomolecules that are hard to come by with other methods. However, the intense X-ray flashes vaporise the samples almost immediately. An international team of scientists, including CFEL DESY groups, has followed how this radiation damage spreads in biomolecules to unprecedented detail [2]. The results are important for the design and interpretation of X-ray laser measurements. They showed that in order to make reliable measurements, researchers need to model the specific parts of a sample rather than assuming all parts of the molecule are equally damaged. The study marks the beginning of a fuller understanding of how very short X-ray pulses produced by X-ray lasers modify the structure of biological molecules.

Discovering ways to control the topological aspects of quantum materials is an important research frontier, because it can lead to desirable electrical and spin transport properties for future device technologies. MPSD scientists from CFEL have discovered a pioneering laser-driven approach to generate a topological state in graphene [3]. The team's new approach consists of illuminating graphene with a strong, circularly polarised laser pulse whose electric field drives electrons in loops. When the material is illuminated, it suddenly behaves like a topological material (Fig. 2). It returns to its normal state once the pulse is gone. This work shows that light is capable of engineering topological properties in topologically trivial materials. The ultrafast appearance of this effect holds great potential for the construction of extremely fast sensors or computers.

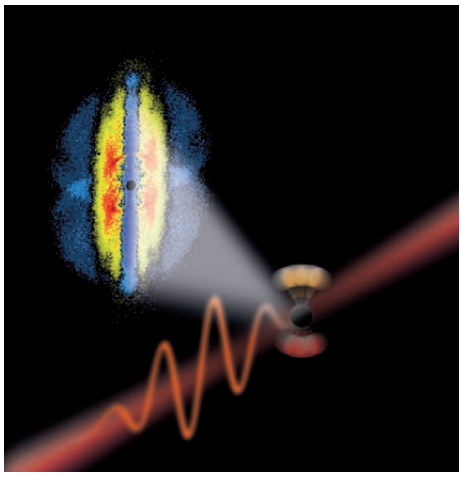

Figure 1
Filming a quantum molecular movie. A carbonyl sulfide molecule is ionised by ultra-intense light and the photoelectrons are projected onto a detector, carrying the signature of electrons' ballet. (Image: DESY, Andrea Trabattoni)

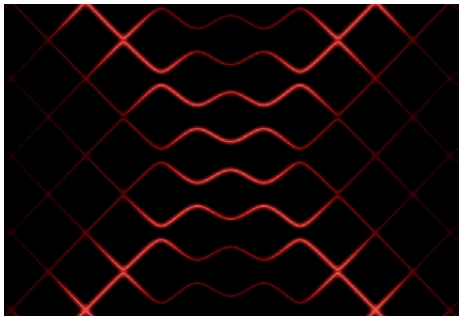

Figure 2
Topological quantum states in graphene induced by light. (Image: MPSD, Benedikt Schulte)

Contact: Ralf Köhn, ralf.koehn@cfel.de

References

1. A. Trabattoni et al., Nat. Commun. 11, 2546 (2020).
2. K. Nass et al., Nat. Commun. 11, 1814 (2020).
3. J. W. McIver et al., Nat. Phys. 16, 38-41 (2020).

Centre for X-ray and Nano Science including the DESY NanoLab

Sound foundations for the nano future

Five strong research partners will be working together at the Centre for X-ray and Nano Science: the Helmholtz Centre Geesthacht (HZG), Christian-Albrechts-Universität zu Kiel (CAU), the Leibniz-Institut für Kristallzüchtung (IKZ), the Technische Universität Hamburg (TUHH) and DESY. The centre will provide excellent facilities for preparing samples for DESY's close-by large-scale X-ray sources. In addition, scientists can make use of complementary research techniques to optimally exploit the research potential available on campus. The CXNS mostly hosts research using X-rays in combination with nano and material sciences. Research topics such as studying optimised materials for energy conversion processes, sensor technology, X-ray imaging techniques or scanning probe microscopy and nano-structuring are all brought together under the roof of CXNS

The building is currently under construction (Fig. 1) in close vicinity to the PETRA III experimental hall 'Max von Laue'. The interior work for the technical infrastructure is ongoing and moving in is scheduled for March 2021. On the ground floor there will be space for 20 high-tech laboratories for several DESY Photon Science teams as well as for the German Engineering Materials Science Centre (GEMS) of the HZG. Furthermore, the CXNS will host offices for research groups of CAU in the frame of the cooperative Ruprecht-Haensel Laboratory.

In 2020 two new partners joined the CXNS: the TUHH as part of the Center for Integrated Multiscale Material Systems (CIMMS) and the IKZ. Research at the CIMMS concentrates on developing new three-dimensional multi-scale multi-functional hybrid materials serving new developments in energy, mobility, medicine. The IKZ focuses on the use of tailor-made crystals for research with synchrotron radiation sources with high temporal resolution. In this way IKZ advances research on different material systems in information technology, high power electronics and alternative energy solutions.

As part of the CXNS, the DESY NanoLab supports projects of internal and external users in nano and materials science projects by providing nano-imaging, nano-structuring, spectroscopy as well as X-ray diffraction methods. These are complementary to the photon-based techniques available for users at the DESY X-ray facilities PETRA III and FLASH. Access to the DESY NanoLab is granted for external users via regular PETRA III or FLASH proposals and European access programmes. Industrial users can access via DESY ITT (Innovation and Technology Transfer).

As of 2021, most of the DESY NanoLab instrumentation will be accommodated in the CXNS. Some of the labs will not be located in the CXNS building but in close vicinity, such as the DESY NanoLab X-ray diffraction lab and the electrochemistry lab (Fig. 2), operated in cooperation with CAU. Both are on their way to full working mode.

Additional to the existing instrumentation, a Scanning Auger Microscope for surface-sensitive chemical analysis with less than 10 nm lateral resolution will complement the DESY NanoLab instrumentation in 2021. Future expansion of the instrumentation is planned in agreement with the expected user requirements.

Contact: Andreas Stierle, andreas.stierle@desy.de

Figure 1

Construction of the CXNS building is almost completed.

Figure 2

The new electrochemistry lab enables preparation of X-ray experiments in the field of electrochemistry, catalysis and corrosion.

Centre for Structural Systems Biology CSSB

We investigate how pathogens infect humans

Figure 1

Scientists approaching CSSB's main entrance. (Image: Jörg Müller)

Like all other scientific institutions around the world, the Covid-19 pandemic has had a significant impact upon CSSB's research, scientific events as well as the daily operation of laboratories and facilities. Our scientists quickly began to use their expertise to contribute to the investigation of SARS-CoV-2 using the cutting-edge technologies available at CSSB (Fig. 1) and on the DESY campus.

SARS-CoV-2 research highlights

CSSB scientists are currently involved in over 10 different projects investigating SARS-CoV-2. Below are some highlights:

Scientists identify sybodies to combat Covid-19

CSSB scientists Christian Löw (EMBL) and Martin Hällberg (Karolinska Institutet) and their collaborators have identified sybodies with the potential to neutralise the coronavirus SARS-CoV-2. One sybody in particular, sybody 23, turned out to be exceedingly effective in blocking the SARS-CoV-2 spike protein's receptor binding domains. Their work holds promise for treating Covid-19 [1].

Alpaca nanobody neutralises the SARS-CoV-2 spike protein

CSSB Research Hotel scientist Martin Hällberg (Karolinska Institutet) and collaborators have demonstrated that an alpaca nanobody effectively neutralises the SARS-CoV-2 spike protein. Their results reveal that blocking the interaction between the viral spike proteins and the human receptors could suppress SARS-CoV-2 replication. Their findings could ultimately be used to develop antiviral treatments against Covid-19 [2].

Antiviral drug, Favipiravir, could kill SARS-CoV-2 viral genome

CSSB Scientific Director Chris Meier (UHH) was involved in a collaborative study that reported the first detailed kinetic and mechanistic analysis of SARS-CoV-2's polymerase enzyme. Using the antiviral drug Favipiravir (Avigan), the researchers have managed to make the virus accumulate too many mutations which overloads its error correcting machinery and ultimately renders the viral genome non-functional [3].

Missing link in replication process of coronaviruses identified

In cooperation with scientists from the Grünewald (HPI, UHH) group, researchers from Leiden University Medical Center found a passage mechanism in the SARS-CoV-2 replication organelles that is mediated by a large crown-shaped molecular pore. This protein structure is a potential new starting point for the development of antiviral drugs [4].

Collaborative research highlights

CSSB scientists (Fig. 2) have not only published exciting new findings regarding coronaviruses but their research in 2020 has also revealed new insights into the architecture of the nuclear pore, identified new proteins in the malaria parasite and demonstrated that the sophisticated molecular machines developed by bacteria could be exploited for therapeutic applications.

Nuclear pore's architecture revealed directly in cells

To initiate infection, many viruses such as influenza, herpes and SARS-CoV-2 must first breach the nuclear pore complex. Using structural biology microscopic techniques combined with integrative modelling, Jan Kosinski (EMBL) and his collaborator Martin Beck, Max Planck Institute of Biophysics and EMBL Heidelberg, recently revealed the cell architecture of the yeast nuclear pore and snapshots of its turnover [5].

How deadly parasites 'glide' into human cells

The research of Christian Löw's (EMBL) and Tim Gilberger's (BNITM/UHH) groups provides new insights into the molecular structure of proteins involved in the gliding movements used by parasites to invade human host cells. Using X-ray crystallography and nuclear magnetic resonance (NMR), the researchers obtained the first molecular structures of essential light chains (ELCs) bound to myosin A in *Toxoplasma gondii* and *Plasmodium falciparum*. Their study shows that

Figure 2

Laboratory at CSSB. (Image: Jörg Müller)

ELCs work like 'molecular stilts' – upon binding myosin A, the ELCs become rigid and start to act as its lever arm. This stiffening lets myosin take longer steps which likely accelerates the parasite's gliding movements (Fig. 3) [6].

New insights into the herpes virus fusion process upon entry into the host cell

CSSB scientists Kay Grünewald (HPI/UHH) and Maya Topf (HPI/UKE) were involved in a collaborative study that used a multi-methodological approach to analyse the fusion process of herpes viruses with the host cell during cell entry. The main focus of the investigation was the prefusion structure determination of the herpes simplex virus 1 (HSV-1) glycoprotein B [7].

Bacteria eExploited for therapeutic applications

The gram-negative bacteria Salmonella possesses a needle-like type III secretion system which delivers bacterial proteins to the human host. CSSB scientist Thomas Marlovits (UKE) and collaborators have developed the basic principles for reprogramming this secretion system to deliver functional binding proteins inside human cells. These principles demonstrate that the sophisticated molecular machines developed by bacteria could be exploited for therapeutic applications [8].

New recruitments

In April 2020, Jens Bosse joined CSSB with a junior professorship for 'Quantitative and Molecular Virology', appointed by Hannover Medical School (MHH). His professorship is financed by the Cluster of Excellence RESIST which seeks to help individuals with weakened immune systems combat infection. The Bosse group's research aims to illuminate the spatiotemporal regulation of viral morphogenesis at the single-particle level.

In August 2020, Holger Sondermann joined CSSB with a joint appointment from DESY and the Christian-Albrechts-Universität zu Kiel. The Sondermann group focuses on understanding the architecture and regulation of signalling systems that control bacterial cell adhesion and biofilm formation.

In October 2020, Maya Topf joined CSSB with a joint appointment from UKE and HPI. The Topf group works on the development of computational modelling approaches that integrate experimental data and bioinformatics to characterise the structure of macromolecular machines.

ERC Starting Grant

Michael Filarsky (UHH) received an ERC Starting Grant for his project looking into the adaptation of the malaria parasite, *Plasmodium falciparum*. The starting grant can be used over a five-year period.

Black Box Science – a glimpse behind the scenes

With an inspiring new video blog project entitled Black Box Science, CSSB group leader Rainer Kaufmann aims to shine a critical light on current scientific culture and start a discussion about the realities of everyday scientific life. The blog, https://blackboxscience.org/, is supported by the Volkswagen Foundation. The first video has received over 148.4K views.

Contact: Chris Meier, chris.meier@cssb-hamburg.de

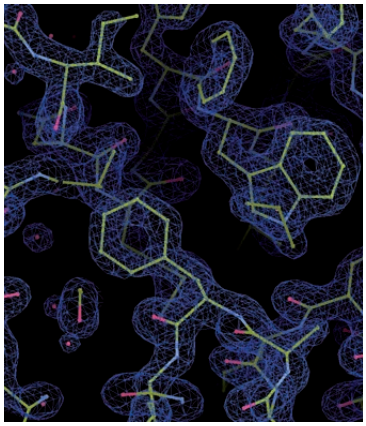

Figure 3

Molecular structure of the essential light chain protein of the Plasmodium glideosome. The blue 'clouds' represent electron density of the protein, with bonds between atoms indicated in yellow and water molecules shown in red. Diffraction data at 1.5 Å phased by Sulfur-SAD was obtained using the PETRA III beamline P12 operated by EMBL Hamburg. (Image: Samuel Pazicky/EMBL)

References

1. T. F. Custódio et al., Nat. Commun. 11, 5588 (2020).
2. L. Hanke et al., Nat. Commun. 11, 4420 (2020).
3. A. Shannon et al., Nat. Commun. 11, 4682 (2020).
4. G. Wolff et al., Science 369, 1395–1398 (2020).
5. M. Allegretti et al., Nature 586, 796–800 (2020).
6. S. Pazicky et al., Commun. Biol. 3, 568 (2020).
7. B. Vollmer et al., Sci. Adv. 6, eabc1726 (2020).
8. A. Chabloz et al., Commun. Biol. 3, 342 (2020).

CSSB Partner Institutions

- Bernhard Nocht Institute for Tropical Medicine (BNITM)
- Deutsches Elektronen-Synchrotron DESY
- European Molecular Biology Laboratory (EMBL)
- Forschungszentrum Jülich (FZJ)
- Hannover Medical School (MHH)
- Heinrich Pette Institute (HPI)
- Helmholtz Centre for Infection Research (HZI)
- Universität Hamburg (UHH)
- University Medical Center Hamburg-Eppendorf (UKE)
- Research Center Borstel (FZB) (associated partner)

CSSB Investors

- Federal Republic of Germany
- Free and Hanseatic City of Hamburg
- Federal State of Lower Saxony
- Federal State of Schleswig-Holstein

European Molecular Biology Laboratory Hamburg Unit

State-of-the-art services and experimental possibilities for structural biology research

The Hamburg Unit of the European Molecular Biology Laboratory (EMBL) is dedicated to providing state-of-the-art services for structural biology research, and to advancing experimental approaches in structural and infection biology. The Covid-19 pandemic has limited the activities at EMBL Hamburg this year, but also opened new opportunities, such as contribution to several Covid-19-related projects, and exploring virtual formats for training.

Research services in structural biology

EMBL operates three beamlines at the PETRA III storage ring for structural biology applications. Beamline P12 enables Small Angle X-ray Scattering (SAXS) experiments while beamlines P13 and P14 are used for Macromolecular X-ray Crystallography (MX). In addition to beamlines, the site offers services at the Sample Preparation and Characterisation (SPC) facility.

After almost a decade of continuous operation, the adaptive X-ray focusing mirrors at beamlines P12 and P14 were replaced by fixed-curvature mirrors of high-surface quality as achieved by ion-beam figuring (Fig. 1). On both beamlines focusing and homogeneity of the X-ray beam has been significantly improved. On P12, the smaller focus size allows to work with smaller volumes of precious protein samples; on P14, smaller crystals than before will be amenable to diffraction data collection.

The EMBL SPC facility, in comparison to the previous reporting period, has almost doubled the number of users to more than 230.

During the initial pandemic lockdown from mid-March until mid-May, the beamlines were re-opened specifically for Covid-19-related projects (see below). With the partial re-opening of EMBL Hamburg in June, the beamlines and the SPC facility became accessible for projects from the standard user programme. Due to new safety conditions, most experiments were carried out via remote (MX) or mail-in (SAXS) access. In June, the site implemented a mechanism allowing rapid access for Covid-19-related projects.

The SAXS Beamline P12 was used in four Covid-19-related projects, including a study in collaboration with CSSB and Karolinska Institutet, which identified synthetic nanobodies with the potential to neutralise SARS-CoV-2, and several studies in collaboration with BioNTech (see below). On both MX beamlines more than 700 diffraction data sets were collected in the context of the project ‘Massive X-ray screening against the SARS-CoV-2 main protease’ contributing important structural information to it (for project information see the ‘Corona Special’ section of this Annual Report. Selected hits found in the crystallographic screening underwent detailed biophysical characterisation in the SPC, which has also contributed to four further Covid-19-related projects.

Research in structural and infection biology

EMBL continuously works on developing methods and resolving structures of most challenging molecules involved in pathogen infections. Most recent success in this field was possible thanks to external collaborations and the highly collaborative spirit of our research groups.

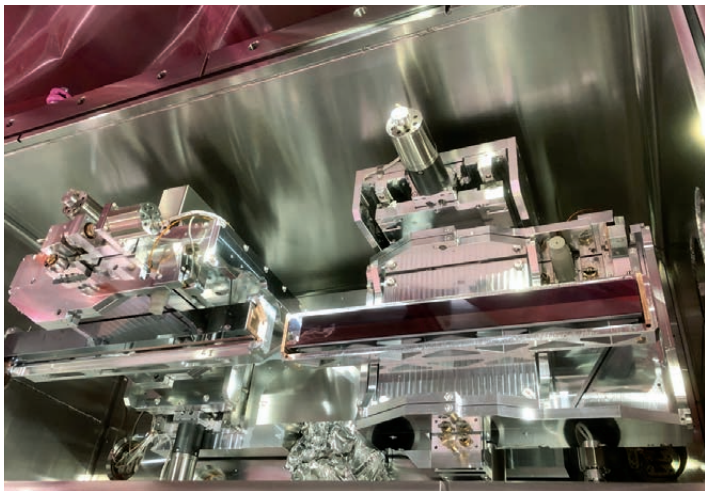

Figure 1

Photograph of the two fixed curvature X-ray mirrors (dark rectangular blocks) mounted in Kirkpatrick-Baez-configuration in the mirror vessel of beamline P14. The synchrotron beam enters the system from the right; the resulting focus size at the sample position is ca. 2 µm x 6 µm. (Photo: Stefan Fiedler/EMBL)

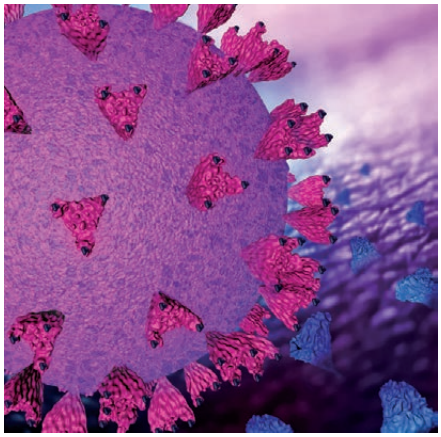

Figure 2

The ability of SARS-CoV-2 to infect cells requires binding between the viral spike protein (magenta) and the human surface protein ACE2 (blue). These interactions can be disrupted by sybodies (black) – synthetic mini-antibodies similar to those produced by camels and llamas. (Image: Rayne Zaayman-Gallant/EMBL)

Christian Löw's group at EMBL/CSSB in collaboration with Karolinska Institutet identified sybodies (synthetic nanobodies) that will potentially block SARS-CoV-2 from infecting human cells [1]. By searching through existing sybody libraries, they found the best binder for the viral spike protein. Structural analysis using SAXS on beamline P12 and electron cryo-microscopy (cryo-EM) revealed that, it binds the spike protein in different conformations (Fig. 2).

Jan Kosinski's group at EMBL/CSSB, together with collaborators from EMBL Heidelberg and the Max-Planck-Institute of Biochemistry in Martinsried, demonstrated that the architecture of the nuclear pore complex differs inside cells compared to its form observed through in vitro studies [2]. The nuclear pore complex is critical for fundamental biological processes because it acts as a gateway that regulates entry and exit of diverse molecules. For example, it transports mRNA from the nucleus to cytoplasm to enable translation.

The group of María García Alai and the SPC facility analysed X-ray crystal structures of a human Major Histocompatibility Complex class I molecule HLA-A*02:01, which is involved in immune response to infections [3]. They found out that in the absence of a ligand the amino acid side chains lining the class I peptide-binding groove undergo coordinated conformation changes between locked and unlocked state.

The group of Meytal Landau at Technion/EMBL published a paper showing that the antimicrobial active core of the human LL-37 involved in the first line of defence against pathogens, self-assembles into a fibril of densely packed helices [4]. This process plays an important role in antibacterial activity and provides immense stability that might enhance bioavailability and biomedical applications.

The Mainz-based biotech company BioNTech, which developed a coronavirus vaccine together with the US company Pfizer, is conducting research on the next generation of RNA vaccines at PETRA III. Using the P12 beamline BioNTech has been investigating, together with the University of Mainz, EMBL and further partners, how so-called messenger RNA (mRNA) can be packaged in nanoparticles so as to be delivered effectively in the target organism [5].

News and events

EMBL Hamburg welcomes two new scientists. Meytal Landau, affiliated to Technion-Israel Institute of Technology, has joined EMBL as new associate group leader. She applies structural biology tools to study functional protein fibrils in bacteria and in protein aggregation diseases. Simon Mortensen joined the EMBL Hamburg faculty as staff scientist in the group of Matthias Wilmanns, who is Head of the EMBL Hamburg Unit. EMBL farewells its faculty member Guillaume Pompidor who has recently moved to DESY in order to work as a beamline scientist at the PETRA III beamline P11.

The Svergun group at EMBL Hamburg released the course 'Solution Scattering from Biological Macromolecules' in an online format for the first time (Fig. 3). The course explored different aspects of SAXS to study the structure of macromolecules. Interest in the course far exceeded the organisers' expectations, as they received over 600 registrations from more than 45 countries.

Contact: Matthias Wilmanns, matthias.wilmanns@embl-hamburg.de

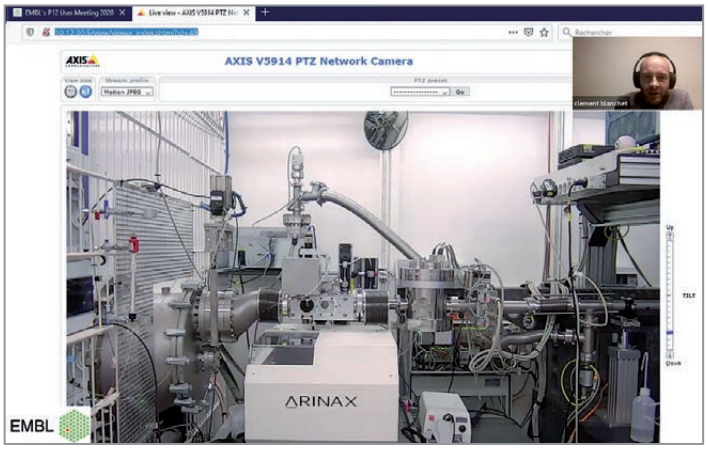

Figure 3

A remote demonstration of the P12 SAXS beamline, recorded by senior technical officer Al Kikhney during a course lecture by Clément Blanchet (top right), staff scientist in EMBL Hamburg's Svergun group. (Image: Al Kikhney/EMBL and Melissa Graewert/EMBL)

References

1. T. F. Custódio et al., Nat. Commun. 11, 5588 (2020).
2. M. Allegretti et al., Nature 586, 796–800 (2020).
3. R. Anjanappa et al., Nat. Commun. 11, 1314 (2020).
4. Y. Engelberg and M. Landau, Nat. Commun. 11, 3894 (2020).
5. C. Siewert et al., Cells 9, 2034 (2020).

The GEMS branch at DESY

Diffraction and imaging techniques optimised for the needs of materials research

Helmholtz-Zentrum Geesthacht operates the German Engineering Materials Science Centre (GEMS). The experimental stations of GEMS at PETRA III are being continuously developed and upgraded for engineering materials science and general imaging users from institutions in Germany and all over Europe. The number of publications remains on a high level and a selection is presented below. New *in situ* techniques are focussing on additive manufacturing (AM) and directional solidification (DS) while a range of new detector systems provide improvements in temporal and spatial resolution at the imaging instruments.

Diffraction

The engineering station (P61A) of the new white-beam beamline P61 will be commissioned at the end of 2020 after the insertion of the beam tube. P61A will have users from the materials science community starting at the beginning of 2021.

Experiments with an *in situ* selective laser melting (SLM) chamber developed by the TU Berlin groups of W. Reimers and E. Uhlmann at P07 [1] tackled current challenges connected with the SLM process including crack-inducing defects and residual stresses. The key advantages of the SLM chamber are the possibility to gather full diffraction rings to improve measurement accuracy, a free choice of the measuring position in the sample, and the feasibility of various measurement modes delivering a range of spatially and temporally resolved data (Fig. 1). The chamber realises boundary conditions, which are close to the industrial process, and could therefore be used to gather unprecedented experimental insights on the build-up of strains and stresses in samples made of the Ni-based alloy Inconel 625 [2]. Several thermal phenomena during the SLM process were shown experimentally, including lateral heat accumulation in a single layer as well as vertical heat accumulation in building direction. The localised heat input induces a complex stress field that involves an outer halo of compressive stresses, which has been experimentally detected. Details can be found in the highlight section of this report.

The large melting zone furnace for directional solidification experiments ('FlexiDS') [3] had been funded within the framework of a BMBF collaborative research project of KIT (M. Heilmeier) and University of Magdeburg (M. Krüger). Especially for high-temperature materials such as Ni-based superalloys used under creep conditions, directional solidification is a promising production process. The crucible-free, inductively heated FlexiDS device (Fig. 2) allows *in situ* studies of the synthesis, transformation and decomposition of materials with a maximum liquidus temperature of 2200 °C via diffraction of high-energy X-rays (P07). The maximum sample diameter is 14 mm which is a compromise between possible X-ray transmission and conditions close enough to relevant industrial processes with regard to temperature distribution in the solid and convection in the melt. The system was used for studying novel high-temperature alloys based on NiAl-(Cr,Mo) [4]. Both ternary alloys, NiAl-Cr and NiAl-Mo, have been studied in the past. In this study, the quaternary system was further examined to estimate the potential of new alloy compositions in detail. The evolving morphologies could be classified as a function of Cr and Mo content.

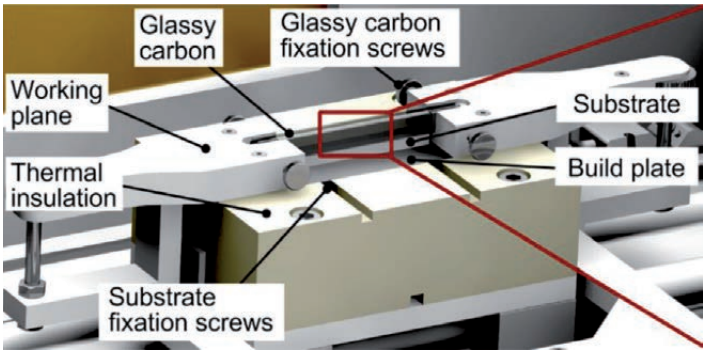

Figure 1

Substrate holder in the SLM chamber. (Image reprinted from [1], with the permission of AIP Publishing.)

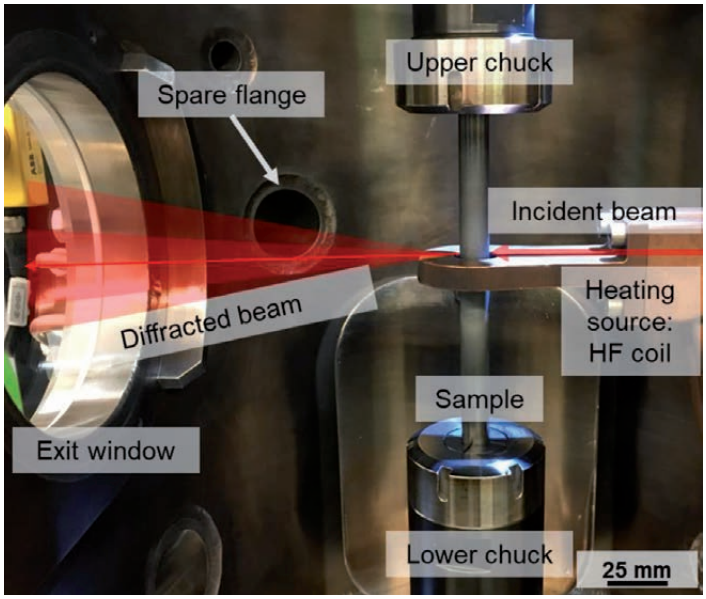

Figure 2

Interior of the FlexiDS process chamber for zone melting. (Image reprinted from [3], with the permission of AIP Publishing.)

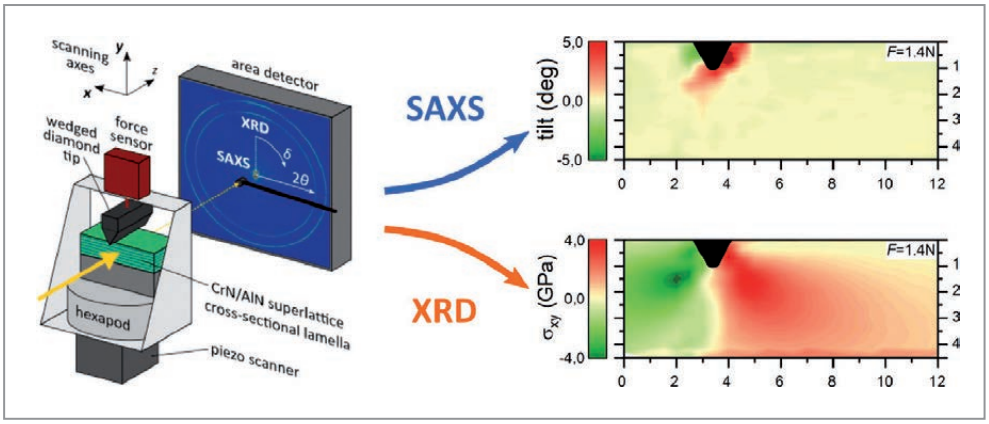

Figure 3

Left: Schematic sketch of the *in situ* indentation experiments at the Nanofocus Endstation of beamline P03. The entire setup is scanned along the axes x and y while the sample is under load. Right: Depending on the sample-to-detector distance, diffraction data is recorded either in small-angle or wide-angle X-ray scattering geometry (SAXS or XRD, respectively). (Image from [7].)

Imaging

The range of detectors available at the Imaging Beamline P05 (IBL) has been complemented with large format, high-resolution CMOS detectors optimised for the beam geometry at P05. Users can now select the detector which is optimised for their individual application: high-dynamic range (up to 16 bit), high resolution (up to 47 megapixels) and high speed (continuous 330 Hz with high resolution). Multiple detectors are now commonly implemented at P05 and at the tomography station of the High Energy Materials Science beamline P07 (HEMS). Full tomography datasets can now be obtained in one second for micro-tomography and in one minute for nano-tomography. A spatial resolution of below 40 nm for absorption and Zernike phase contrast imaging has been achieved, using tailored optics obtained through a cooperation with Paul Scherrer Institut (Switzerland). The new EIGER 9M detector at the Nanofocus Endstation of beamline P03 provides a sensitivity three orders of magnitude higher and a data rate 50 times that of the previously used CCD detector. All these instruments are optimised for *in situ* experiments, as they are often demanded in materials research and demonstrated by the following examples:

Serial femtosecond crystallography (SFX) at X-ray free-electron lasers extends the sensitivity and applicability of X-ray diffraction to structural biology but requires continuous replenishment of sample into the X-ray beam. Gasdynamic virtual nozzles (GDVNs), which focus the liquid stream with gas to diameters much smaller than that of the nozzle orifice, have proven to be a robust SFX sample delivery method. Aberration-free *operando* X-ray microtomography at P05 has been used to study efficient equivolumetric millisecond fluid-flow dynamics and mixing in channels with 3D features integrated into the nozzle [5]. Those devices improve serial diffraction sample delivery workflows to ultimately reveal the temporal sequence of biomolecular reactions and conformational changes in order to decipher the mechanism and regulation of dynamic biological processes.

Lithium-ion batteries are found in practically every mobile device and have become indispensable for our everyday lives. The search for further improvement of these battery systems requires techniques that can visualise the processes causing the ageing of the battery cells under *operando* conditions. In an experiment performed at the P05 microtomography station researchers investigated the growth behaviour of the electrochemically generated lithium microstructure and the morphology changes during operation, as well as the associated failure processes of commercially available separator materials [6]. The results underline the importance of morphological disturbances for the performance of lithium-ion batteries.

Nanocrystalline microscopic thin films have properties that cannot be found in bulk material. The mechanical characterisation of such structures is of great interest but very difficult due to the small length scales and is usually carried out *ex situ* using electron microscopy. The Nanofocus Endstation of beamline P03 was used to perform a micromechanical *in situ* analysis of a CrN-AlN superlattice thin-film cross-section sample in order to map residual stresses and morphological changes while the sample was being loaded with the wedge-shaped diamond tip of a nanoindenter [7]. The results show e.g. a high compressive strength of about 13 GPa and a layer rotation, as shown in Fig. 3. A similar *in situ* nanoindentation experiment was carried out on glass [8]. The structural modification of vitreous silicon dioxide in the stress field of the diamond tip was investigated by means of small-angle X-ray scattering (SAXS), also at P03. The results show that different structural length scales determine the shear strain and isotropic compaction in vitreous silica.

In both fields — diffraction and imaging — the examples above illustrate successful materials research which could be realised by continuously advancing the instrumentation.

Contact: Christina Krywka, christina.krywka@hzg.de
Peter Staron, peter.staron@hzg.de
Martin Müller, martin.mueller@hzg.de

References

1. E. Uhlmann et al., Rev. Sci. Instrum. 91, 075104 (2020).
2. F. Schmeiser et al., Addit. Manuf. 32, 101028 (2020).
3. C. Gombola et al., Rev. Sci. Instrum. (2020).
4. C. Gombola et al., Metals 10, 961 (2020).
5. J. Knoška et al., Nature Commun. 11, 657 (2020).
6. D. Zhou et al., Nano Energy, 105196 (2020).
7. J. Todt et al., Acta Materialia 195, 425-432 (2020).
8. S. Fuhrmann et al., Front. Mater. 7, 173 (2020).

DESY Photon Science at the European XFEL

Status of the user consortia of the Helmholtz International Beamline

SFX

The international SFX Consortium, led by DESY, contributes methodologies and instrumentation for serial femtosecond crystallography experiments at the 'Single Particles, Clusters, and Biomolecules and Serial Femtosecond Crystallography' (SPB/SFX) instrument of the European XFEL.

Serial crystallography has become a prominent method at all X-ray FEL facilities. The high pulse rate available at the European XFEL provides unique advantages attained by measuring datasets in a much shorter time with reduced sample consumption than had previously been possible. Combined with the Adaptive Gain Integrating Pixel Detector (AGPID) that records thousands of diffraction frames per second, and liquid jets that rapidly move crystals across the beam [1], these capabilities have allowed for the implementation of novel efficient sample delivery systems that promise even lower sample consumption per structure in future [2]. In the last year, the downstream interaction region of the instrument was commissioned for in-atmosphere experiments. A scanning system from DESY named the Road Runner, coupled with a Jungfrau detector from the Paul Scherrer Institute, was commissioned and will be used to measure the structures of membrane proteins under various environmental conditions.

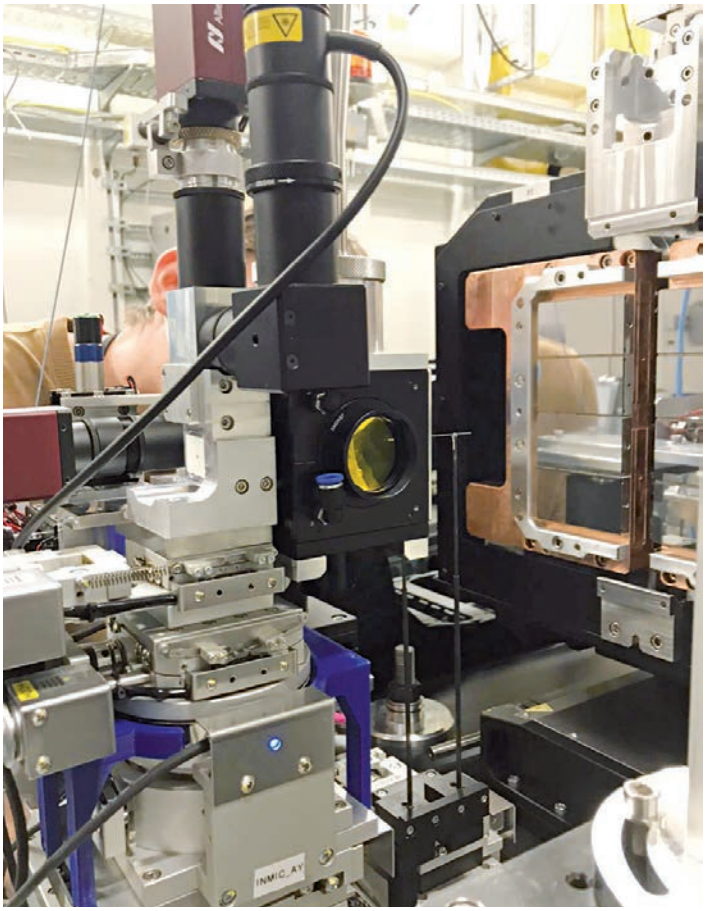

Figure 1

The downstream measurement station at the the SPB/SFX instrument of the European XFEL, configured here for serial crystallography.

While the hardships of the Covid-19 pandemic certainly hampered operations and developments, much effort was made by the SPB/SFX scientists to conduct SFX experiments with minimal on-site presence by the users. This will hopefully open the technique to even more groups.

hRIXS

The Heisenberg RIXS consortium (hRIXS) has received the spectrometer and associated end stations on the experimental floor of European XFEL from the Company Bestec. The system installation and integration into the European XFEL environment – as an essential step towards commissioning – has been ongoing in 2020. Moreover, online workshops on experimental capabilities were conducted in the fall of 2020 to intensify exchange with the scientific user community. These measures increased awareness for the unique capabilities that resonant inelastic soft X-ray scattering (RIXS) at the transform limit in energy and time is going to provide for both chemical and functional materials science.

Design values of the hRIXS spectrometer are resolving powers up to 20000 in an energy range of 250-1600 eV combined with transform limited temporal information. hRIXS has breakthrough potential in the quest to determine static properties and transient excitations in structure, charge, spin and orbital polarisation for chemical processes as well as a wide range of energy and bio-relevant materials. Two complementary, exchangeable end stations optimised for measurements on solid-state and liquid/gas phase targets create the sample

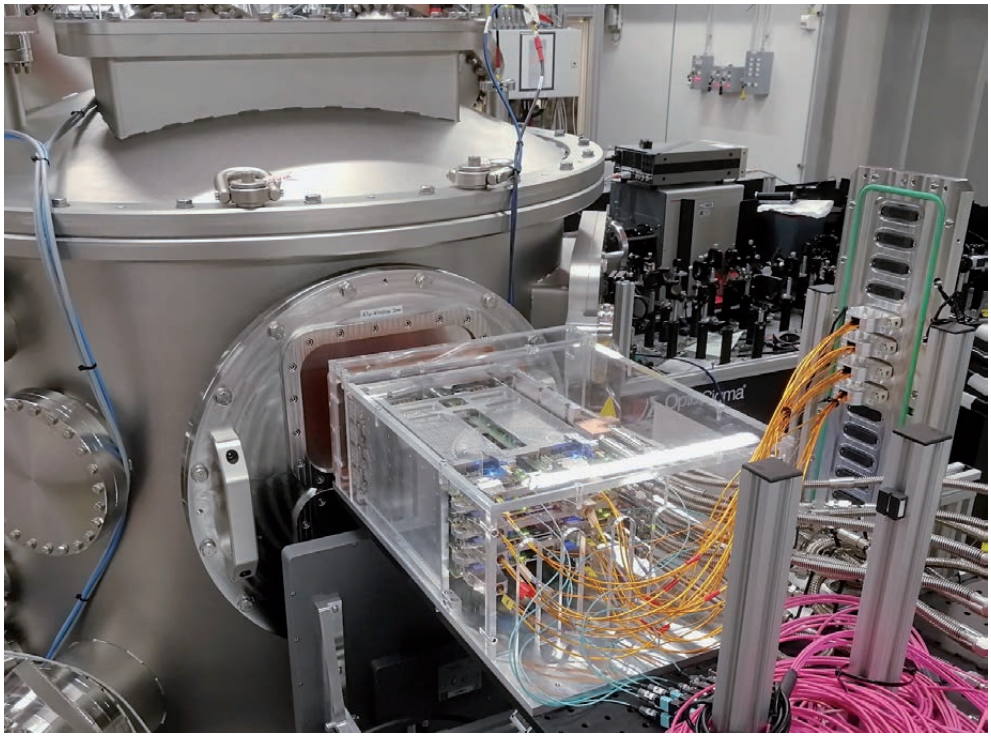

Figure 2
AGIPD 0.5 MPx prototype detector system at Interaction Chamber 2 at the HED instrument of the European XFEL.

environments needed. Funding is provided by the Helmholtz Association via strategic investment in the Helmholtz-International Users consortium hRIXS. The project is partially supported by the ERC Advanced Grant 'EDAX' at Potsdam University. A high-end detector capability is funded by Finnish partners through a FIRI grant. The hRIXS consortium includes partners from Germany, Switzerland, Finland, France, Sweden, Italy and the UK. The project is coordinated by Potsdam University in close collaboration with DESY and European XFEL.

HIBEF

Different drivers for experiments at the High Energy Density (HED) instrument of European XFEL are contributed by the HIBEF user consortium, which is led by the Helmholtz-Zentrum Dresden-Rossendorf in collaboration with DESY and the Central Laser Facility (CLF) from Rutherford Appleton Laboratory (UK) as the major consortium partners. This includes optical lasers and a diamond-anvil cell (DAC) setup with an AGIPD detector as well as a platform for diffraction experiments using pulsed magnetic fields.

In 2020 installation of the high-intensity laser ReLaX has been completed and first test experiments have been successfully performed. These included commissioning of an HAPG analysing crystal setup, which discriminates the bremsstrahlung background produced by the laser sample interaction from the SAXS signals. The high-energy laser DIPOLE 100X, which is contributed by CLF, is currently recommissioned at European XFEL. This system will enable high-pressure science like ramped and shock compression reaching multi-Mbar pressures and multi-eV temperatures. The beam transport system, frequency doubling unit and the velocity interferometer system for any reflector (VISAR) have been designed and are now in production. The diffraction platform in Interaction Chamber 2 for use in conjunction with the DiPOLE laser is currently in procurement and manufacturing.

Since its start of operation in 2019 the DAC setup contributed by DESY for the study of materials under static compression was successfully used in a first campaign by an international research team. An in-air AGIPD detector prototype was successfully tested for DAC experiments in combination with X-ray heating and pulsed laser heating. The MHz frame rate of this detector allows to exploit the European XFEL pulse train structure for the study of fast processes. The setup for dynamically driven DACs will be completed in the first half of 2021. A capacitor bank and a dedicated coil, designed by HZDR, produce high magnetic fields. The capacitor bank passed the final design review in 2020, first solenoid coil tests and procurement of a heavy load goniometer started.

With the described advancements the instruments are prepared for several community proposals relying on HIBEF contributions which are scheduled for beamtime in the first half of 2021: the ReLaX laser commissioning, X-ray heating of low-Z materials in a DAC, dynamic compression experiments in dynamic DACs (dDACs) and pulsed laser heating in DACs.

Contact:
SFX: Henry Chapman, CFEL/DESY and Universität Hamburg, henry.chapman@desy.de
HIBEF: Thomas Cowan, HZDR, t.cowan@hzdr.de
hRIXS: Alexander Föhlisch, Potsdam University and HZB, alexander.foehlisch@helmholtz-berlin.de

References

1. J. Knoska et al., Nat. Commun. 11, 657 (2020).
2. A. Echelmeier et al., Nat. Commun. 11, 4511 (2020).

DESY Innovation and Technology Transfer

Envisaged spin-off will offer complex thin film deposition

Thin film structures are essential building blocks for scientific and technological applications. They can consist of a single film to serve as electrical contact or can be stacked to hundreds of layers for complex optics. In photon science, users require elaborate film structures with atomic layer precision, nowadays even in large numbers of identical quality. Only this ensures the repeatability and reproducibility of serial measurement approaches with destructive beam properties. Industry on the other side lacks specialised vacuum equipment for three-dimensional coatings and needs new approaches to obtain novel thin film materials. DESY's planned deposition spin-off will tackle all of these demands.

The spin-off team has emerged from an in-house group with a long tradition in self-developed vacuum thin film technology (Magnetism and Coherent Phenomena / Röhlsberger). The group has recently set up two magnetron sputter-deposition devices with innovative and patented mechaniscs [1], which could serve as a strong basis for unique coating tasks that would not be commercially available otherwise. The first device enables functional thin film developments as well as complex multilayer coatings on small and medium sized planar and three-dimensional objects. The second one, which has been developed within the Helmholtz validation project HVF-059 "Magnetic Sensors" and was finalised in 2020 (Fig. 1), can now be used to transfer thin film technologies to significantly larger scales of industrial relevance.

Figure 1

View into the new four metre long vacuum deposition chamber with seven magnetron sputter sources. The device enables precise multilayer deposition on objects up to one metre in length or 25 centimetre in width, as well as homogeneous coatings of three-dimensional objects. Sample stage, aperture system and the rectangular sputter sources can be freely positioned during the deposition, enabling a new level of flexibility for the coating process.

Next to multilayer deposition on planar substrates with a length of up to one meter, this automated second device enables an unrivalled high-quality coating of three-dimensional objects with a film structure precision in the monolayer regime. This capability is supported by an in-house-developed control software that facilitates linear and rotary movements of the sample/object and the sputter sources in the ultra-high vacuum (UHV) chamber to adjust the angle and direction of the deposited atoms relative to the surface. In this way, this system can be also used to perform oblique incidence deposition (OID) as an effective method to customise the layer properties, such as porosity as well as structural and magnetic anisotropies.

Currently, both of the UHV devices can be used to perform multilayer coatings of up to seven materials in one run: metals, oxides and ceramics via DC, RF and pulsed power supplies. The possibility of reactive deposition and *in situ* annealing enlarges the deposition portfolio, and quality control is ensured via automated processing and post characterisation.

DESY and the Helmholtz Association have confirmed to support this project via the Helmholtz Enterprise Fund in November 2020 and will enable the team to launch their spin-off next year. The aim is to offer this service with full capacity in the second half of 2021. Up to then, photon science users, but also industrial companies, are welcome to discuss their deposition demands with the team and benefit from demonstrator depositions to test the functionality.

Contact: Mehdi Ramin Moayed, mehdi.ramin@desy.de
Kai Schlage, kai.schlage@desy.de

Reference

1. K. Schlage et al., An apparatus for depositing material on the surface of a substrate, EP18179694.7

DESY Photon Science facilities on the research campus Hamburg-Bahrenfeld (August 2020).

Facts and Numbers

FLASH

Experimental halls and parameters

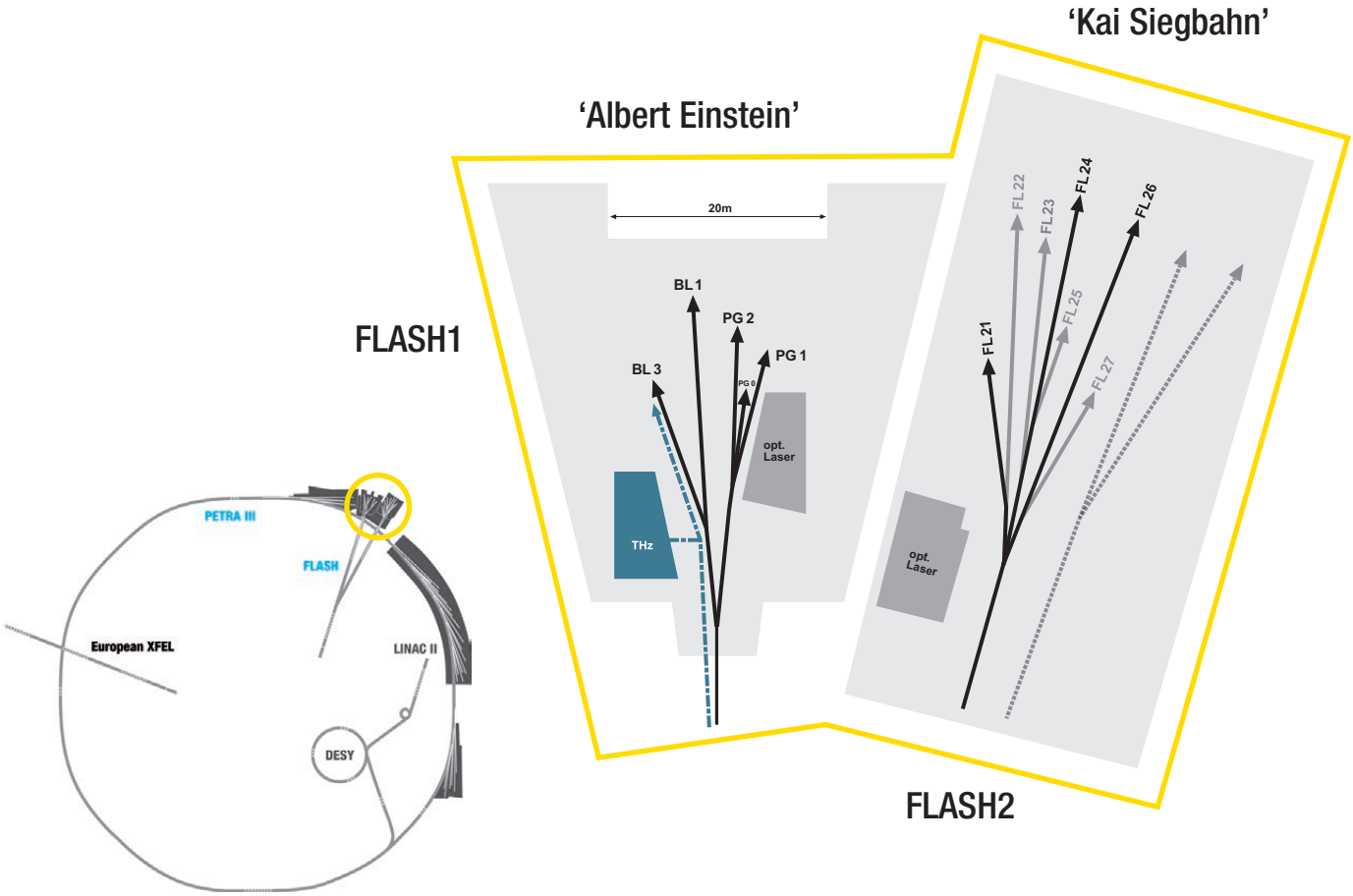

FLASH - machine parameters

	FLASH1	FLASH2
Electron energy range	0.35 – 1.25 GeV	0.4 – 1.25 GeV
Normalised emittance at 1 nC (rms)	1.4 mm mrad	1.4 mm mrad
Energy spread	200 keV	500 keV
Electron bunch charge	0.02 – 1.2 nC	0.02 – 1 nC
Peak current	1 – 2.5 kA	1 – 2.5 kA
Electron bunches per second (to be shared between FL1 and FL2)	5000	5000

FLASH - lasing parameters

	FLASH1	FLASH2
Photon energy fundamental	24 – 295 eV	14 – 310 eV
Wavelength fundamental	51 – 4.2 nm	90 – 4 nm
Photon pulse duration (FWHM)	30 – 200 fs	10 – 200 fs (estimated)
Peak power	1 – 5 GW	1 – 5 GW
Single photon pulse energy (average)	1 – 500 µJ	1 – 1000 µJ
Spectral width (FWHM)	0.7 – 2 %	0.5 – 2 %
Photons per bunch	10^{11} – 10^{14}	10^{11} – 10^{14}
Peak brilliance photons/sec/mm^2/mrad^2/0.1%	10^{28} – 10^{31}	10^{28} – 10^{31}

PETRA III

Experimental halls and parameters

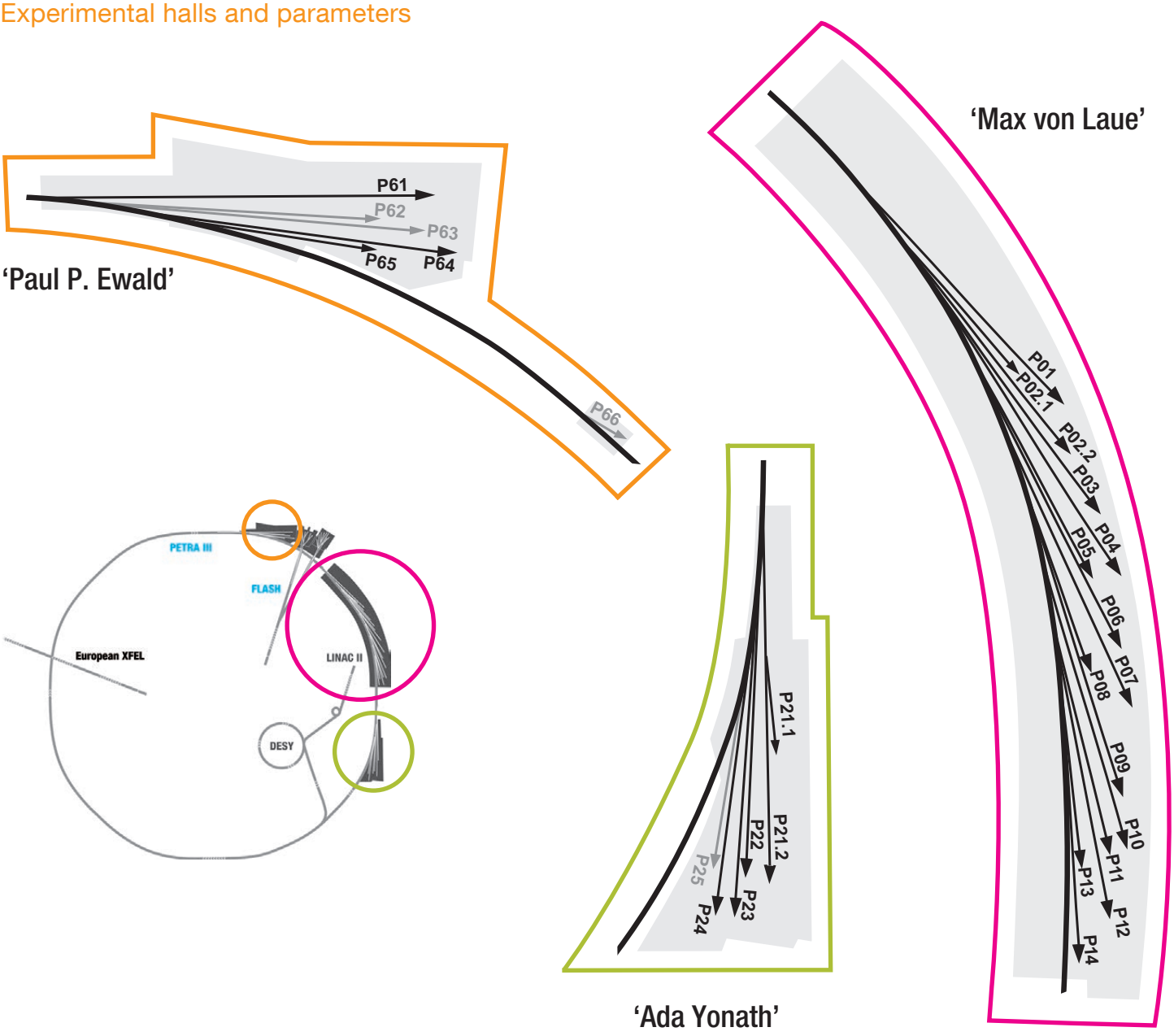

PETRA III - machine parameters

Electron energy	6.08 GeV
Circumference of the storage ring	2304 m
Number of bunches	960 or 480 (brightness mode) 60 or 40 (timing mode)
Bunch separation	8 ns, 16 ns, 128 ns, 192 ns
Electron beam current	100 mA (timing mode) 120mA (brightness mode)
Horizontal electron beam emittance	1.3 nmrad
Vertical electron beam emittance	0.01 nmrad
Electron beam energy spread (rms)	0.1%
Horizontal x vertical beam size (rms) at 5 m undulator (high β section) and 10 keV photon energy	141 µm x 5.2 µm
Horizontal x vertical beam size (rms) at 5 m undulator (low β section) and 10 keV photon energy	36 µm x 5.7 µm

FLASH

Beamlines

FLASH1 experimental hall 'Albert Einstein'

BL1	non-monochromatic FEL photons Kirkpatrick-Baez (KB) focusing optics, FEL focal spot of ~7 µm × 8 µm (FWHM)	
	split-and-delay unit for XUV pump – XUV probe experiments (mirrors for 13.57 nm, - 30 ps to + 650 ps delay)	*TU Berlin*
	optional pump – probe experiments using the FLASH1 optical laser system for BL1 and BL3	
	4-mirror polariser for variable FEL polarisation from 30 – 70 eV	*TU Berlin*
	permanent end station: multipurpose CAMP chamber with pnCCD detectors, electron and ion spectrometers and collinear incoupling optics for optical laser	
BL2	BL2 has been dismantled and is no longer available	
BL3	non-monochromatic FEL photons, spectral range: > 4.5 nm (carbon coated optics) focused to ~ 20 µm / unfocussed beam size ~ 5 – 10 mm (FWHM, depending on wavelength)	
	optional pump – probe experiments using the FLASH1 optical laser system for BL1 and BL3	
	4-mirror polariser for variable FEL polarisation from 30 – 70 eV	*TU Berlin*
	optional pump – probe experiments using THz radiation: - tunable: 10 – 230 µm; up to 150 µJ/pulse; ~ 10% bandwidth - broadband at 200 µm; up to 10 µJ/pulse; ~ 100% bandwidth - synchronised and phase stable to X-ray pulses (down to 5 fs) - delivered to the experiment via vacuum beamline as: (i) ultra-high vacuum (~ 10^{-8} mbar), shorter delay between THz and X-ray (~ 4 m path difference); can accommodate up to 0.3 m wide setup (ii) high vacuum (~ 10^{-6} mbar), longer delay between THz and X-ray (~ 7 m path difference); can accommodate up to 2 m wide setup - UHV chamber with mounts for refocusing XUV optics to compensate for XUV/THz path delay	
	about 3 × 4 m platform for user-provided end station	
PG1	high resolution plane grating XUV monochromator (SX 700 type, < 10^{-4} bandwidth, carbon coated optics): - variable combination of photon flux and resolution (from high flux to high resolution) - controlled temporal-spectral properties at moderate resolution for pump – probe experiments - high photon flux with harmonic filtering Kirkpatrick-Baez (KB) refocusing optics, FEL focal spot down to 5 µm FWHM (vertically, monochromator exit slit size dependent)	
	permanent end station: - XUV-Raman spectrometer for high-resolution and time-resolved RIXS measurements on solid samples (15 - 400 K, resolving power ~ 1700, time resolution 170 - 300 fs FWHM) - optional pump – probe experiments (RIXS; XAS + reflectivity with angular resolution) using the FLASH1 optical laser system for PG1 and PG2	
PG2	uses the same monochromator as PG1 50 µm focus	
	XUV beam splitter with variable time delay (±6 ps) for time resolved studies	
	optional pump – probe experiments using FLASH1 optical laser system for PG1 and PG2	
	about 3 × 4 m platform for user-provided end station	

FLASH1 optical / NIR laser system for pump – probe experiments for beamlines **BL1 and BL3**

central wavelength	810 nm
spectral bandwidth	25 nm
intra-burst repetition rate	single pulse
number of pulses per burst	1
pulse duration	< 60 fs FWHM, < 200 ps FWHM (uncompressed)
timing jitter to FEL	< 60 fs rms
pulse energy	0 – 10 mJ (before coupling to chamber), 0 – 7 mJ (at interaction region)
polarisation	flexible
peak intensity	> 10^{14} W/cm²
time delay to FEL	- 4 ns to + 4 ns, 10 fs resolution, larger delays optional
energy stability	< 10% pulse-to-pulse peak (3% rms)

Harmonic generation conversion to 400 nm, 266 nm and 200 nm central wavelength are available with conversion efficiencies of > 30% SHG, > 5% THG

FLASH1 optical / NIR laser system for pump – probe experiments for beamlines **PG1 and PG2**

central wavelength	1030 nm
spectral bandwidth	30 to 50 nm (pre-set for experiment)
intra-burst repetition rate	1 MHz
number of pulses per burst	1 – 800
pulse duration	60 – 100 fs FWHM
timing jitter to FEL	< 75 fs rms
pulse energy	0 – 30 µJ (at interaction point)
polarisation	flexible
peak intensity	> 10^{14} W/cm^2
time delay to FEL	- 4 ns to + 4 ns, 10 fs resolution, larger delays optional
energy stability	< 10% pulse-to-pulse peak (3% rms)

Harmonic generation conversion to 515 nm, 343 nm or 257 nm central wavelength can be provided

FLASH2 experimental hall 'Kai Siegbahn'

FL24	non-monochromatic FEL photons wavelength range: 4 – 90 nm fundamental Kirkpatrick-Baez (KB) focusing optics with variable foci down to < 10 µm (FWHM)/unfocussed beam size ~ 5 – 10 mm (FWHM, depending on wavelength)	
	optional pump – probe experiments using FLASH2 optical laser system	
	grazing incidence split-and-delay unit with ±12 ps time delay	*Univ. Münster*
	about 3 × 4 m platform for user-provided end station	
FL26	non-monochromatic FEL photons wavelength range: 6 – 90 nm fundamental	
	optional pump – probe experiments using FLASH2 optical laser system	
	permanent end station: - reaction microscope (REMI) for time-resolved AMO spectroscopy - grazing incidence delay-line and refocusing optics: FEL focal spot < 10 µm × 10 µm (FWHM, depending on wavelength) - ±2.7 ps time delay range, 1 fs precision	*MPI-K Heidelberg*

FLASH2 optical / NIR laser system for pump – probe experiments for beamlines **FL24 and FL26**

central wavelength	700 to 900 nm (fast tuneable)
spectral bandwidth	30 to 100 nm (pre-set for experiment)
intra-burst repetition rate	100 kHz
number of pulses per burst	1 – 80
pulse duration	15 – 35 fs FWHM (compressed to 1.1 × bandwidth limit), < 500 fs FWHM (uncompressed)
timing jitter to FEL	< 75 fs rms
pulse energy	0 – 250 µJ (before coupling to chamber), 0 – 150 µJ (at interaction region)
polarisation	flexible
focus size (1/e^2 diameter)	FL24: < 100 µm, FL26: < 50 µm
peak intensity	> 10^{14} W/cm^2
time delay to FEL	- 4 ns to + 4 ns, 10 fs resolution, larger delays optional
energy stability	< 10% pulse-to-pulse peak (3% rms)

Harmonic generation conversion to 400 nm and 266 nm central wavelength are available with conversion efficiencies of > 30% SHG, > 5% THG

All FLASH beamlines provide online photon diagnostics for intensity, wavelength and beam position, fast shutter, aperture and filter sets.

Acknowledgement

We would like to acknowledge all contributions to the development and operation of FLASH and PETRA III beamlines and instruments provided within the framework of BMBF-Verbundforschung, and as part of collaborations with the Department of Science and Technology (Government of India) 'India@DESY', the Ruprecht-Haensel-Laboratory (Kiel University), the Max Planck Society and the Forschungszentrum Jülich.

PETRA III

Beamlines

PETRA III experimental hall 'Max von Laue'

Beamline and instruments		Operated by
R	*indicates possibility of remote user operation*	
P01	High Resolution Dynamics 10 m U36 | 2.5 – 80 keV	DESY
	Nuclear resonant scattering	DESY
	Resonant inelastic scattering	DESY | MPG
	X-ray Raman scattering	DESY | MPG
P02.1	Powder Diffraction and Total Scattering 2 m U23 | 60 keV	DESY
	Standard and *in situ* powder diffraction	DESY
	Standard and *in situ* total scattering	DESY
P02.2	Extreme Conditions 2 m U23 | 10 – 60 keV	DESY
	Laser heated experiment for diamond anvil cells	DESY
	General purpose experiment for high pressure applications	DESY
P03	Micro and Nano-SAXS/WAXS 2 m U29 | 8 – 23 keV	DESY
	Micro-beam small and wide angle scattering	DESY
	Nano-beam scattering and diffraction	DESY | HZG | collaborators
P04	Variable Polarisation Soft X-rays 5 m UE65 | 250 – 2800 eV	DESY
	UHV diffractometer and soft X-ray spectrometer	DESY
	Photon-ion spectrometer (PIPE)	DESY | collaborators
	Ultra-high resolution photoelectron spectroscopy (ASPHERE)	DESY | collaborators
	Soft X-ray absorption holographic imaging instrument	DESY | collaborators
	Nano-focus apparatus for spatially resolved spectroscopy	DESY | collaborators
P05	Micro and Nano-Imaging 2 m U29 | 8 – 50 keV	HZG
	Micro-tomography	HZG
	Nano-tomography	HZG
P06	Hard X-ray Micro- and Nano-probe 2 m U32 | 5 – 100 keV	DESY
	Micro-probe	DESY
	Nano-probe	DESY
P07	High Energy X-ray Materials Science 4 m IVU21 | 50 – 200 keV	HZG
	Surface diffraction and grazing incidence total scattering	DESY
	Heavy load diffractometer	HZG
	Grain mapper	HZG
	High energy tomography	HZG
P08	High Resolution Diffraction 2 m U29 | 5.4 – 29.4 keV	DESY
	High resolution diffractometer	DESY
	Liquid surface diffractometer	DESY | collaborators
	Langmuir trough in-plane diffractometer	DESY
P09	Resonant Scattering and Diffraction 2 m U32 | 2.7 – 31 keV	DESY
	Single crystal resonant elastic X-ray scattering and diffraction (4 K < T < 750K)	DESY
	Single crystal REXS with magnetic fields (0.3 K < T < 300 K; B < 14 T)	DESY
	High pressure single crystal REXS (4 K < T < 300 K; p < 30 GPa)	DESY
	X-ray circular magnetic dichroism (> 4 K; < 6 T; < 2 T for linear dichroism)	DESY
	X-ray resonant magnetic reflectivity	DESY
P10	Coherence Applications 5 m U29 | 4 – 20 keV	DESY
	X-ray photon correlation spectroscopy (SAXS/WAXS geometry) (5 – 15 keV)	DESY
	Bragg coherent diffraction imaging (5 – 13 keV)	DESY
	GINIX – Nano-focusing setup (8 and 13.8 keV)	DESY | collaborators
P11	Bio-Imaging and Diffraction 2 m U32 | 2.4 – 30 keV	DESY
R	Macromolecular crystallography (6 – 26 keV)	DESY | HZI | U Lübeck
	Serial crystallography (6 – 26 keV)	DESY

Beamline and instruments		Operated by
	R *indicates possibility of remote user operation*	
P12	Bio SAXS 2 m U29 | 4 – 20 keV	EMBL
	R Small angle and wide angle X-ray scattering	EMBL
	Time resolved X-ray scattering	EMBL
	Anomalous small angle X-ray scattering	EMBL
P13	Macromolecular Crystallography 2 m U29 | 4.5 – 17.5 keV	EMBL
	R Macromolecular crystallography	EMBL
P14	Macromolecular Crystallography and Imaging 2 m U29 | 6 – 20 keV	EMBL
	R Macromolecular crystallography (6 – 20 keV)	EMBL
	R Serial crystallography (6 – 20 keV)	EMBL
	High throughput micro-tomography (6 – 20 keV)	EMBL
	Time-resolved serial crystallography (12.7 keV)	EMBL | U Hamburg

PETRA III experimental hall 'Ada Yonath'

P21.1	Swedish Materials Science Beamline side branch: 2 m U29 | 50, 80, 100 keV	Center for X-rays in Swedish Materials Science (CeXS) | DESY
	Diffuse scattering and total scattering	CeXS | DESY
P21.2	Swedish Materials Science Beamline 4 m IVU21 | 40 – 150 keV	Center for X-rays in Swedish Materials Science (CeXS) | DESY
	Multi-purpose triple-axis diffractometer	CeXS | DESY
	Small angle scattering	CeXS | DESY (in commissioning)
	Grain mapper	CeXS | DESY (in commissioning)
P22	Hard X-ray Photoelectron Spectroscopy 2 m U33 | 2.4 – 15 keV	DESY
	Hard X-ray photoelectron spectrometer (HAXPES)	DESY
	Ambient pressure XPS (POLARIS)	DESY | collaborators
	Hard X-ray photoemission electron microscope (HAXPEEM)	DESY | collaborators
P23	*In situ* Nano-Diffraction Beamline 2 m U32 | 5 – 35 keV	DESY
	XRD and secondary processes, *in situ* and complex environments	DESY
	Tomography	DESY|KIT (operation planned 2022)
P24	Chemical Crystallography 2 m U29 | 8, 15 – 44 keV	DESY
	Single crystal diffraction in complex sample environments	DESY
	Small molecule crystallography	DESY
P25	t.b.d.	not yet funded

PETRA III experimental hall 'Paul P. Ewald'

P61	High Energy Wiggler Beamline 10 x 4 m damping wigglers | white beam btw. 30 – 250 keV	
	High energy engineering materials science	HZG (operation planned I-2021)
	Large volume press — extreme conditions	DESY
P62	Anomalous Small Angle X-ray Scattering 2 m U32 | 3.5 – 35 keV	DESY (operation planned I-2021)
	Anomalous small angle X-ray scattering	DESY
	SAXS tomography	DESY
P63	t.b.d.	not yet funded
P64	Advanced X-ray Absorption Spectroscopy 2 m U32 | 4 – 44 keV	DESY
	Ex situ and *in situ* XAS	DESY
	High-resolution X-ray emission spectroscopy (non-resonant and resonant)	DESY
	QEXAFS	DESY
P65	Applied X-ray Absorption Spectroscopy 36 cm U32 | 4 – 44 keV	DESY
	Ex situ and *in situ* XAFS of bulk samples	DESY
P66	Superlumi *(between PETRA III halls 'Paul P. Ewald' and 'Max von Laue')* Bending magnet | 4 – 40 eV	DESY (operation planned 2021)
	Time-resolved luminescence spectroscopy	DESY

Beamtime statistics 2020

FLASH
Operation period 2020

	User beamtime	Machine studies and user experiment preparation	Maintenance	Shutdown and commissioning	Cryo-experiment*
FLASH (Linac)					
1 Jan – 26 Oct	2354 h	1562 h	20 h	1431 h	
planned for 27 Oct – 31 Dec	672 h	516 h	12 h	377 h	
Corona break				568 h	1272 h
FLASH1					
1 Jan – 26 Oct	1637 h				
planned for 27 Oct – 31 Dec	336 h				
FLASH2					
1 Jan – 26 Oct	1028 h				
planned for 27 Oct – 31 Dec	336 h				

*The Cryo-Experiment was a special type of machine operation 2020 during the Corona break (mid-April to early June)

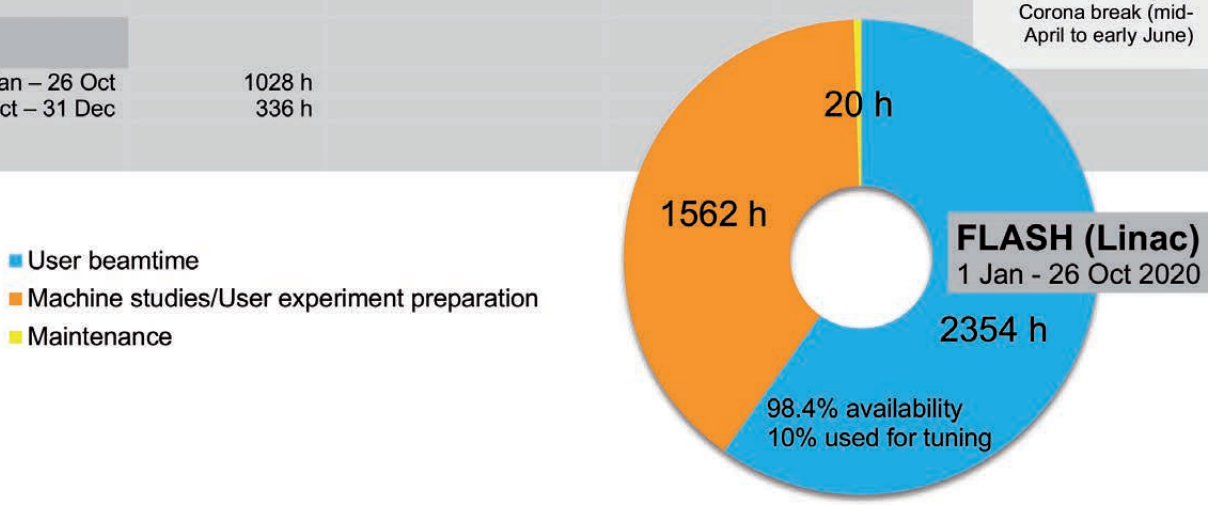

PETRA III
Operation period 2020

	User beamtime	Machine studies and test runs	Maintenance	Shutdown
1 Jan – 10 Dec	4569 h	992 h	154 h	
planned for 11 Dec – 31 Dec	228 h	11 h		
				2830 h

run periods:
2 Mar – 5 Jul
Corona shutdown 20 – 30 March
Corona research 31 March – 3 May
3 Aug – 21 Dec

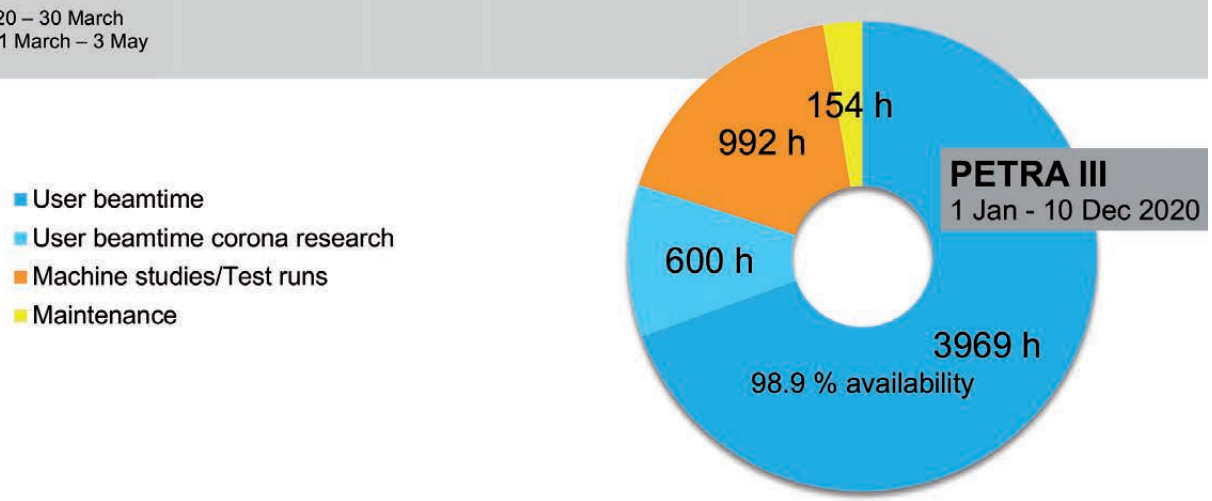

Committees 2020

Photon Science Committee PSC — advises the DESY Photon Science management

Christian David (chair)	Paul Scherrer Institut, Villigen, CH
Stefan Eisebitt (vice chair)	MBI and Technische Universität Berlin, DE
Serena DeBeer	MPI-CEC, Mülheim an der Ruhr, DE
Kristina Djinovic-Carugo	Universität Wien, AT
Jan-Dierk Grunwaldt	Karlsruher Institut für Technologie, Karlsruhe, DE
Mark Heron	Diamond Light Source Ltd, Didcot, UK
Simo Huotari	University of Helsinki, FI
Sarah Köster	Georg-August-Universität Göttingen, DE
Edvin Lundgren	Lund University, SE
Arwen Pearson	CUI, Universität Hamburg, DE
Thomas Pfeifer	MPI for Nuclear Physics, Heidelberg, DE
Harald Reichert	ESRF, Grenoble, FR
Daniela Rupp	Eidgenössische Technische Hochschule Zürich, CH
Bernd Schmitt	Paul Scherrer Institut, Villigen, CH
Thomas Schröder	Humboldt-Universität zu Berlin and IKZ, Berlin, DE
Andrea Somogyi	Synchrotron SOLEIL, Saint-Aubin, FR
Stefan Vogt	Argonne National Laboratory, Lemont, US
Nele Müller (PSC secretary)	DESY, Hamburg, DE

Laser Advisory Committee LAC — advises DESY and European XFEL

Jonathan Zuegel (chair)	Laboratory For Laser Energetics, Rochester, US
Miltcho Danailov	Elettra-Sincrotrone Trieste, IT
Thomas Dekorsy	Deutsches Zentrum für Luft- und Raumfahrt e.V., Stuttgart, DE
Alan Fry	SLAC, Menlo Park, US
Patrick Georges	Institut d'Optique Paris, FR
Catherine Le Blanc	Ecole Polytechnique,Laboratoire LULI, FR
Emma Springate	STFC Rutherford Appleton Laboratory, US
William E. White	SLAC, Menlo Park, US
Jörg Hallmann (LAC secretary)	European XFEL, Schenefeld, DE
Nele Müller (LAC secretary)	DESY, Hamburg, DE

DESY Photon Science User Committee DPS-UC — represents the user community

Peter Müller-Buschbaum (chair)	Technische Universität München, DE
Natalia Dubrovinskaia	Universität Bayreuth, DE
Markus Mezger	MPI für Polymerforschung, Mainz, DE
Daniela Rupp	Eidgenössische Technische Hochschule Zürich, CH
Gregor Witte	Ludwig-Maximilians-Universität München, DE

Komitee Forschung mit Synchrotronstrahlung KFS — representative body of the German SR and FEL user community (election in autumn 2020)

Bridget Murphy (chair until 2020)	Christian-Albrechts-Universität zu Kiel, DE
Jan-Dierk Grunwaldt (vice chair until 2020)	Karlsruher Institut für Technologie, Karlsruhe, DE
Peter Albers (-2020)	Evonik Technology & Infrastructure GmbH, DE
Stefan Eisebitt (-2020)	MBI and Technische Universität Berlin, DE
Ronald Frahm (-2020)	Universität Wuppertal, DE
Taisia Gorkhover (2020-)	Universität Hamburg, DE
Christian Gutt	Universität Siegen, DE
Birgit Kanngießer	Technische Universität Berlin, DE
Sarah Köster	Georg-August-Universität Göttingen, DE
Dirk Lützenkirchen-Hecht (2020-)	Bergische Universität Wuppertal, DE
Kai Rossnagel (-2020)	Christian-Albrechts-Universität zu Kiel, DE
Hermann Schindelin (-2020)	Julius-Maximilians-Universität Würzburg, DE
Andrea Thorn (2020-)	Julius-Maximilians-Universität Würzburg, DE

The European Synchrotron and FEL User Organisation ESUO (Executive Board)

Carla Bittencourt	Université de Mons, BE
Martin Feiders	Radboud Universiteit, Nijmegen, NL
Annick Froideval	Helmholtz-Zentrum Dresden-Rossendorf, DE
Krystyna Jablonska	Institute of Physics, PAN, Warsaw, PL
Derek Logan	Lund University, SE
Carlo Mariani	Sapienza Università di Roma, IT
Ullrich Pietsch	Universität Siegen, DE
Ryszard Sobierajski	Institute of Physics, PAN, Warsaw, PL

For national delegates please see: http://www.wayforlight.eu/en/users/esuo/

Project Review Panels 2020

Bulk and surface diffraction	P08 I P23 I P24
Derek (Del) Atkinson	University of Durham, GB
Michael Hanke	Paul-Drude-Institut für Festkörperelektronik, Berlin, DE
Christiane A. Helm	Universität Greifswald, DE
Beate Kloesgen	University of Southern Denmark Odense, DK
Fouad Maroun	Ecole Polytechnique Palaiseau, FR
Reinhard Neder	Friedrich-Alexander-Universität Erlangen-Nürnberg, DE
Beatriz Noheda	University of Groningen, NL
Oliver Oeckler	Universität Leipzig, DE
Sander van Smaalen	Universität Bayreuth, DE
Matthias Zschornak	Technische Universität, Bergakademie Freiberg, DE
Florian Bertram, Dimitri Novikov, Martin Tolkiehn (PRP secretaries)	DESY, Hamburg, DE

Coherent applications	P10
Sylvain Bohic	Research Centre INSERM, Grenoble, FR
Manfred Burghammer	ESRF, Grenoble, FR
Ralf Busch	Universität des Saarlandes, Saarbrücken, DE
Gaetano Campi	Consiglio Nazionale delle Ricerche, Roma, IT
Birgit Hankiewicz	Universität Hamburg, DE
Guido Meier	MPI für Struktur und Dynamik der Materie, Hamburg, DE
Ullrich Pietsch	Universität Siegen, DE
Beatrice Ruta	Université Claude Bernard, Lyon, FR
Jesper Wallentin	Lund University, SE
Michael Sprung (PRP secretary)	DESY, Hamburg, DE

EXAFS	P64 I P65
Matthias Bauer	Universität Paderborn, DE
Dmitry Doronkin	Karlsruher Institut für Technologie (KIT), Karlsruhe, DE
Stephan Klemme	Westfälische Wilhelms-Universität, Münster, DE
Aleksej Kuzmin	University of Latvia, Riga, LV
Christina Roth	Universität Bayreuth, DE
Karel Saksl	Slovak Academy of Sciences, Kosice, SK
Claudia Schnohr	Universität Leipzig, DE
Kajsa Sigfridsson Clauss	MAX IV Laboratory, Lund, SE
Andrea Zitolo	Synchrotron SOLEIL, Gif sur Yvette, FR
Wolfgang Caliebe, Edmund Welter (PRP secretaries)	DESY, Hamburg, DE

Extreme conditions	P02.2 I P61 LVP
Daniel Errandonea	Universitat de València, ES
Ulrich Häussermann	Stockholm University, Stockholm, SE
Nadège Hilairet	Université des Sciences et Techniques, Lille, FR
Konstantin Litasov	Russian Academy of Sciences, Moscow, RU
Malcolm McMahon	University of Edinburgh, GB
Marco Merlini	Università degli Studi di Milano, IT
Guillaume Morard	Sorbonne Université, Paris, FR
Carmen Sanchez-Valle	Westfälische Wilhelms-Universität, Münster, DE
Chrystele Sanloup	Sorbonne Université, Paris, FR
Andreas Zerr	Université Paris Nord, FR
Hanns-Peter Liermann, Robert Farla (PRP secretaries)	DESY, Hamburg, DE

HAXPES	P22
Maria Hahlin Uppsala	University Uppsala, SE
Martina Müller	Universität Konstanz, DE
Christian Papp	Friedrich-Alexander-Universität Erlangen-Nürnberg, DE
Anna Regoutz	University College London, GB
Vladimir N. Strocov	PSI, Villigen, CH
Christoph Schlüter (PRP secretary)	DESY, Hamburg, DE

High energy diffraction	P07 (DESY) I P21.1 I P21.2
Emil Bozin	Brookhaven National Laboratory, Upton, US
Per-Anders Carlsson	Chalmers University of Technology, Gothenborg, SE
Magnus Colliander	Chalmers University of Technology, Gothenborg, SE
Jens Gibmeier	Karlsruher Institut für Technologie (KIT), Karlsruhe, DE
Markus Hücker	Weizmann Institute of Science, Rehovot, IL
Kirsten Marie Jensen	University of Copenhagen, DK
Herbert Over	Justus-Liebig-Universität, Gießen, DE
Walter Reimers	Technische Universität Berlin, DE
Joachim Wollschläger	Universität Osnabrück, DE
Ann-Christin Dippel, Martin von Zimmermann, Ulrich Lienert (PRP secretaries)	DESY, Hamburg, DE

Imaging	P05 I P06
Matthias Alfeld	Delft University of Technology, NL
Martin Bech	Lund University, SE
Ulrike Boesenberg	European XFEL, Schenefeld, DE
Oliver Bunk	PSI, Villigen, CH
David Fenning	University of California, San Diego, US
Frank Friedrich	Universität Hamburg, DE
Julia Herzen	Technische Universität München, Garching, DE
Florian Meirer	University of Utrecht, NL
Bert Mueller	Universität Basel, Allschwil, CH
Guillermo Requena	RWTH Aachen, DE
Jürgen Thieme	Brookhaven National Laboratory, Upton, US
Katarina Vogel-Mikus	University of Ljubljana, SI
Fabian Wilde, Gerald Falkenberg (PRP secretaries)	DESY, Hamburg, DE

Inelastic, magnetic and resonant scattering	P01 | P09
Manuel Angst	Forschungszentrum Jülich GmbH, DE
Elizabeth Blackburn	Lund University, SE
Kristina Kvashnina	Helmholtz-Zentrum Dresden-Rossendorf (HZDR), DE
Catherine McCammon	Universität Bayreuth, DE
Daniel Merkel	Wigner Research Centre for Physics, Budapest, HU
Marco Moretti	Politecnico di Milano, IT
Valerio Scagnoli	ETH Zürich, CH
Volker Schünemann	Technische Universität Kaiserslautern, DE
Joachim von Zanthier	Friedrich-Alexander-Universität Erlangen-Nürnberg, DE
Ilya Sergeev, Sonia Francoual (PRP secretaries)	DESY, Hamburg, DE

Materials science (HZG)	P07 (HZG) | P61 (HZG)
Jeremy Epp	Leibniz-IWT, Bremen, DE
Guillaume Geandier	Institut Jean Lamour, Nancy, FR
Astrid Haibel	Beuth Hochschule für Technik, Berlin, DE
Patrick Huber	Technische Universität Hamburg-Harburg, DE
Ingo Manke	Helmholtz Zentrum Berlin f. Materialien und Energie, DE
Svea Mayer	Montan Universität, Leoben, AT
Thomas Niendorf	Universität Kassel, DE
Wolfgang Pantleon	Technical University of Denmark, Lyngby, DK
Dieter Lott (PRP secretary)	Helmholtz-Zentrum Geesthacht, DE

Powder diffraction	P02.1
Dorthe Bomholdt Ravnsbæk	University of Southern Denmark, Odense, DK
Robert Dinnebier	MPI für Festkörperforschung, Stuttgart, DE
Mads Ry Jørgensen	Aarhus University, DK
Gregor Kieslich	Technische Universität München, Garching, DE
Simon Pauly	Leibniz-IFW, Dresden, DE
Martin Sahlberg	Uppsala University, SE
Anatoliy Senyshyn	Technische Universität München, Garching, DE
Florian Spieckermann	Montan Universität, Leoben, AT
Claudia Weidenthaler	MPI fuer Kohlenforschung, Mülheim a.d. Ruhr, DE
Mirijam Zobel	Universität Bayreuth, DE
Martin Etter (PRP secretary)	DESY, Hamburg, DE

SAXS/WAXS/GISAXS	P03 | P62
Alexander Gerlach	Universität Tübingen, DE
Thomas Hellweg	Universität Bielefeld, DE
Marianne Liebi	Chalmers University of Technology, Gothenborg, SE
Fredrik Lundell	KTH Royal Institute of Technology, Stockholm, SE
Giuseppe Portale	University of Groningen, NL
Konrad Schneider	Leibniz-Institut für Polymerforschung Dresden e.V., DE
Stephan Roth, Sylvio Haas (PRP secretaries)	DESY, Hamburg, DE

Soft X-ray and VUV	P04
Yves Acremann	ETH Zürich CH
Arno Ehresmann	Universität Kassel, DE
Mark Golden	University of Amsterdam, NL
Jan-Erik Rubensson	Uppsala University, SE
Emma Sokell	University College, Dublin, IE
Moritz Hoesch	DESY, Hamburg, DE

Soft X-ray FEL Experiments	FLASHs
Christoph Bostedt	PSI, Villigen, CH
Hermann Dürr	Uppsala University, SE
Marion Harmand	Sorbonne Université, Paris, FR
Chris Jacobsen	Argonne National Laboratory, Argonne, US
Claudio Masciovecchio	Sincrotrone Trieste, IT
Robert Schoenlein	SLAC National Accelerator Laboratory, Menlo Park, US
Marc Simon	Sorbonne Université, Paris, FR
Marc Vrakking	Max-Born-Institut Leibniz Gesellschaft, Berlin, DE
Martin Weinelt	Freie Universität Berlin, DE
Elke Plönjes-Palm, Rolf Treusch (PRP secretaries)	DESY, Hamburg, DE

PEC: EMBL Life Science beamlines P12-P14 / PRP Bio-crystallography at P11	
Savvas Savvides (chair)	Ghent University, BE
Pau Bernadó	CBS/CNRS, Montpellier, FR
Kristina Djinovic-Carugo	Universität Wien, AT
Gwyndaf Evans	Diamond Light Source, Didcot, GB
Robert Fischetti	Argonne National Laboratory, US
Mariusz Jaskolski	Adam Mickiewicz University of Poznan, PL
Gergely Katona	University of Gothenburg, SE
Annette E. Langkilde	University of Copenhagen, DK
Javier Pérez	Synchrotron SOLEIL, Saint-Aubin, FR
Teresa Santos-Silva	Universidade NOVA de Lisboa, PT
Zehra Sayers	Sabanci University, Istanbul, TR
Joel L. Sussman	Weizmann Institute of Sciences, Rehovot, IL
Maria A. Vanoni	University of Milan, IT
Mark J. van Raaij	CNB-CSIC, ES
Gregor Witte	Ludwig-Maximilians-Universität München, DE
Christian Schroer (DESY observer)	DESY, Hamburg, DE

Photographs and Graphics:

Gesine Born, Berlin
Andrea Cartella, DESY
CFEL
Spyros Chatziefthymiou, DESY
Andre L. C. Conceição, DESY
CSSB
DESY
EMBL
European XFEL
Luca Gelisio, DESY
Nico Giordano, DESY
Sebastian Günther, DESY
Axel Heimken
Tobias Herr, DESY
Christoph Heyl, Jena/DESY
Claudia Höhne, Hamburg
Horizon Europe/European Comission
HZG
Kiel University
Felix Lehmkühler, DESY
lichtecht, Hamburg
Britta Liebaug, DESY
Marta Mayer, DESY
Alke Meents, DESY
MPG
MPSD
Jörg Müller
Heiner Müller-Elsner, Hamburg
Heshmat Noei, DESY
Chen Shen, DESY
Reimo Schaaf, Hamburg
Stephan Stern, DESY
Andrea Trabattoni, DESY
Universität Hamburg
Universität Lübeck

Acknowledgement

We would like to thank all the authors and all those who have contributed to the realisation of this Annual Report.

Imprint

Publishing and Contact:
Deutsches Elektronen-Synchrotron DESY
A Research Centre of the Helmholtz Association

Hamburg location:
Notkestr. 85, 22607 Hamburg, Germany
Tel.: +49 40 8998-0, Fax: +49 40 8998-3282
desyinfo@desy.de

Zeuthen location:
Platanenallee 6, 15738 Zeuthen, Germany
Tel.: +49 33762 7-70, Fax: +49 33762 7-7413
desyinfo.zeuthen@desy.de

Photon Science at DESY
Tel.: +49 40 8998-2304, Fax: +49 40 8998-4475
photon-science@desy.de
photon-science.desy.de

www.desy.de

ISBN 978-3-945931-34-9

Online version:
photon-science.desy.de/annual_report

Realisation:
Wiebke Laasch, Daniela Unger

Editing:
Sadia Bari, Lars Bocklage, Günter Brenner, Thomas Keller, Wiebke Laasch, Britta Niemann, Leonard Müller, Nele Müller, Christoph Schlüter, Sang-Kil Son, Sebastian Trippel, Daniela Unger, Thomas White

Layout: Sabine Kuhls-Dawideit, Büro für Grafik und Design, Halstenbek

Printing and image processing: EHS Druck GmbH, Schenefeld

Copy deadline: December 2020

HELMHOLTZ
RESEARCH FOR GRAND CHALLENGES

Deutsches Elektronen-Synchrotron DESY
A Research Centre of the Helmholtz Association

The Helmholtz Association is a community of 19 scientific-technical and biological-medical research centres. These centres have been commissioned with pursuing long-term research goals on behalf of the state and society. The Association strives to gain insights and knowledge so that it can help to preserve and improve the foundations of human life. It does this by identifying and working on the grand challenges faced by society, science and industry. Helmholtz Centres perform top-class research in strategic programmes in six core fields: Energy, Earth & Environment, Health, Aeronautics, Space and Transport, Matter, and Key Technologies.

www.helmholtz.de